Time-resolved spectroscopic studies of hematite photoelectrodes for photoelectrochemical water splitting

Mark Forster

June 2017

Supervisor: Dr. Alexander Cowan

Thesis submitted to the University of Liverpool in partial fulfilment of the degree of Doctor in Philosophy

Contents

Abstract

Time-resolved spectroscopic studies of hematite photoelectrodes for photoelectrochemical water splitting applications

Mark Forster

Harnessing the large quantities of energy delivered to the earth by the sun is one of the most promising routes to a clean, inexhaustible energy supply. However, the diurnal nature of sunlight and its variation in intensity around the globe necessitates an efficient means of storing (and transporting) solar energy on a large scale. The production of solar fuels provides a potential solution by capturing and storing solar energy in the form of chemical bonds to yield fuels which can then be stored, transported and used, as and when required.[1]

The majority of the work in this thesis focuses on the development of the metal oxide semiconductor, α-Fe_2O_3 (hematite), and its application as a photoelectrode in photoelectrochemical (PEC) water splitting systems. α-Fe_2O_3 is a promising photoelectrode material due to its suitable bandgap, low toxicity, stability, abundance and low cost.[2] However, current α-Fe_2O_3 materials are well below the maximum theoretical efficiency due to limiting factors including: poor conductivity[3], short electron–hole lifetimes[4], slow oxygen evolution reaction kinetics[5] and short hole diffusion length (2–4 nm)[6]. Modifications to α-Fe_2O_3 such as doping, nanostructuring and surface treatments are known to significantly improve activity[2] and it is vitally important that the mechanisms of improvement are fully rationalised. The work presented here uses transient absorption spectroscopy (TAS) and electrochemical measurements to probe the charge carrier dynamics and address the activity of a range of recently developed α-Fe_2O_3 photoelectrodes, including oxygen deficient hematite and acid treated hematite. The presence of trap states in α-Fe_2O_3 photoelectrodes is also addressed, and the effect surface treatments have on such trap states are explored. Finally, shell isolated nanoparticles for enhanced Raman spectroscopy (SHINERS)[7] is explored as an *in situ* technique for probing the mechanism of water oxidation on a metal oxide surface.

1. N. Armaroli and V. Balzani, *ChemPubSoc Eur.*, 2016, **22**, 32–57.

2. K. Sivula, F. Le Formal, and M. Grätzel, *ChemSusChem*, 2011, **4**, 432–449.

3. F. J. Morin, *Phys. Rev.*, 1951, **83**, 1005–1010.

4. N. J. Cherepy, D. B. Liston, J. A. Lovejoy, H. Deng, and J. Z. Zhang, *J. Phys. Chem. B*, 1998, **5647**, 770–776.

5. M. Dare-Edwards, J. Goodenough, A. Hamnett, and P. Trevelick, *J. Chem. SOC., Faraday Trans. I*, 1983, **79**, 2027–2041.

6. K. Sivula, R. Zboril, F. Le Formal, R. Robert, A. Weidenkaff, J. Tucek, J. Frydrych, and M. Grätzel, *J. Am. Chem. Soc.*, 2010, **132**, 7436–44.

7. J. F. Li, Y. F. Huang, Y. Ding, Z. L. Yang, S. B. Li, X. S. Zhou, F. R. Fan, W. Zhang, Z. Y. Zhou, D. Y. Wu, B. Ren, Z. L. Wang, and Z. Q. Tian, *Nature*, 2010, **464**, 392–395.

List of publications

During the course of this PhD the following papers have been published in peer-review journals:

- Mark Forster, Richard J. Potter, Yichuan Ling, Yi Yang, David R. Klug, Yat Li, and Alexander J. Cowan. "Oxygen Deficient α-Fe_2O_3 Photoelectrodes: A Balance between Enhanced Electrical Properties and Trap-Mediated Losses." **Chemical Science**, 2015, **6** (7), 4009–4016. (**Chapter 2**).
- Yi Yang, Mark Forster, Yichuan Ling, Gongming Wang, Teng Zhai, Yexiang Tong, Alexander J Cowan, and Yat Li. "Acid Treatment Enables Suppression of Electron-Hole Recombination in Hematite for Photoelectrochemical Water Splitting." **Angewandte Chemie International Edition**, 2016, **55** (10), 3403–3407. (**Chapter 4**).
- T. Mavrič, M. Valant, M. Forster, A.J. Cowan, U. Lavrenčič, and S. Emin. "Design of a Highly Photocatalytically Active ZnO/$CuWO_4$ Nanocomposite." **Journal of Colloid and Interface Science**, 2016, **483**, 93–101.
- Gaia Neri, Mark Forster, James J Walsh, Craig M. Robertson, Tom J. Whittles, Pau Farràs, and Alexander J. Cowan. "Photochemical CO_2 Reduction in Water Using a Co-Immobilised Nickel Catalyst and a Visible Light Sensitiser." **Chemical Communications**, 2016, **52** (99), 14200-14203.
- A chapter was also contributed to the following book: Black TiO_2 Nanomaterials for Energy Applications, Book, **World Scientific**, Feb 2017.

Acknowledgements

There are many people I would like to thank for their collaborations, help and support throughout my PhD studies.

Firstly, I would like to thank my supervisor Dr. Alex Cowan for giving me the opportunity to carry out my PhD and also for his invaluable guidance and support throughout. Alex has been the best supervisor one could hope for, and has built an excellent research group which has been a pleasure to work in. Alex's enthusiasm and dedication to science has been inspiring and we need more people like him.

Secondly, I would like to thank everyone in the Cowan group for their help with experiments, their advice, for making the lab a friendly and fun place to work and for being easy paintball targets.

I gratefully acknowledge all of the colleagues and collaborators who provided samples, measurements and their expertise: Professor Yat Li and his fantastic group at the University of Santa Cruz for many successful collaborations, Dr. Richard Potter at the University of Liverpool for ALD measurements and useful discussions, Professor Laurence Hardwick and all his group (especially Mr Tom Galloway and Dr. Laura Cabo Fernandez) for access to equipment and for help with Raman spectroscopy measurements, Professor David Klug for loan of equipment, Dr. Steph Pendlebury and Professor James Durrant and his group at Imperial College London for allowing me to visit and carry out ultrafast TAS measurements, the (now closed) EPSRC Laser Loan Pool and Dr. Frank Jaeckel for access to Ultrafast TAS equipment at the University of Liverpool and Mr Jonathan Lee for his help with measurements, Professor Matt Rosseinsky and his group (especially Dr. Troy Manning, Dr. Davide Innocenti and Mr Christos Tzitzeklis) for XRD and PLD measurements, Dr. Tobias Heil and Dr. Karl Dawson at NiCaL for help with SEM, TEM and EDX measurements, Dr. Saim Emin and co-

workers at the University of Nova Gorica for collaborations and Mr Ebenezer Tetsi for help with XRD analysis.

I would like to thank all the technical support staff at Liverpool for their great help, especially Vince Vasey for allowing me to constantly raid his cupboards for electrical supplies.

I would like to thank everyone in the Stephenson Institute, I've made so many friends here and it has been an amazing place to work. Thanks also to the efforts of the Stephenson tea room team for maintaining a steady supply of coffee, Penguins and prawn cocktail crisps, and for removing Filipe's mouldy food from the back of the fridge.

Thanks to all my family and friends for their support and for helping me to keep calm and relaxed during the last 4 years. A special thanks to Gaia for sharing the burden of the job with me, and for being there when it counts, you were the most important discovery.

Abbreviations

The following is a list of commonly abbreviated terms used throughout this thesis. Each term is denoted in full for the first time that they are referred to in the main text.

ABPE	Applied bias photon-to-current efficiency
ALD	Atomic layer deposition
APCE	Absorbed photon-to-current efficiency
APTMS	(3-Aminopropyl)trimethoxysilane
CB	Conduction band
CV	Cyclic voltammetry
CW	Continuous wave
EIS	Electrochemical impedance spectroscopy
EPR	Electron paramagnetic resonance
α-Fe_2O_3	Iron oxide (Hematite)
FTO	Fluorine doped tin oxide
HER	Hydrogen evolution reaction
IMPS	Modulated photocurrent impedance spectroscopy
IPCE	Incident photon-to-current efficiency
IR	Infrared
LED	Light-emitting diode
NA	Numerical aperture of the microscope
Nd:YAG	Neodymium-doped yttrium aluminium garnet
NHE	Standard hydrogen electrode
OER	Oxygen evolution reaction
OPA	Optical parametric amplifier
PEC	Photoelectrochemical
PLA	Polylactic acid
PLD	Pulsed laser deposition
RHE	Reversible hydrogen electrode
SCLJ	Semiconductor liquid junction
SERS	Surface enhanced Raman spectroscopy
SHINERS	Shell isolated nanoparticles for enhanced Raman spectroscopy
STEM	Scanning transmission electron microscopy
SEM	Scanning electron microscopy
STH	Solar to hydrogen
TA	Transient absorption
TAS	Transient absorption spectroscopy
TEM	Transmission electron microscopy
TMA	Trimethylaluminium
TPC	Transient photocurrent spectroscopy
UV	Ultraviolet
XRD	X-ray diffraction
VB	Valence band
Vis	Visible
V_O	Oxygen vacancy

β	Stretching exponent
ε	Extinction coefficient
ε_0	Vacuum permittivity
τ	Lifetime (time constant)
λ	Wavelength
A	Absorption
ΔA	Change in absorption
c	Speed of light
C	Pre exponential factor for Arrhenius equation
e	Charge of an electron
E	Energy
E_{FB}	Flat-band potential
E^o	Standard electrode potential
ΔG^o	Gibbs free energy change
h	Planck constant
I	Light intensity
k	Rate constant
k_{obs}	Observed rate
N_d	Donor density
$O.D.$	Optical density
$\Delta O.D.$	Change in optical density
V	Voltage
$t_{1/2}$	Half-life
t	Time
V	Voltage
W_{SC}	Space charge width

1

Introduction

Contents

1.1 The renewable energy landscape and solar fuels

There is urgent need for sustainable, carbon-free energy production, driven by increasing concerns over diminishing fossil fuel supplies and the threat these fuels pose to our climate and ecosystems. This demand for new fuels has rejuvenated interest in the development of solar energy conversion and storage technologies. Harnessing the massive quantities of energy delivered to us by the sun is one of the most promising routes to clean, inexhaustible energy, and is something nature has been taking advantage of for billions of years in the form of photosynthesis. The capture of solar energy and its direct conversion to electricity in the form of traditional photovoltaic devices is progressing well, however, the diurnal nature of sunlight and its variation in intensity around the globe is a significant problem. In order to overcome the limitation due to intermittency, an efficient means of storing (and transporting) solar energy on a large scale is needed.

Solar fuels provide a potential solution to the problem of gathering and storing solar energy on the global scale. In an approach comparable to photosynthesis, solar energy is captured and stored in the form of chemical bonds to yield fuels such as H_2 and CO, which can then be stored, transported and used as and when required. The production of fuels from solar energy fundamentally involves the absorption of sunlight in the form of photons and the subsequent use of this energy to generate electrons and holes, reducing and oxidising equivalents, which are able to drive energetically uphill chemical reactions to produce fuels. The simplest solar fuel that can be envisaged is H_2 generated by the splitting of water to generate H_2 and O_2. Water splitting is an endothermic process (237 kJ mol^{-1}, Equations 1-3), corresponding to 1.23 eV per electron transferred.[1] It is also possible to couple water oxidation with the reduction of compounds such as CO_2 to form carbon based feedstocks (CO, CH_3OH)[2]. Such feedstocks are desirable as they make up the building blocks for a wide range of industrial processes.

$$2H_2O \rightarrow O_2 + 4H^+ + 4e^- \qquad (E^o = 1.23\,V_{RHE})(OER), \qquad (1)$$

$$4H^+ + 4e^- \rightarrow 2H_2 \qquad (E^o = 0.00\,V_{RHE})(HER), \qquad (2)$$

$$2H_2O \rightarrow O_2 + 2H_2 \qquad (E^o cell = 1.23\,V_{RHE}), \qquad (3)$$

Figure 1 shows the amount of sunlight reaching sea level which can be potentially harvested to produce energy. The minimum photon energy of 1.23 eV (1008 nm) required to split water accounts for a significant portion of the energy of the solar spectrum (~ 78%), covering the entire ultraviolet and visible range as well as part of the near infrared region.

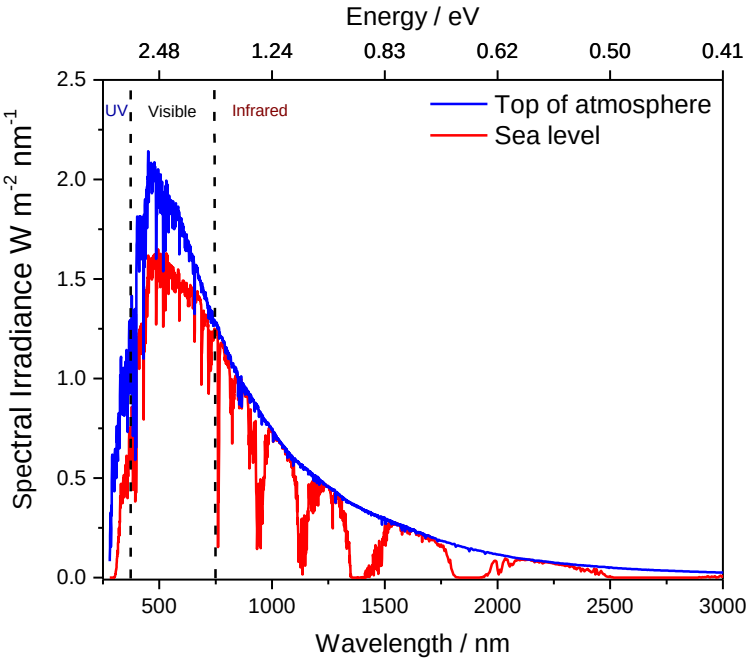

Figure 1 - Solar irradiance as a function of both energy and wavelength, measured at the top of the atmosphere (blue) and for air mass 1.5 global (AM1.5G) (red). Data is taken from the American Society for Testing and Materials (ASTM) reference spectra: ASTMG173-03.[3]

Numerous approaches to utilising solar energy to drive the half reactions for water oxidation (Equation 1) and hydrogen evolution (Equation 2) have been explored,[4] including, but not

limited to the use of coupled photovoltaic-electrolysers,[5] photobiological systems,[6] photothermal/photochemical materials,[7] molecular photocatalysts[8] and light absorbing semiconductor materials[9]. Amongst these, the use of semiconducting photocatalysts and photoelectrodes are of particular interest due to the potential of developing materials that meet both cost and efficiency requirements.[10]

1.2 Semiconductor photocatalysis

Semiconductors are crystalline or amorphous solids with distinct electrical characteristics which lie between those of a metal and an insulator.[11] The band structure of a semiconductor consists of a filled valence band and an empty conduction band similar to that of an insulator, however the distance between the two bands of a semiconductor (the band gap) is small enough that excitation of electrons from the valence band to the conduction band is possible. As a simplification, semiconductors can be defined as materials whose band gap for electronic excitations lies between zero and approximately 4 electron volts (eV), with traditional semiconductors possessing much smaller bandgaps, while materials with zero band gap are metals or semimetals, and those with an energy gap larger than 4 eV are more typically known as insulators.[11]

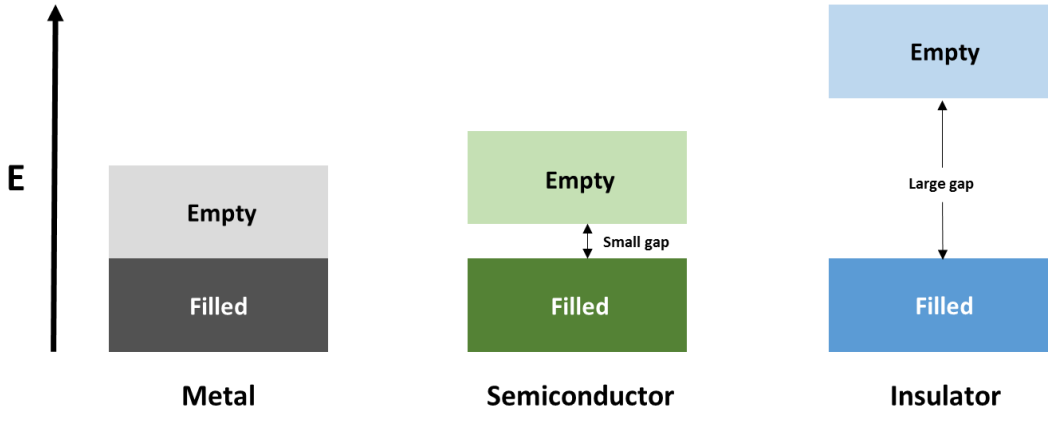

Figure 2 – Band gap diagrams of a metal, semiconductor and insulator.

The small band gap of semiconductors allows them to absorb photons of light to generate excited electrons in the conduction band and holes in the valence band. In order for a photon to be absorbed its energy must exceed the semiconductor band gap energy (Eg). Unlike molecular absorbers which have defined excited states, semiconductors have a continuum of states in both their highest occupied levels (the valence band) and their lowest unoccupied levels (the conduction band), so that the absorption coefficient generally does not decline with increasing excitation energy but instead continually increases above the band gap of the semiconductor.[12]

An ideal semiconductor for water splitting needs to have a suitably sized band gap in order to maximise the absorption of energetically useful photons. Additionally, the valence band needs to be at a potential positive of the H_2O/O_2 couple (4 electrons, 1.23 V_{RHE}) and the conduction band needs to be sufficiently negative to enable hydrogen production (H^+/H_2, 2 electrons, 0 V_{RHE}). Although this may appear to make the minimum band gap requirement 1.23 eV, the Gibbs free energy change of the water splitting reaction does not take into account the energy losses in the semiconductor device, of which there are two major contributions.[13] Firstly there is a thermodynamic loss related to the entropy of mixing associated with the production of conduction band electrons by photon absorption. Secondly, there is a kinetic loss due to the overpotentials for the OER and HER.[12–14] Together these losses account for approximately 0.8 eV making the generally accepted minimum band gap of a semiconductor closer to 2 eV.[12–14] Figure 3 shows a range of semiconductors and their band gap energies and positions at pH 1.

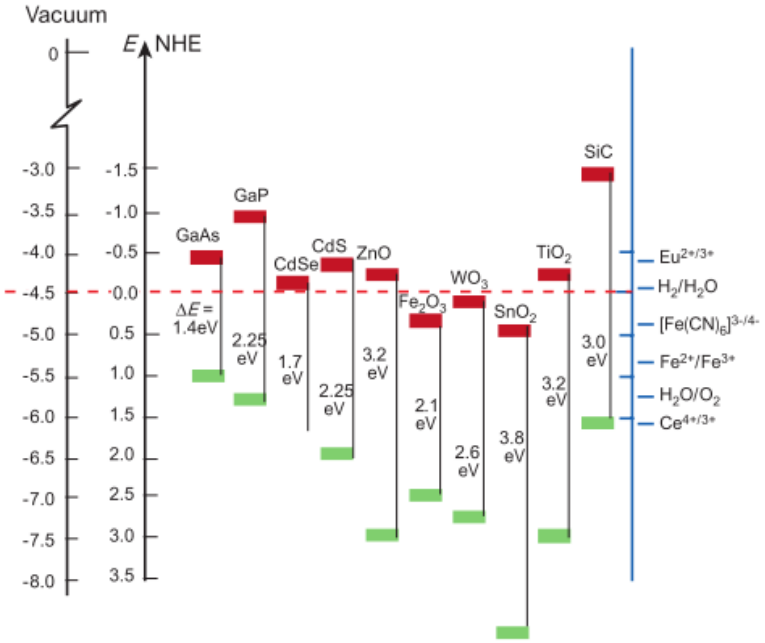

Figure 3 – Band positions of several semiconductors in contact with aqueous electrolyte at pH 0. The lower edge of the conduction band (red colour) and upper edge of the valence band (green colour) are presented along with the band gap in electron volts. The energy scale is indicated in electron volts using either the normal hydrogen electrode (NHE) or the vacuum level as a reference. On the right side the standard potentials of several redox couples are presented against the standard hydrogen electrode potential. Graph originally produced by Michael Grätzel.[15]

The simplest type of semiconductor photocatalyst systems take the form of particles or powders suspended in aqueous solution where the photogenerated holes in the valence band and electrons in the conduction band directly oxidise and reduce water at the semiconductor surface,[14] Figure 4a. In this system the semiconductor must meet the band gap size and alignment criteria discussed above so that it can absorb light and simultaneously carry out the oxidation and reduction reactions. A further consideration is that the material must have sufficient stability against photocorrosion with larger band gap semiconductors typically exhibiting higher stability. Because of these requirements, the number of suitable semiconductor materials for direct water splitting is limited (see Figure 3). Critically, the need to have a material with a relatively large band gap to meet stability requirements limits the ability to achieve high solar energy to hydrogen conversion efficiencies as only the higher energy portion (typically UV) of the solar spectrum can be harvested.[14]

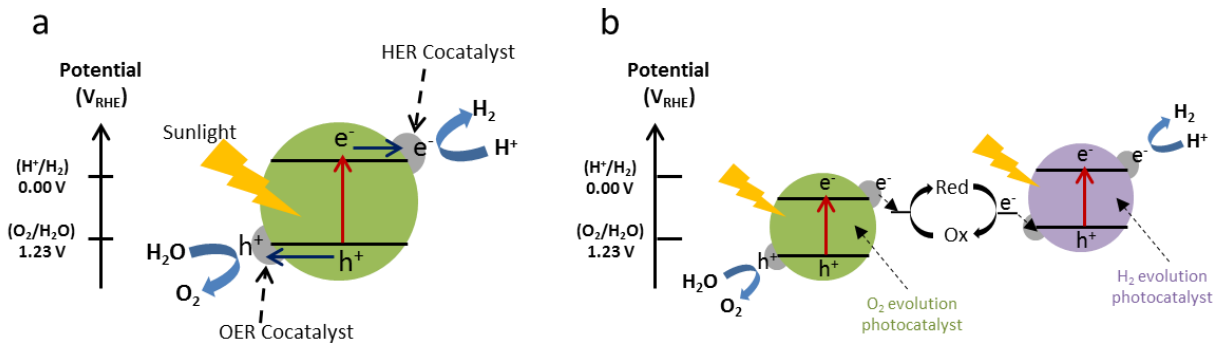

Figure 4 – Diagrams showing photocatalytic water splitting under illumination for (a) a single photocatalyst particle in a particle reactor and (b) a Z-scheme approach using two different photocatalysts combined with a shuttle electron mediator. Additional catalysts can be attached to the surface to assist the reaction kinetics.

One route to improving semiconductor photocatalysis is to use a Z-scheme approach similar to that used in natural photosynthesis.[16,17] In a typical artificial Z-scheme photocatalytic system two different photocatalysts (one for the oxidation reaction and one for the reduction reaction) are combined, generally using an appropriate shuttle electron mediator, as shown in Figure 4b. Visible light can be used more efficiently in a Z–scheme system because the range of solar energy for driving each photocatalyst is reduced. The electron mediator can be an acceptor/donor pair in solution such as IO_3^-/I^-[17] or a solid state interface such as graphene oxide[18]. Mediator free systems are also possible and consist of a heterostructure interface were two catalysts are physically joined.[19] Unfortunately, Z-scheme systems still suffer from various problems including back reactions, visible light absorption of the redox mediators and short-term stability.[16]

An alternative approach to water splitting using semiconductor materials can be achieved photoelectrochemically. Photoelectrochemical (PEC) water splitting[15,20–22] is based on conventional water electrolysis where two electrodes are connected and immersed into aqueous electrolyte, at which point a sufficient voltage is applied across the electrodes to enable the splitting of water and a current to flow. In a PEC cell, one or both (tandem) of the electrodes are photoactive semiconductors which are able to absorb light and drive the appropriate

reactions at their surface, lowering the required electrical energy input, as shown in Figure 5. The use of an additional electrical energy input (an external bias) can aid the semiconductor(s), enabling the use of a wider range of materials with narrower band gaps and hence better light harvesting properties. A working PEC system comprises of a sealed cell with the two electrodes divided by a conducting membrane to separate the O_2 and H_2 gas products.

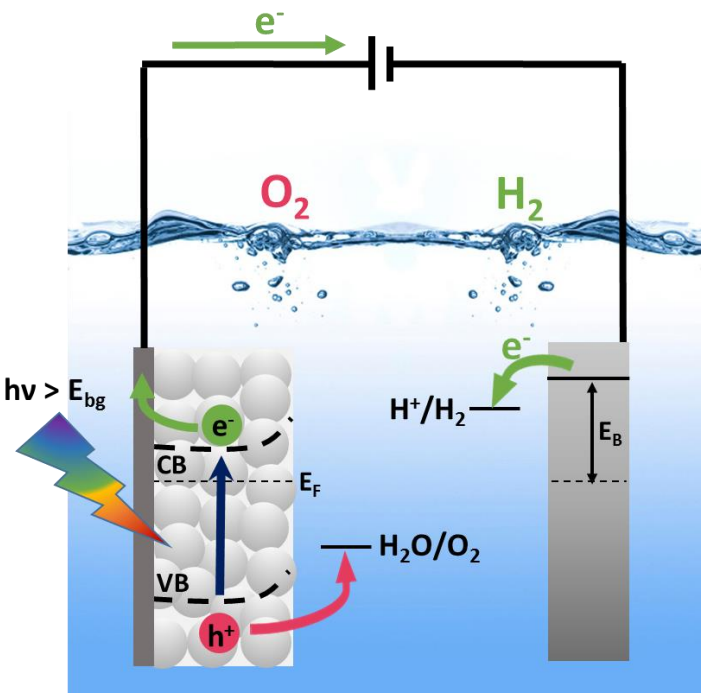

Figure 5 – The basic working principles of a photoelectrochemical (PEC) cell. The cell consists of a photoanode for water oxidation on the left and a metal cathode for hydrogen evolution on the right. In a functioning system the two electrodes would be separated by a conducting membrane to separate the gas products.

In 1968 Boddy[23] reported light-driven oxygen evolution at an n-type rutile (TiO_2) single-crystal electrode. This was quickly followed by the seminal report of Fujishima and Honda in 1972[24] (which has over 20000 citations at the time of writing this thesis) who demonstrated light-driven water splitting in a PEC cell comprising of an n-type rutile photoanode and a platinum cathode. Since then, many studies have been published on this topic.[25] Photoelectrochemical water splitting forms the basis of this thesis and the energetics of such a system will be explained in the following section.

1.3 The energetics of an n-type photoanode in a PEC cell

The water oxidation side of a PEC system is particularly challenging as it requires the formation of 4 holes and often involves slow surface kinetics. In light of this, finding a suitable photoanode material is of significant importance. This section will briefly introduce the energetics of an n-type semiconductor used as a photoanode in a PEC cell for water splitting, such as that shown in Figure 5. In such a device only the OER occurs at the semiconductor surface, making it necessary for the semiconductor valence band to be at a potential positive of the H_2O/O_2 couple. Whilst it may also be desirable for the conduction band to lie negative of the H^+/H_2 couple, the use of an additional electrical energy input means that this is no longer an intrinsic requirement.

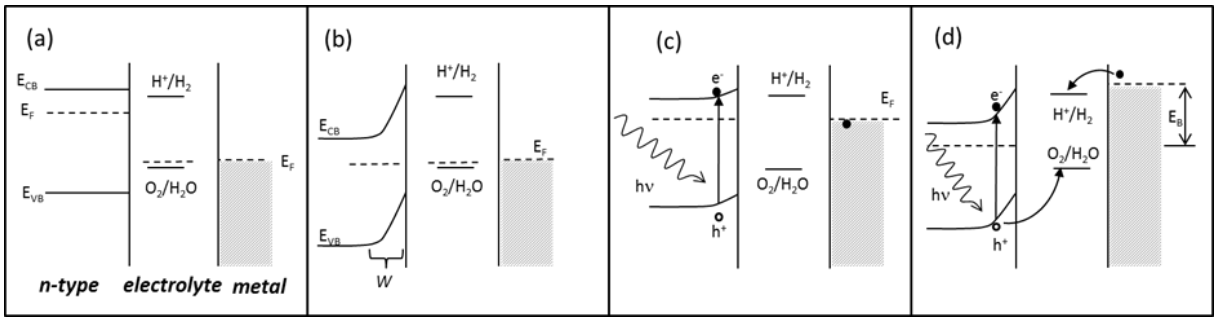

Figure 6 - Energetics of an n-type semiconductor/metal photoelectrochemical cell with an aqueous electrolyte. Prior to contact being made between the semiconductor and the electrolyte in the dark (a), where E_{CB}, E_{VB} and E_F are the conduction band, valence band and Fermi level energies respectively. After contact in the dark, (b) electrons have flowed from the semiconductor to the solution such that the Fermi level of the semiconductor, E_F, matches that of the electrolyte. In a semiconductor where the surface states pin the energy level, band bending occurs, with the resultant region of positive charge in the semiconductor distributed over the depletion width (W). Under strong illumination when the two electrodes are shorted together (c) the quasi electron Fermi level rises, flattening the bands. Under illumination an applied bias (E_B) can be used to raise the metal Fermi level above the potential of the H^+/H_2 couple (d) and to maintain the band bending in the semiconductor, aiding charge separation. Figure initially produced in ref [26].

An energy level diagram for an n-type semiconductor brought into contact with a liquid electrolyte containing a redox couple is shown in Figure 6. Typically, the Fermi level of an n-type semiconductor lies above the potential of the redox couple in solution and charge flows between the semiconductor and the electrolyte until equilibrium of the Fermi levels is established, Figure 6b.[12,27] The value of the Fermi level in the semiconductor changes much more than that of the electrolyte as the solution has far more states per unit energy than the semiconductor's band gap region. Because of the interfacial charge flow, the electrode at equilibrium possesses excess positive charge, arising from the ionised dopant atoms in the semiconductor, and the solution possesses excess negative charge. This positive charge is spread out over a width of the semiconductor known as the depletion width, W, and the negative charge is spread over a much narrower region close to the electrode. The strength of the resultant electric field across the semiconductor depends on the potential dropped in the solid, which, in turn, is a function of the initial difference in the Fermi level of the semiconductor relative to the electrolyte and the depletion width. Under the influence of this electric field, charge carriers (electrons or holes) generated within the depletion width are swiftly separated, with holes being swept to the semiconductor surface and electrons to the bulk (Figure 6c). Under intense illumination when the electrodes are short circuited the high rate of charge generation can disturb the equilibrium and lead to a raising of the Fermi level and a reduction of the band bending with often a subsequent decrease in charge separation yields. Application of an external bias (EB) across the n-type semiconductor can help to maintain the band bending in the semiconductor, aiding charge separation, and in many PEC cells it is also required to raise the metal Fermi level above the potential of the H^+/H_2 couple, (Figure 6d). The use of an external electrical energy input does limit the efficiency of the PEC device, which is often reported as an applied bias photon-to-current efficiency (ABPE)[28,29] making it desirable to develop materials that require a lower electrical energy input. ABPE is shown in equation 4,

where j_{ph} is the photocurrent density, V_B is the applied bias and P_{total} is the power density which takes into account the illumination power as a function of illuminated electrode area.

$$\text{ABPE} = \left[\frac{\left|j_{ph}(\text{mA cm}^{-2})\right| \times |(1.23 - \text{V}_B)(\text{V})|}{\text{P}_{total}\ (\text{mW cm}^{-2})}\right] \quad (4)$$

Solar-to-hydrogen (STH) conversion efficiencies are also commonly reported in the literature for systems which require no external energy input, as shown in equation 5, where j_{ph} is the photocurrent density, η_f is the faradaic efficiency for hydrogen evolution and P_{total} is the power density. It should be noted that STH measures the efficiency of the entire PEC cell including all of its components (counter electrodes, electrolyte, separators, wires etc.) and so it is not so useful for measuring the intrinsic efficiency of the photoelectrode within the cell.

$$\text{STH} = \left[\frac{\left|j_{ph}(\text{mA cm}^{-2})\right| \times 1.23(V) \times \eta_f}{\text{P}_{total}\ (\text{mW cm}^{-2})}\right]_{AM1.5G} \quad (5)$$

Another important metric of efficiency is the incident photon to current efficiency (IPCE, Equation 6) which is a measure of current collected (j_{ph}) at a particular photon flux ($\varphi(\lambda)$) as a function of wavelength.[13] IPCEs are reported at stated applied biases but do not provide any information on the bias dependence of the PEC cell itself. The efficiency of the electrode is often described in terms of three fundamental processes: (i) the efficiency of light harvesting at a particular wavelength ($\eta_{LH}(\lambda)$), (ii) the efficiency of initial charge separation and transport to the semiconductor liquid junction (SCLJ, hole) and the semiconductor current collector junction (electron) ($\eta_{sep}\ (\lambda)$) and (iii) the efficiency of the hole transfer reaction at the interface ($\eta_{int}\ (\lambda)$), Equation 6.[30]

$$IPCE(\lambda) = \eta_{LH}(\lambda) \times \eta_{sep}(\lambda) \times \eta_{int}(\lambda) \quad (6)$$

Electron-hole recombination occurs in competition with the charge separation, transport and transfer reactions and it is the kinetic balance of these processes which is a significant factor in controlling the efficiency of a device. Recombination can occur via a number of different pathways (Figure 7).[12] If absorption of the photon occurs in the bulk of the semiconductor, outside of the depletion region, charge carriers can rapidly recombine prior to hole transport to the SCLJ. In a similar manner even in the depletion region recombination can occur if charge separation and transport is not sufficiently efficient. Indirect recombination can also take place if electrons either traverse or tunnel through the potential barrier at the SCLJ, leading to reduction of O_2 or water splitting intermediates.[12] The presence of trap or defect states, often at the semiconductor surface, can also lead to enhanced recombination losses if the rate of trap-mediated recombination is large enough to compete with the hole transfer reaction. Each of these processes can in principle respond differently to variations such as changes in dopant density, temperature, illumination intensity and electric field strength.

In short, for a semiconductor material to be a realistic candidate for PEC water splitting it needs to be capable of absorbing a significant fraction of the visible spectrum, maintain efficient charge separation, transport charges efficiently, drive the water oxidation and/or water reduction reaction(s) and remain stable in the often harsh electrolyte conditions.

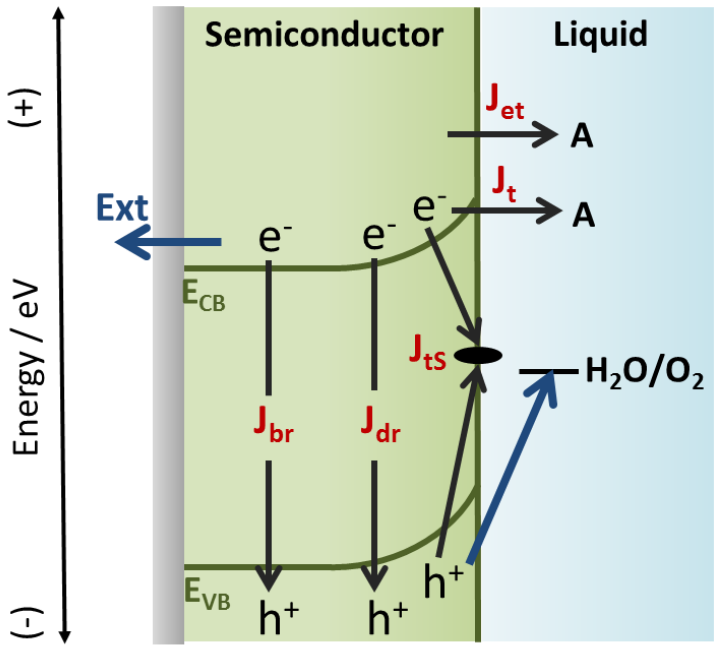

Figure 7 - Recombination pathways for photoexcited carriers in an n-type semiconductor photoelectrochemical cell can be broken down into different categories, represented by the arrows in the diagram. The electron-hole pairs can recombine via radiative or nonradiative recombination in the bulk of the semiconductor (J_{br}), depletion-region recombination (J_{dr}), trap state recombination due to defects (J_{ts}), indirect surface recombination following tunnelling (J_t), and indirect recombination following majority carriers traversing the interfacial barrier (J_{et}). Electron collection by the back contact and hole reaction with the redox couple (e.g. oxidation of water to O_2) are processes that contribute positively to device efficiency (thick blue arrows). Figure based on reference [12].

1.4 Metal oxide semiconductors for PEC water splitting

Although PEC water splitting has received significant attention in recent years, research efforts have yet to find a material that adequately fulfils all of the criteria outlined in sections 1.2 and 1.3. Metal oxide semiconductors such as α-Fe_2O_3[31–34], TiO_2[35–37], $BiVO_4$[38–40] and WO_3[41–43] are one of the more promising group of materials, particularly for use as photoanodes, due to their natural abundance, ease of synthesis, chemical stability and low cost.

Hematite (α-Fe_2O_3) displays many of the desirable traits common to metal oxide semiconductors and has received significant attention regarding its application as a PEC photoanode. Some excellent review articles regarding the use of α-Fe_2O_3 as a photoanode for

water splitting have been previously produced by Grätzel *et al.*[31] and Zhang *et al.*[44] Iron is the fourth most common element in the earth's crust (~5% by weight)[45] making α-Fe_2O_3 (the main ore of iron) notably abundant and low cost. α-Fe_2O_3 also offers excellent chemical stability in oxidative environments at pHs > ~4.[46] There are numerous routes to synthesising α-Fe_2O_3.[44] Solution based methods such as hydrothermal[47], solvothermal[48] and sol-gel[49] routes are fast and scalable and have been used to produce a wide range of nanostructures. Vapour deposition methods such chemical vapour deposition,[50] sputtering[51] and atomic layer deposition[52] have been used to produce both thin films and nanostructures. Other routes include electrochemical deposition[53], thermal oxidation of iron metal[54] and thermal pyrolysis[55]. Perhaps most significantly, α-Fe_2O_3 possesses a favourable band gap energy of 1.9–2.2 eV[31] resulting in a typical optical extinction spectrum such as that shown in Figure 8. The optical absorption spectra of hematite and Fe^{3+} substances and their various transitions have been well studied.[44,56,57] These transitions include ligand-to-metal charge transfer (LMCT) transitions (~250-400 nm, and can tail to lower energies), pair excitation processes corresponding to the simultaneous excitation of two Fe^{3+} centres which occur at energies given approximately by the sum of two single-ion Fe^{3+} ligand field transitions (~400-600 nm) and ligand field transitions or d-d transitions (~600-900 nm). A double exciton process yields the strongest absorption band at around 535 nm and is primarily responsible for the red/orange colour of hematite.[44,56,57]

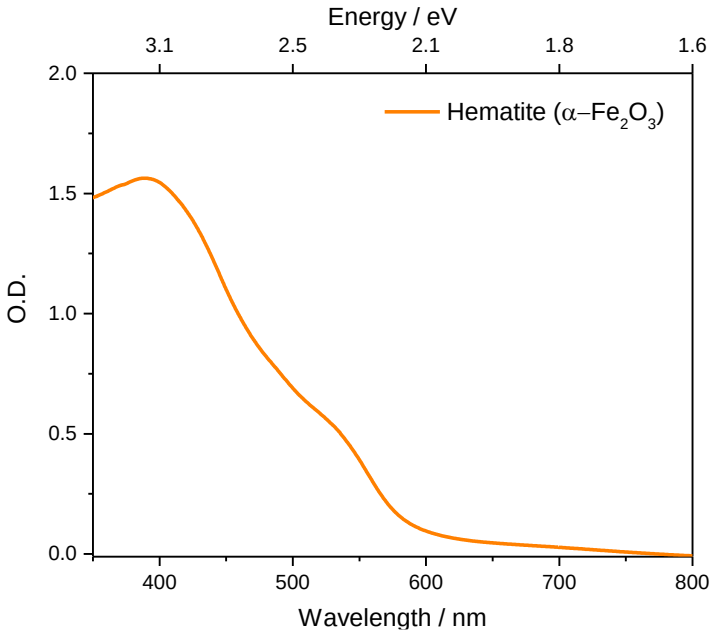

Figure 8 – Extinction spectrum of a thin film α-Fe_2O_3 photoanode measured in transmission mode between 350-800 nm.

The band gap of α-Fe_2O_3 gives a theoretical solar-to-hydrogen (STH) efficiency of ~15.3%[13,33] and a maximum water splitting photocurrent density of ~12.6 mA cm^{-2} under AM 1.5G solar irradiation (100 mW cm^{-2}).[31] In the ideal case where the overpotential for the electrochemical reaction approaches zero, photocurrent can be measured at all potentials more anodic than the flat band potential (V_{FB}). This gives an optimum photocurrent onset potential for hematite of ~ 0.4 V_{RHE}.[31,34] The photocurrent for an ideal hematite photoanode is shown by the solid black trace in Figure 9a. Despite their desirable traits, α-Fe_2O_3 and other metal oxides suffer from many efficiency limiting factors including: poor conductivity,[58] short electron-hole lifetimes,[59] slow oxygen evolution reaction kinetics[60] and a low visible light absorption coefficient coupled to a short hole diffusion length (2–4 nm).[61] Current materials typically require a large electrical bias (overpotential) to enable effective charge separation and limit electron-hole recombination, therefore limiting efficiency.[34,62] These problems have to date led to materials with much lower efficiencies than the theoretical maximum and typically exhibit photocurrents

and onset potentials similar to the solid grey trace in Figure 9a. One of the current benchmark α-Fe_2O_3 photoanodes has a photocurrent of ~4.32 mA cm^{-2} at an applied bias of 1.23 V_{RHE} and a photocurrent onset potential of ~0.7 V_{RHE}.[33]

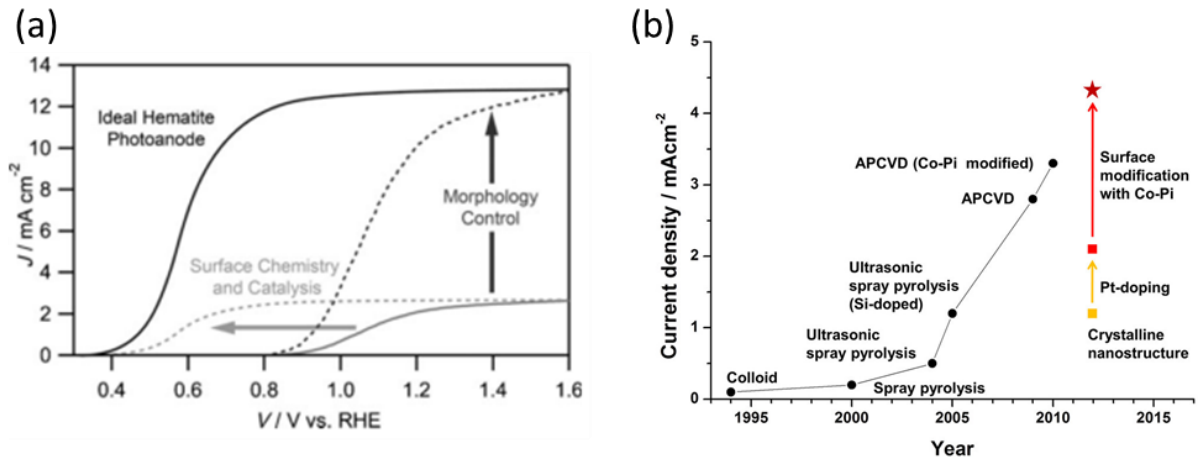

Figure 9 - (a) A common strategy for improving hematite performance is shown with respect to the photocurrent density, J, vs. voltage behaviour for an idealised hematite photoanode (solid black trace) compared to the typical performance (solid grey trace) under AM1.5G 100 mWcm^{-2} simulated sunlight, and the expected effects of improving the surface chemistry and the morphology. (b) Historical improvement in the performance of hematite photoanodes are presented in terms of photoelectrochemical water oxidation current density generated under standard condition (1 sun and 1.23 V vs. RHE). (a) is reproduced from reference [31] and (b) from reference [33].

Because of the attractive intrinsic properties of metal oxides and the theoretical efficiencies of materials such as α-Fe_2O_3, significant attention has been paid towards modifying these materials to overcome their limitations in order to obtain materials which exhibits low onset potentials and high photocurrents. Approaches to tailor their properties to improve efficiency include combinations of doping, nanostructuring, co-catalysis and surface treatments. Figure 9b highlights some of the strategies used in an attempt to reach the ~12.6 mA cm^{-2} photocurrent maximum of α-Fe_2O_3 in addition to some of the historical improvements in performance that have been used to reach the current benchmark. A useful review article which discusses these

approaches in detail was recently published by Li *et al*.[63] and a brief overview will be provided here.

Doping photoelectrodes with certain elements is one of the most commonly used methods of altering the properties of the materials and improving PEC efficiency. In the case of a wide band gap photoelectrode such as TiO_2, doping with extrinsic elements (such as N, S, C and transition metals) is often used to narrow the band gap and shift the light absorption edge, which in turn raises the PEC efficiency. However, for a wide band gap photoelectrode doped with main group-elements, the absorption coefficients in the visible region are still very low. Doping with elements can also introduce crystal defects which can lead to increased levels of recombination. Despite intense research into doped wideband gap semiconductors for >20 years only minimal successes have been achieved suggesting that in order to significantly improve the efficiency of a PEC system it may be desirable to improve existing materials with narrow intrinsic band gaps. In the case of photoelectrodes with narrow band gaps, such as Fe_2O_3 (~2.2 eV)[31] and $BiVO_4$ (~2.4 eV),[39] tuning their band structures by doping with extrinsic elements is often used to improve electrical properties with the aim of increasing the carrier concentration and the minority carrier diffusion length. Examples of dopants incorporated into hematite include Si,[64] Sn,[65] Ti,[66] and the incorporation of oxygen vacancies.[67]

In addition to doping, controlling the morphology of a photoelectrode can also significantly improve performance. To obtain high PEC efficiency, a photoelectrode film must be thick enough to maximise light absorption while also allowing charges generated in the bulk to reach the surface, where they can be collected.[68] As shown in Figure 10, porous structures or nanostructures (such as nanorods, nanotubes, and nanowires) have attracted much attention as they result in relatively short transfer distances of minority carriers and increased surface reaction sites, helping to lower the recombination probability of carriers and improving PEC performance.[69]

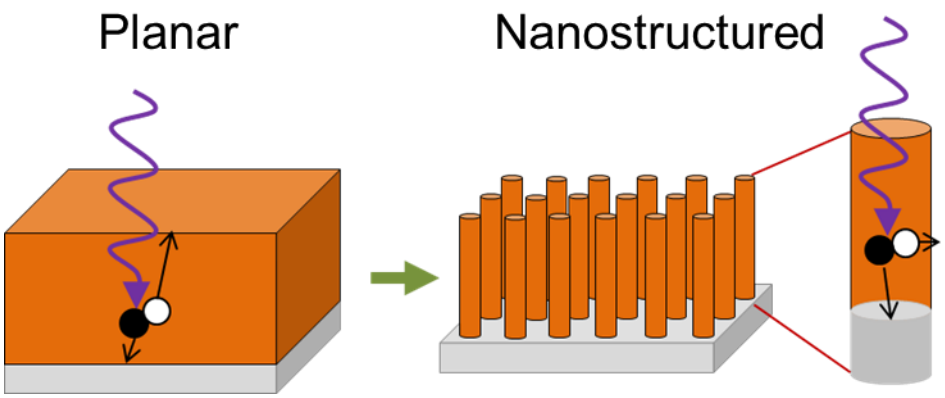

Figure 10 – Diagram showing how a nanostructured photoelectrode can maintain thickness to improve light absorption while also reducing the distance charges need to travel to reach the surface and increasing the surface area.

Surface modifications of photoelectrodes can provide further improvements in efficiency. Kinetic limitations can lead to sluggish surface chemistry and attaching a catalyst to the surface can assist in driving the desired chemical reactions.[68,31] The addition of co-catalysts to the surface of photoelectrodes typically results in improved photocurrent onset potentials (a cathodic shift for hematite). Examples of oxygen evolving catalysts deposited onto the surface of hematite to improve the photocurrent onset potential include cobalt phosphate (Co-Pi)[70,71] and IrO_2 nanoparticles.[72] In addition to catalysing the surface reaction, catalysts such as Co-Pi have also been reported to enhance the magnitude of the space charge/electron depletion layer thereby retarding electron/hole recombination.[73,74] Surface catalysts can also alter the selectivity of the surface reaction, leading to the production of a range of fuels.[75] Surface modifications also come in the form of passivation layers and surface treatments which are often used to improve stability by acting as a protection layer, or inhibit deleterious reactions by passivating or removing surface or near surface states which are acting as recombination sites.[76] Passivation layers tend to be photo-inactive and it is usually desirable for them to be very thin (~1-2nm). They can be deposited in a number of ways including atomic layer deposition,[77] electrochemical deposition,[78] sputtering,[79] dip casting[80] and spin coating.[81]

Recent examples of passivation include the loading of certain oxide layers such as Al_2O_3[82] and Ga_2O_3[76] onto the surface which have been reported to lead to increased PEC performance through minimisation of trap enabled recombination.[76] Figure 11 and Figure 12 show the effects of overlayers used for catalysis, passivation and stabilisation.

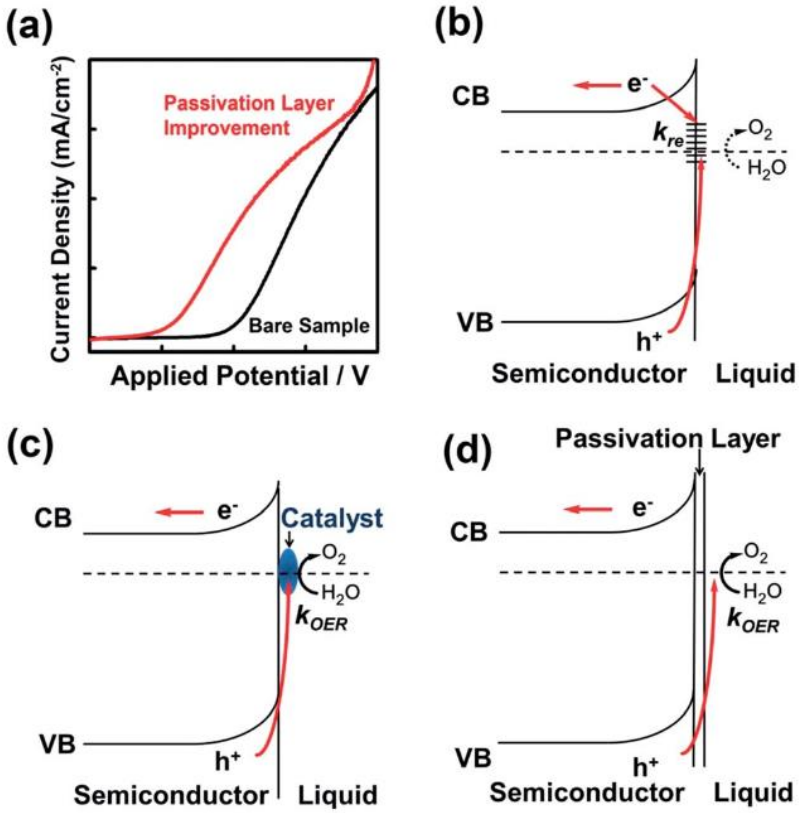

Figure 11 - Comparison of an n-type semiconductor photoanode and the effect on surface states with/without a passivation layer in a water-splitting PEC cell: a) the schematic J-V curves of a photoanode with (red trace) and without (black trace) a surface passivation layer; b) surface defect states in the band structure, which lead to high charge recombination and inefficient water oxidation by the photogenerated holes; c) application of an OER catalyst layer, which promotes facile hole transfer across the interface to the catalyst for improving water oxidation; d) application of a thin noncatalytic surface layer to passivate defect states, strongly suppressing surface recombination for improving water oxidation. Reproduced from reference [83].

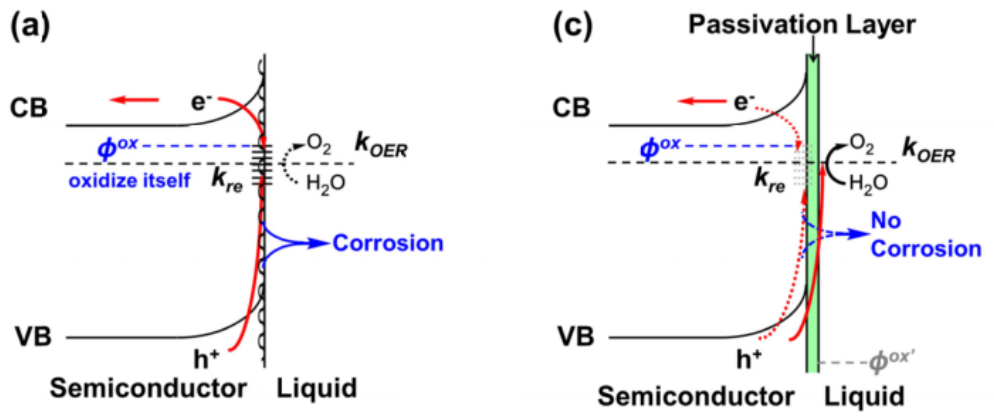

Figure 12 - Comparison of a semiconductor photoelectrode with/without a stabilising passivation layer. (a) shows a schematic illustration of the band structure of an n-type semiconductor photoelectrode experiencing corrosion when contacting an aqueous electrolyte. (c) shows the semiconductor protected from corrosion with a passivation layer. ϕ^{ox} stands for the corrosion potential of the n-type semiconductor, which should be more positive than the OER reaction energy level. Corrosion may reduce the light absorption and/or generate more surface defect states, resulting in a more positive onset potential and a reduced photocurrent. Reproduced from reference [83].

Table 1 summarises some of the reported thin-layers which have been deposited onto photoanodes for oxygen evolution.

year	base SC	coating (thickness, nm)[a]	deposition method	electrolyte	pH	stability, time (at J, mA cm^{-2})	E_{onset} vs ref (V)	E_{onset} vs OER (V)[b]	Vshift[c] (mV)
1975	n-GaP	Au(–)	evaporation	borate buffered 0.5 M K_2SO_4	9.2	–	+0.5 vs SCE	+0.05	560
1975	n-GaP	Pd(–)	evaporation	borate buffered 0.5 M K_2SO_4	9.2	–	–	–	600
1975	n-Si	Au(–)	evaporation	borate buffered 0.5 M K_2SO_4	9.2	–	–	–	170
1975	n-Si	Pd(–)	evaporation	borate buffered 0.5 M K_2SO_4	9.2	–	–	–	150
1977	n-GaP	Au(40)	sputter or evaporation	buffered 0.5 M K_2SO_4	4.3	–	−0.45 vs SCE	−1.18	300–500
1977	n-GaP	Ag(30)	sputter or evaporation	buffered 0.5 M K_2SO_4	4.3	–	−0.5 vs SCE	−1.23	–
1977	n-Si, n-GaAs, n-GaP, n-InP, n-CdS	TiO_2(–)	CVD	Na_2SO_4	–	w	–	–	–
1977	n-GaAs, n-GaAlAs	Al_2O_3, TiO_2, Si_3N_4	sputtering	Na_2SO_4 + NaOH	–	–	–	–	–
1977	n-GaAs, n-GaAlAs	SnO_2, Nb_2O_5	electrodep	Na_2SO_4 + NaOH	–	–	–	–	–
1980	n-Si	Fe_2O_3(2.5-800)	sputtering/oxidation	0.1 M NaOH	13	–	+0.4 vs SCE	+0.2	–
1983	n-Si	ITO(3-100)/RuO_2(–)	sputtering	buffered NaOH	12	–	+0.2 vs SCE	−0.1	–
1984	n-Si	Fe_2O_3(75)/Pd(10)	electron-beam evaporation	0.2 M KOH	13.3	–	+0.36 vs Hg/HgO	+0.01	–
1984	n-Si	Pt-SiO_x(10)/Pt	photoanodic oxidation	0.5 M H_2SO_4	0	100 h (1)	+1.4 vs NHE	+0.17	–
1986	n-Si	Pt or Pd(–)/MnO_x(20)	chemical bath deposition	0.5 M K_2SO_4	13, 7	600 h (1)	+0.6, +1.2 vs NHE	+0.14, +0.38	500, 500
1987	n-GaAs	Pt or Pd(–)/MnO_x(20)	chemical bath deposition	0.5 M NaOH	13	>80 min (11)	−0.4 vs NHE	−0.86	–
1987	n^+n-Si, n+p-Si	Ni(30)	sputtering	1 M KOH	14	~45 min	+0.25 vs Hg/HgO	−0.06	370
1987	n^+n-Si, n^+p-Si	Pt(3)	sputtering	1 M KOH	25	>8 h	+0.51 vs Hg/HgO	+0.2	170
1989	n-Si	Cr_2O_3(–) /TiO_2(–)/ SbO_x(–)	CVD/sol–gel	1 M H_2SO_4 + 1 M isopropyl alcohol	~0	20 h (2.0)	+0.5 vs SCE	−0.50	–
1991	n-Si	BP(–)	CVD	1 M H_2SO_4	~0	–	+0.4 SCE	−0.6	–
1994	n-GaAs	ITO(230)	sputtering	0.5 M $NaClO_4$	–	–	–	–	–
2004	a-Si:Ge nip	ITO(–) /Fe_2O_3(–)	sputtering or spray pyrolysis	–	–	–	–	–	650
2011	n-Si	TiO_2(2)/ Ir(3)	ALD	1 M H_2SO_4	0	8 h (5.1)	–	−0.22	532
2011	n-Si	TiO_2(2)/ Ir(3)	ALD	0.4 M Na_2HPO_4 and 0.6 M Na_2HPO_4 and NaOH	7	8 h (5.1)	–	−0.28	565
2011	n-Si	TiO_2(2)/ Ir(3)	ALD	1 M NaOH	14	24 h (15)	–	−0.20	555
2011	a-Si	ITO(70)/ Co-oxide	–	1 M potassium borate	9.2	3 h (~3.7)	−0.4 vs RHE	−1.63	
2012	n-Si	NiO_x(30)	sol–gel	buffered Na_2SO_4	7.25	30 min	–	−0.05	300
2012	n-Si	Ti-Fe_2O_3(20)	CVD	NaOH-$NaHPO_4$ 1 M NaOH	13.8	–	+1.2 vs RHE	0	~400
2012	Ta_3N_5	CoO_x(–)	impregnation	1 M KOH	13.6	2 h (1)	+0.6 vs RHE	−0.60	
2012	n-GaN	NiO	spin coating + annealing	1 M NaOH	14	110 h (0.5 mL $cm^{-2}h^{-1}$)	–	–	–
2013	n-Si	Ni(2)	e-beam evaporation	1 M KOH	14	12 h (10)	–	−0.15	~500
2015	n-CdTe	NiO_x(75)	sputtering	1 M KOH	14	1000 h (22.9)	+1.15 vs RHE	−0.07	440
2015	np^+-Si	Ti(5)/TiO_2(100)/IrO_x	sputtering	1 M H_2SO_4 or 1 M $HClO_4$	0	60 h (23)	+1 vs RHE	−0.23	500
2015	ZnO	Ta_3O_5 (–)	ALD	0.1 M KOH	13	5 h (0.8)	+0.5 vs RHE	−0.73	–
2015	np^+-InP	NiO_x(75)	sputtering	1 M KOH	14	48 h (20.8)	+0.85 vs RHE	−0.37	390
2015	np^+-Si	$NiCo_2O_4$ (40)	sputtering	1 M KOH	14	72 h (30)	+1 vs RHE	−0.23	600

year	base SC	coating (thickness, nm)[a]	deposition method	electrolyte	pH	stability, time (at J, mA cm^{-2})	E_{onset} vs ref (V)	E_{onset} vs OER (V)[b]	Vshift[c] (mV)
2013	n-Si	Ni(2)	e-beam evaporation	0.65 M K-borate and 0.35 M Li-borate	9.5	80 h (10)	–	−0.05	~500
2013	n-Si	$NiRuO_x$(30)	sputtering	buffered Na_2SO_4	7.25	2 h (1)	–	−0.05	–
2013	n-Si	MnO_x(10)	ALD	1 M KOH	13.6	~30 min (10)	–	−0.025	450
2013	$BiVO_4$	CoO_x(1)	ALD	0.1 M KOH	13	30 min (1.5)	+0.40 vs RHE	−0.83	–
2013	$BaTaO_2N$	CoO_x(−), CoO_x + IrO_x(−), CoO_x + RuO_x(−)	calcination	0.1 M Na_2HPO_4(aq) and 0.1 M Na_2HPO_4(aq)	8	1 h (2)	–	−0.30	300
2013	TaON	$CaFe_2O_4$ + Co-Pi cocatalyst	electrophoretic deposition + calcination	0.1 M potassium phosphate buffer solution	11	3 h (0.5)	+0.6 vs RHE	−0.63	–
2014	n-GaP	TiO_2(118)/ NiO_x(2)	ALD, e-beam evaporation	1 M KOH	13.7	>5 h (2.5)	−0.16 vs SCE	−0.35	590
2014	np$^+$-GaAs	TiO_2(118)/Ni/NiO_x(2)	ALD, e-beam evaporation	1 M KOH	13.7	>25 h (14)	−0.38 vs SCE	−0.57	810
2014	np$^+$-Si	ITO(100)/Au(5)/ ITO(100)/NiOx(−)	sputtering	1 M NaOH	14	2.5 h (10.8)	–	−0.05	388
2014	np$^+$-Si	CoO_x(2)	ALD	1 M NaOH	13.6	24 h (30)	+1.1 vs RHE	−0.13	610
2014	$BiVO_4$	FeOOH(−)/ NiOOH(−)	(photo) electrodeposition	phosphate buffer	7	50 h (2.6)	+0.2 vs RHE	−1.0	–
2014	$BiVO_4$	$CaFe_2O_4$ (−) + Co-Pi cocatalyst (−)	electrophoretic deposition + calcination	0.1 M potassium phosphate buffer solution	7	2 h (2)	+0.3 vs RHE	−0.93	–
2014	n-Si	TiO_2(3-143)/ Ni/ NiO_x(100)	ALD, e-beam evaporation	1 M KOH	13.7	–	+0.03 vs SCE	−0.16	430
2014	np$^+$-Si	TiO_2(68)/ Ni/NiO_x(100) islands	ALD, e-beam evaporation	1 M KOH	13.7	>100 h (35)	+0.12 vs SCE	−0.07	520
2014	$BiVO_4$	TiO_2(1)/Ni(2)	ALD, sputtering	0.1 M KOH	13	2 h (1.4)	+0.6 vs RHE	−0.63	–
2014	n-CdTe	TiO_2(100-140)/ NiO_x(2)	ALD, e-beam evaporation	1 M KOH	14	100 h (20)	+0.7 vs RHE	−0.53	–
2014	Ta_3N_5	ferrihydrite (−) + Co_3O_4 cocatalyst (−)	chemical bath deposition + calcination	1 M NaOH	13.6	6 h (5)	0.7 vs RHE	−0.53	–
2014	np$^+$-Si	Ir/IrO_x(4)	sputtering	1 M H_2SO_4	0	18 h (25.5)	+1.05 vs RHE	−0.18	–
2014	np$^+$-Si	Fe-treated NiO (50)	sputtering	1 M KOH	14	300 (15)	+1.05 vs RHE	−0.18	–
2015	n-Si microwire	TiO_2(94)/ $NiCrO_x$(40)	ALD and sputtering	1 M KOH	13.6	–	–	+0.07	180
2015	np$^+$-Si microwire	TiO_2(94)/ Ni(40)	ALD and sputtering	1 M KOH	13.6	2200 h (4.5)	–	−0.13	440
2015	np$^+$-Si	NiO_x(75)	sputtering	1 M KOH	14	1200 h (30)	–	−0.25	520
2015	HTJ-Si	NiO_x(75)	sputtering	1 M KOH	14	200 h (34)	+0.95 vs RHE	−0.28	600
2015	a-Si:H	NiO_x(75)	sputtering	1 M KOH	14	100 h (5.4)	+1.1 vs RHE	−0.12	
2015	$BiVO_4$	CoO_x (1 wt %)/NiO(~6)	bulk calcination/ALD	0.1 M KPi	7	16 h (2.5)	+0.4 vs RHE	−0.83	–

Table 1 - Summarises some of the reported thin-layers which have been deposited onto photoanodes for oxygen evolution. [a]Outermost layer is the final layer listed, layer closest to the semiconductor is the first layer listed. [b]The voltage vs. the thermodynamic potential (as calculated); negative means more negative past the thermodynamic potential. [c]The voltage shift from the dark electrocatalysis on a metal or degenerate electrode that are comparable to the electrocatalytic behaviour of as-reported photoanodes. [d](−) data not specified or parameter not reported. (w) Effective water oxidation not demonstrated. (v) Possibly photocorrosion. Reproduced from reference [84].

Table 2 summarises some of the thin-layers which have been deposited onto α-Fe_2O_3 photoanodes.

Year	Coating	Method	Electrolyte	pH	Stability	Shift (mV)	Ref
2010	IrO_2	Electrophoresis	1M NaOH	13.6	-	-200	[72]
2011	Al_2O_3	ALD	1M NaOH	13.6	>5 min	-80	[82]
2011	SnO_2	Drop cast	1M NaOH	13.6	-	-	[85]
2011	CoO_x	Electrodeposition	0.1M NaOH	12.6	-	-100	[86]
2014	Ga_2O_3	CBD	1M NaOH	13.6	-	-200	[87]
2015	$NiFeO_x$	Drop cast	Phosphate buffer	11.8	>10 hours	-	[88]
2015	TiO_2	Drop cast/anneal	1M NaOH	13.6	-	-200	[89]
2016	FeOOH	SILAR	1M NaOH	13.6	-	-50	[90]

Table 2 –Summarises some of the reported thin-layers which have been deposited onto α-Fe_2O_3 photoanodes. Shift refers the observed photocurrent onset shift in mV. ALD is atomic layer deposition, CBD is chemical bath deposition and SILAR is successive ionic layer adsorption and reaction.

Despite significant efforts to improve activity by doping, morphology control, surface treatments and overlayers, current efficiencies of α-Fe_2O_3 photoelectrodes still remain significantly lower than the theoretical maximum. In order to further develop photoelectrodes such as α-Fe_2O_3, techniques which are able to probe materials *in situ* and rationalise their activity are vitally important. The following section will describe transient absorption spectroscopy (TAS) as one such technique.

1.5 Transient absorption spectroscopy (TAS)

Transient absorption spectroscopy (TAS or TA spectroscopy) is a time-resolved spectroscopic technique for the study of dynamic processes in materials or chemical compounds. In TAS a reaction or photophysical process is initiated using a short pulse of light, usually from a laser. The change in concentration of short lived intermediates is then measured by studying the change in optical density, ΔO.D. (often assumed to be equal to the change in absorbance, A) of the sample as a function of time. This technique makes it possible to study processes with lifetimes as short as femtoseconds (fs), and as long as seconds and minutes if required. TAS systems typically probe in the ultraviolet, visible and near-infrared spectral regions, although other wavelengths such as X-rays[91] and Terahertz[92] are also reported. The basic principle of TAS can be summarised in equations 7-10 which show the log ratio between the incoming light (I_0) and the light that has passed through the sample and is detected (I_1):

$$A = \log_{10}\left(\frac{I_0}{I_1}\right) \quad (7)$$

$$\Delta A = A_{excited\ state} - A_{ground\ state} = \log_{10}\left(\frac{I_{0excited}}{I_{1\mathrm{excited}}}\right) - \log_{10}\left(\frac{I_{0ground}}{I_{1ground}}\right) \quad (8)$$

$$\Delta A = \log_{10}(I_{0\mathrm{excited}}) - \log_{10}(I_{1\mathrm{excited}}) - \log_{10}(I_{0ground}) + \log_{10}(I_{1ground}) \quad (9)$$

As the incoming light (I_0) remains constant, the equation simplifies to:

$$\Delta A = \log_{10}\left(\frac{I_{1ground}}{I_{1\mathrm{excited}}}\right) \quad (10)$$

Early TAS methods (known as flash photolysis) were demonstrated by Ronald Norrish and George Porter in 1949-1950 and their contributions to the field, together with Manfred Eigen led them to win the Nobel Prize in chemistry in 1967[93,94] Their early experiments used a flash

lamp (short millisecond pulses) to initiate photochemical reactions which could then be monitored spectroscopically. More recently, TAS has been further improved by developments in laser technology and electronics, allowing processes to be probed on faster timescales and with higher sensitivity.

Figure 13 shows the working principles of a typical TAS (flash photolysis) system for nanosecond-second timescales. A white light source such as that of a Xe lamp is used to produce a probe light which is then passed through a monochromator to isolate a single probe wavelength (I_0). This low power probe light is then passed through the sample and into a detector connected to an oscilloscope which then measures the incoming light continuously. The ground state absorption ($I_{1ground}$) of the sample is first measured as shown in Figure 13a. A short laser pulse (typically several nanoseconds or less) is then used to excite (pump) the sample to generate a photophysical process, at which point the change in optical density (if any) resulting from this process is measured as a function of time after excitation, Figure 13b. A 3-dimensianal spectrum (ΔO.D. vs. λ vs. t) can then be acquired by repeating the measurement at a range of probe wavelengths.

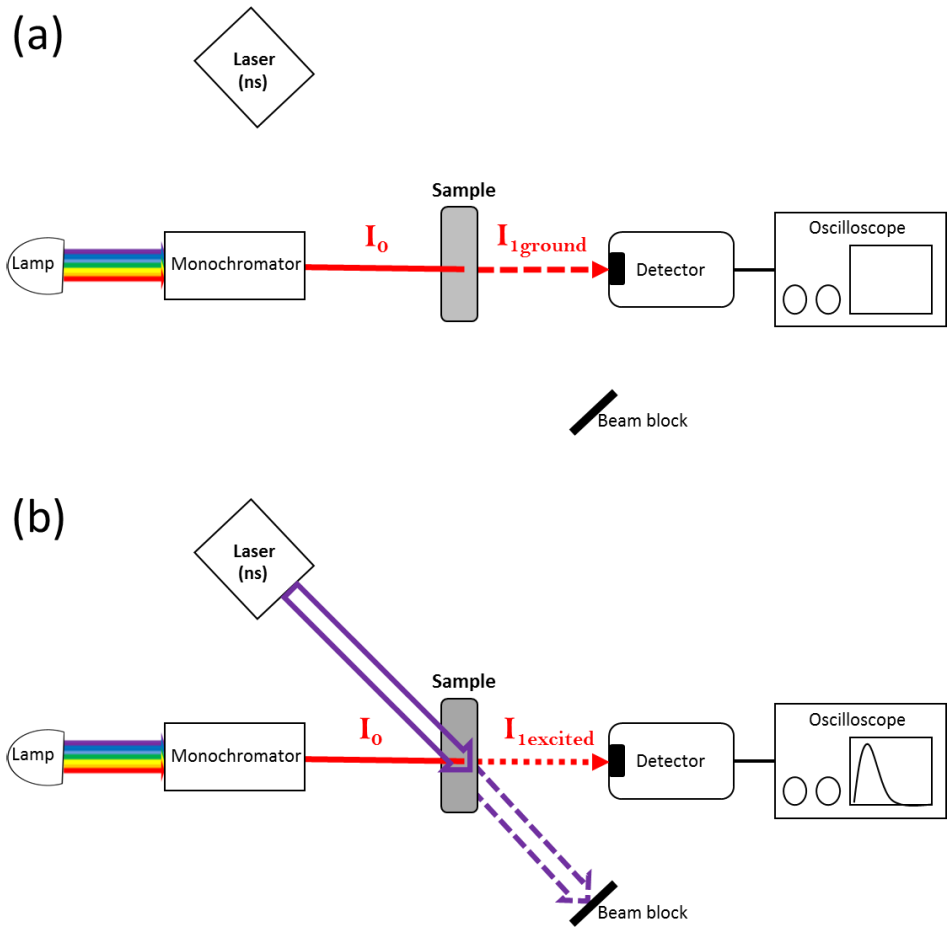

Figure 13 – Diagram showing the working principles of a typical transient absorption spectroscopy (TAS) system. A white light source produces a probe light which is then passed through a monochromator to isolate a single probe wavelength. This low power probe light is then passed through the sample and is continuously detected by a photodiode connected to an oscilloscope. The ground state absorption of the sample is first measured, (a). A short laser pulse (typically several nanoseconds or less) is then used to excite the sample at which point the change in optical density (if any) is measured as a function of time after excitation, (b). A 3-dimensianal spectrum (ΔO.D. vs. λ vs. t) can then be acquired by repeating the measurement at a range of probe wavelengths.

Modern lasers are capable of generating light pulses as short as several femtoseconds, however the time resolution of the flash-photolysis method for TAS is usually limited to a few nanoseconds, meaning faster processes cannot be observed.[95,96] Several factors limit the capability of the method described in Figure 13. Firstly, higher time resolution demands higher powered monitoring light.[95] This problem can be solved by using monochromatic continuous wave (CW) lasers, however continuously exposing the sample to such a high power 'probe' light risks unwanted excitation or damage. Of equal significance is the time response of the

electrical components (such as detectors, amplifiers, oscilloscopes) which are currently unable to respond on femtosecond/picosecond timescales.

In order to overcome the limitations of the traditional flash photolysis type systems, an approach such as that shown in Figure 14 is used to measure ultrafast processes. An ultrafast laser pulse (femtoseconds) is split to produce both the pump and probe light. The pump beam is used to excite the sample, while the probe beam is passed through an adjustable delay line and a crystal to generate white light. The delayed probe light is then passed through the sample and detected by an imaging spectrometer as a full spectrum (ΔO.D. vs. λ) at a single time point, t after excitation (Figure 14a). A 3-dimensianal spectrum (ΔO.D. vs. λ vs. t) is then built up by repeating the measurement at a range of delay line distances, which adjusts the time at which the probe reaches the sample following excitation (Figure 14b). While flash photolysis has an upper time resolution limit of several nanoseconds, most ultrafast pump-probe systems have a lower limit (often on the order of 100 ns) due to practicalities related to the length of the delay line. As a result, both systems are usually required to probe a material from the ultrafast to the very slow timescales.

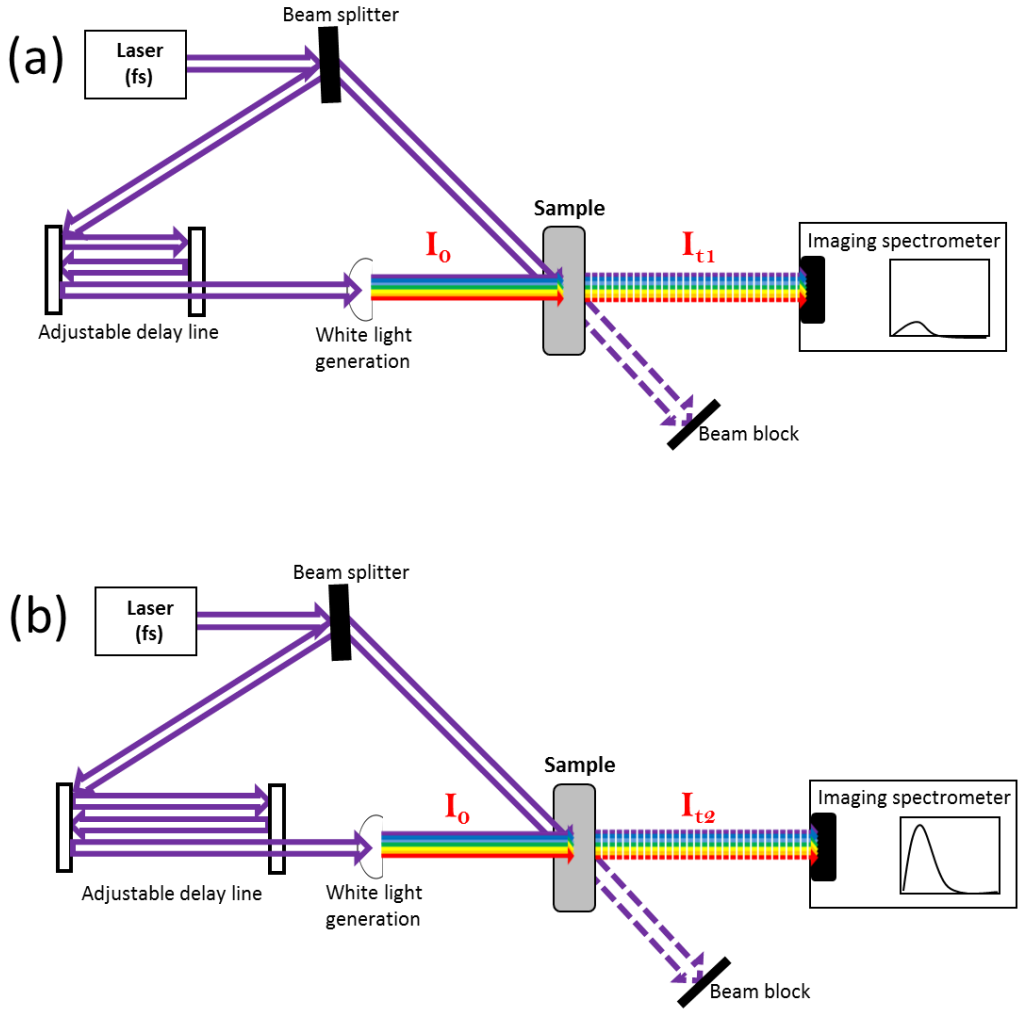

Figure 14 – Diagram showing the working principles of an ultrafast transient absorption spectroscopy (TAS) system. An ultrafast laser pulse (femtoseconds) is split to produce both the pump and probe light. The pump beam is used to excite the sample, while the probe beam is passed through an adjustable delay line and a crystal to generate white light which is then passed through the sample and detected as a full spectrum (ΔO.D. vs. λ) at a single time point, (a). A 3-dimensianal spectrum (ΔO.D. vs. λ vs. t) is then built up by repeating the measurement at a range of delay line distances which adjusts the time at which the probe reaches the sample following excitation, (b).

The changes in optical density measured by TAS are usually very small (on the order of $1x10^{-3}$ ΔO.D. or smaller). Better signal-to-noise ratios are achieved when the light incident on the detector is higher. Additionally, signals are usually passed through an amplification stage and measurements are averaged over many repeat measurements (several hundred shots) to remove noise.

Figure 15a shows a typical TAS spectrum which presents the change in optical density (ΔO.D.) as a function of time after excitation at a range of probe wavelengths. A spectrum such as that shown in Figure 15a provides an overview of the photo-induced processes occurring following excitation and can consist of multiple absorption features (if multiple processes are occurring simultaneously). These features can exist as increases in absorption (such as excitation into an unoccupied state) or decreases in absorption (such as a ground state bleach), can be narrow or broad, and can often overlap with each other. When a feature of interest is identified, a kinetic trace (ΔO.D. *vs.* time) such as that shown in Figure 15b can be isolated. The kinetic trace can then be fitted to extract the decay rates and lifetimes of the process or processes involved.

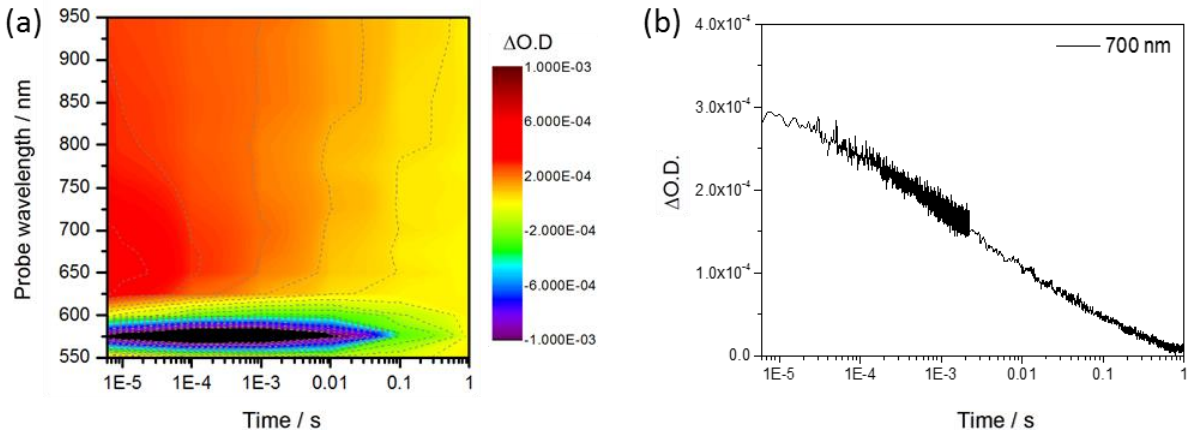

Figure 15 – (a) A typical 3-dimensional TAS spectrum showing the ΔO.D. as a colour plot, with probe wavelengths on the y-axis and time after excitation on the x-axis. (b) A kinetic trace showing ΔO.D. as a function of time at a specific wavelength.

An excellent overview which addresses the analysis and fitting of TAS data is provided by Nikolai Tkachenko in Optical Spectroscopy (2006).[97] Kinetic traces can often be fitted to exponential decay functions. A quantity is subject to exponential decay if it decreases at a rate proportional to its current value. Equation 11 shows a single exponential decay function were $\frac{d(\Delta O.D.)}{dt}$ is the change in optical density as a function of time as measured by TAS, A is a

coefficient related to the magnitude of the excited population immediately after excitation (i.e. the magnitude at $t_{=0}$) and can be positive or negative, k is the overall rate of decay of the excited population and t is the time after excitation.

$$\frac{d(\Delta O.D.)}{dt} = Ae^{-(kt)} \qquad (11)$$

In addition to the rate of decay (k), the mean lifetime (τ) (also known as the exponential time constant) of the population can be obtained from the relationship shown in equation 12.

$$\tau = \frac{1}{k} \qquad (12)$$

Furthermore, the half-life ($t_{1/2}$) can be obtained using the relationship shown in equation 13. $t_{1/2}$ is the time required for the decaying quantity to fall to one half of its initial value and is often considered a more intuitive characteristic of an exponential decay.

$$t_{\frac{1}{2}} = \frac{\ln(2)}{k} \qquad (13)$$

When a kinetic trace is made up of multiple populations of excited states it can be described by a multi-exponential function such as the bi-exponential decay shown in equation 14, which provides separate decay rates for each population.

$$\frac{d(\Delta O.D.)}{dt} = A_1 e^{-(k_1 t)} + A_2 e^{-(k_2 t)} \qquad (14)$$

Stretched exponential functions can also be used to fit data and are obtained by inserting a fractional power law into the exponential function using a stretching exponent (β) between 0 and 1, (equation 15). Stretched exponential functions are commonly used to describe systems in which the depletion of a population is also dependent on time which stretches the decay, or where using multi-exponential decay functions to describe multiple discrete components is

unsuitable. Examples of systems were stretched exponential decays can be suitable include fluorescence decays[98] or decays of long-lived trapped charges[99].

$$\frac{d(\Delta O.D.)}{dt} = A_1 e^{-(k_1 t)^{\beta}} \quad (15)$$

It should be noted that ΔO.D. results from the sum of the measureable electron and hole signals at a given wavelength meaning the use of exponential decay functions such as those shown here are limited, and attempting to fit overlapping signals can be problematic. Furthermore, care should be taken to avoid over-parameterisation of fitting functions in order to limit erroneous results.

While TAS can be an excellent method for probing photophysical processes of a range of samples including solutions, suspensions and thin films, it does have limitations. Perhaps the most significant one is that TAS usually requires a sample which is able to transmit enough light to generate a signal, and therefore highly absorbing or scattering samples are often unsuitable. This can be a complex dilemma, especially when probing in the UV-Vis region, as many photoactive materials which would benefit from TAS analysis are designed with maximum light absorption in mind. It is possible to measure TAS using reflectance rather than transmission, however again the number of suitable samples are limited as this requires a highly reflecting surface. Unstable samples can also be problematic due to the extended lengths of time which are typically required to obtain good signal to noise TAS data.

1.6 TAS of metal oxide photoelectrodes

As shown in Figure 16, TAS is well suited to the study of PEC water splitting materials such as thin film photoelectrodes under working conditions, and in recent years it has provided insight into the yields and rates of electron/hole processes such as charge separation, charge

trapping, charge transfer and recombination. TAS of PEC systems can be a particularly powerful tool when coupled to electrochemical techniques such as transient photocurrent and transient photovoltage measurements which can provide information on the quantity and rate of charge extraction from an electrode to the external circuit.

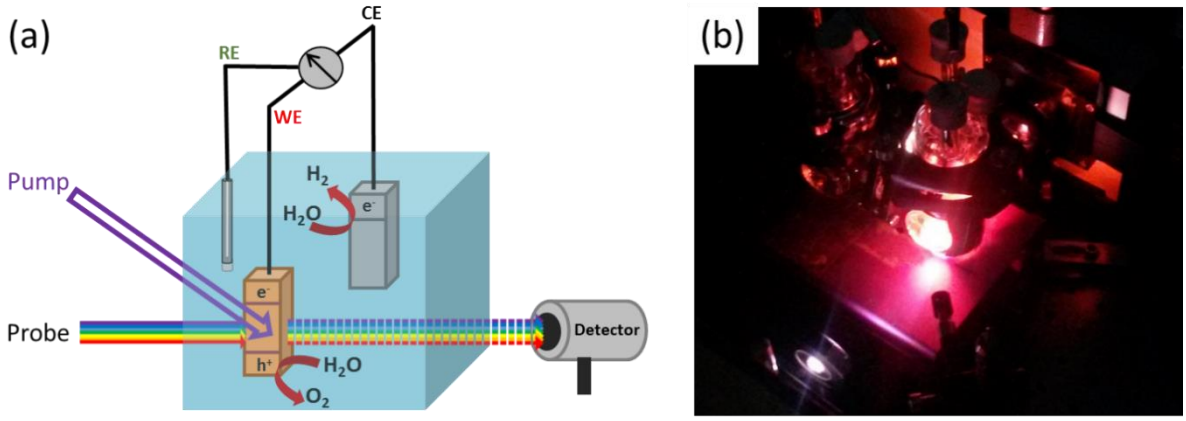

Figure 16 – (a) A schematic illustrating a TAS measurement of a photoelectrode under working photoelectrochemical conditions. The measurement allows the effect of applied bias on charge carrier dynamics to be studied. WE is the working electrode, RE is the reference electrode and CE is the counter electrode. (b) A photograph taken at the University of Liverpool showing a TAS measurement (flash photolysis) of a hematite photoelectrode in a 2-compartment photoelectrochemcial cell.

TiO_2 is perhaps the photoelectrode material which has been most studied by TAS. In a seminal report by Bahnemann *et al.* in 1984 the charge carriers in a colloidal solution of TiO_2 were first identified, in which two characteristic absorption peaks at 475 nm and at > 650 nm assigned to photogenerated holes and electron respectively.[100] More recently, TAS has been used to study TiO_2 photoelectrode films to provide evidence for four-hole water oxidation chemistry.[101] This was quickly followed by TAS of TiO_2 photoelectrodes in a complete photoelectrochemical cell.[62] TAS studies of metal oxide photoelectrodes such as α-Fe_2O_3[102,103], TiO_2[62,104], ZnO[105,106], WO_3[42,107] and $BiVO_4$[108,109] have since become well established in the literature. The next section will outline the recent literature/results of TAS of α-Fe_2O_3 for water splitting.

1.7 TAS of α-Fe_2O_3

Chapters 2-4 of this thesis will describe work in which TAS has been used to rationalise the activity of several hematite photoanodes for PEC water slitting applications. Like TiO_2, α-Fe_2O_3 has been well studied using TAS. Many previous reports of transient absorption spectroscopy of α-Fe_2O_3 have focused on ultrafast timescales, and typically reported very fast (<75–150 ps) decay kinetics assigned to the recombination dynamics of photoinduced electrons and holes.[59,103,110] Such studies have reported only a very small percentage of charge carriers remaining a few hundreds of nanoseconds after laser excitation. It should be noted that ultrafast studies are typically carried out with high excitation densities, resulting in high photoinduced charge carrier densities, and therefore fast bimolecular (non-geminate) recombination. It is unclear to what extent such ultrafast recombination dynamics relate to α-Fe_2O_3 photoanodes under continuous solar irradiation in a PEC cell. TAS studies of α-Fe_2O_3 photoelectrodes which employ lower excitation densities are also reported in the literature, focusing on the detection of photogenerated charge carriers on the microsecond-second timescales.[73,102,111] This timescale is particularly relevant as hole transfer from hematite to water is known to be a slow process in the absence of a catalyst, meaning that holes need to avoid recombination and live for up to ~1-2 seconds.[111] These previous TAS studies of α-Fe_2O_3 photoelectrodes have examined numerous aspects of the photo-physics and chemistry from fs to s timescales, including: the rates of charge trapping,[102,112] the effect of applied bias on charge trapping and recombination,[102,112] kinetic competition between slow electron-hole recombination and water oxidation[111] and the role of co-catalysts on hole kinetics.[76,113,114,87] Of particular significance has been the realisation that a key requirement for water splitting is the ability to accumulate very long-lived holes at the SCLJ, with apparent rate constants for water splitting ranging from 0.1–6 s^{-1},[111,115] correlating with a significant measured thermal barrier for hole transfer.[116] The slow hole transfer kinetics of water oxidation provide ample time for undesirable

recombination between bulk electrons and surface accumulated holes to occur on the millisecond timescales. This has been shown to occur in Si-α-Fe_2O_3 at applied potentials lower than 0.2 $V_{Ag/AgCl}$ (pH ~13.7), significantly lowering photoelectrochemical activity.[117]

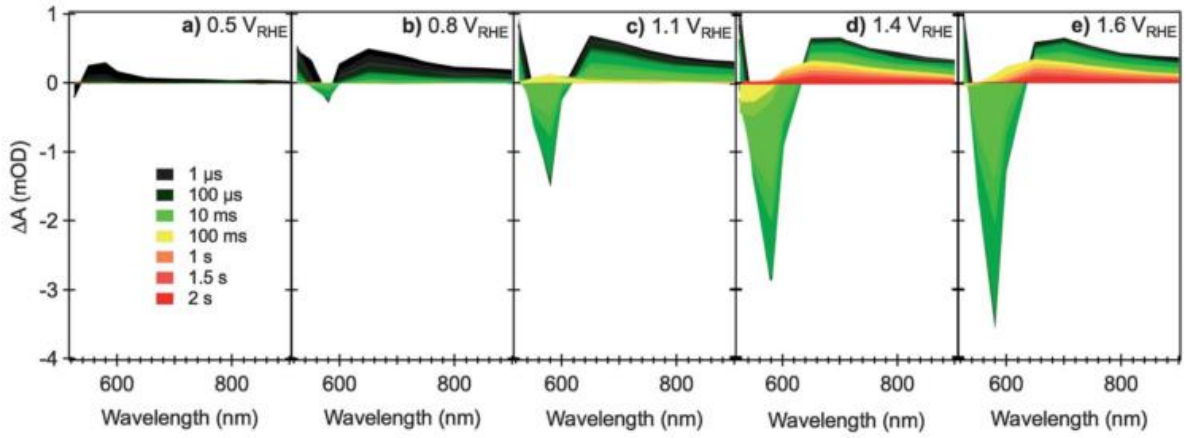

Figure 17 - Transient absorption spectra of nanostructured Si-doped CVD hematite photoanodes under different applied electrical bias as indicated in figures (a) to (e), relative to RHE, in 0.1M NaOH. The measurements are performed in a three-electrode cell, with Pt gauze as counter electrode and Ag/AgCl (0.3 M NaCl) as reference. The nanostructure photoanodes are excited with a UV laser pulse (355 nm, 200 mJ cm^{-2}, 0.33 Hz) and monitored with the output of a monochromated Xe lamp (75 W). The colour code for the spectra time delays is shown in (a).

Two key features are observed when probing α-Fe_2O_3 in the visible/NIR region. Firstly a broad positive feature is observed, typically spanning *ca.* 500-900 nm (although it is usually reported to be >600 nm with a maximum at *ca.* 650 nm). This feature has been reported in numerous types of hematite photoelectrodes and is assigned to photo-holes.[73,102,117–119] These holes appear to accumulate at/near the surface as evidenced by hole scavengers, the addition of which significantly reduces the magnitude.[117] The magnitude and lifetime of this feature varies significantly between different types of hematite films, however, a common trend between films is that increasing the applied bias to more positive potentials usually increases the magnitude of the feature due to increased band bending and therefore more efficient charge separation. The second TAS feature of hematite when probing in the visible/NIR region is a sharp feature centred at *ca.* 575 nm. In the absence of a bias this feature exists as a short-lived

(*ca.* μs-ms) positive signal. When a positive bias is applied, this initially positive feature quickly inverts into a bleach (decrease in optical density) on ps timescales before finally recovering back to zero on ms-s timescales. The magnitude of the bleach increases with increasing positive bias. This feature can also be observed using steady-state UV/Vis absorbance measurements where a positive feature with the same shape of that in the TAS measurements grows in with increasing positive bias.[102] The feature at *ca.* 575 nm has been proposed to be due to localised trap states close to the band edge, possibly related to the presence of oxygen vacancies or defects.[102,112,118] Under positive bias the Fermi level is lowered and trap state occupancy is lowered, enabling the promotion of valence band electrons to the vacant trap states upon absorption of visible photons. Using both fs and ms TAS, Durrant *et al.*[102] were the first to show that following UV excitation of hematite held at potentials significantly positive of the flat band potential, rapid photoelectron trapping can occur in the oxidised states, which leads to the bleaching of the 575 nm feature. Figure 17 shows a typical α-Fe_2O_3 TAS spectrum previously obtained in the literature,[102] while Figure 18 shows a visual representation of the two transitions occurring in hematite as probed by TAS measurements.

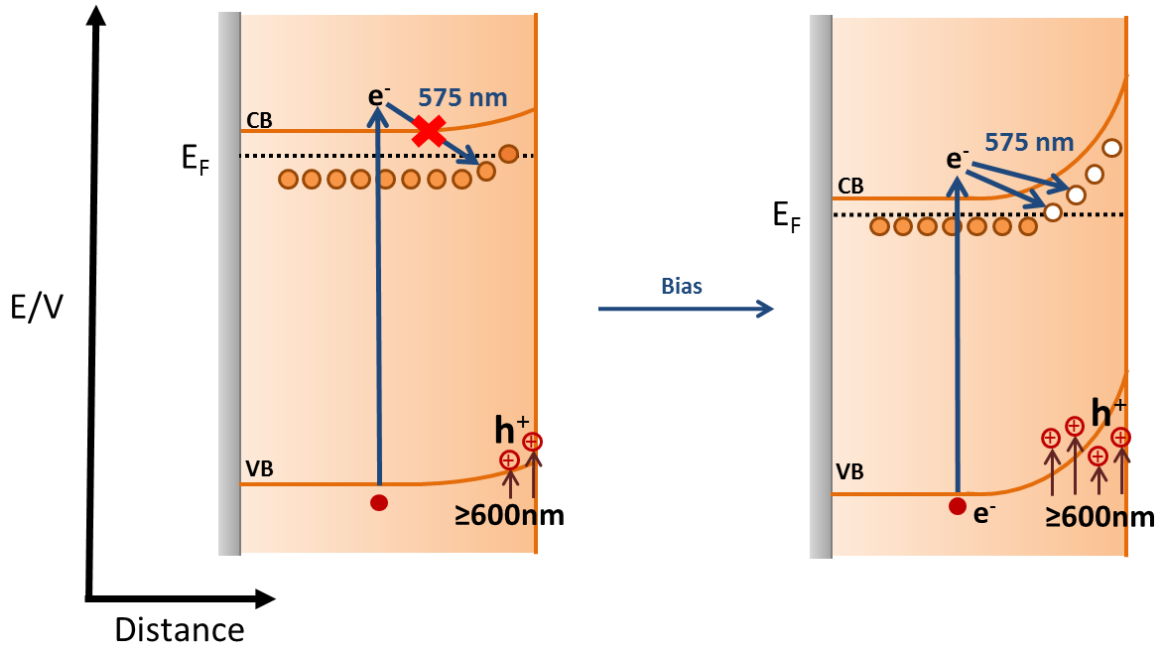

Figure 18 - Schematic showing hematite TAS assignments. The feature at λ > 600 nm is assigned to photo-holes which accumulate in increasing numbers near the surface as the positive bias is increased. The bleach at ~575 nm is observed under a positive bias and is assigned to photo-electron trapping at localised states which is primarily occurring on the sub-microsecond timescale, in line with Barroso et al.[102]

It should be noted that there are conflicting reports in the literature regarding the identity of the spectral feature observed at *ca.* 575 nm. Several other groups have investigated the 575 nm feature using steady-state absorbance in conjunction with electrochemical impedance spectroscopy (EIS), modulated photocurrent impedance spectroscopy (IMPS) and cyclic voltammetry and have proposed that it is related to a water oxidation intermediate, possibly Fe(IV)=O.[120–125] In this thesis the TAS data has been interpreted in terms of the model proposed by Durrant *et al.* in which the 575 nm feature is assigned to photoelectron trapping. Chapter 3 will address the debate regarding the 575 nm feature in further detail and will provide further evidence supporting the assignment of electron trapping at V_O sites as opposed to a water oxidation intermediate.

Very recently, TAS measurements have also been carried out with a more sustained excitation phase using LEDs.[119,126] These measurements essentially combine transient and steady state

absorption monitoring to more effectively understand processes occurring at equilibrium. Le Formal *et al.*[119] have used this technique to carry out a rate law analysis of the order of water oxidation as a function of surface hole density on a hematite photoanode. Their study revealed a transition from a slow, first order reaction at low accumulated hole density (low light intensity) to a faster, third order mechanism once the surface hole density is sufficient to enable oxidation of nearest neighbour metal atoms. This technique is useful as determining the mechanistic details of the multiredox water oxidation reaction has proved challenging.

1.8 The water oxidation mechanism at a metal oxide surface

The oxidation of water to molecular oxygen is a step common to all approaches which convert sunlight to fuel and so determining the precise mechanism of this process is vital. The mechanism of natural water oxidation by photosynthesis is not yet fully understood and the mechanism of artificial water oxidation such as that taking place on a metal oxide surface is even less known. The surfaces of metal oxides such as hematite have been found to play a significant role in determining the efficiency of water oxidation, however, previous works have only allowed hypotheses to be made regarding the identity of relevant surface species.[119,122,123] Due to the mismatch in timescales for recombination which is often very fast, and hole transfer kinetics to the electrolyte which is often very slow, it can be difficult to determine slow mechanistic features with pump-probe TAS measurements.[111] Furthermore, while some spectroscopic studies, including the use of infrared spectroscopy, have been carried out to probe the precise chemical nature of artificial water oxidation intermediates, progress has proved challenging.[123,127,128] Chapter 5 of this thesis will discuss current insight into the water oxidation mechanism at metal oxide surfaces and will explore the use of Shell Isolated Nanoparticles for Enhanced Raman Spectroscopy (SHINERS) as a potential method for probing chemical identities of reaction intermediates *in situ*. An overview of the current

progress made towards detecting water oxidation intermediates at metal oxide surfaces, and an introduction to Raman spectroscopy and SHINERS will be provided separately in chapter 5.

1.9 References

1. R. M. Navarro Yerga, M. C. Álvarez Galván, F. del Valle, J. A. Villoria de la Mano, and J. L. G. Fierro, *ChemSusChem*, 2009, **2**, 471–485.

2. T. Y. T. Inui, M. Anpo, K. Izui, S. Yanagida, *Adv. Chem. Conversions Mitigating Carbon Dioxide, Proc. Fourth Int. Conf. Carbon Dioxide Util.*, 1997, **114**, 1–699.

3. *ASTM G173-03 (2012), Stand. Tables Ref. Sol. Spectr. Irradiances Direct Norm. Hemispherical 37° Tilted Surface. West Conshohocken, PA ASTM Int. Available online https//doi.org/10.1520/G0173-03R12*.

4. K. Rajeshwar, R. McConnell, and S. Licht, *Solar Hydrogen Generation*, Springer New York, 2008.

5. J. Jia, L. C. Seitz, J. D. Benck, Y. Huo, Y. Chen, J. W. D. Ng, T. Bilir, J. S. Harris, and T. F. Jaramillo, *Nat. Commun.*, 2016, **7**, 13237.

6. J. Benemann, *Int. J. Hydrogen Energy*, 1997, **22**, 979–987.

7. L. B. Hoch, P. G. O'Brien, A. Jelle, A. Sandhel, D. D. Perovic, C. A. Mims, and G. A. Ozin, *ACS Nano*, 2016, **10**, 9017–9025.

8. A. J. Esswein and D. G. Nocera, *Chem. Rev.*, 2007, **107**, 4022–4047.

9. X. Chen, S. Shen, L. Guo, and S. S. Mao, *Chem. Rev.*, 2010, **110**, 6503–6570.

10. B. a. Pinaud, J. D. Benck, L. C. Seitz, A. J. Forman, Z. Chen, T. G. Deutsch, B. D. James, K. N. Baum, G. N. Baum, S. Ardo, H. Wang, E. Miller, and T. F. Jaramillo,

Energy Environ. Sci., 2013, **6**, 1983.

11. P. Y. Yu and M. Cardona, *Fundamentals of Semiconductors*, Springer Berlin Heidelberg, 2010.

12. N. S. Lewis, *Inorg. Chem.*, 2005, **44**, 6900–6911.

13. A. Murphy, P. Barnes, L. Randeniya, I. Plumb, I. Grey, M. Horne, and J. Glasscock, *Int. J. Hydrogen Energy*, 2006, **31**, 1999–2017.

14. K. Maeda and K. Domen, *J. Phys. Chem. Lett.*, 2010, **1**, 2655–2661.

15. M. Grätzel, *Nature*, 2001, **414**, 338–334.

16. H. Li, W. Tu, Y. Zhou, and Z. Zou, *Adv. Sci.*, 2016, **3**, 1500389.

17. K. Maeda, *ACS Catal.*, 2013, **3**, 1486–1503.

18. A. Iwase, Y. H. Ng, Y. Ishiguro, A. Kudo, and R. Amal, *J. Am. Chem. Soc.*, 2011, **133**, 11054–11057.

19. Y. Huang, Y. Liu, D. Zhu, Y. Xin, and B. Zhang, *J. Mater. Chem. A*, 2016, **4**, 13626–13635.

20. L. M. Peter and K. G. Upul Wijayantha, *ChemPhysChem*, 2014, **15**, 1983–1995.

21. E. L. Miller, *Energy Environ. Sci.*, 2015, **8**, 2809–2810.

22. M. S. Prévot and K. Sivula, *J. Phys. Chem. C*, 2013, **117**, 17879–17893.

23. P. J. Boddy, *J. Electrochem. Soc.*, 1968, **115**, 199–203.

24. A. Fujishima and K. Honda, *Nature*, 1972, **238**, 37–38.

25. Y. Lin, G. Yuan, R. Liu, S. Zhou, S. W. Sheehan, and D. Wang, *Chem. Phys. Lett.*, 2011, **507**, 209–215.

26. M. Forster and A. J. Cowan, in *Black TiO 2 Nanomaterials for Energy Applications*, World Scientific (Europe), 2017, pp. 215–248.

27. L. M. Peter, in *Photocatalysis*, Royal Society of Chemistry, Cambridge, 2016, pp. 1–28.

28. Z. Chen, T. F. Jaramillo, T. G. Deutsch, A. Kleiman-Shwarsctein, A. J. Forman, N. Gaillard, R. Garland, K. Takanabe, C. Heske, M. Sunkara, E. W. McFarland, K. Domen, E. L. Miller, J. a. Turner, and H. N. Dinh, *J. Mater. Res.*, 2010, **25**, 3–16.

29. H. Dotan, N. Mathews, T. Hisatomi, M. Grätzel, and A. Rothschild, *J. Phys. Chem. Lett.*, 2014, **5**, 3330–3334.

30. A. J. Cowan, W. Leng, P. R. F. Barnes, D. R. Klug, and J. R. Durrant, *Phys. Chem. Chem. Phys.*, 2013, **15**, 8772.

31. K. Sivula, F. Le Formal, and M. Grätzel, *ChemSusChem*, 2011, **4**, 432–449.

32. Y. Lin, G. Yuan, S. Sheehan, S. Zhou, and D. Wang, *Energy Environ. Sci.*, 2011, **4**, 4862.

33. J. Y. Kim, G. Magesh, D. H. Youn, J.-W. Jang, J. Kubota, K. Domen, and J. S. Lee, *Sci. Rep.*, 2013, **3**, 2681.

34. K. Sivula, *J. Phys. Chem. Lett.*, 2013, **4**, 1624–1633.

35. J. Nowotny, T. Bak, M. Nowotny, and L. Sheppard, *Int. J. Hydrogen Energy*, 2007, **32**, 2609–2629.

36. M. Ni, M. K. H. Leung, D. Y. C. Leung, and K. Sumathy, *Renew. Sustain. Energy Rev.*, 2007, **11**, 401–425.

37. G. Wang, H. Wang, Y. Ling, Y. Tang, X. Yang, R. C. Fitzmorris, C. Wang, J. Z. Zhang, and Y. Li, *Nano Lett.*, 2011, **11**, 3026–33.

38. T. W. Kim and K.-S. Choi, *Science*, 2014, **343**, 990–994.

39. K. Sayama, A. Nomura, T. Arai, T. Sugita, R. Abe, M. Yanagida, T. Oi, Y. Iwasaki, Y. Abe, and H. Sugihara, *J. Phys. Chem. B*, 2006, **110**, 11352–60.

40. Y. H. Ng, A. Iwase, A. Kudo, and R. Amal, *J. Phys. Chem. Lett.*, 2010, **1**, 2607–2612.

41. X. Liu, F. Wang, and Q. Wang, *Phys. Chem. Chem. Phys.*, 2012, **14**, 7894.

42. F. M. Pesci, A. J. Cowan, B. D. Alexander, J. R. Durrant, and D. R. Klug, *J. Phys. Chem. Lett.*, 2011, **2**, 1900–1903.

43. J. Su, L. Guo, N. Bao, and C. a Grimes, *Nano Lett.*, 2011, **11**, 1928–1933.

44. D. a. Wheeler, G. Wang, Y. Ling, Y. Li, and J. Z. Zhang, *Energy Environ. Sci.*, 2012, **5**, 6682.

45. M. Fleischer, *J. Chem. Educ.*, 1954, **31**, 446.

46. B. Beverskog and I. Puigdomenech, *Corros. Sci.*, 1996, **38**, 2121–2135.

47. Z. Li, X. Lai, H. Wang, D. Mao, C. Xing, and D. Wang, *Nanotechnology*, 2009, **20**, 245603.

48. H.-J. Kim, K.-I. Choi, A. Pan, I.-D. Kim, H.-R. Kim, K.-M. Kim, C. W. Na, G. Cao, and J.-H. Lee, *J. Mater. Chem.*, 2011, **21**, 6549–6555.

49. K. Woo, H. J. Lee, J.-P. Ahn, and Y. S. Park, *Adv. Mater.*, 2003, **15**, 1761–1764.

50. J.-J. Wu, Y.-L. Lee, H.-H. Chiang, and D. K.-P. Wong, *J. Phys. Chem. B*, 2006, **110**, 18108–18111.

51. S. Kment, P. Schmuki, Z. Hubicka, L. Machala, R. Kirchgeorg, N. Liu, L. Wang, K. Lee, J. Olejnicek, M. Cada, I. Gregora, and R. Zboril, *ACS Nano*, 2015, **9**, 7113–7123.

52. J. A. Klug, N. G. Becker, S. C. Riha, A. B. F. Martinson, J. W. Elam, M. J. Pellin, and T. Proslier, *J. Mater. Chem. A*, 2013, **1**, 11607.

53. R. L. Spray and K. S. Choi, *Chem. Mater.*, 2009, **21**, 3701–3709.

54. P. Hiralal, S. Saremi-Yarahmadi, B. C. Bayer, H. Wang, S. Hofmann, K. G. Upul Wijayantha, and G. A. J. Amaratunga, *Sol. Energy Mater. Sol. Cells*, 2011, **95**, 1819–1825.

55. A. Duret and M. Grätzel, *J. Phys. Chem. B*, 2005, **109**, 17184–17191.

56. Y. P. He, Y. M. Miao, C. R. Li, S. Q. Wang, L. Cao, S. S. Xie, G. Z. Yang, B. S. Zou, and C. Burda, *Phys. Rev. B*, 2005, **71**, 125411.

57. N. M. Abdul Rashid, C. Haw, W. Chiu, N. H. Khanis, A. Rohaizad, P. Khiew, and S. Abdul Rahman, *CrystEngComm*, 2016, **18**, 4720–4732.

58. F. J. Morin, *Phys. Rev.*, 1951, **83**, 1005–1010.

59. N. J. Cherepy, D. B. Liston, J. A. Lovejoy, H. Deng, and J. Z. Zhang, *J. Phys. Chem. B*, 1998, **5647**, 770–776.

60. M. Dare-Edwards, J. Goodenough, A. Hamnett, and P. Trevelick, *J. Chem. SOC., Faraday Trans. I*, 1983, **79**, 2027–2041.

61. K. Sivula, R. Zboril, F. Le Formal, R. Robert, A. Weidenkaff, J. Tucek, J. Frydrych, and M. Grätzel, *J. Am. Chem. Soc.*, 2010, **132**, 7436–44.

62. A. J. Cowan, J. Tang, W. Leng, J. R. Durrant, and D. R. Klug, *J. Phys. Chem. C*, 2010, **114**, 4208–4214.

63. Z. Li, W. Luo, M. Zhang, J. Feng, and Z. Zou, *Energy Environ. Sci.*, 2013, **6**, 347–370.

64. I. Cesar, K. Sivula, A. Kay, R. Zboril, and M. Grätzel, *J. Phys. Chem. C*, 2009, **113**,

772–782.

65. Y. Ling, G. Wang, D. A. Wheeler, J. Z. Zhang, and Y. Li, *Nano Lett.*, 2011, **11**, 2119–25.

66. P. Zhang, A. Kleiman-Shwarsctein, Y.-S. Hu, J. Lefton, S. Sharma, A. J. Forman, and E. McFarland, *Energy Environ. Sci.*, 2011, **4**, 1020.

67. Y. Ling, G. Wang, J. Reddy, C. Wang, J. Z. Zhang, and Y. Li, *Angew. Chem. Int. Ed. Engl.*, 2012, **51**, 4074–9.

68. M. G. Walter, E. L. Warren, J. R. McKone, S. W. Boettcher, Q. Mi, E. a Santori, and N. S. Lewis, *Chem. Rev.*, 2010, **110**, 6446–73.

69. R. van de Krol, Y. Liang, and J. Schoonman, *J. Mater. Chem.*, 2008, **18**, 2311.

70. D. K. Zhong, M. Cornuz, K. Sivula, M. Grätzel, and D. R. Gamelin, *Energy Environ. Sci.*, 2011, **4**, 1759.

71. B. Eftekharinia, A. Moshaii, A. Dabirian, and N. S. Vayghan, *J. Mater. Chem. A*, 2017, **5**, 3412–3424.

72. D. S. Tilley, M. Cornuz, K. Sivula, and M. Grätzel, *Angew. Chemie Int. Ed.*, 2010, **49**, 6405–6408.

73. M. Barroso, C. A. Mesa, S. R. Pendlebury, A. J. Cowan, T. Hisatomi, K. Sivula, M. Grätzel, D. R. Klug, and J. R. Durrant, *Proc. Natl. Acad. Sci. U. S. A.*, 2012, **109**, 15640–5.

74. F. Lin and S. W. Boettcher, *Nat. Mater.*, 2013, **13**, 81–86.

75. B. Kumar, M. Llorente, J. Froehlich, T. Dang, A. Sathrum, and C. P. Kubiak, *Annu. Rev. Phys. Chem.*, 2012, **63**, 541–69.

76. R. Liu, Z. Zheng, J. Spurgeon, and X. Yang, *Energy Environ. Sci.*, 2014, **7**, 2504.

77. T. Wang, Z. Luo, C. Li, and J. Gong, *Chem. Soc. Rev.*, 2014, **43**, 7469–84.

78. B. Klahr, S. Gimenez, F. Fabregat-Santiago, J. Bisquert, and T. W. Hamann, *J. Am. Chem. Soc.*, 2012, **134**, 16693–700.

79. M. J. Kenney, M. Gong, Y. Li, J. Z. Wu, J. Feng, M. Lanza, and H. Dai, *Science*, 2013, 342, 836–40.

80. A. Bulusu, S. A. Paniagua, B. A. Macleod, A. K. Sigdel, J. J. Berry, D. C. Olson, S. R. Marder, and S. Graham, *Langmuir*, 2013, **29**, 3935–3942.

81. J. Li, S. Kim, S. Edington, J. Nedy, S. Cho, K. Lee, A. J. Heeger, M. C. Gupta, and J. T. Yates Jr, *Sol. Energy Mater. Sol. Cells*, 2011, **95**, 1123–1130.

82. F. Le Formal, N. Tétreault, M. Cornuz, T. Moehl, M. Grätzel, and K. Sivula, *Chem. Sci.*, 2011, **2**, 737–743.

83. R. Liu, Z. Zheng, J. Spurgeon, and X. Yang, *Energy Environ. Sci.*, 2014, **7**, 2504.

84. S. Hu, N. S. Lewis, J. W. Ager, J. Yang, J. R. McKone, and N. C. Strandwitz, *J. Phys. Chem. C*, 2015, **119**, 24201–24228.

85. R. L. Spray, K. J. McDonald, and K.-S. Choi, *J. Phys. Chem. C*, 2011, **115**, 3497–3506.

86. M. Barroso, A. J. Cowan, S. R. Pendlebury, M. Grätzel, D. R. Klug, and J. R. Durrant, *J. Am. Chem. Soc.*, 2011, **133**, 14868–71.

87. L. Steier, I. Herraiz-Cardona, S. Gimenez, F. Fabregat-Santiago, J. Bisquert, S. D. Tilley, and M. Grätzel, *Adv. Funct. Mater.*, 2014, **24**, 7681–7688.

88. J.-W. Jang, C. Du, Y. Ye, Y. Lin, X. Yao, J. Thorne, E. Liu, G. McMahon, J. Zhu, A. Javey, J. Guo, and D. Wang, *Nat. Commun.*, 2015, **6**, 7447.

89. M. G. Ahmed, I. E. Kretschmer, T. A. Kandiel, A. Y. Ahmed, F. A. Rashwan, and D. W. Bahnemann, *ACS Appl. Mater. Interfaces*, 2015, **7**, 24053–24062.

90. A. J. Abel, A. M. Patel, S. Y. Smolin, B. Opasanont, and J. B. Baxter, *J. Mater. Chem. A*, 2016, **4**, 6495–6504.

91. Y. Pertot, C. Schmidt, M. Matthews, A. Chauvet, M. Huppert, V. Svoboda, A. von Conta, A. Tehlar, D. Baykusheva, J. Wolf, and H. J. Wörner, *Science*, 2017, **355**, 264–267.

92. S. L. Dexheimer, *Terahertz Spectroscopy: Principles and Applications*, CRC Press, 2008.

93. R. G. W. Norish and G. Porter, *Nature*, 1949, **164**, 658–658.

94. G. Porter, *Proc. R. Soc. A Math. Phys. Eng. Sci.*, 1950, **200**, 284–300.

95. N. V Tkachenko, in *Optical Spectroscopy*, Elsevier, 2006, pp. 129–149.

96. N. V Tkachenko, in *Optical Spectroscopy*, Elsevier, 2006, pp. 185–215.

97. N. V Tkachenko, in *Optical Spectroscopy*, Elsevier, 2006, pp. 263–285.

98. K. C. Lee, J. Siegel, S. E. Webb, S. Lévêque-Fort, M. J. Cole, R. Jones, K. Dowling, M. J. Lever, and P. M. French, *Biophys. J.*, 2001, **81**, 1265–1274.

99. F. M. Pesci, G. Wang, D. R. Klug, Y. Li, and A. J. Cowan, *J. Phys. Chem. C*, 2013, **117**, 25837–25844.

100. D. Bahnemann, A. Henglein, J. Lilie, and L. Spanhel, *J. Phys. Chem.*, 1984, **88**, 709–711.

101. J. Tang, J. R. Durrant, and D. R. Klug, *J. Am. Chem. Soc.*, 2008, **130**, 13885–13891.

102. M. Barroso, S. R. Pendlebury, A. J. Cowan, and J. R. Durrant, *Chem. Sci.*, 2013, **4**, 2724.

103. Z. Huang, Y. Lin, X. Xiang, W. Rodríguez-Córdoba, K. J. McDonald, K. S. Hagen, K.-S. Choi, B. S. Brunschwig, D. G. Musaev, C. L. Hill, D. Wang, and T. Lian, *Energy Environ. Sci.*, 2012, **5**, 8923.

104. X. Wang, A. Kafizas, X. Li, S. J. A. Moniz, P. J. T. Reardon, J. Tang, I. P. Parkin, and J. R. Durrant, *J. Phys. Chem. C*, 2015, **119**, 10439–10447.

105. C. Bauer, G. Boschloo, E. Mukhtar, and A. Hagfeldt, *Chem. Phys. Lett.*, 2004, **387**, 176–181.

106. R. L. Willis, C. Olson, B. O'Regan, T. Lutz, J. Nelson, and J. R. Durrant, *J. Phys. Chem. B*, 2002, **106**, 7605–7613.

107. I. Grigioni, K. G. Stamplecoskie, E. Selli, and P. V Kamat, *J. Phys. Chem. C*, 2015, **119**, 20792–20800.

108. Y. Ma, S. R. Pendlebury, A. Reynal, F. Le Formal, and J. R. Durrant, *Chem. Sci.*, 2014, **5**, 2964.

109. J. Ravensbergen, F. F. Abdi, J. H. van Santen, R. N. Frese, B. Dam, R. van de Krol, and J. T. M. Kennis, *J. Phys. Chem. C*, 2014, **118**, 27793–27800.

110. L. Fu, Z. Wu, X. Ai, J. Zhang, Y. Nie, S. Xie, G. Yang, and B. Zou, *J. Chem. Phys.*, 2004, **120**, 3406–13.

111. F. Le Formal, S. R. Pendlebury, M. Cornuz, S. D. Tilley, M. Grätzel, and J. R. Durrant, *J. Am. Chem. Soc.*, 2014, **136**, 2564–74.

112. S. R. Pendlebury, X. Wang, F. Le Formal, M. Cornuz, A. Kafizas, S. D. Tilley, M. Grätzel, and J. R. Durrant, *J. Am. Chem. Soc.*, 2014, **136**, 9854–9857.

113. T. Hisatomi, F. Le Formal, M. Cornuz, J. Brillet, N. Tétreault, K. Sivula, and M. Grätzel,

Energy Environ. Sci., 2011, **4**, 2512.

114. T. Wang, Z. Luo, C. Li, and J. Gong, *Chem. Soc. Rev.*, 2014, **43**, 7469–7484.

115. H. K. Dunn, J. M. Feckl, A. Müller, D. Fattakhova-Rohlfing, S. G. Morehead, J. Roos, L. M. Peter, C. Scheu, and T. Bein, *Phys. Chem. Chem. Phys.*, 2014, **16**, 24610–24620.

116. A. J. Cowan, C. J. Barnett, S. R. Pendlebury, M. Barroso, K. Sivula, M. Grätzel, J. R. Durrant, and D. R. Klug, *J. Am. Chem. Soc.*, 2011, **133**, 10134–10140.

117. S. R. Pendlebury, A. J. Cowan, M. Barroso, K. Sivula, J. Ye, M. Grätzel, D. R. Klug, J. Tang, and J. R. Durrant, *Energy Environ. Sci.*, 2012, **5**, 6304–6312.

118. M. Forster, R. J. Potter, Y. Ling, Y. Yang, D. R. Klug, Y. Li, and A. J. Cowan, *Chem. Sci.*, 2015, **6**, 4009–4016.

119. F. Le Formal, E. Pastor, S. D. Tilley, C. a Mesa, S. R. Pendlebury, M. Grätzel, and J. R. Durrant, *J. Am. Chem. Soc.*, 2015, **137**, 6629–6637.

120. B. Klahr, S. Gimenez, O. Zandi, F. Fabregat-Santiago, and T. Hamann, *ACS Appl. Mater. Interfaces*, 2015, **7**, 7653–7660.

121. C. Y. Cummings, F. Marken, L. M. Peter, A. a Tahir, and K. G. U. Wijayantha, *Chem. Commun.*, 2012, **48**, 2027.

122. B. Klahr and T. Hamann, *J. Phys. Chem. C*, 2014, **118**, 10393–10399.

123. O. Zandi and T. W. Hamann, *Nat. Chem.*, 2016, **8**, 778–783.

124. N. Yatom, O. Neufeld, and M. Caspary Toroker, *J. Phys. Chem. C*, 2015, **119**, 24789–24795.

125. T. Takashima, K. Ishikawa, and H. Irie, *J. Phys. Chem. C*, 2016, **120**, 24827–24834.

126. Y. Ma, C. A. Mesa, E. Pastor, A. Kafizas, L. Francàs, F. Le Formal, S. R. Pendlebury,

and J. R. Durrant, *ACS Energy Lett.*, 2016, **1**, 618–623.

127. M. Zhang, M. de Respinis, and H. Frei, *Nat. Chem.*, 2014, **6**, 362–7.

128. D. M. Herlihy, M. M. Waegele, X. Chen, C. D. Pemmaraju, D. Prendergast, and T. Cuk, *Nat. Chem.*, 2016, **8**, 1–7.

2

Oxygen deficient α-Fe_2O_3 photoelectrodes: a balance between enhanced electrical properties and trap-mediated losses

Contents

2.1 Introduction

Although the band gap and band energies of α-Fe_2O_3 (~2.1 eV) lead to a maximum theoretical solar-to-hydrogen (STH) efficiency of ~15.3%,[1] the actual achieved STH efficiencies of α-Fe_2O_3 photoelectrodes are substantially below this value, typically in the range of 1–2%[2] as a result of the limiting factors discussed in chapter 1, including: poor conductivity,[3] short electron–hole lifetimes,[4] slow oxygen evolution reaction kinetics,[5] a low visible light absorption coefficient coupled to short hole diffusion lengths (2–4 nm).[6] Higher photocurrent densities have been achieved through nanostructuring which has the aim of increasing the concentration of charges generated close to the semiconductor liquid junction (SCLJ) to overcome the short hole diffusion length.[7] In such nanostructured electrodes, dopants are known to be critical for photoelectrochemical activity, with un-doped α-Fe_2O_3 electrodes being electrically insulating[7] and often photoelectrochemically inactive.[8] A wide variety of extrinsic dopants have been explored including Si,[8–10] Sn,[11–13] Ti,[13–15] Pt[16,17] which lead to both enhanced long range charge transport and the formation of a sufficient electric field for charge separation at the SCLJ within the nanostructured domains.[8]

The introduction of oxygen vacancies (V_O) has also been demonstrated as an effective approach to improve the activity of α-Fe_2O_3 photoelectrodes,[18–20] in addition to a wide range of other metal oxides.[18,21–23] A recent report by our collaborators Li *et al.*[19] showed that the decomposition of β-FeOOH nanowires in an oxygen deficient atmosphere resulted in highly oxygen deficient hematite (α-Fe_2O_{3-x}) photoelectrodes for water oxidation, with a photocurrent of 3.4 mA cm^{-2} (at 1.4 V_{RHE}) being achieved under simulated solar light of 100 mW cm^{-2}. The enhanced activity, ease of inclusion of V_O, ability to process at temperatures as low as 350 °C[24] and reports of a synergistic effect of extrinsic dopants with intrinsic V_O sites[20,25] has led to a surge of interest[19,20,25–28] in the controlled inclusion of V_O in hematite over the last several years.

An oxygen vacancy is typically defined as a type of point defect in which the oxygen atom is missing,[29] and the creation of a V_O leaves behind two electrons per missing oxygen atom. Typically the removal of oxygen atoms to leave behind two electrons would be expected to increase the overall majority carrier electron concentration and therefore improve conductivity. Furthermore, one of the characteristics of many transition-metal oxides is the possibility to change the metal oxidation state, opening up new possibilities to redistribute the electrons involved in the bonding with the oxygen atom which has been removed to form the vacancy. In the case of hematite this leads to the reduction of nearby Fe^{3+} into Fe^{2+}.[18,28,29] Iron reduction to Fe^{2+} can be both beneficial and unfavourable for water splitting applications. The Fe^{3+}/Fe^{2+} mix is expected to increase conductivity and carrier mobility by increasing electron hopping between Fe^{3+} and Fe^{2+}.[25] Conversely, it has been known for over 25 years that the inclusion of V_O/Fe^{2+} sites within α-Fe_2O_3 leads to the formation of a donor band ~80 meV below the conduction band[30] and high concentrations of Fe^{2+} sites are thought to act as recombination centres for photoexcited holes.[31] DFT studies of hematite in which the photocurrent onset potential is predicted to be improved by finding the optimum concentration of V_O's have also been reported.[32]

Given the potential advantages of V_O inclusion[26,33–35] it is important that the fundamental processes are well understood. The higher incident photon to current efficiency (IPCE) of α-Fe_2O_{3-x} (64% at 0.50 $V_{Ag/AgCl}$, pH ~13.7) compared to the air annealed sample (α-Fe_2O_3, 0.57% at 0.50 $V_{Ag/AgCl}$, pH ~13.7) in the report of Li *et al*.[19] correlated with the presence of Fe^{2+} sites as measured by XPS and a large increase in the measured donor density (N_d). However, to date research has for the most part concentrated on material development and few direct measurements of the actual mechanism of enhanced activity for oxygen deficient hematite are reported.

A further complication is that although the inclusion of V_O results in a large increase in photocurrent, the onset potentials remain relatively high for α-Fe_2O_{3-x} materials, typically 0.0 $V_{Ag/AgCl}$ (pH ~13.7) or greater[19,24] compared to as low as *ca.* -0.4 $V_{Ag/AgCl}$ (pH ~13.7) found for a more state of the art atomic layer deposited (ALD) α-Fe_2O_3 electrode following a high temperature (800 ^oC) treatment. This high onset potential leads to typical efficiencies for oxygen deficient hematite that are significantly lower than other state of the art hematite photoelectrodes.[36,37]

This chapter reports a TAS driven study of α-Fe_2O_{3-x} photoelectrodes under working photoelectrochemical conditions. A detailed kinetic analysis is carried out to rationalise the bias dependent activity of α-Fe_2O_{3-x} compared to the analogous film without intentional oxygen vacancy insertion (α-Fe_2O_3). The onset potential of α-Fe_2O_{3-x} is also addressed and atomic layer deposition of Al_2O_3 is explored as a route to altering hematite surface states and improving this poor onset potential.

2.2 Results and discussion

2.2.1 Synthesis and characterisation of α-Fe_2O_3 (air annealed) and α-Fe_2O_{3-x} (oxygen deficient) hematite

For this study fresh α-Fe_2O_3 (air annealed) and α-Fe_2O_{3-x} (oxygen deficient) films were prepared by our collaborators Li *et al*[19] (details are provided in the experimental chapter, chapter 6). Briefly, β-FeOOH nanowire films were first prepared on a FTO substrate through hydrolysis of $FeCl_3$ (0.15 M) in a high ionic strength (1 M $NaNO_3$), and low pH (pH 1.5, adjusted by HCl) environment at 95°C for 4 hr. β-FeOOH films were then sintered in air at 550°C for 2 hr to form α-Fe_2O_3. For preparing α-Fe_2O_{3-x}, β-FeOOH films were annealed in a tube furnace in an oxygen-deficient atmosphere (N_2 + air).

XRD recorded at the University of Liverpool confirmed that the β-FeOOH nanowires were completely converted into hematite for both the α-Fe_2O_3 and α-Fe_2O_{3-x} samples in line with the past study,[19] Figure 19.

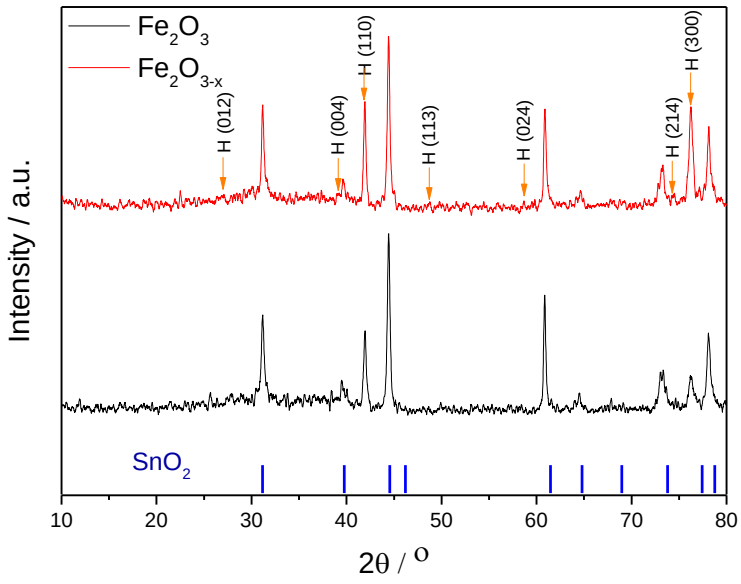

Figure 19 - XRD of α-Fe_2O_3 and α-Fe_2O_{3-x} collected on FTO substrate using a Panalytical X'Pert PRO HTS X-Ray Diffractometer. Diffraction patterns were recorded from 10 to 80° 2 theta with a step size of 0.017° at 1.6° per minute.

The morphologies of α-Fe_2O_3 and α-Fe_2O_{3-x} were examined by SEM (Figure 20) and were found to possess similar structures with typical nanorod dimensions of *ca.* 70 nm by 700 nm, in line with the structures previously reported.[19]

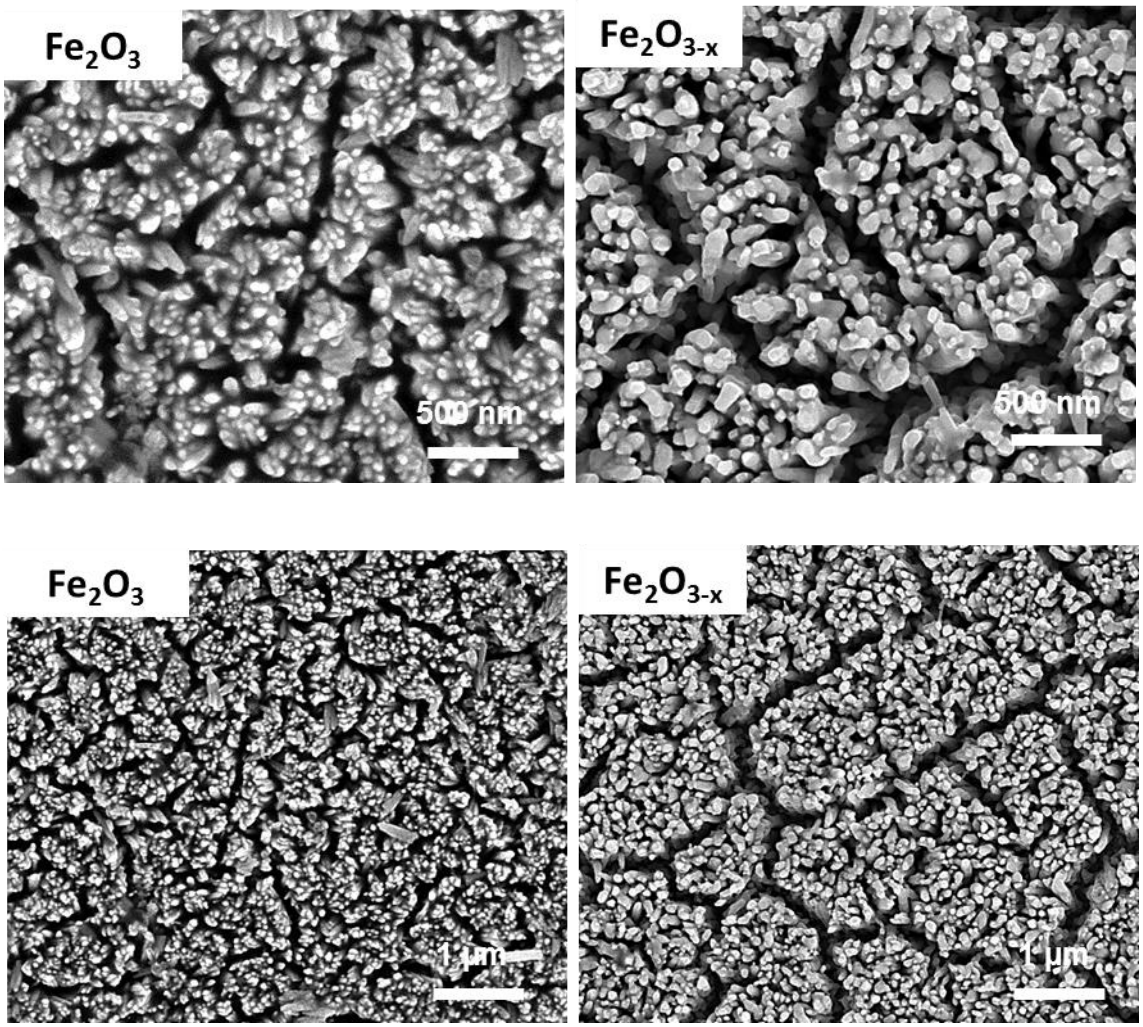

Figure 20 - Scanning electron microscopy images of α-Fe_2O_3 and α-Fe_2O_{3-x}.

UV-Vis extinction spectra were recorded between 350-800 nm for α-Fe_2O_3 and α-Fe_2O_{3-x}, Figure 21. The absorbance spectra of α-Fe_2O_3 and α-Fe_2O_{3-x} have a similar shape and are consistent with typical hematite films in the literature.[38] The difference in magnitude at lower wavelengths is attributed to a difference in film thickness between α-Fe_2O_3 and α-Fe_2O_{3-x}.

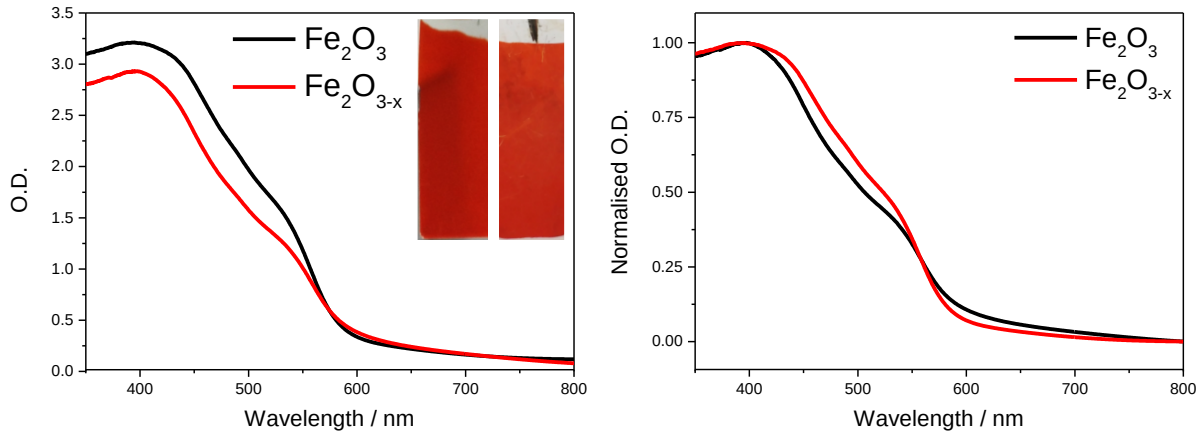

Figure 21 - UV-Vis extinction spectra of α-Fe_2O_3 and α-Fe_2O_{3-x} measured from 350 – 800 nm in transmission mode. Inset shows photographs of α-Fe_2O_3 (right) and α-Fe_2O_{3-x} (left).

α-Fe_2O_{3-x} is expected to have a significantly higher donor density than α-Fe_2O_3 due to the incorporation of oxygen vacancies. The increased presence of oxygen vacancies in α-Fe_2O_{3-x} was linked to an increase in the presence of Fe^{2+} and was observed in the original study by Li *et al.*[19]using XPS. Mott-Schottky analysis confirms the expected higher donor density in the oxygen deficient film (Figure 22), giving values of N_d = 6.4 x 10^{19} cm^{-3} and E_{FB} = -0.66V for α-Fe_2O_3 and N_d = 1.2 x 10^{20} cm^{-3} and E_{FB} = -0.60 V for α-Fe_2O_{3-x}.

The donor density can be estimated from the gradient of the Mott-Schottky plot using the relationship in equation 1[19], were *e* is the charge of an electron, ε is the dielectric constant of hematite (80)[8], ε_0 is the permittivity of vacuum (8.854 x10^{-12} F m^{-1}) and *C* is the capacitance derived from the Mott-Schottky plot at each potential.

$$N_d = \left(\frac{2}{e\varepsilon\varepsilon_0}\right)\left[\frac{d\left(1/C^2\right)}{dV}\right]^{-1} \qquad (1)$$

It should be noted that for ideal Mott-Schottky measurements a flat surface is required. A nanostructured surface such as that of α-Fe_2O_3 and α-Fe_2O_{3-x} will cause a significant degree of uncertainty, and as such, the precise numbers obtained should not be considered accurate. However, comparing two films of the same structure is expected to provide suitable data for comparison purposes.

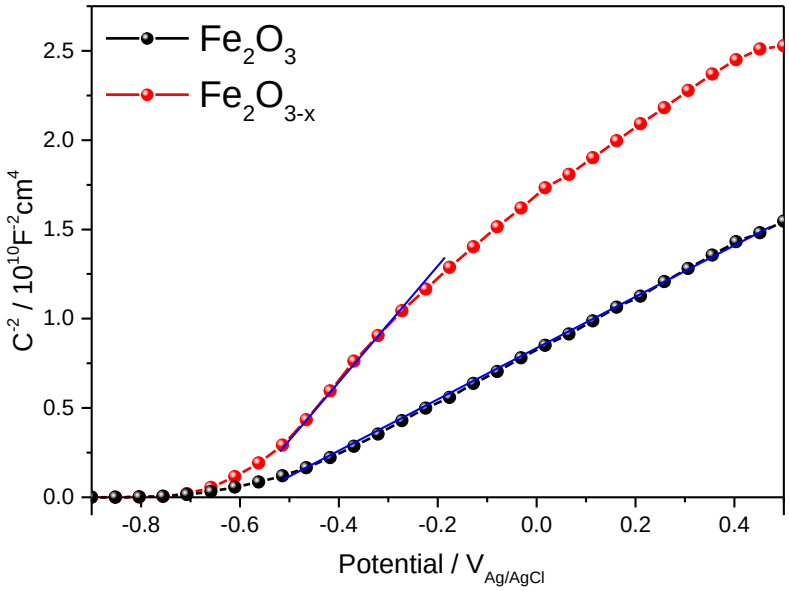

Figure 22 - Mott-Schottky plots of α-Fe_2O_3 giving N_d = 6.4 x 10^{19} cm^{-3} and E_{FB} = -0.66 $V_{Ag/AgCl}$ and α-Fe_2O_{3-x} giving N_d = 1.2 x 10^{20} cm^{-3} and E_{FB} = -0.60 $V_{Ag/AgCl}$. The measurements were carried out in 1 M NaOH (pH ~13.7).

The photoelectrochemical activities of both α-Fe_2O_3 and α-Fe_2O_{3-x} were assessed through linear sweep voltammograms measured in 1 M NaOH using a portion of the output of a 75 W Xe lamp (*ca.* 0.1 sun), scanning at 5 mV s^{-1}. This low power light source was primarily used in this mechanistic study as it allowed us to measure the photo-electrochemical response of the sample inside the transient spectrometer using the same cell as in the TAS measurements.

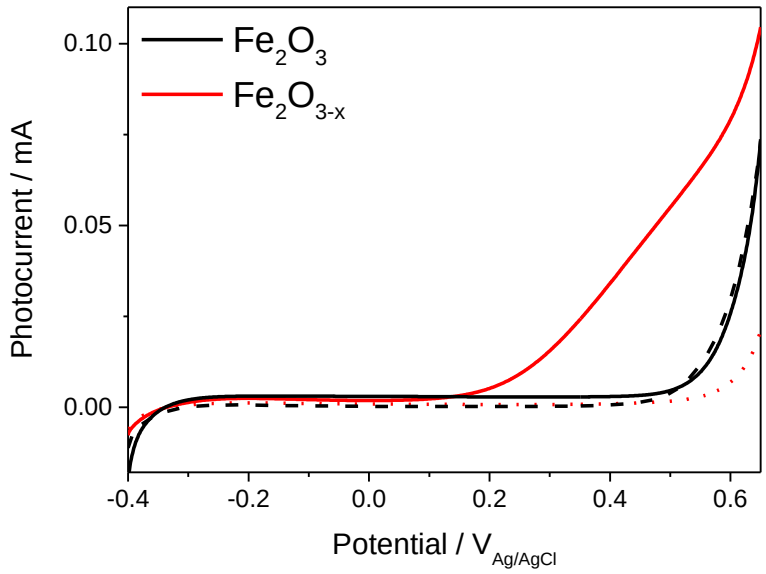

Figure 23 - Linear sweep voltammograms for α-Fe_2O_3 (black) and α-Fe_2O_{3-x} (red), 5 mV s^{-1}, under low power white light illumination in 1 M NaOH (pH ~13.7). The solid lines are under ca. 0.1 sun and the dashed lines are in the dark.

In line with previous reports,[39,40] α-Fe_2O_{3-x} produced a reasonable photocurrent at potentials positive of 0.2 $V_{Ag/AgCl}$, assigned to photoelectrochemical water oxidation, Figure 23. In contrast to α-Fe_2O_{3-x}, the air annealed (550 ^oC) α-Fe_2O_3 sample shows no significant photocurrent (-0.4 to 0.5 $V_{Ag/AgCl}$, pH ~13.7). Furthermore and again in line with previous reports,[19] a small anodic shift in the dark current onset is observed indicating that the surface of Fe_2O_{3-x} is less catalytic. As both films have similar preparation routes, morphology and light harvesting properties, the difference in activity between these films is attributed to the presence of V_O which appear critical for enabling photoelectrochemical water splitting in these nanostructured films.

2.2.2 Transient absorption spectroscopy (TAS) of α-Fe_2O_3 *vs.* α-Fe_2O_{3-x}

In order to rationalise the observed photoelectrochemical response of α-Fe_2O_{3-x} reported here and elsewhere,[19] TAS was carried out to probe the charge carrier dynamics. TAS offers a route

to directly measure the yields and dynamics of excited charge carriers in photoelectrodes *in-situ* and to understand the effect of material modification and treatments (such as V_O doping) on these yields and dynamics.[41–43] Previous TAS studies of α-Fe_2O_3 photoelectrodes have examined numerous aspects of the photo-physics and chemistry of extrinsically doped α-Fe_2O_3, including the role of co-catalysts on hole kinetics,[44–47] and the effect of bias on charge trapping and recombination, from fs to s timescales.[48,49] A detailed overview of the TAS studies carried out on α-Fe_2O_3 is provided in chapter 1. In this chapter we have interpreted the data in terms of the model proposed by Durrant *et al.*[49] in which the 575 nm feature is assigned to photoelectron trapping.

Initial evidence for the trap state model previously proposed by Durrant *et al.*[49] can be observed by steady-state absorbance spectroscopy. Figure 24 shows the steady state absorbance spectra of α-Fe_2O_3 and α-Fe_2O_{3-x} at a range of applied electrical bias *vs.* a negative bias close to the flat-band potential (-0.3 $V_{Ag/AgCl}$, pH ~13.7). As the positive bias is increased a feature centred at *ca.* 575 nm grows. This feature has been reported before[49] and is assigned to the emptying (oxidation) of the trap states in hematite. The assignment of this feature to a water splitting intermediate, as has been alternatively proposed, is initially ruled out as it is observed at potentials prior to the minimum for dark electrolysis (~0.5 $V_{Ag/AgCl}$). This steady-state absorbance feature is much larger in α-Fe_2O_{3-x}, attributed to an increased number of oxygen vacancies and therefore increased number of trap states.

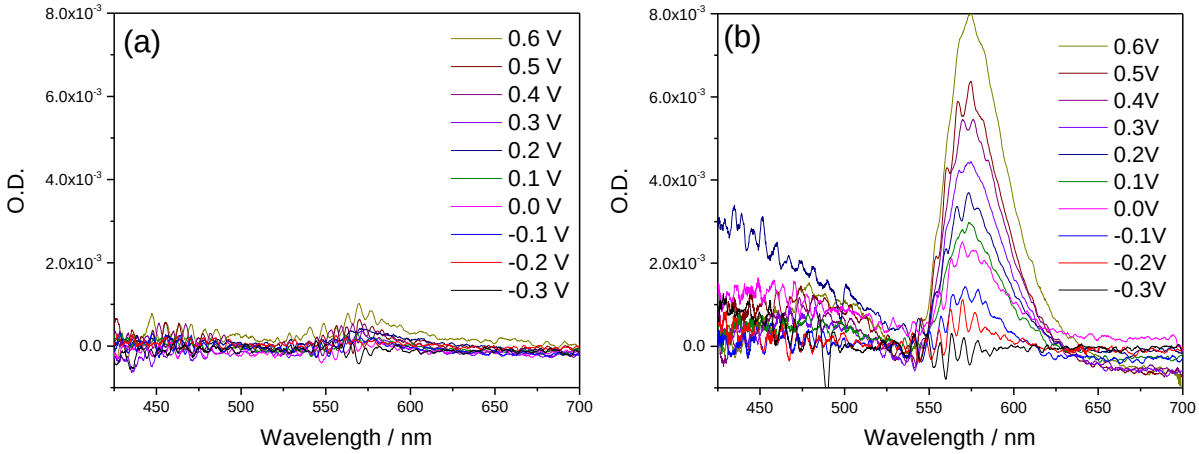

Figure 24 - Difference steady-state absorption spectra of (a) α-Fe_2O_3 and (b) α-Fe_2O_{3-x} under various applied electrical bias vs. a background bias of -0.3 $V_{Ag/AgCl}$ in 1M NaOH (pH ~13.7) (close to the flat-band potential).

Initial TAS measurements for α-Fe_2O_3 and α-Fe_2O_{3-x} are shown below, Figure 25. For these TAS measurements the excitation energy used (~100 μJ cm^{-2}) leads to photo-generated carrier densities several orders of magnitude lower (equation 2) than the calculated oxygen vacancy density as measured by Mott-Schottky (α-Fe_2O_3 giving a N_d of 6.4 x 10^{19} cm^{-3} and α-Fe_2O_{3-x} giving a N_d of 1.2 x 10^{20} cm^{-3}, Figure 22).

$$\frac{Excitation\ energy\ (\sim 100\ \mu J\ cm^{-2})}{355\ nm\ photon\ energy\ (\sim 5.6x10^{-13}\ \mu J)} = 1.79 \times 10^{14}\ photons\ cm^{-2} \qquad (2)$$

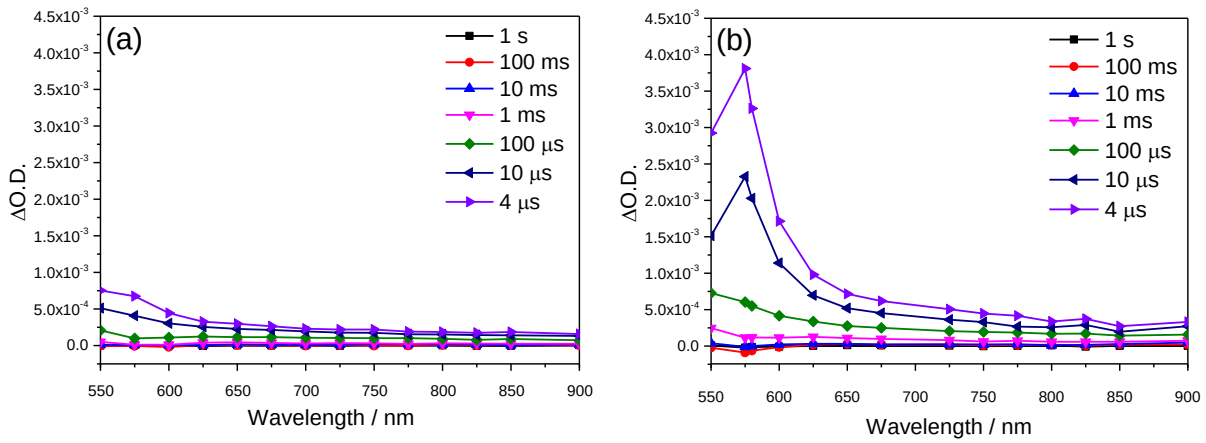

Figure 25 - TAS spectra of (a) α-Fe_2O_3 and (b) α-Fe_2O_{3-x} in an argon purged quartz cuvette (no electrical bias), following 355 nm laser excitation (6 ns pulse, ~100 µJ cm^{-2}).

Figure 25 shows the TAS spectra of α-Fe_2O_3 and α-Fe_2O_{3-x} in argon (no electrochemical cell), probed from 550-900 nm following UV excitation. The spectra show two positive features: a narrow band centred at *ca.* 575 nm (the same band observed in steady-state absorbance measurements) assigned to oxidation of electron trap states and a broad positive feature assigned to photo-holes spanning from 650-900 nm (which is also expected to be overlapping with the 575 nm feature). The magnitude of the 575 nm feature is significantly larger in α-Fe_2O_{3-x}, again attributed to an increased number of oxygen vacancies and therefore an increased number of electron trap sites. The broad hole signal is also larger in α-Fe_2O_{3-x} indicating a higher yield of charge separation which is consistent with a more active material.

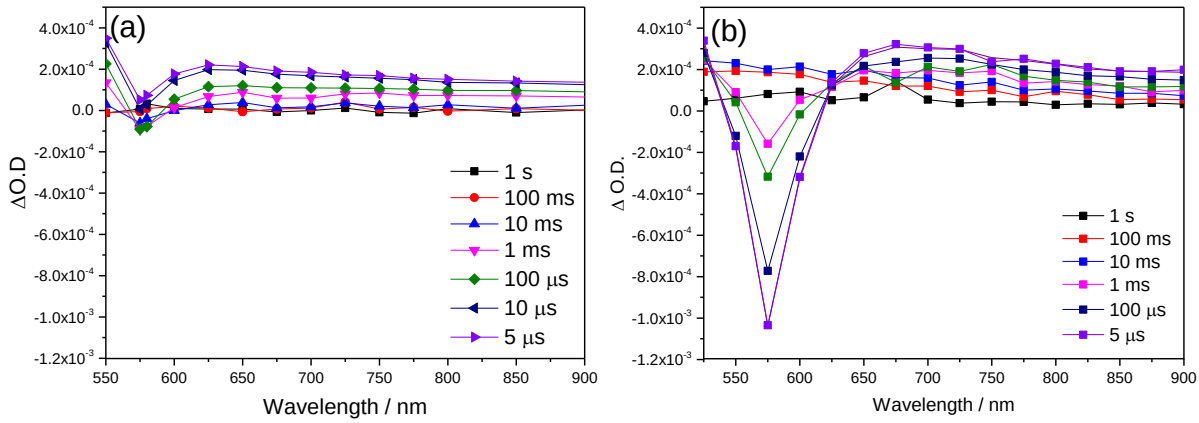

Figure 26 - TAS spectra of α-Fe_2O_3 and α-Fe_2O_{3-x} measured in a photoelectrochemical cell (1M NaOH, pH ~13.7) with an applied electrical bias of 0.4 $V_{Ag/AgCl}$, following 355 nm laser excitation (6 ns pulse, ~100 µJ cm^{-2}).

Figure 26 shows the same TAS measurements as Figure 25, this time under a photoelectrochemical bias (0.4 $V_{Ag/AgCl}$ (pH ~13.7)). At this potential a large photocurrent assigned to water oxidation is observed for α-Fe_2O_{3-x}, Figure 23. Most noticeably, under an electrochemical bias the 575 nm feature inverts and now exists as a bleach (decrease in optical density) which decays back to zero on ms timescales. This is proposed to be due to the positive bias lowering the trap state occupancy (oxidising the states). These vacant trap states are then able to quickly trap photoelectrons resulting in the bleach at 575 nm. The slow decay of the bleach back to zero is the result of electrons slowly de-trapping. The 575 nm bleach is significantly larger in α-Fe_2O_{3-x}, similar to the positive feature which occurs without a bias.

In order to more thoroughly understand the charge carrier dynamics in α-Fe_2O_3 and α-Fe_2O_{3-x} and understand why α-Fe_2O_{3-x} has such drastically improved activity the TAS measurements were carried out at a range of potentials. Figure 27 shows these TAS measurements as 3D contour plots. The potentials were chosen in order to represent different regions of the α-Fe_2O_{3-x} photocurrent plot; 0.0 V represents a region before photocurrent onset, 0.2 V represents a region near the photocurrent onset and 0.4 V represents a region of high photocurrent.

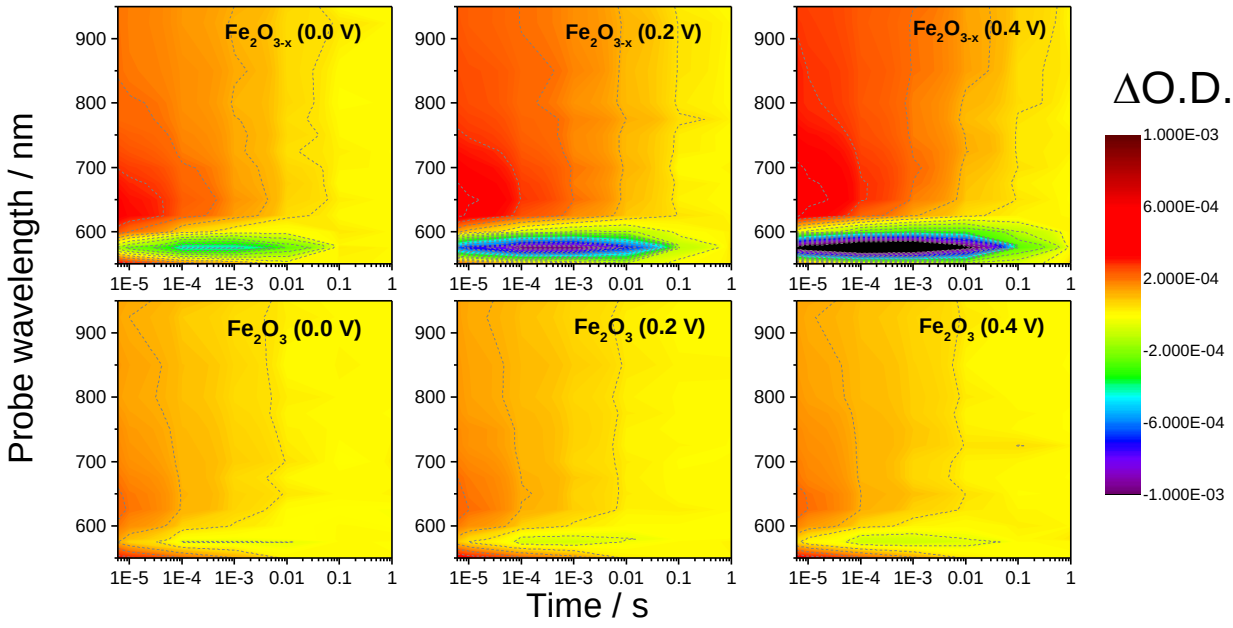

Figure 27 - TAS spectra of α-Fe_2O_3 and α-Fe_2O_{3-x} at various applied bias (vs. Ag/AgCl) in 1 M NaOH (pH ~13.7) following 355 nm laser excitation (6 ns pulse, ~100 μJ cm^{-2}).

The plots in Figure 27 show a general trend in which both hole and electron trap features increase in magnitude with increasing positive bias. This behaviour is in line with numerous past TAS studies on Si-doped and Nb-doped α-Fe_2O_3 photo-electrodes.[49–51] The 575 nm feature increases with increasing positive bias as more oxidised trap states become available. The hole magnitude and/or lifetime is expected to increase with increasing positive bias due to the increased band bending which improves charge separation. When comparing α-Fe_2O_3 to α-Fe_2O_{3-x}, both features are significantly larger in α-Fe_2O_{3-x} at all potentials indicating larger yields of charge carriers. In order to further visualise the difference in charge carrier dynamics the single wavelength kinetics are plotted in Figure 28, including additional applied bias measurements at -0.2 $V_{Ag/AgCl}$ (pH ~13.7) and 0.5 $V_{Ag/AgCl}$ (pH ~13.7). The hole kinetics are obtained at a probe wavelength of 700 nm and the electron trap kinetics are obtained at a probe wavelength of 575 nm.

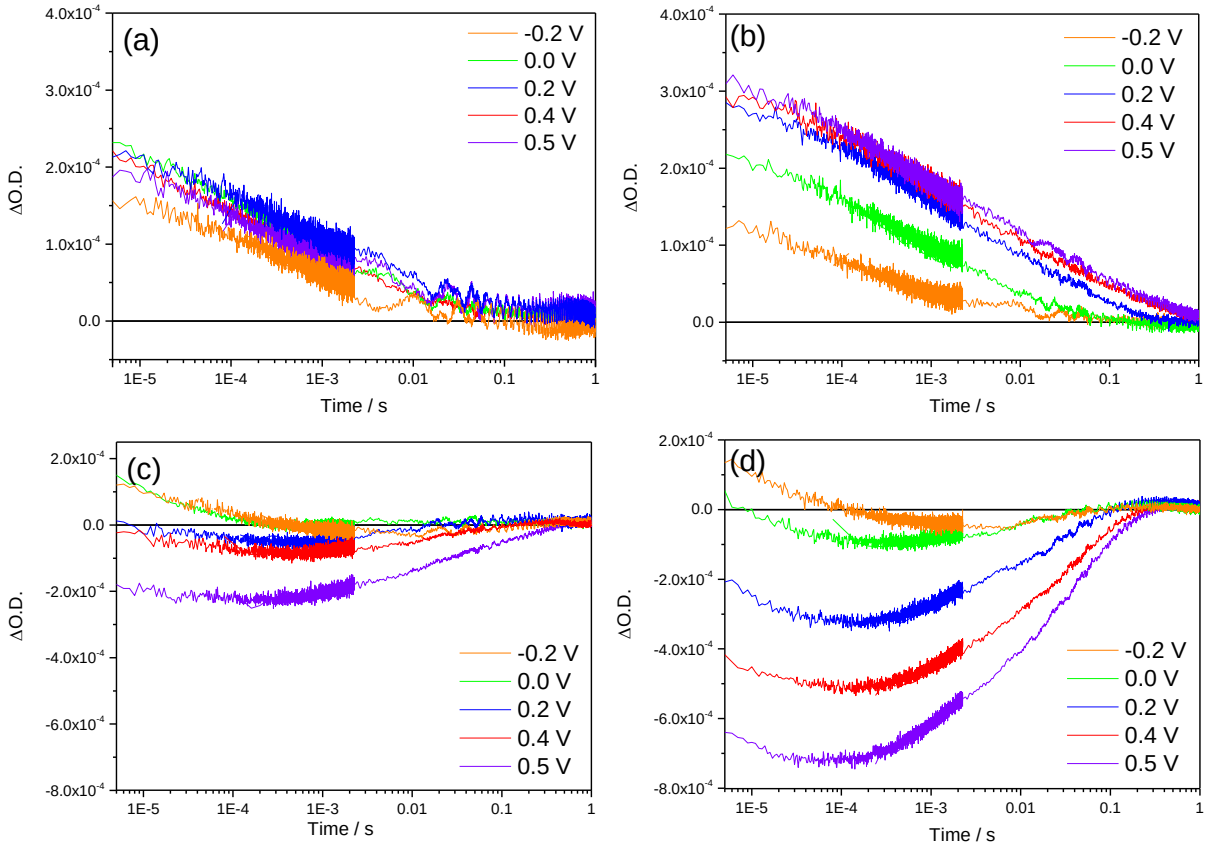

Figure 28 - TAS decay traces probed at 700 nm for (a) α-Fe_2O_3 and (b) α-Fe_2O_{3-x}. TAS traces probed at 575 nm for (c) α-Fe_2O_3 and (d) α-Fe_2O_{3-x}. Measurements were carried out at a range of applied bias vs. Ag/AgCl in 1 M NaOH (pH ~13.7) following 355 nm laser excitation (6 ns pulse, ~100 μJ cm^{-2}).

Initially we concentrate on the yield and kinetics of the photo-holes in α-Fe_2O_3 and α-Fe_2O_{3-x}. At all potentials investigated there is an increased yield of photo-holes in α-Fe_2O_{3-x} compared to α-Fe_2O_3 at the earliest timescales studied (5 μs), Figure 28a *vs.* Figure 28b. The increased photo-hole yield at 5 μs could indicate more efficient initial charge separation in the oxygen deficient hematite, however a detailed study of the photo-hole kinetics at 0.4 $V_{Ag/AgCl}$ (pH ~13.7) (Figure 29) shows only a *ca.* 35% difference in photo-hole yield at 5 μs (assuming a similar extinction coefficient for both materials).

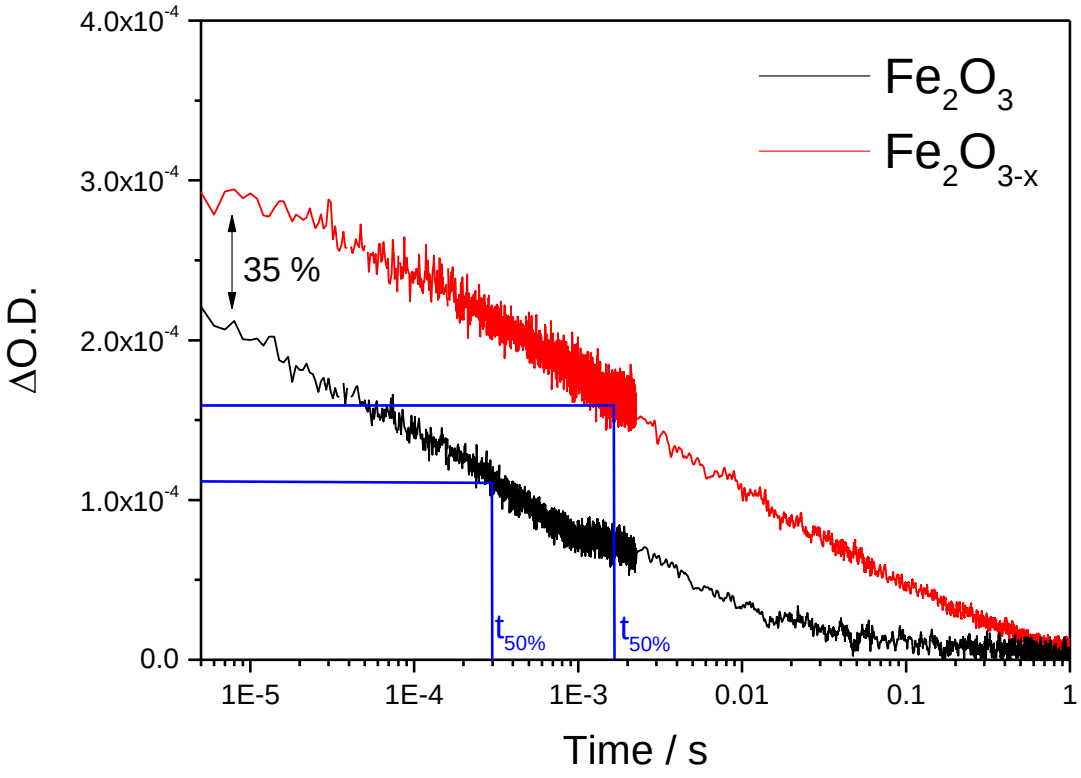

Figure 29 - TAS decay traces probed at 700 nm of α-Fe_2O_3 and α-Fe_2O_{3-x} at 0.4 vs. *Ag/AgCl in 1 M NaOH (pH ~13.7) following 355 nm laser excitation (6 ns pulse, ~100 μJ cm^{-2}).*

The relatively small difference in photo-hole yields between α-Fe_2O_3 and α-Fe_2O_{3-x} suggests that a previously[19,47] proposed enhancement in initial charge separation yield in V_O rich materials with higher electron densities is not likely to be the primary factor for the differences in activity between α-Fe_2O_3 and α-Fe_2O_{3-x}, where the IPCE values increase *ca.* 100-fold (0.57% to 64% at 0.50 $V_{Ag/AgCl}$, pH ~13.7). Instead, of greater significance is the rate of photo-hole decay in α-Fe_2O_3 compared to α-Fe_2O_{3-x}. The difference in decay rates can initially be seen from the $t_{50\%}$ values of α-Fe_2O_3 ($t_{50\%}$ = 0.30 ms) and α-Fe_2O_{3-x} ($t_{50\%}$ = 1.60 ms) obtained from Figure 29. $t_{50\%}$ is defined as the time required for the change in optical density to decay to 50% of the earliest measured magnitude (5 μs in this experiment). Previous studies have indicated that the increased donor density and improved conductivity of α-Fe_2O_{3-x} would be expected to aid both initial charge separation and electron transport/extraction as a result of deeper band bending which reduces bulk electron–hole recombination and therefore increase the photo-hole

lifetime.[24,52] In order to asses if such a change in photoelectron dynamics is the cause of the improved photo-hole lifetime and the improved activity of α-Fe_2O_{3-x} section 2.2.3 compares the transient photocurrent of α-Fe_2O_3 and α-Fe_2O_{3-x}.

2.2.3 Transient photocurrent (TPC) of α-Fe_2O_3 *vs.* α-Fe_2O_{3-x} and the role of back electron recombination

Transient photocurrent (TPC) measures the current between the hematite working electrode and the platinum counter electrode following UV excitation. A resistor of a known resistance is placed into the photoelectrochemical cell circuit and then the voltage drop across this resistor is measured using an oscilloscope. The same laser pump light source is used for both TPC and TAS allowing for direct correlation between these measurements. Figure 30a shows the TPC of α-Fe_2O_3 and α-Fe_2O_{3-x} at an applied bias of 0.4 $V_{Ag/AgCl}$ (pH ~13.7).

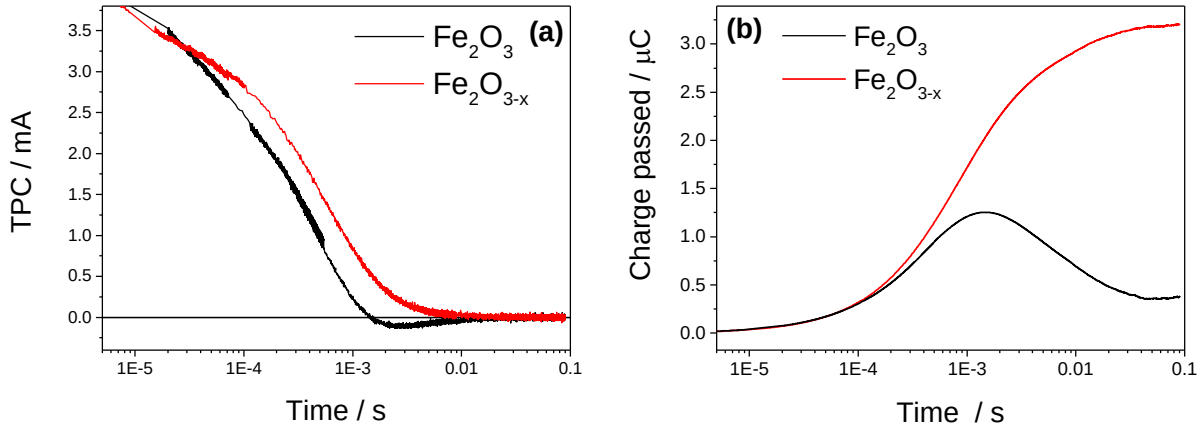

Figure 30 - (a) TPC decays of α-Fe_2O_3 and α-Fe_2O_{3-x} held at 0.4 $V_{Ag/AgCl}$ (pH ~13.7) and (b) the converted total charge passed following 355 nm laser excitation (6 ns pulse, ~100 µJ cm^{-2}).

The TPC traces of both α-Fe_2O_3 and α-Fe_2O_{3-x} are relatively similar at early times (<0.5 ms) indicating that, contrary to expectations, initial photoelectron extraction to the external circuit

appears to occur effectively even in the air annealed, poorly doped α-Fe_2O_3 sample. Instead the difference in photo-hole kinetics and photo-electrochemical activity appears to be due to slow back-electron transfer from the external circuit into the air annealed α-Fe_2O_3, which is indicated by the negative current on timescales of 1–10 ms after photon absorption, Figure 30a (black line). This back-electron transfer process has been previously described by Florian *et al.* [39] and is known to retard the photocurrent in photoelectrode devices. Figure 31 shows a simple model of the kinetic competition between the bias dependent back electron–hole recombination pathway and holes accumulating at the surface.

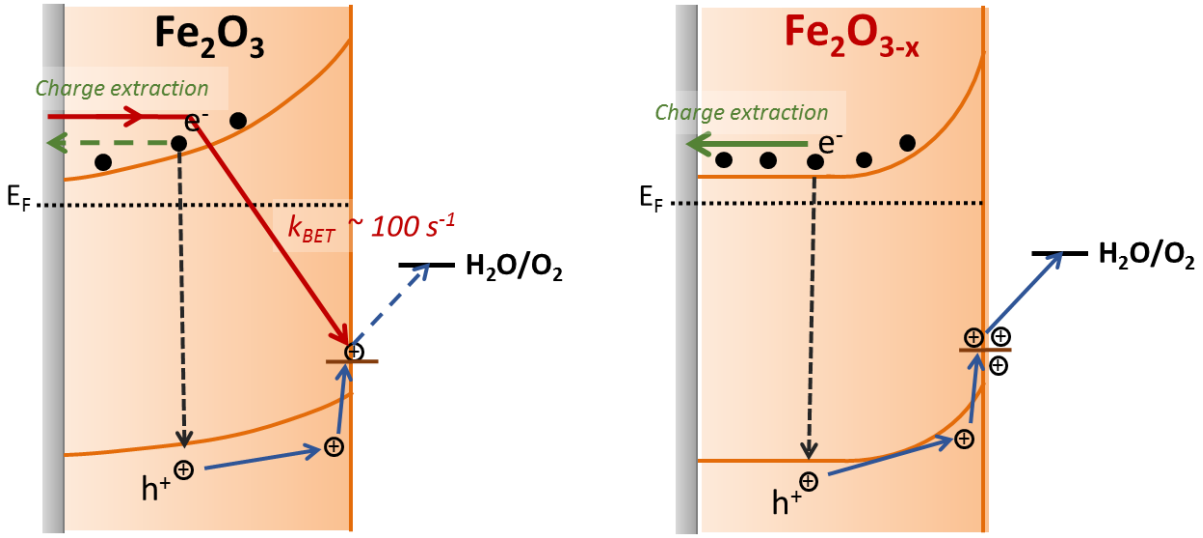

Figure 31 - Diagram showing the effect of back-electron recombination in α-Fe_2O_3 and how the increased donor density of α-Fe_2O_{3-x} blocks this pathway. Back electron transfer is denoted by the red arrow, bulk recombination by the black arrows, electron extraction by the green arrows and hole transfer to solution by the blue arrows.

The significance of this back-electron transfer process becomes more apparent when the TPC is integrated to provide a measure of charge passed as shown in Figure 30b. For α-Fe_2O_3 the total charge re-injected from the external circuit approximately matches that initially extracted from the α-Fe_2O_3 photoelectrode leading to limited net gain. To understand how this back-electron transfer varies with potential Figure 32 shows TPC at a range of applied biases. Back-

electron transfer is present in α-Fe_2O_3 at all applied biases studied by TPC (-0.2, 0.0 and 0.2 $V_{Ag/AgCl}$), leading to a minimal net transient photocurrent which explains the poor steady state photocurrent for these films (Figure 23). In contrast, α-Fe_2O_{3-x} shows no signs of back-electron transfer (Figure 32) at any measured applied bias and it is this which is likely responsible for the large improvement in photocurrent (Figure 23). It should be noted that due to large variations in noise during these measurements the magnitudes of the signals recorded by TPC should be treated with caution.

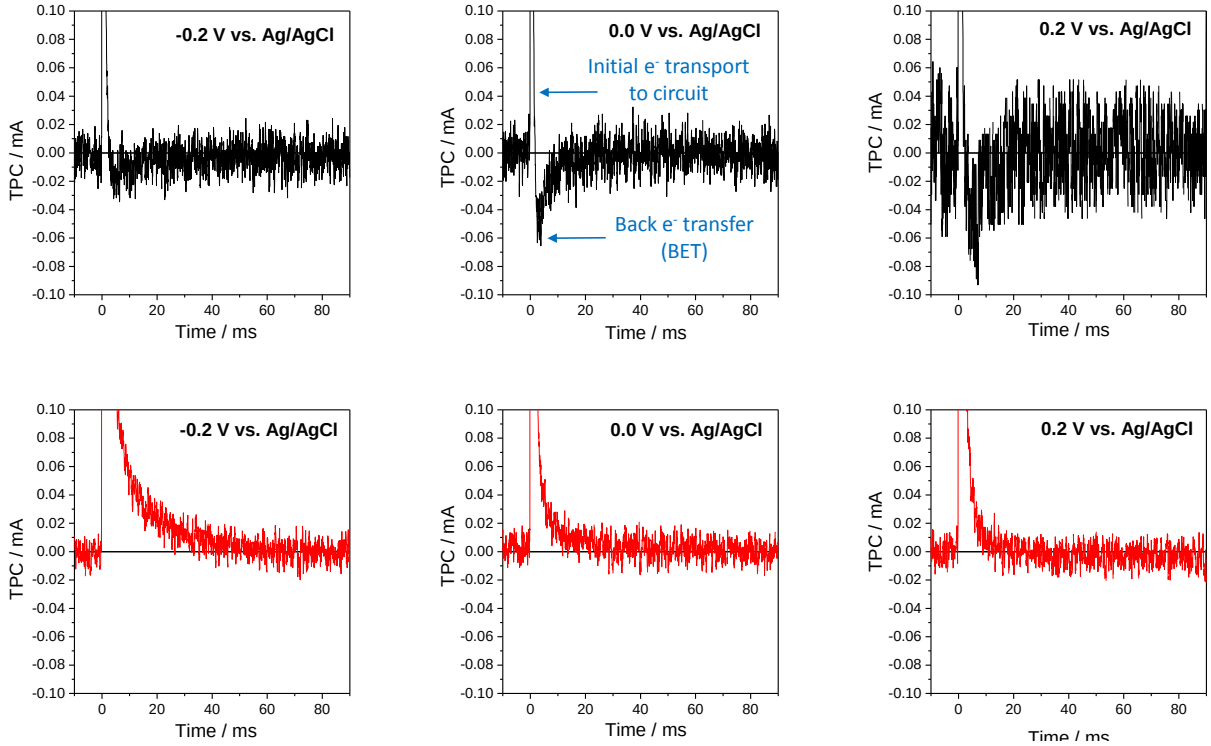

Figure 32 - Transient photocurrent measurements at various applied bias of a) α-Fe_2O_3 (black) showing positive signal on slower timescales where charge is re-injected as a result of back-electron transfer on ms timescales and b) α-Fe_2O_{3-x} (red) showing no charge re-injection. The figures are zoomed in so as to highlight the presence/absence of the smaller back-electron transfer feature.

It is important to know the fate of the electrons in α-Fe_2O_3 following back-electron transfer as a recent study on Si– α-Fe_2O_3 showed the presence of a recombination process between surface

trapped holes and bulk hematite electrons on the milliseconds timescale resulting from a flow of electrons back into the photoelectrode from the external circuit. This process is critical as these long lived holes would otherwise be facilitating water oxidation.

To determine whether the electrons measured by TPC in our study were recombining with the holes measured by TAS in α-Fe_2O_3, the normalised TAS kinetics (probed at 700 nm) assigned to holes were overlaid with the integrated TPC (charge passed) measured under the same conditions, Figure 33.

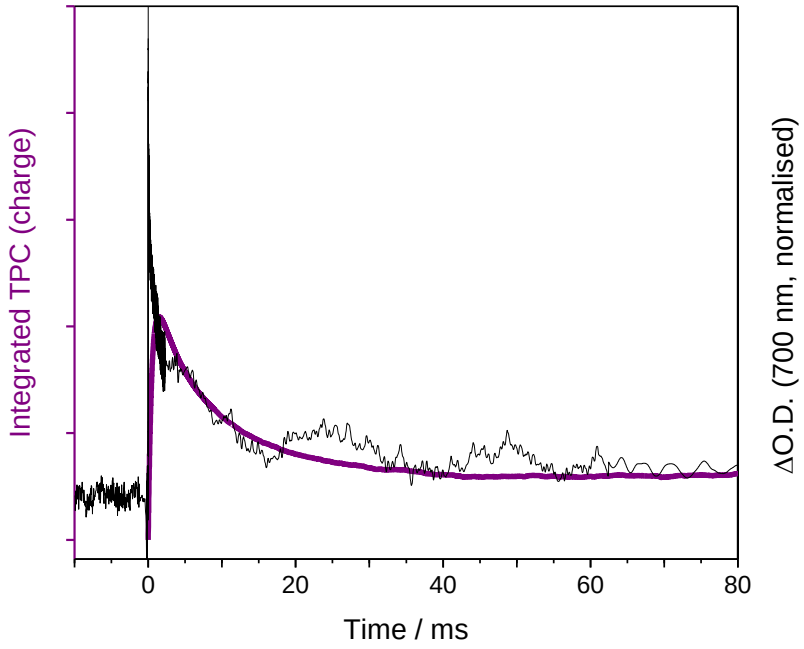

Figure 33 - Overlay of the normalised decay of the TA signal assigned to holes with the integrated TPC (charge extracted) of α-Fe_2O_3 measured at 0.4 $V_{Ag/AgCl}$ in 1M NaOH (pH ~13.7) following 355 nm laser excitation (6 ns pulse, ~100 μJ cm^{-2}).

The overlay of the integrated TPC decay and TAS in Figure 33 show an excellent agreement indicating that back-electrons are recombining with the accumulated photo-holes measured by TAS. It is important to confirm whether the photo-holes measured using TAS on the μs–ms timescales are accumulating at or close to the SCLJ in the films studied here, as hole trapping

elsewhere in the defect-rich Fe_2O_{3-x} is possible. In order to determine the location of the holes in the materials the TAS measurements were carried out in the presence of a hole scavenger, Figure 34 and Figure 35. Hydrogen peroxide (H_2O_2) is a commonly used hole scavenger due to its near unity efficiency for the removal of holes in α-Fe_2O_3 that are at or close to the SCLJ.[53]

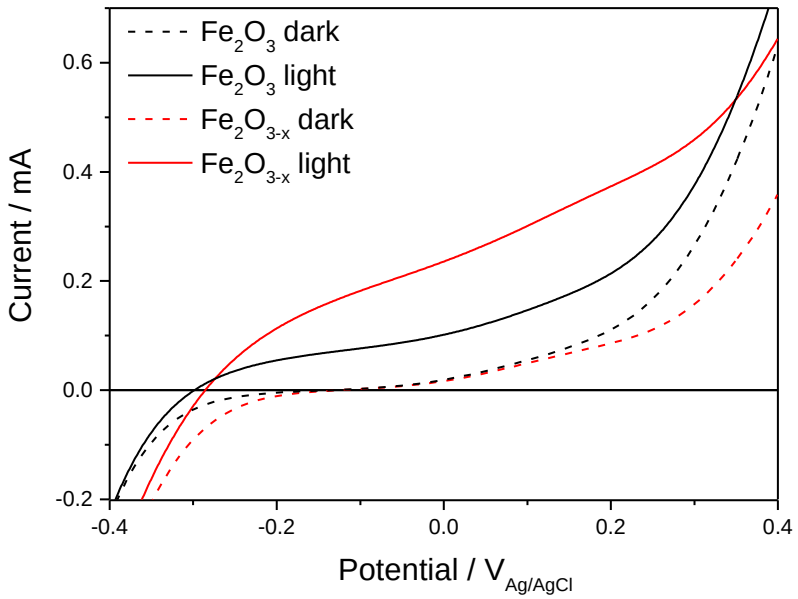

Figure 34 - Linear sweep voltammograms for α-Fe_2O_3 (black) and α-Fe_2O_{3-x} (red), 5 mV s^{-1}, under white light illumination using a 75 W Xe lamp (solid line, ca. 10 mW cm^{-2}) and in the dark (dashed line) in 1M NaOH (pH ~13.7) with the presence of a hole scavenger (0.5 M H_2O_2).

In the presence of 0.5 M H_2O_2 a photocurrent is observed at potentials as low as -0.3 $V_{Ag/AgCl}$ for both α-Fe_2O_3 and α-Fe_2O_{3-x} confirming that (i) initial charge separation is effective in both materials at potentials well below the water oxidation photocurrent onset potential and that (ii) in both samples the photo-holes are able to reach the surface to participate in oxidation reactions, Figure 34. The significantly higher photocurrent for the oxygen deficient sample in the presence of H_2O_2 (*ca.* x2) is in line with the higher initial charge separation efficiencies. As mentioned previously, the indication that the initial charge separation efficiency in α-Fe_2O_{3-x} is approximately 35-50% higher than that of α-Fe_2O_3 is not sufficient to explain the

complete lack of water splitting activity of α-Fe_2O_3. TAS experiments in the presence of H_2O_2 show a decrease in the hole yield at the earliest time-scales studied (5 μs) in α-Fe_2O_{3-x} when compared to experiments in the absence of a hole scavenger. This indicates that holes are present at the SCLJ and are transferring into solution at time scales earlier than the resolution of our measurements. This proves a lower limit for the lifetime of transport and accumulation of holes at the SCLJ of 5 μs, Figure 35.

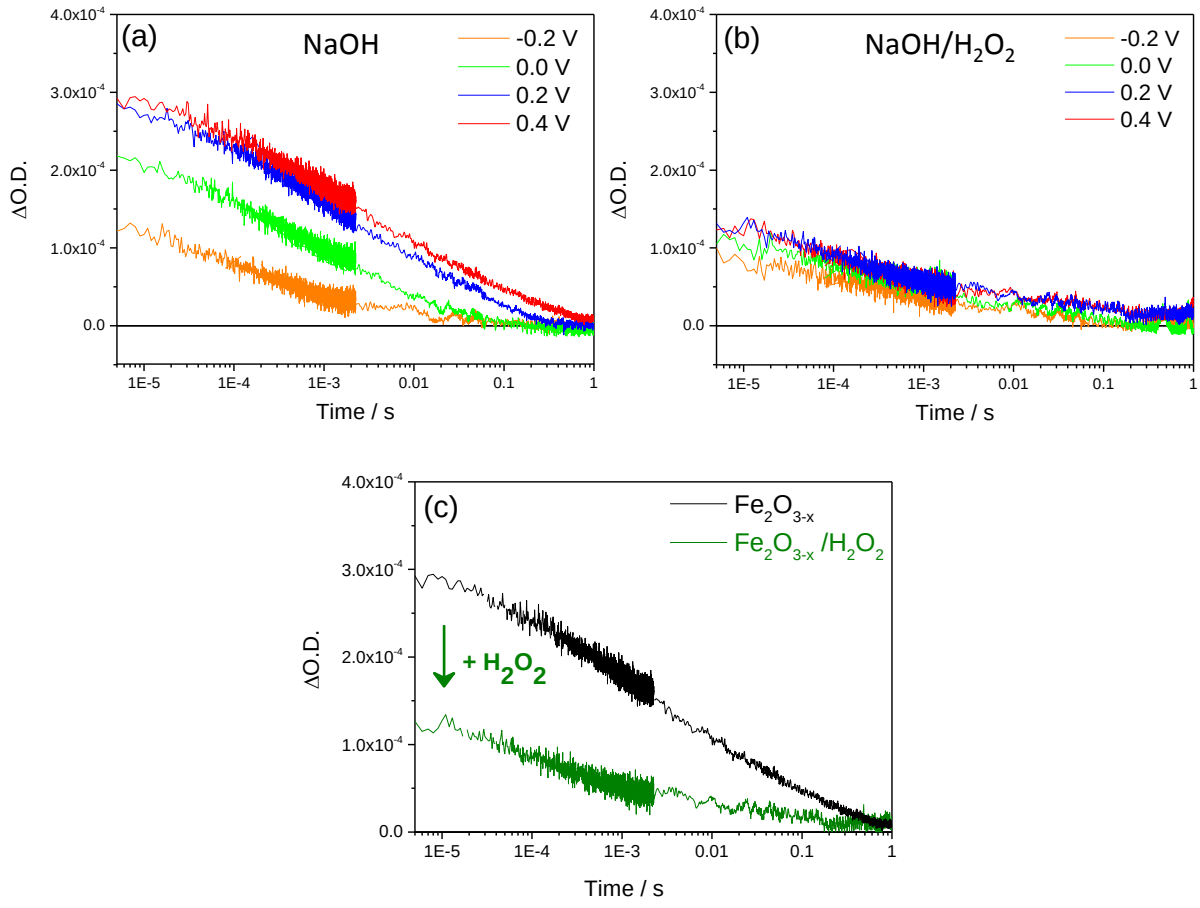

Figure 35 - TAS hole decay traces of α-Fe_2O_{3-x} probed at 700 nm at a range of applied bias vs. Ag/AgCl in (a) 1 M NaOH (pH ~13.7) and (b) 1 M NaOH /0.5 M H_2O_2 following 355 nm laser excitation (6 ns pulse, ~100 μJ cm^{-2}). (c) Overlay of the 700 nm signal for α-Fe_2O_{3-x} in NaOH (pH ~13.7) and in NaOH/H_2O_2 at 0.4 $V_{Ag/AgCl}$.

The above results suggest that back-electron transfer and resulting recombination with holes at the surface plays a critical role in the poor performance of α-Fe_2O_3 compared to α-Fe_2O_{3-x},

which exhibits no back-electron transfer. The lack of back electron transfer in α-Fe_2O_{3-x} can be rationalised by Mott-Schottky measurements of the films (Figure 22) which show a higher donor density (N_d) in the V_O rich photoelectrode (α-Fe_2O_3 N_d = 6.7x10^{19} cm^{-3} compared to α-Fe_2O_{3-x} N_d = 1.2x10^{20} cm^{-3}). This *ca.* two-fold increase in donor density is expected to significantly decrease the width of the space charge layer (W_{SC}) in α-Fe_2O_{3-x}, a factor related to the electric field close to the SCLJ. To provide an indication of how the level of V_O modifies the width of the space charge layer when under a positive bias, and hence the strength of the electric field close to the SCLJ, the representative values of W_{SC} have been calculated at different potentials anodic of flat band (Figure 36) using equation 3, where *E* is the applied bias, E_{FB} is the flatband potential, *q* is the charge of an electron, N_d is the donor density, ε is the dielectric constant of hematite (80)[8] and ε_0 is the vacuum permittivity:[47]

$$W_{SC} = \sqrt{\frac{2\varepsilon\varepsilon_O}{qN_d}(E - E_{FB})} \qquad (3)$$

The calculations show that the large increase in N_d in the α-Fe_2O_{3-x} electrode significantly decreases the width of the space charge layer (W_{sc}) which is calculated to go from 12 nm for α-Fe_2O_3 to 8 nm for α-Fe_2O_{3-x} at 0.4 $V_{Ag/AgCl}$ (pH ~13.7).

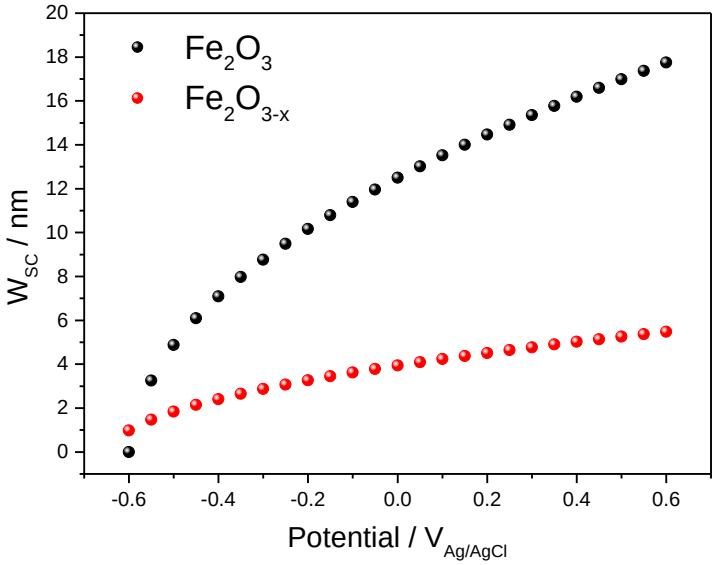

Figure 36 - Space charge layer width calculations of Fe_2O_3 and Fe_2O_{3-x} giving the width in nanometres as a function of applied bias.

The narrower W_{SC} in α-Fe_2O_{3-x} compared to Fe_2O_3 is expected as a result of the increased V_O doping. This observation suggests that the blocking of back-electron transfer in Fe_2O_{3-x} does not occur as a result of the space charge region.

To summarise this section, the above studies have shown that the improved doping due to the presence of V_O is a significant factor in rationalising the enhanced activity of α-Fe_2O_{3-x}, as hypothesised in several previous studies.[19,24,45,47,54] The primary reason for the enhanced activity of α-Fe_2O_{3-x} is not found to be due to more efficient initial charge separation (although this is improved by ~ 35-50%) or injection kinetics but instead the blocking of the back flow of electrons from the bulk towards the SCLJ preventing recombination with surface accumulated photoholes as shown in Figure 31.

A similar model which describes competition between the bias dependent back electron–hole recombination pathway and the rate of water oxidation has been shown elsewhere to account for observed photoelectrochemical activity of Si–α-Fe_2O_3 electrodes without the need for the inclusion of inter-band trap states.[39] Specifically the photocurrent onset potential of their Si-

doped α-Fe_2O_3 photoelectrode, which had a similar N_d (~10^{20} cm^{-3})[39] to the α-Fe_2O_{3-x} samples examined here (1.2x10^{20} cm^{-3}), correlated with the potential at which back electron–hole recombination became slow enough to enable surface hole accumulation and water oxidation to occur (*ca.* 0.0 $V_{Ag/AgCl}$, pH ~13.7). Here we find that back electron–hole recombination in α-Fe_2O_{3-x} is blocked at potentials as low as -0.2 $V_{Ag/AgCl}$ (pH ~13.7) (Figure 32) and no correlation is noted with the photocurrent onset potential, *ca.* 0.15 $V_{Ag/AgCl}$ (Figure 23). This gives rise to an intriguing question, given that our TPC and TAS show that holes can be accumulated at potentials as low as -0.2 $V_{Ag/AgCl}$ and that the slow back electron hole recombination pathway has been prevented at these low potentials: why is the photocurrent onset potential for water oxidation so positive (~0.15 $V_{Ag/AgCl}$) with α-Fe_2O_{3-x} photoelectrodes? The next section addresses the role of trap-mediated recombination in α-Fe_2O_{3-x} and how this may be related to the increased levels of V_O in the film.

2.2.4 The role of trap state mediated recombination

We now turn to the potential role of electron trap states in rationalising the behaviour of α-Fe_2O_{3-x} as it has been proposed that oxygen vacancies may act as a "mixed blessing",[47] with the enhanced electrical properties being balanced with a potential increase in trap-mediated electron–hole recombination at the introduced defect sites.[54] Following absorption of a UV photon by hematite under a positive applied bias we initially observed a bleaching at *ca.* 575 nm on the μs-s timescales which is assigned to photoelectron trapping at this inter-band state. The slow recovery on the millisecond timescale of the trap state feature is due to the subsequent de-trapping of the photoelectrons, Figure 37. The magnitude of this feature is significantly larger in α-Fe_2O_{3-x} compared to α-Fe_2O_3, suggesting the higher V_O density in α-Fe_2O_{3-x} is enabling more electron trapping, supporting the hypothesis that the V_O states ~80 meV below the conduction band are giving rise to the TAS signal.

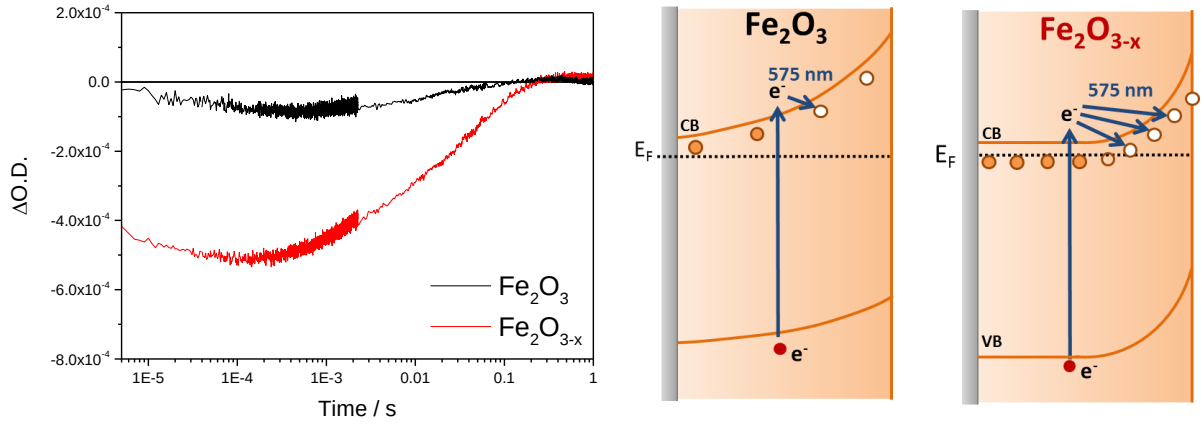

Figure 37 - TAS decay traces probed at 575 nm of α-Fe_2O_3 and α-Fe_2O_{3-x} at 0.4 $V_{Ag/AgCl}$ in 1 M NaOH (pH ~13.7) following 355 nm laser excitation (6 ns pulse, ~100 μJ cm^{-2}). The schematic on the right shows the increased concentration of trap states related to V_O concentration which leads to the increased 575 nm TAS signal in Fe_2O_{3-x}. Orange circles are filled trap states and white circles are oxidised trap states which can trap photogenerated electrons.

Figure 38 shows the fitted TAS kinetics of α-Fe_2O_{3-x} probed at 575 nm. In line with the assignment of the 575 nm feature to photoelectrons trapping and then de-trapping, the change in occupancy of the 575 nm trap state at 0.4 $V_{Ag/AgCl}$ (pH ~13.7) is well suited to the integrated rate equation for an intermediate species in a consecutive reaction scheme as shown in equation 4.

$$[A] \xrightarrow{k_1} [B] \xrightarrow{k_2} [C] \qquad (4)$$

Equation 4 can be modified to produce equation 5, where [A] represents the initial yield of photoelectrons, k_1 can be considered the rate of electron trapping of the photoexcited electrons, the intermediate species [B] can be considered the population of trapped electrons, which is directly proportional to the magnitude of the TAS signal probed at 575 nm ([B] = α*ΔOD_{575nm},

where α is constant related to the extinction coefficient), and k_2 can be considered the rate of de-trapping of these electrons as shown in equation 5.

$$[A] \xrightarrow{k_{trap}} (\alpha * \Delta OD_{575nm}) \xrightarrow{k_{detrap}} [C] \quad (5)$$

Equations 6-8 show the rate equations describing the concentration of each species.

$$\frac{d[A]}{dt} = -k_{trap}\,[A] \quad (6)$$

$$\frac{d\Delta OD_{575nm}}{dt} = k_{trap}\,[A] - k_{detrap}\,(\Delta OD_{575nm}) \quad (7)$$

$$\frac{d[C]}{dt} = k_{detrap}\,(\Delta OD_{575nm}) \quad (8)$$

Integration of equation 7 produces the integrated rate equation, equation 9, where the rate constants k_{trap} and k_{detrap} correspond to the rate of photoelectron trapping and de-trapping of electrons, t is time, β is a stretching exponent and A is a pre-exponential factor related to the initial yield of photoelectrons and y_0 is a Y offset term.

$$\Delta OD_{575}(t) = \frac{k_{trap}}{k_{detrap} - k_{trap}} \left(e^{(-k_{trap}\, t)^{\beta 1}} - e^{(-k_{detrap}\, t)^{\beta 2}} \right) [A]_0 + y_0 \quad (9)$$

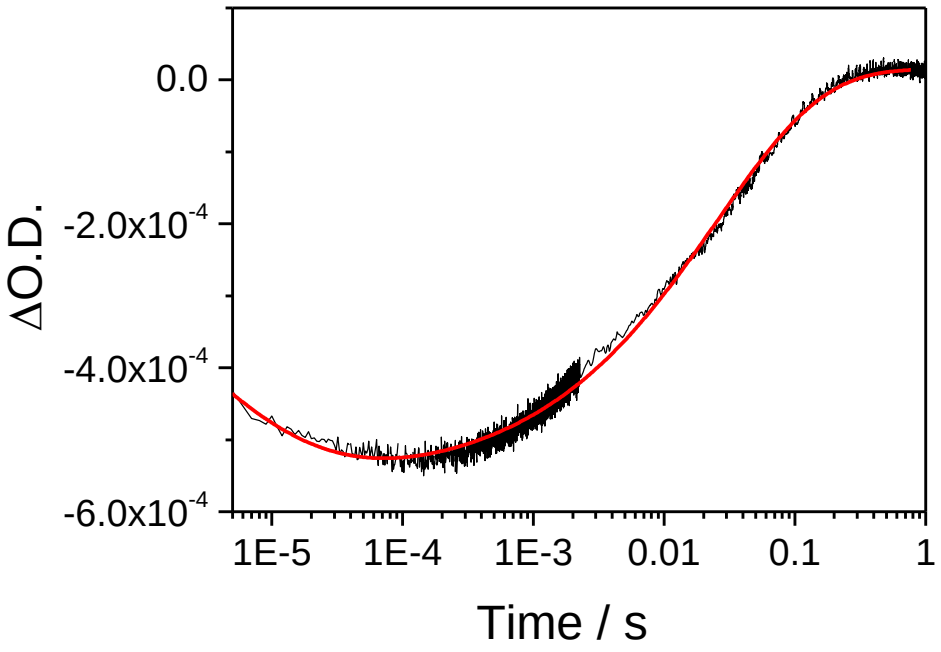

Figure 38 - TAS trace probed at 575 nm (electron trap-state) of α-Fe_2O_{3-x} fitted to a biphasic stretch exponential representing trapping and de-trapping of electrons. The measurement was carried out at 0.4 $V_{Ag/AgCl}$ in 1M NaOH (pH ~13.7) following 355 nm laser excitation (6 ns pulse, ~100 μJ cm^{-2}).

In this chapter the rate equations shown in equations 5-9 are used to fit the TAS kinetics probed at 575 nm. However, it should be noted that as the understanding of the trapping and de-trapping processes developed during the course of this work (later chapters), evidence was obtained suggesting that the trapped electrons can exist as more than one population (such as the example shown in equation 10 and Figure 39). In the study presented here, over parameterisation was a concern and therefore the detrapping process was fit to a single component. In the studies discussed in later chapters the potential errors from overly complex fitting were minimised by focussing only on the detrapping component of the 575 nm TAS feature as opposed to both trapping and detrapping (typically fitted to mono-exponential or bi-exponential functions) and Chapter 3 will discuss this in more detail. The presence of more

than one electron trap population as discussed above may explain the slight deviation of the fit line from the curve shown in Figure 38.

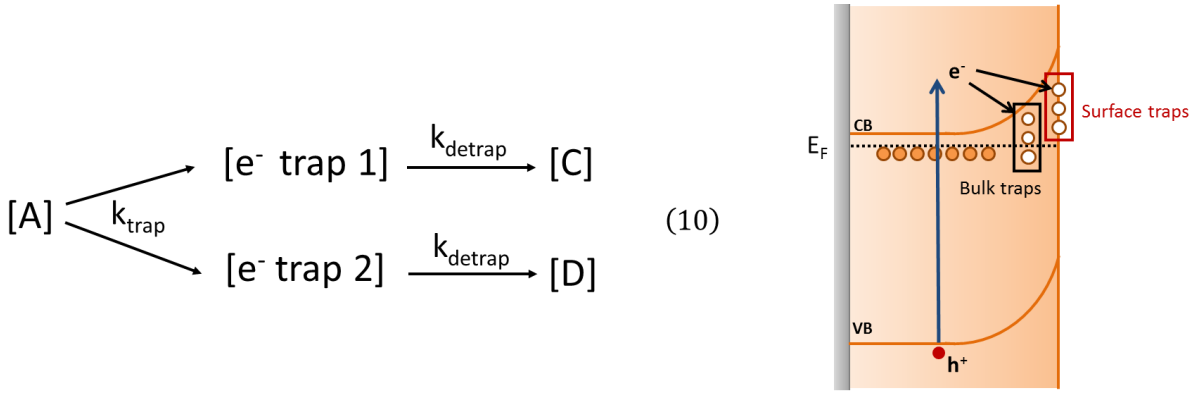

Figure 39 - Schematic showing the possibility of two populations of trap states as depicted by equation 10.

For now we focus on the fit shown in Figure 38. The fitting in Figure 38 provided the following parameters:

Magnitude	Lifetime (s)	Rate (s^{-1})	Stretching factor
A_1: (2.1±0.4)x10^{-3}	τ_1: (1.4±0.3)x10^{-6}	k_{trap}: (7.0±0.4)x10^{5}	β_1: 0.40±0.01
A_2: (-5.9±0.2)x10^{-4}	τ_2: (0.025±0.008)x10^{-5}	k_{detrap}: 40.00±0.11	β_2: 0.57±0.01

Table 3 – Main parameters obtained from the biphasic stretch-exponential fit of the 575 nm TAS signal assigned to photoelectron trapping and de-trapping. A is a pre-exponential factor related to the magnitude, τ is the mean lifetime, k is the rate constant and β is a stretching component. τ and k are related by τ = 1/k.

k_{trap} and k_{detrap} were found to have rates of *ca.* (7.0±0.4)x10^5 s^{-1} and 40.00±0.11 s^{-1}, respectively. Photoelectron trapping has been shown to occur on the ps–ms timescales and it is likely we have only fitted the tail of the trapping process here.[48] In previous studies by Barroso *et al.*[49] the de-trapping rate of photoelectrons in Si-doped hematite correlated to the TPC decay rate as well as a distinct fast decay component in the hole population, leading to an assignment of both

electron extraction and electron–hole recombination following de-trapping in the bulk of the electrode. In order to assess if electron extraction is a significant process following electron detrapping in α-Fe_2O_{3-x}, TPC measuring extracted electrons has been overlaid with TAS measuring trapped electrons in Figure 40.

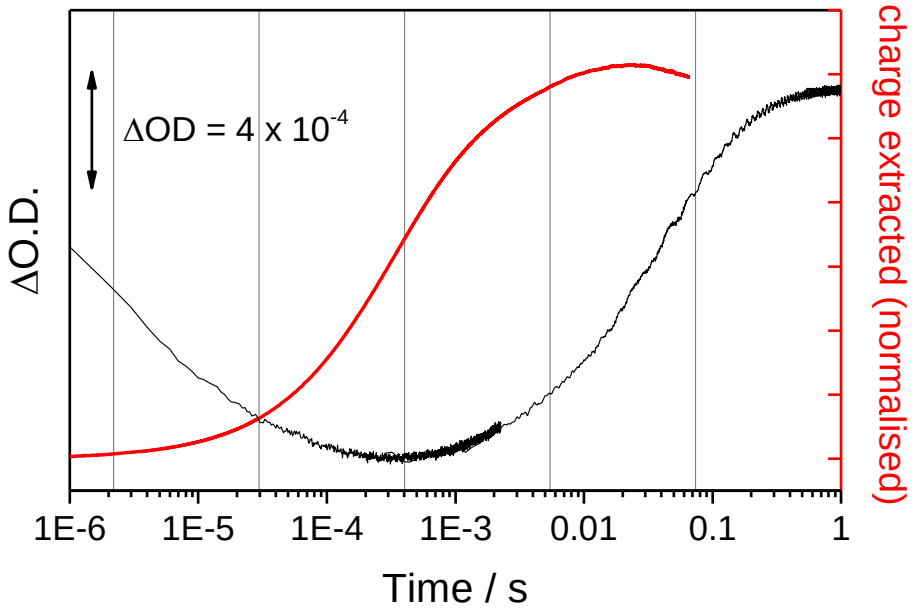

Figure 40 - (a) Overlay of the TAS trace recorded at 575 nm, assigned to an inter-band trap state, and the normalised charge extracted for α-Fe_2O_{3-x} following 355 nm laser excitation (6 ns pulse, ~100 μJ cm^{-2}).

The rate of decay of the integrated TPC (charge) signal at 0.4 $V_{Ag/AgCl}$ is fitted to a single exponential decay (Equation 11 and Figure 41) with a rate constant of *ca.* (3.8±0.2)x10^4 s^{-1}.

$$\Delta OD_{700}(t) = A_1 e^{-(k_1 t)^{\beta_1}} + y_0 \quad (11)$$

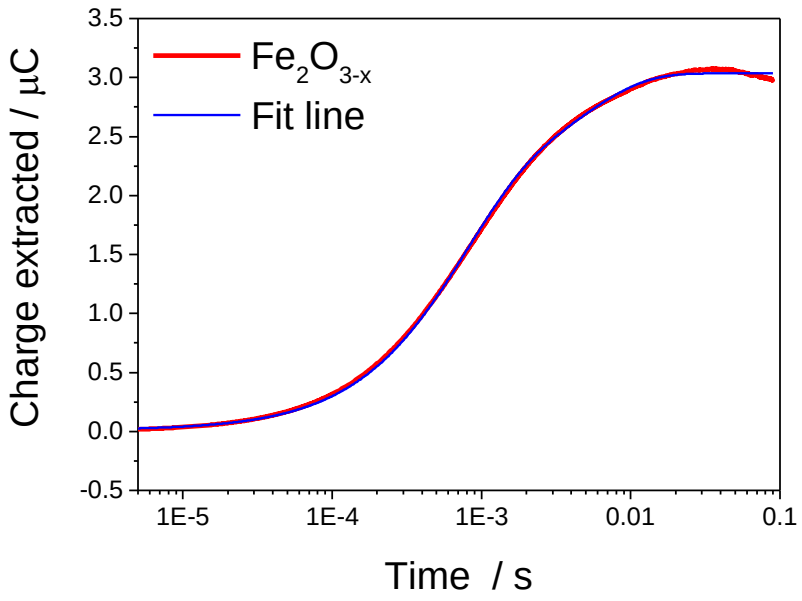

Figure 41 - Single stretch exponential fit of the integrated TPC (charge) of α-Fe_2O_{3-x} following 355 nm laser excitation (6 ns pulse, ~100 μJ cm^{-2}).

The fitting in Figure 41 provided the following parameters:

Magnitude	Lifetime (s)	Rate (s^{-1})	Stretching factor
A: (6±4)x10^{-6}	τ: (2.7±0.1)x10^{-5}	*k*: (3.8±0.2)x10^{4}	β: 0.46±0.01

Table 4 - Shows the main parameters obtained from the single stretch-exponential fit of the integrated TPC signal in Figure 41. A is a pre-exponential factor related to the magnitude, τ is the mean lifetime, k is the rate constant and β is a stretching component. τ and k are related by τ = 1/k.

The lack of correlation between the TPC and TAS kinetics in Figure 40 suggests that the trapped electrons are unable to reach the external circuit following de-trapping. In the absence of photoelectron extraction it is therefore expected that electron–hole recombination is the dominant fate of the de-trapped electrons. α-Fe_2O_{3-x} is a sample with a high concentration of surface defect sites,[24,55] and so it is expected that a significant level of electron trapping occurs near the surface, closer to the sites of photo-hole accumulation leading to predominantly electron–hole recombination upon de-trapping. Hole scavenger measurements in the previous

section (Figure 34 and Figure 35) provide additional evidence that a significant level of recombination with trap state electrons occurs close to the SCLJ were it was demonstrated that a large portion of the hole population reached the surface of α-Fe_2O_{3-x} within the time resolution of our experiment (5 μs), i.e. prior to photoelectron de-trapping.

Further evidence that the 575 nm signal is that of trapped electrons and that these electrons are recombining with surface accumulated holes is provided by monitoring the effect of the hole scavenger, H_2O_2. Following the addition of H_2O_2 and thus the rapid removal of holes, the 575 nm feature increases in magnitude and lifetime. This effect is shown in Figure 42 and Figure 43. The increase in magnitude and lifetime of trapped electrons in the presence of a hole scavenger can be rationalised by the reduced availability of holes at the surface of hematite leading to suppression of the recombination pathway between these holes and the trapped electrons measured by TAS, and hence increasing the lifetime and magnitude of electron trapping.

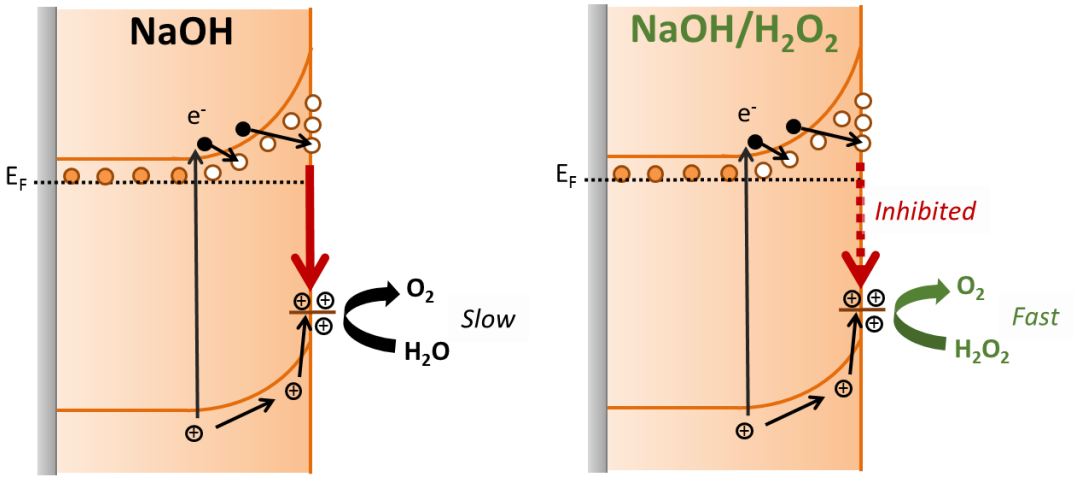

Figure 42 - Schematic showing the suppression of recombination between surface holes and trapped electrons in the presence of the hole scavenger, H_2O_2. The increased rate of removal of surface holes in the presence of H_2O_2 reduces their availability for recombination, slowing down the rate of decay of the trapped electrons and increasing the lifetime of the signal probed by TAS at 575 nm. Orange circles are filled trap states and white circles are oxidised trap states which can trap photogenerated electrons.

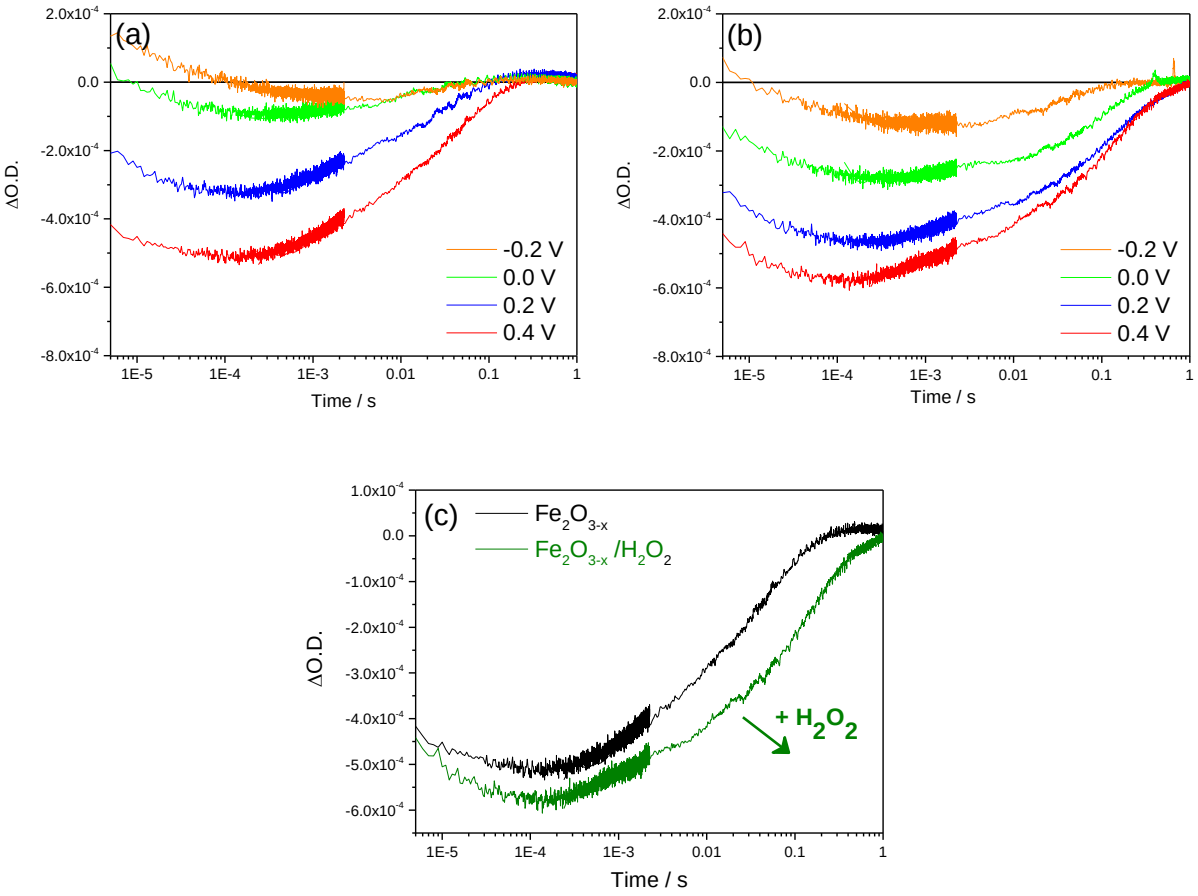

Figure 43 - TAS decay traces probed at 575 nm of α-Fe_2O_{3-x} at a range of applied potentials vs. Ag/AgCl in (a) 1 M NaOH (pH ~13.7) and (b) 1M NaOH (pH ~13.7) with a hole scavenger (0.5 M H_2O_2) following 355 nm laser excitation (6 ns pulse, ~100 μJ cm^{-2}). (c) Overlay of the 575 nm signal for α-Fe_2O_{3-x} in NaOH (pH ~13.7) and in NaOH/H_2O_2 at 0.4 $V_{Ag/AgCl}$.

In order to further understand the decay pathways of the holes accumulating on the hematite surface as measured by TAS, the kinetics probed at 700 nm were fitted. In light of the previous results, it was hypothesised that the photo-hole TAS kinetics of α-Fe_2O_{3-x} at 0.4 $V_{Ag/AgCl}$ (pH ~13.7) would consist of three distinct kinetic processes on the μs–s timescale corresponding to: (1) fast (μs) electron–hole recombination in the bulk of the photoelectrode, (2) electron–hole recombination at the surface of the photoelectrode involving trapped electrons and (3) hole transfer from the hematite surface into solution as part of the water oxidation reaction. An excellent fit of the 700 nm TAS signal of α-Fe_2O_{3-x} can indeed be achieved using the triphasic stretched exponential function shown in equation 12 and Figure 44:

$$\Delta OD_{700}(t) = A_1 e^{-(k_1 t)^{\beta 1}} + A_2 e^{-(k_2 t)^{\beta 2}} + A_3 e^{-(k_3 t)^{\beta 3}} + y_0 \quad (12)$$

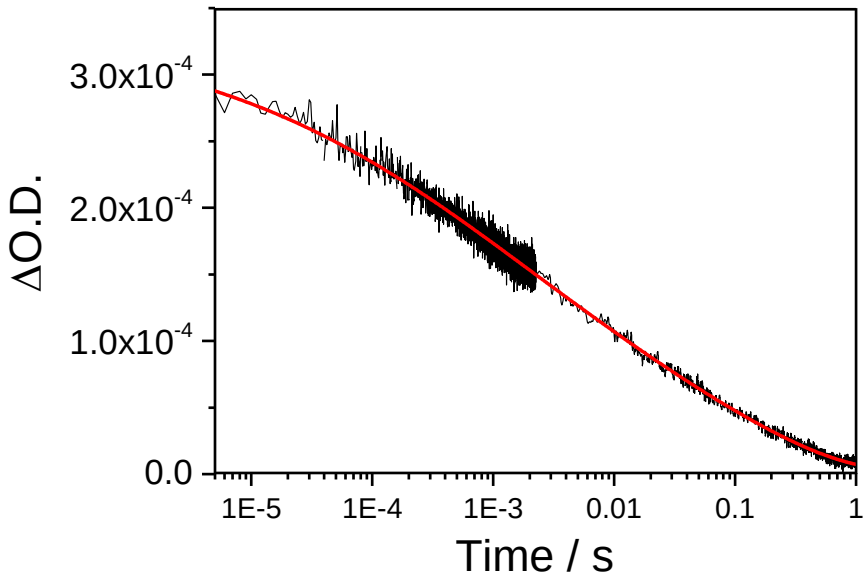

Figure 44 - TAS trace probed at 575 nm (electron trap-state) of α-Fe_2O_{3-x} fitted to a tri-exponential fit. The measurement was carried out at 0.4 $V_{Ag/AgCl}$ following 355 nm laser excitation (6 ns pulse, ~100 μJ cm^{-2}) in 1M NaOH (pH ~13.7).

The fitting in Figure 44 provided the following parameters:

Magnitude	Lifetime (s)	Rate (s^{-1})	Stretching factor
A_1: (2.2±0.2)x10^{-4}	τ_1: (5.2±0.3)x10^{-4}	k_1: (2.0±0.1)x10^3	β_1: 0.30±0.01
A_2: (5.8±1.1)x10^{-5}	τ_2: 0.025±0.003	k_2: 40±5	β_2: 0.5±0.1
A_3: (6±1)x10^{-5}	τ_3: 0.28±0.01	k_3: 3.6±0.1	β_3: 0.7±0.1

Table 5 - Main parameters obtained from the triphasic stretch-exponential fit of the 575 nm TAS signal assigned to photoelectron trapping and de-trapping. A is a pre-exponential factor related to the magnitude, τ is the mean lifetime, k is the rate constant and β is a stretching component. τ and k are related by τ = 1/k.

The three components obtained from the fit of the photo-hole decay are rationalised as follows: The fast decay rate (~ (2.0±0.1)x10^3 s^{-1}) is assigned to bulk electron–hole recombination in the photoelectrode. The second component has a decay rate of 40±5 s^{-1}. This matches with the rate of photoelectron de-trapping obtained in Figure 38 which had a rate of 40.00±0.11 s^{-1}, further the occurrence of trap-mediated recombination of trapped electrons with holes at the SCLJ. The final component has a rate of a ~ 3.6±0.1 s^{-1} and is assigned to hole transfer from hematite into solution. The assignment of this slowest kinetic phase of the hole decay is in line with previously measured rate constants for water oxidation on α-Fe_2O_3 which have ranged from ~ 0.2–6 s^{-1}.[49,56] The assignment of this slow component is further supported by a plot of the yield of very long-lived photo-holes (at 200 ms) versus the applied bias which roughly correlates with the measured photocurrent response of α-Fe_2O_{3-x}, Figure 45.

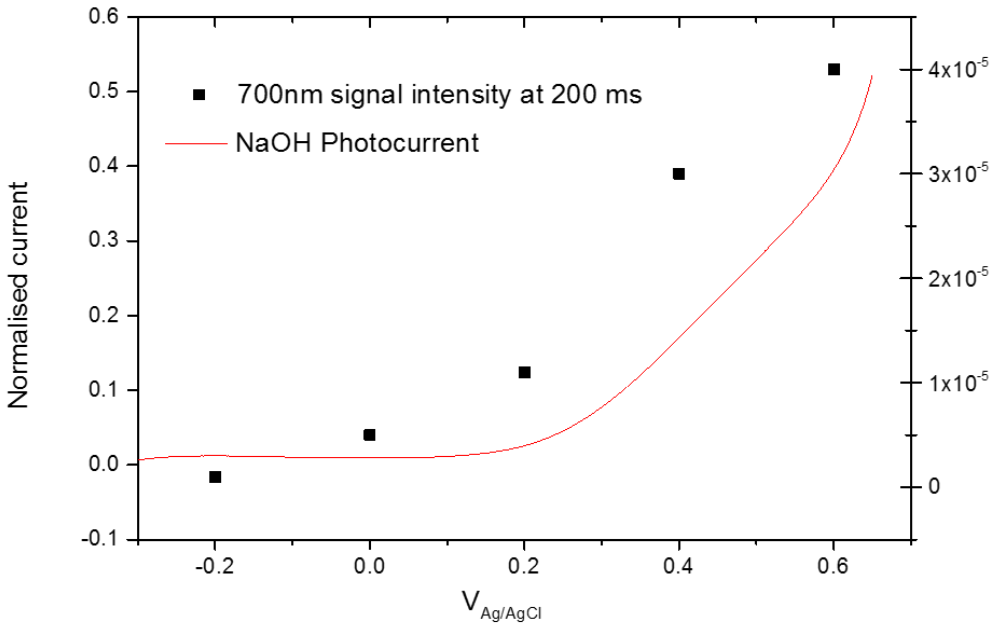

Figure 45 - A plot of the yield of very long-lived photoholes (at 200 ms) versus the applied bias which strongly correlates with the measured photocurrent response of α-Fe_2O_{3-x}.

Interestingly the amplitude of the fitting components, i.e. the separate populations of holes that are decaying by each pathway, is the same for trap-mediated recombination (A_2: (6±1)x10^{-5}) and hole transfer into solution (A_3: (6±1)x10^{-5}) even at 0.4 $V_{Ag/AgCl}$ (pH ~13.7) demonstrating that a high level of trap mediated recombination is a critical factor limiting the efficiency of α-Fe_2O_{3-x}.

The above analysis is also further supported by the fit of the hole trace in the presence of H_2O_2. Equation 13 and Figure 46 show the fitting of the hole decay in the presence of H_2O_2:

$$\Delta OD_{700}(t) = A_1 e^{-(k_1 t)^{\beta 1}} + A_2 e^{-(k_2 t)^{\beta 2}} + y_0 \quad (13)$$

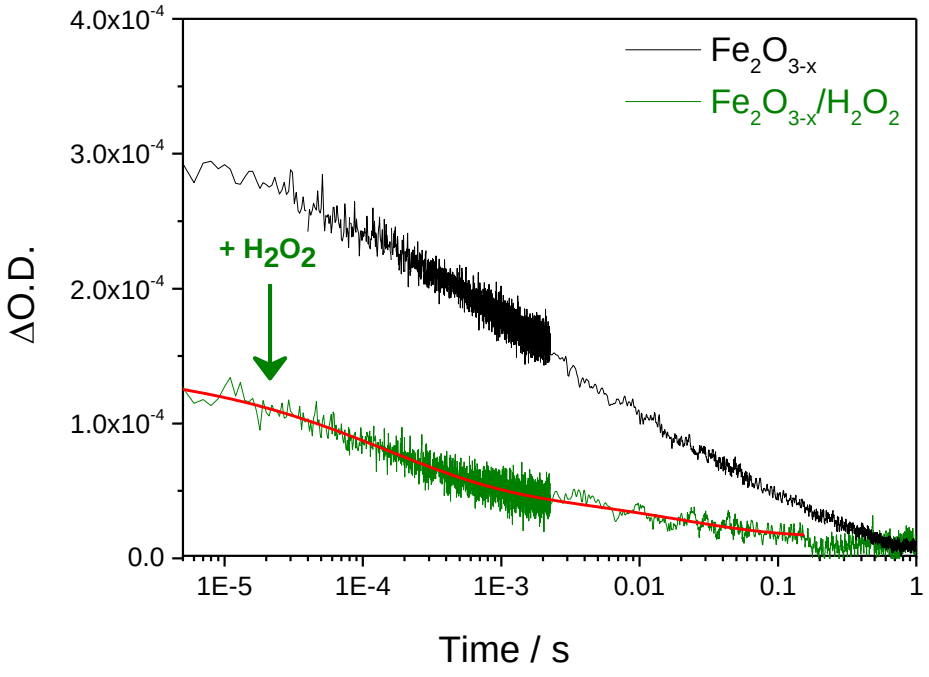

Figure 46 - Fitting of TAS trace of α-Fe_2O_{3-x} recorded a 700 nm (photoholes) in the presence of hydrogen peroxide hole scavenger. Measurement was carried out at 0.4 $V_{Ag/AgCl}$ following 355 nm laser excitation (6 ns pulse, ~100 μJ cm^{-2}) in 1 M NaOH (pH ~13.7)/0.5 M H_2O_2. The black line shows the same measurement without H_2O_2 for reference.

The fitting of Figure 46 provided the following parameters:

Magnitude	Lifetime (s)	Rate (s^{-1})	Stretching factor
A_1: (1.1±0.1)x10^{-4}	τ_1: (3.5±0.1)x10^{-4}	k_1: (2.9±0.1)x10^3	β_1: 0.30±0.03
A_2: (2.7±0.4)x10^{-5}	τ_2: 0.026±0.003	k_2: 39±5	β_2: 0.5±0.1

Table 6 - Main parameters obtained from the biphasic stretch-exponential fit of the 575 nm TAS signal assigned to photoelectron trapping and de-trapping. A is a pre-exponential factor related to the magnitude, τ is the mean lifetime, k is the rate constant and β is a stretching component. τ and k are related by τ = 1/k.

As expected, H_2O_2 appears to remove the slow water oxidation component and the hole trace instead fits well to a biphasic stretched exponential function, with k_{bulk} = (2.9±0.1)x10^3 s^{-1} and k_{detrap} =39±5 s^{-1} present, but k_{WO} absent, confirming the assignment of the slowest kinetic component to water oxidation. We are able to now construct a full kinetic scheme accounting for processes observed in α-Fe_2O_3 and α-Fe_2O_{3-x} in these studies, Figure 47.

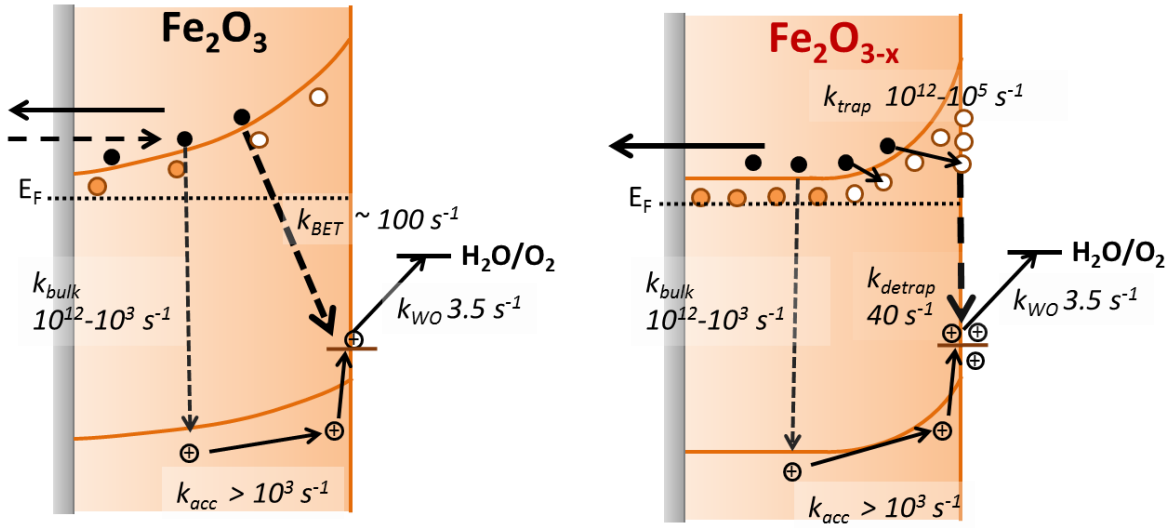

Figure 47 - Simplified energy diagrams showing the processes involving photo-generated charges following UV laser excitation of α-Fe_2O_3 and α-Fe_2O_{3-x} under a positive bias. Rate constants are those determined at 0.4 $V_{Ag/AgCl}$ (pH ~13.7) as described in the main text. In contrast to α-Fe_2O_3 which has been air annealed, no slow recombination between surface accumulated holes and bulk electrons (k_{BET}) is observed for α-Fe_2O_{3-x}. Orange circles are filled trap states and white circles are oxidised trap states which can trap photogenerated electrons.

α-Fe_2O_3 is significantly hindered by back-electron transfer leading to electron-hole recombination and minimal photocurrent. The introduction of V_O into this material to form α-Fe_2O_{3-x} increases the donor density resulting in a narrower W_{SC} which blocks back-electron recombination and enhances the photocurrent. Despite the improvement in photocurrent maximum, onset potential of α-Fe_2O_{3-x} is still quite high compared to other hematite films and this is assigned, at least in part, to large amounts of slow trap mediated recombination with surface accumulated holes. This undesirable trap mediated recombination is proposed to be related to increased levels of V_O acting as trap states throughout the oxygen deficient material. It is known that the preparation of α-Fe_2O_{3-x}, by thermal decomposition of β-FeOOH in an oxygen deficient atmosphere[19] leads to the formation of V_O both in the bulk of α-Fe_2O_{3-x} and at the surface.[26] It has been proposed by several authors that a possible cause of the high onset potentials in α-Fe_2O_{3-x} is the increased concentration of surface defect states.[45,54] Surface defects in hematite are known to lead to Fermi level pinning and increased levels of trap mediated recombination, and the selective passivation of such states in stoichiometric α-Fe_2O_3 has proven to be a highly effective approach to improving photoelectrode activity.[54] Removal of the states solely on the α-Fe_2O_{3-x} surface by passivation, whilst maintaining a suitably high concentration of V_O both within the bulk and close to the SCLJ may be anticipated to be a route to obtaining both the desired improved N_d whilst lowering the level of trap-mediated recombination. The next section discusses the effect of surface passivation of α-Fe_2O_{3-x} by deposition of Al_2O_3 overlayers.

2.2.5 Passivating surface trap states in α-Fe_2O_{3-x} with Al_2O_3 overlayers

Previously in the literature, the passivation of surface states in hematite has been investigated and achieved in a number of ways including: the use of high temperature annealing steps,[37] the deposition of catalytic species such as CoPi, IrO_x, $NiFeO_x$[44,57] and the use of inert metal oxides such as Al_2O_3 and Ga_2O_3 overlayers grown by atomic layer deposition (ALD).[45,47,58]

The deposition of Al_2O_3 by atomic layer deposition (ALD) was considered as a promising route to passivating the surface of α-Fe_2O_{3-x} due the low temperature required (120 ^oC) for the deposition and the reduced oxygen pressures typically used for ALD which were expected to limit the loss of bulk oxygen vacancies in α-Fe_2O_{3-x}. ALD Al_2O_3 layers have been previously shown to decrease the photocurrent onset potentials of Si-doped α-Fe_2O_3 electrodes by *ca.* 100 mV,[9] and have also been shown to decrease the surface capacitance of α-Fe_2O_3 electrodes,[59,60] indicating the passivation of surface trap states. The preliminary study carried out here has used ALD to form an *ca.* 1 nm Al_2O_3 layer on α-Fe_2O_{3-x}. This thickness was chosen as previous experiments with Si–α-Fe_2O_3[9] have indicated that it provides reasonable coverage and stability for the duration of an experiment (the film is stable for up to 20 minutes in 1 M NaOH used here) whilst remaining thin enough to allow for hole tunnelling from the α-Fe_2O_3 to water. Al_2O_3 was deposited onto α-Fe_2O_{3-x} by Dr. Richard Potter at the University of Liverpool using thermal ALD (full details can be found in the experimental section). Figure 48 shows the photocurrent of α-Fe_2O_{3-x} measured under white light illumination (*ca.* 50 mW cm^{-2}) before and after the deposition of Al_2O_3.

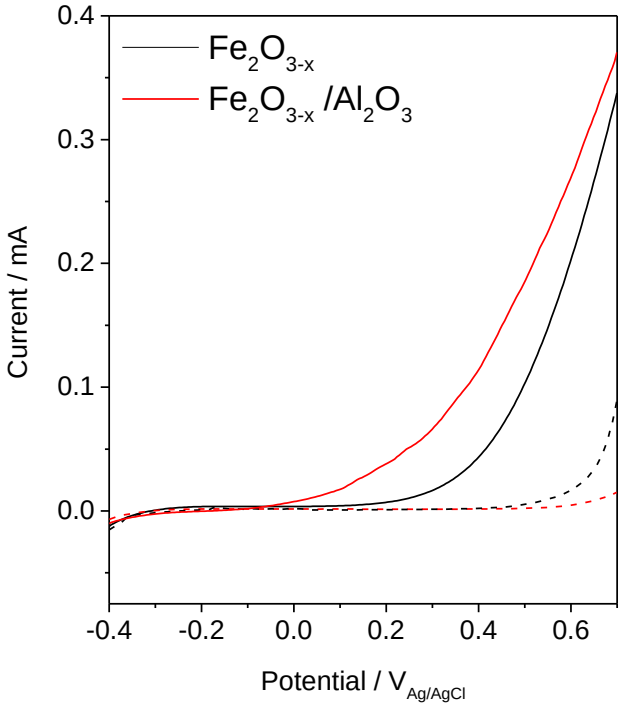

*Figure 48 - Photocurrent of α-Fe_2O_{3-x} before (black) and after (red) deposition of an ALD Al_2O_3 layer (~1 nm, red trace) recorded using a low power 150W Xe lamp (*ca. *50 mW cm^{-2}), dark traces are shown as dashed lines.*

The deposition of Al_2O_3 leads to a large cathodic shift in the photocurrent onset potential (*ca.* 200 mV, -0.05 $V_{Ag/AgCl,}$ pH ~13.7) indicating that the overlayer had passivated surface states which were previously inhibiting activity. Enhanced electrocatalytic activity for water oxidation due to the presence of Al_2O_3 can be ruled out as the current onset potential in the dark is shifted anodically following ALD. Al_2O_3 was also deposited onto an air annealed α-Fe_2O_3 sample, Figure 49. No significant change in photocurrent was observed in α-Fe_2O_3 following ALD. This is in line with expectations as the factor limiting α-Fe_2O_3 efficiency is not surface states but back-electron recombination due to poor doping.

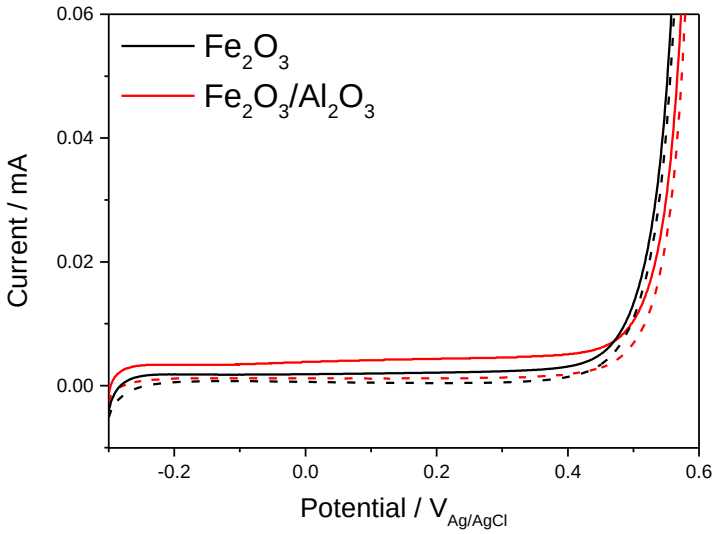

Figure 49 - Photocurrent of α-Fe_2O_3 before (black) and after (red) deposition of ALD Al_2O_3 layer (~1 nm, red trace) recorded using a 75 W Xe lamp, dark traces are shown as dashed lines.

To confirm that the improved photoelectrochemical activity of the α-Fe_2O_{3-x}/Al_2O_3 sample is related to the hypothesised decrease in trap mediated surface electron–hole recombination, TAS kinetics of the 575 nm trap states at 0.4 $V_{Ag/AgCl}$ (pH ~13.7) have been measured following ALD, Figure 50.

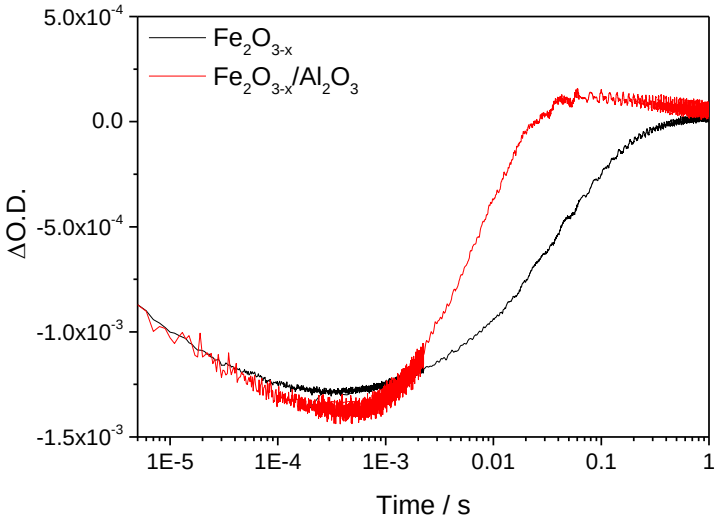

Figure 50 - TAS decay traces probed at 575 nm of α-Fe_2O_{3-x} (0.4 $V_{Ag/AgCl}$ in 1M NaOH (pH ~13.7) following 355 nm laser excitation (6 ns pulse, ~100 μJ cm^{-2}) before (black) and after (red) deposition of an ALD Al_2O_3 layer (~1 nm, red trace) recorded using a low power 75W Xe lamp, dark traces are shown as dashed lines.

The large bleaching of the TAS signal is observed at 575 nm even after the Al_2O_3 treatment, showing that a significant concentration of trap states remain following Al_2O_3 deposition. These unaltered trap states are likely in the bulk of α-Fe_2O_{3-x}, away from the surface. Critically, while there is no change in the magnitude of the signal, there is a near four-fold increase in the rate of de-trapping with the α-Fe_2O_{3-x}/Al_2O_3 sample (k_{detrap} *ca.* 150 s^{-1}, Figure 50, red line) compared to the measured rate of de-trapping for α-Fe_2O_{3-x} (k_{detrap} *ca.* 40 s^{-1}, Figure 50, black line), indicating that photoelectrons in the ALD treated sample are trapped at energetically shallower sites. To the best of our knowledge this report represents the first TAS study of the role of an ALD Al_2O_3 passivation treatment on hematite. Furthermore, in contrast to the untreated α-Fe_2O_{3-x} sample, where de-trapping leads to significant levels of recombination with surface trapped holes, there is now an excellent agreement between the recovery of the TAS trap state band at 575 nm and the rate of charge extraction as measured by TPC for α-Fe_2O_{3-x}/Al_2O_3, Figure 51.

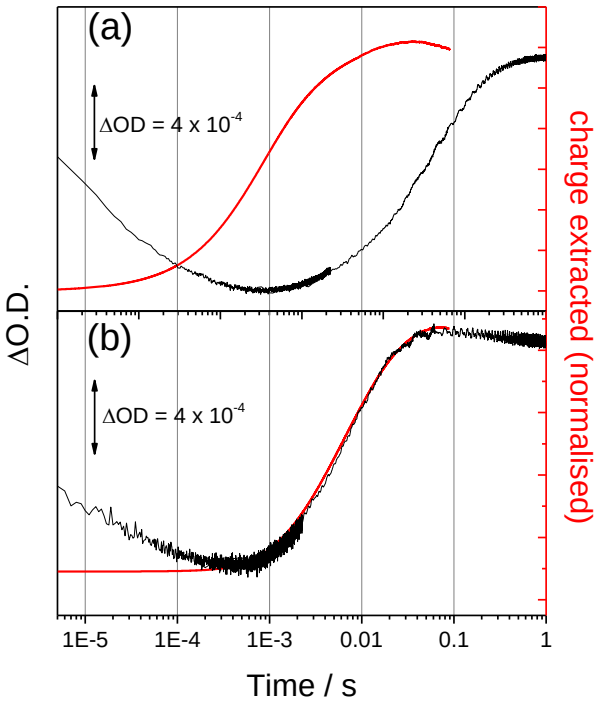

Figure 51 - Overlay of the TAS trace recorded at 575 nm, assigned to an inter-band trap state, and the normalised charge extracted for (a) α-Fe_2O_{3-x} and (b) α-Fe_2O_{3-x}/Al_2O_3 following 355 nm laser excitation (6 ns pulse, ~100 μJ cm^{-2}).

The decrease in trap-mediated recombination with surface holes is further supported by the observation of an increase in the yield of very long-lived photo-holes in α-Fe_2O_{3-x}/Al_2O_3, Figure 52.

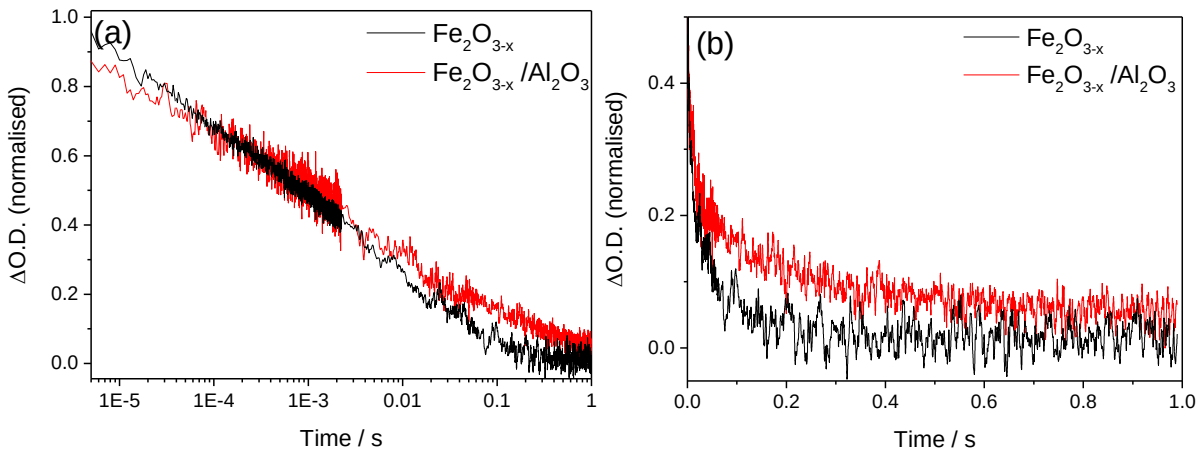

Figure 52 – (a) TAS traces recorded at 700 nm (photo-holes) of α-Fe_2O_{3-x} (black) and α-Fe_2O_{3-x} /Al_2O_3 (red) at 0.4 $V_{Ag/AgCl}$ in 1 M NaOH (pH ~13.7) following 355 nm laser excitation (6 ns pulse, ~100 μJ cm^{-2}). (b) The same TA traces with non-logarithmic time base.

The experiments with Al_2O_3 lead to the conclusion that a portion of the de-trapped electrons are no longer recombining with holes at the surface and are instead reaching the external circuit in appreciable quantities. We assign the change in kinetics of the transient photocurrent and trap state occupancy to the passivation of the surface trap states. In the absence of a significant concentration of surface trap states, photoelectrons are able to be trapped at inter-band trap states in the α-Fe_2O_{3-x} bulk, which are spatially separated from the population of surface accumulated holes, limiting trap-mediated recombination and enabling electron transport to the external circuit, thus lowering the photocurrent onset potential.

The combination of α-Fe_2O_{3-x} with Al_2O_3 preserved the Vo in the bulk of α-Fe_2O_{3-x} providing the desirably narrower W_{SC} while also removing the trap states linked to V_O at the surface which caused recombination problems with surface holes. Figure 53 shows simplified kinetic models for α-Fe_2O_{3-x} and α-Fe_2O_{3-x}/Al_2O_3.

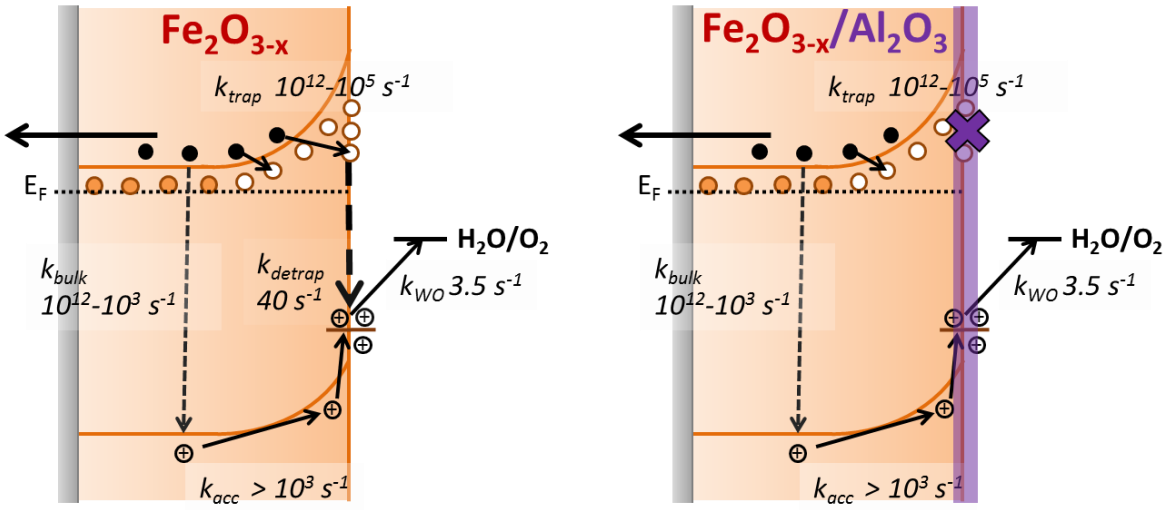

Figure 53 - Simplified energy diagrams showing the processes involving photo-generated charges following UV laser excitation of α-Fe_2O_{3-x} and α-Fe_2O_{3-x}/Al_2O_3 under a positive bias. Rate constants are those determined at 0.4 $V_{Ag/AgCl}$ as described in the main text. The addition of Al_2O_3 passivated electron trap states at the surface, reducing the amount of trap-mediated recombination with holes accumulating at/near the surface. Orange circles are filled trap states and white circles are oxidised trap states which can trap photogenerated electrons.

2.3 Conclusions

The annealing of hematite in oxygen deficient atmospheres is being increasingly explored as an approach to improving the electrical properties, however conflicting reports exist regarding the mechanism of enhancement.[49,59] In contrast to previously proposed mechanisms which have often indicated improved charge transport as being a significant factor,[18] here it is found that the primary effect of the introduction of oxygen vacancies is to block the slow recombination of bulk electrons with surface accumulated holes, the so called "back electron recombination" pathway at even moderate applied biases (-0.2 $V_{Ag/AgCl}$, pH ~13.7). This is due to the formation of a strong electric field close to the SCLJ arising from the improved electrical properties.

The very anodic photocurrent onset potential of α-Fe_2O_{3-x} has also been addressed. As the initial part of the study indicated that electron-trap mediated recombination with surface holes played a role in the poor onset potential, ALD-deposited Al_2O_3 was investigated as a surface

passivation treatment. The Al_2O_3 overlayer reduced the lifetime of the electron trap TAS signal by *ca.* 4-fold and resulted in an improvement in the photocurrent onset potential of *ca.* 200 mV, validating the initially proposed model. Figure 54 summarises these results.

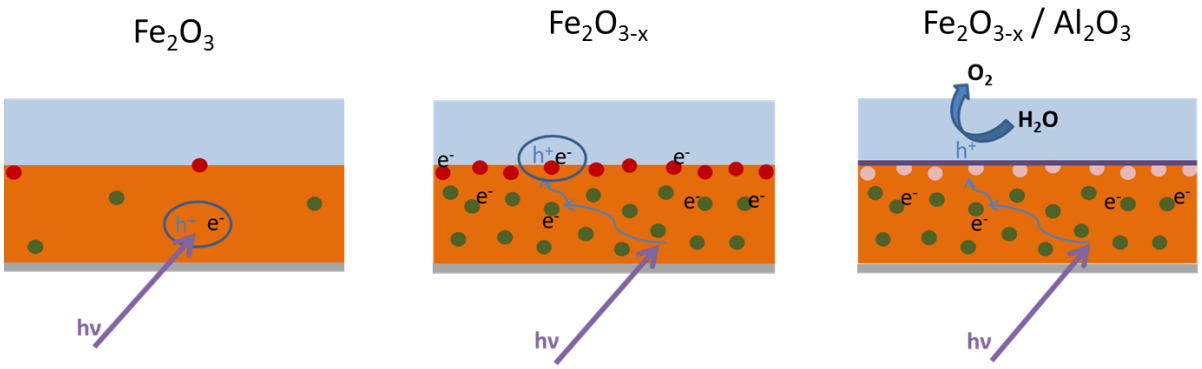

Figure 54 - Cartoon showing the dual effect of the presence of oxygen vacancies in hematite photoelectrodes. Oxygen vacancies in the bulk contribute towards the blocking of the back electron recombination with surface holes. Oxygen vacancies at the surface lead to trapping of electrons near the surface resulting in trap mediated recombination with holes, competing with water oxidation.

This study includes, to the best of our knowledge, the first TAS measurements on ALD Al_2O_3-coated hematite, providing important insights into this widely used surface treatment. Unfortunately the poor stability of Al_2O_3 in the photoelectrochemical conditions used here (degrades after ~20 minutes) prevented a more detailed mechanistic study of the effect of the overlayer. The next chapter will discuss results obtained using a more stable passivating overlayer.

2.4 References

1. K. Sivula, F. Le Formal, and M. Grätzel, *ChemSusChem*, 2011, **4**, 432–449.

2. J. Y. Kim, G. Magesh, D. H. Youn, J.-W. Jang, J. Kubota, K. Domen, and J. S. Lee, *Sci. Rep.*, 2013, **3**, 2681.

3. F. J. Morin, *Phys. Rev.*, 1951, **83**, 1005–1010.

4. N. J. Cherepy, D. B. Liston, J. A. Lovejoy, H. Deng, and J. Z. Zhang, *J. Phys. Chem. B*, 1998, **5647**, 770–776.

5. M. Dare-Edwards, J. Goodenough, A. Hamnett, and P. Trevelick, *J. Chem. SOC., Faraday Trans. I*, 1983, **79**, 2027–2041.

6. K. Sivula, R. Zboril, F. Le Formal, R. Robert, A. Weidenkaff, J. Tucek, J. Frydrych, and M. Grätzel, *J. Am. Chem. Soc.*, 2010, **132**, 7436–44.

7. A. Kay, I. Cesar, and M. Grätzel, *J. Am. Chem. Soc.*, 2006, **128**, 15714–21.

8. I. Cesar, K. Sivula, A. Kay, R. Zboril, and M. Grätzel, *J. Phys. Chem. C*, 2009, **113**, 772–782.

9. I. Cesar, A. Kay, J. a Gonzalez Martinez, and M. Grätzel, *J. Am. Chem. Soc.*, 2006, **128**, 4582–4583.

10. S. Saremi-Yarahmadi, K. G. U. Wijayantha, A. A. Tahir, and B. Vaidhyanathan, *J. Phys. Chem. C*, 2009, **113**, 4768–4778.

11. Y. Ling, G. Wang, D. A. Wheeler, J. Z. Zhang, and Y. Li, *Nano Lett.*, 2011, **11**, 2119–25.

12. C. D. Bohn, A. K. Agrawal, E. C. Walter, M. D. Vaudin, A. A. Herzing, P. M. Haney, A. A. Talin, and V. A. Szalai, *J. Phys. Chem. C*, 2012, **116**, 15290–15296.

13. N. T. Hahn and C. B. Mullins, *Chem. Mater.*, 2010, **22**, 6474–6482.

14. M. G. Ahmed, I. E. Kretschmer, T. A. Kandiel, A. Y. Ahmed, F. A. Rashwan, and D. W. Bahnemann, *ACS Appl. Mater. Interfaces*, 2015, **7**, 24053–24062.

15. R. Franking, L. Li, M. a. Lukowski, F. Meng, Y. Tan, R. J. Hamers, and S. Jin, *Energy Environ. Sci.*, 2013, **6**, 500–512.

16. O. Neufeld and M. C. Toroker, *J. Phys. Chem. C*, 2015, **119**, 5836–5847.

17. A. Mao, N.-G. Park, G. Y. Han, and J. H. Park, *Nanotechnology*, 2011, **22**, 175703.

18. G. Wang, Y. Ling, and Y. Li, *Nanoscale*, 2012, **4**, 6682.

19. Y. Ling, G. Wang, J. Reddy, C. Wang, J. Z. Zhang, and Y. Li, *Angew. Chem. Int. Ed. Engl.*, 2012, **51**, 4074–9.

20. A. Pu, J. Deng, M. Li, J. Gao, H. Zhang, Y. Hao, J. Zhong, and X. Sun, *J. Mater. Chem. A*, 2014, **2**, 2491.

21. G. Wang, H. Wang, Y. Ling, Y. Tang, X. Yang, R. C. Fitzmorris, C. Wang, J. Z. Zhang, and Y. Li, *Nano Lett.*, 2011, **11**, 3026–33.

22. X. Liu, F. Wang, and Q. Wang, *Phys. Chem. Chem. Phys.*, 2012, **14**, 7894.

23. H. L. Tan, A. Suyanto, A. T. De Denko, W. H. Saputera, R. Amal, F. E. Osterloh, and Y. H. Ng, *Part. Part. Syst. Charact.*, 2017, **34**, 1600290.

24. Y. Ling, G. Wang, H. Wang, Y. Yang, and Y. Li, *ChemSusChem*, 2014, **7**, 848–53.

25. T.-Y. Yang, H.-Y. Kang, U. Sim, Y.-J. Lee, J.-H. Lee, B. Koo, K. T. Nam, and Y.-C. Joo, *Phys. Chem. Chem. Phys.*, 2013, **15**, 2117.

26. M. Li, J. Deng, A. Pu, P. Zhang, H. Zhang, J. Gao, Y. Hao, J. Zhong, and X. Sun, *J. Mater. Chem. A*, 2014, **2**, 6727.

27. C. Zhu, C. Li, M. Zheng, and J.-J. Delaunay, *ACS Appl. Mater. Interfaces*, 2015, **7**, 22355–22363.

28. M. Rioult, D. Stanescu, E. Fonda, A. Barbier, and H. Magnan, *J. Phys. Chem. C*, 2016, **120**, 7482–7490.

29. G. Pacchioni, *ChemPhysChem*, 2003, **4**, 1041–1047.

30. K. Kobayashi, G. Okada, and J. Kumanotani, *J. Mater. Sci. Lett.*, 1988, **7**, 853–854.

31. K. Sivula, in *Photoelectrochemical Hydrogen Production*, Springer US, 2012, vol. 102, pp. 121–156.

32. X. Zhang, P. Klaver, R. van Santen, M. C. M. van de Sanden, and A. Bieberle-H?tter, *J. Phys. Chem. C*, 2016, **120**, 18201–18208.

33. J. Engel and H. L. Tuller, *Phys. Chem. Chem. Phys.*, 2014, **16**, 11374–80.

34. J. Lee and S. Han, *Phys. Chem. Chem. Phys.*, 2013, **15**, 18906–14.

35. J. Deng, X. Lv, J. Gao, A. Pu, M. Li, X. Sun, and J. Zhong, *Energy Environ. Sci.*, 2013, **6**, 1965.

36. B. Klahr, S. Gimenez, F. Fabregat-Santiago, J. Bisquert, and T. W. Hamann, *Energy Environ. Sci.*, 2012, **5**, 7626.

37. O. Zandi and T. W. Hamann, *J. Phys. Chem. Lett.*, 2014, **5**, 1522–1526.

38. D. a. Wheeler, G. Wang, Y. Ling, Y. Li, and J. Z. Zhang, *Energy Environ. Sci.*, 2012, **5**, 6682.

39. F. Le Formal, S. R. Pendlebury, M. Cornuz, S. D. Tilley, M. Grätzel, and J. R. Durrant, *J. Am. Chem. Soc.*, 2014, **136**, 2564–74.

40. S. R. Pendlebury, M. Barroso, A. J. Cowan, K. Sivula, J. Tang, M. Gr?tzel, D. Klug, and

J. R. Durrant, *Chem. Commun.*, 2011, **47**, 716–718.

41. A. Yamakata, J. J. M. Vequizo, and M. Kawaguchi, *J. Phys. Chem. C*, 2014, **119**, 1880–1885.

42. K. Furuhashi, Q. Jia, A. Kudo, and H. Onishi, *J. Phys. Chem. C*, 2013, **117**, 19101–19106.

43. F. M. Pesci, G. Wang, D. R. Klug, Y. Li, and A. J. Cowan, *J. Phys. Chem. C*, 2013, **117**, 25837–25844.

44. R. Liu, Z. Zheng, J. Spurgeon, and X. Yang, *Energy Environ. Sci.*, 2014, **7**, 2504.

45. T. Hisatomi, F. Le Formal, M. Cornuz, J. Brillet, N. Tétreault, K. Sivula, and M. Grätzel, *Energy Environ. Sci.*, 2011, **4**, 2512.

46. T. Wang, Z. Luo, C. Li, and J. Gong, *Chem. Soc. Rev.*, 2014, **43**, 7469–7484.

47. L. Steier, I. Herraiz-Cardona, S. Gimenez, F. Fabregat-Santiago, J. Bisquert, S. D. Tilley, and M. Grätzel, *Adv. Funct. Mater.*, 2014, **24**, 7681–7688.

48. S. R. Pendlebury, X. Wang, F. Le Formal, M. Cornuz, A. Kafizas, S. D. Tilley, M. Grätzel, and J. R. Durrant, *J. Am. Chem. Soc.*, 2014, **136**, 9854–9857.

49. M. Barroso, S. R. Pendlebury, A. J. Cowan, and J. R. Durrant, *Chem. Sci.*, 2013, **4**, 2724.

50. A. J. Cowan, C. J. Barnett, S. R. Pendlebury, M. Barroso, K. Sivula, M. Grätzel, J. R. Durrant, and D. R. Klug, *J. Am. Chem. Soc.*, 2011, **133**, 10134–10140.

51. S. R. Pendlebury, A. J. Cowan, M. Barroso, K. Sivula, J. Ye, M. Grätzel, D. R. Klug, J. Tang, and J. R. Durrant, *Energy Environ. Sci.*, 2012, **5**, 6304–6312.

52. N. Iordanova, M. Dupuis, and K. M. Rosso, *J. Chem. Phys.*, 2005, **122**, 144305.

53. H. Dotan, K. Sivula, M. Grätzel, A. Rothschild, and S. C. Warren, *Energy Environ. Sci.*,

2011, **4**, 958–964.

54. K. Sivula, *J. Phys. Chem. Lett.*, 2013, **4**, 1624–1633.

55. D. L. A. De Faria, *J. Raman Spectrosc.*, 1997, **28**, 873–878.

56. H. K. Dunn, J. M. Feckl, A. Müller, D. Fattakhova-Rohlfing, S. G. Morehead, J. Roos, L. M. Peter, C. Scheu, and T. Bein, *Phys. Chem. Chem. Phys.*, 2014, **16**, 24610–24620.

57. T. Wang, Z. Luo, C. Li, and J. Gong, *Chem. Soc. Rev.*, 2014, **43**, 7469–84.

58. F. Le Formal, N. Tétreault, M. Cornuz, T. Moehl, M. Grätzel, and K. Sivula, *Chem. Sci.*, 2011, **2**, 737–743.

59. B. Klahr and T. Hamann, *J. Phys. Chem. C*, 2014, **118**, 10393–10399.

60. F. Le Formal, K. Sivula, and M. Grätzel, *J. Phys. Chem. C*, 2012, **116**, 26707–26720.

3

Ta_2O_5 as a stable surface passivating overlayer for α-Fe_2O_3

Contents

3.2 Introduction

In the previous chapter transient absorption spectroscopy (TAS) was used to rationalise the efficiency of α-Fe_2O_{3-x}, a hematite photoelectrode intrinsically doped with oxygen vacancies. Trap states in the bulk of the material were proposed to have a drastically different effect to trap states located near the surface. The effect of introducing V_O was two-fold. Firstly, the increased donor density as a result of bulk V_O dopants helped to block back electron recombination[1]: the very slow (millisecond) recombination of surface holes with bulk electrons. Secondly, the increased V_O concentration was linked to an increase in surface trap states and surface trap mediated recombination, negatively impacting performance. Atomic layer deposition (ALD) of a ~1 nm thick Al_2O_3 overlayer was used to passivate the unwanted trap states near the surface which led to an improvement in the onset potential assigned to a reduction in surface trap mediated recombination. The Al_2O_3 overlayer provided useful insight as a proof of principle study which correlated a cathodic shift in onset potential with a change in electron de-trapping kinetics. Unfortunately the instability of Al_2O_3 in the alkaline (pH = 13.7) working photoelectrochemical conditions prevented more detailed analysis. The improvement in onset potential was only temporary, reverting back to the original value within 20 minutes, as the Al_2O_3 overlayer was destroyed.[2,3]

In order to understand the role of 'passivating' overlayers and the exact nature of the states they alter in more detail, more comprehensive studies are required. To this end, an overlayer with higher stability is desirable so that measurements can be carried out under working photoelectrochemical conditions for extended periods of time without destruction of the overlayer. This chapter describes the selection and deposition of Ta_2O_5 as a more stable alternative to Al_2O_3. As a trial run, Ta_2O_5 was first deposited onto a set of Sn-doped hematite films synthesised using a commonly reported route.[4] The Ta_2O_5 overlayer was then deposited onto α-Fe_2O_{3-x} in an attempt to further the conclusions reached in chapter 2. The remainder of

this chapter discusses the possible nature of surface states on hematite photoelectrodes and addresses conclusions reached by other groups. Finally, a temperature dependent TAS experiment is described in an attempt to approximate the energies of the trap states in hematite.

3.3 Results and discussion

3.3.1 Ta_2O_5 as a stable photoelectrode overlayer

In order to fairly assess solely the passivation effect on surface states, an overlayer which is optically transparent, non-catalytic and inert with respect to both hematite and the alkaline electrolyte is desirable. It is possible to use hematite in less alkaline or even mildly acidic media, however, 1 M NaOH (pH ~13.7) is most commonly chosen as it provides a high ion concentration (the presence of OH^-). In the interest of remaining consistent with the majority of the literature and with our previous study of Al_2O_3 discussed in chapter 2, 1 M NaOH (pH ~13.7) was chosen as the electrolyte for the experiments in this chapter. An additional requirement for this particular study was for the overlayer to possess a relatively low deposition temperature as oxygen present in the atmosphere is likely to fill oxygen vacancies in the oxygen deficient α-Fe_2O_{3-x} samples used. Although it is not the focus of this study, a lower deposition temperature would also potentially make scale up more cost effective. Al_2O_3 is commonly used/discussed in the literature[3,5,6] and was chosen for the work in chapter 2 because of its ease of application, its large band gap (~7.0 -8.8 eV) which ensures no light (UV, Visible, NIR) is absorbed by the overlayer, and its low deposition temperature of 120 ^oC.[7] The position of the band edges should also be taken into consideration. In the case of Al_2O_3 the valence band (VB) and conduction band (CB) edges straddle those of hematite, preventing additional unwanted charge transfer from the excited hematite to the Al_2O_3, which can potentially cause complications in the analysis. The mechanism tentatively proposed in chapter 2 assumed

charge tunnelling through the Al_2O_3 insulator layer, hence there is no requirement for the VB of the overlayer to align with the VB of α-Fe_2O_3 to facilitate transfer between layers. Doing so may be useful for charge separation but would lead to a loss of oxidising potential, in addition to complications of our fundamental mechanistic analysis.

There are a number of commonly used protecting/passivating overlayers aside from Al_2O_3 in the literature. In particular, TiO_2[8,9] has been explored extensively and is known to offer high stability in alkaline environments. However, while TiO_2 is typically referred to as a large band gap semiconductor (~3.2 eV), it is still able to absorb UV light. 355 nm UV light is typically used in our TAS measurements and therefore having an overlayer that absorbs this light may complicate analysis, and for this reason TiO_2 was ruled out. Ga_2O_3 is another overlayer material which has been implemented in several studies.[10,11] Ga_2O_3 is reported to be stable, however it is not currently clear whether Ga_2O_3 acts as an 'inert' passivating layer. Some studies indicate that it does not act innocently at the surface of a photelectrode and that it is able to facilitate charge redistribution. As the behaviour of Ga_2O_3 is not fully understood,[10,11] its use was ruled out from this study as a result. Several other catalytic overlayers such as Co-Pi[12] are also common place in the literature, and in addition to Ga_2O_3, these were ruled unsuitable for this study due to their potentially charge redistributing/catalytic nature. In an effort to find an overlayer that was both stable and passive, attention was turned to Ta_2O_5, a material known to possess a wide band gap (~4 eV) and offer stability over a wide pH range.[13,14] In addition to its insulating properties, Ta_2O_5 is reported to possess VB and CB edges which straddle those of hematite, making it a promising candidate for trap state passivation studies of hematite, Figure 55.

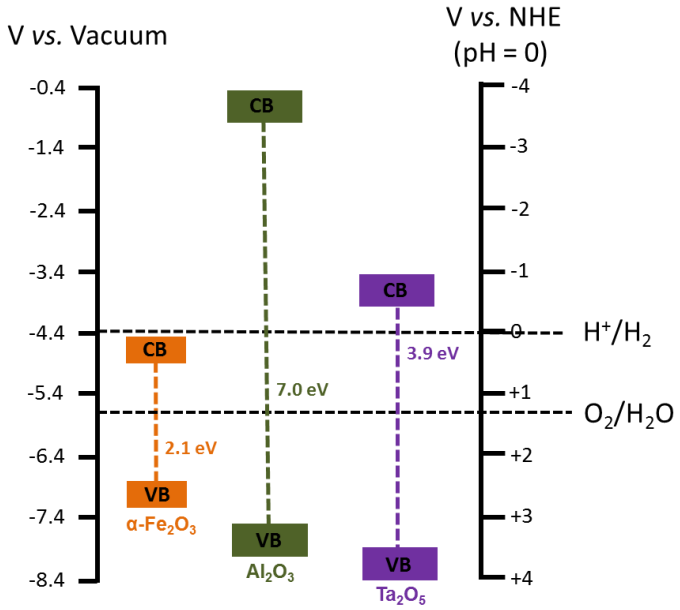

Figure 55 - Approximate valence and conduction band positions based on literature values of α-Fe_2O_3[15], Al_2O_3[7,16] and Ta_2O_5[13,17].

There is to our knowledge only one report in which Ta_2O_5 is used as an overlayer on a photoelectrode device, where Gong *et al.*[18] deposited it using atomic layer deposition (ALD) as a protecting layer onto an unstable ZnO photoelectrode. The photocurrent conversion efficiency of the ZnO was increased two-fold following deposition of Ta_2O_5 and this was postulated to be due to suppression of surface recombination. The promising results reported by Gong *et al.* suggest that a similar approach could be successful for hematite, therefore Ta_2O_5 was chosen for further investigation.

3.3.2 Photo-response and stability of Ta_2O_5 deposited by ALD

Firstly, the stability and electrocatalytic/photo-response of ALD Ta_2O_5 was investigated. Ta_2O_5 was deposited by Dr. Richard Potter at the University of Liverpool using thermal ALD with $Ta(NMe_2)_5$ and water as the precursors at 200 ^oC; full details can be found in the experimental section. In order to assess the photoelectrochemical response of Ta_2O_5 under light, a ~20 nm

layer was deposited onto a FTO glass substrate. The photoelectrochemical behaviour under white light was compared to an uncoated FTO glass substrate, Figure 56. As predicted from the approximate band gap of Ta_2O_5, no light response was observed, however a small cathodic shift in the electrocatalytic onset potential was noted. This shift in electrocatalytic onset potential could suggest the Ta_2O_5 layer is acting catalytically, however the onset is *ca.* 0.3 V more anodic than the $E^0_{H2O/O2}$ of 0.23 $V_{Ag/AgCl}$ at pH ~13.7 (1.23 *vs.* V_{RHE}). This observation will be discussed further in the next section (3.3.3) were it is found that once Ta_2O_5 is deposited onto hematite, the cathodic shift no longer occurs.

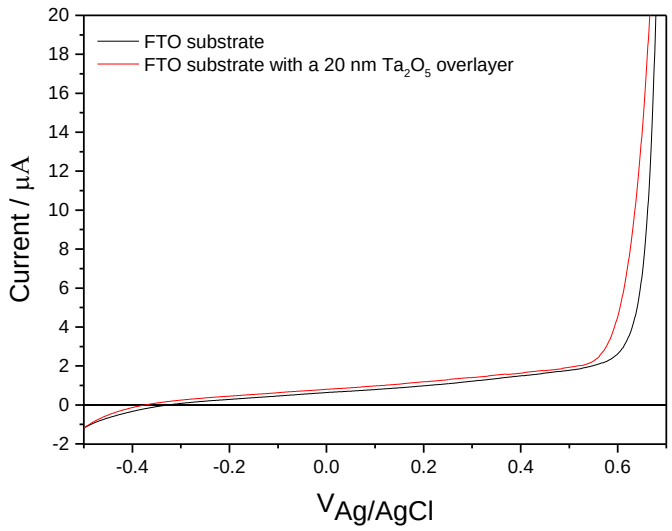

Figure 56 - Linear sweep voltammograms of FTO glass substrate and FTO glass substrate coated with ~20 nm of Ta_2O_5, measured under 50 mW cm^{-2} white light illumination at 10 mV s^{-1} in 1 M NaOH (pH ~13.7).

The stability of Ta_2O_5 in 1 M NaOH (pH ~13.7) electrolyte was tested and compared to Al_2O_3. ~20 nm thick films were deposited onto standard silicon wafers and immersed into 1 M NaOH electrolyte at room temperature (24 ^oC) or at 50 ^oC. Wafers were then removed at certain time intervals and the thickness of the film was measured by ellipsometry to determine approximate stability times, Figure 57. In line with previous reports regarding the instability of Al_2O_3, 27

nm of Al_2O_3 was completely removed after 20 minutes at room temperature, Figure 57a. In contrast, the Ta_2O_5 layer was found to be completely stable over a 24 hour period at room temperature and at 50 ^oC, Figure 57b.

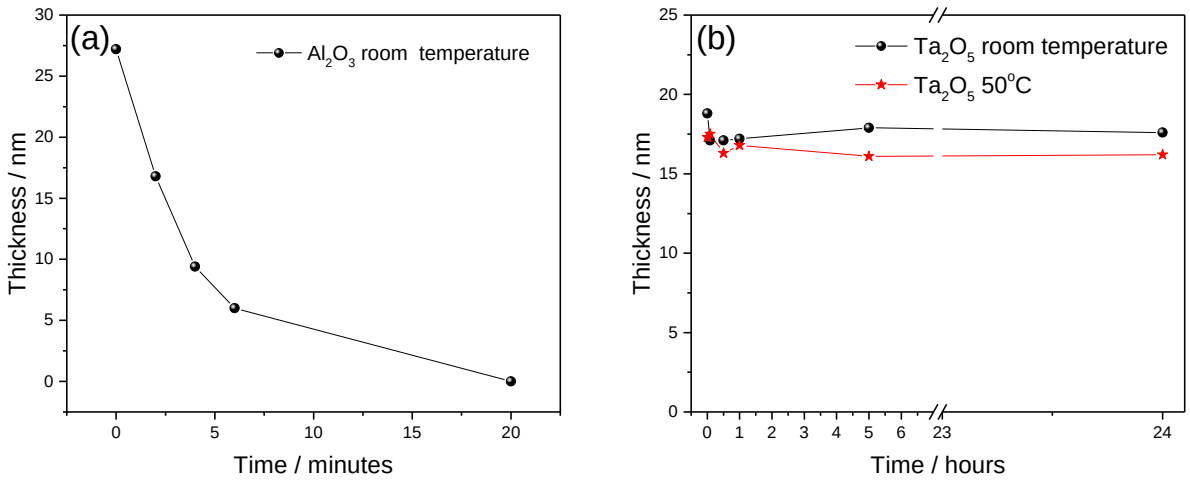

Figure 57 - Thickness of (a) Al_2O_3 and (b) Ta_2O_5 with respect to time immersed in 1 M NaOH (pH ~13.7) at room temperature (24 ^oC) and additionally at 50 ^oC for Ta_2O_5. The layers were deposited onto standard silicon wafers and thickness was measured by ellipsometry.

The ellipsometry data is further supported by the photographs in Figure 58 which shows a silicon wafer partially coated with ~2 nm of Ta_2O_5 before and after exposure to 1 M NaOH (pH ~13.7) for 72 hours at room temperature. The exposed silicon is significantly eroded and dulled by the electrolyte whereas coated section at the top remains undamaged.

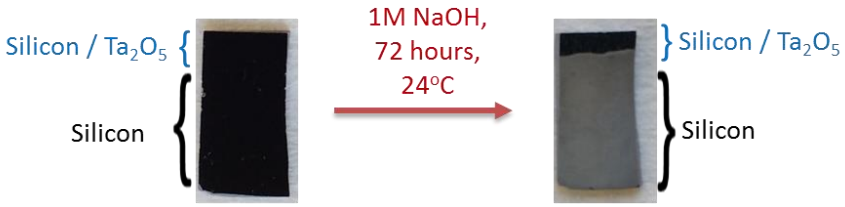

Figure 58 - Photographs of a silicon wafer partially coated in ~2 nm of Ta_2O_5. The wafer has been immersed in 1 M NaOH (pH ~13.7) for 72 hours at room temperature (24 ^oC). The initial shiny, black surface of the wafer is preserved under the Ta_2O_5 layer, while the exposed wafer is eroded and dulled by the 1 M NaOH (pH ~13.7).

3.3.3 Synthesis of nanostructured hematite films and deposition of Ta_2O_5

Although the primary motivation for developing the Ta_2O_5 overlayer was to progress the passivation study of α-Fe_2O_{3-x} presented in chapter 2, it is also useful to see if Ta_2O_5 overlayers have an impact on hematite films more generally. This section outlines the synthesis of a set of hematite films using a common synthesis route[4] which was carried out in order to establish the effect of Ta_2O_5 on hematite more broadly. Figure 60 shows the procedure used to synthesise batches of hematite films. First, FTO glass was cut into 25 mm x 50 mm pieces and washed by sonicating in acetone for 20 minutes, followed by sonicating in ethanol for 20 mins and finally sonicating in water for 20 minutes. The pieces of washed glass were then placed into a glass vessel. *ca.* 80% of the films were then immersed into a solution of $FeCl_3.6H_2O$ (0.15 M) and $NaNO_3$ (1 M) in water, leaving the top edge of each piece of FTO exposed for electrical contact. The vessel was sealed and heated at 95 ^oC for 4 hours. After 4 hours β-FeOOH was formed on both sides of the glass. The back side of the glass (non conducting side) was thoroughly cleaned to remove the β-FeOOH and the front side was gently rinsed to remove only the excess β-FeOOH. The films were dried in air and then heated in a muffle furnace in air at 550 ^oC for 2 hours to convert β-FeOOH into α-Fe_2O_3. The films were then heated a second time at 500 ^oC or 700 ^oC to incorporate Sn from the FTO substrate, as a dopant.[4] A higher temperature results in a more active film, however exceeding 750 ^oC causes undesirable deformation and cracking of the glass susbtrate making optical studies challenging.

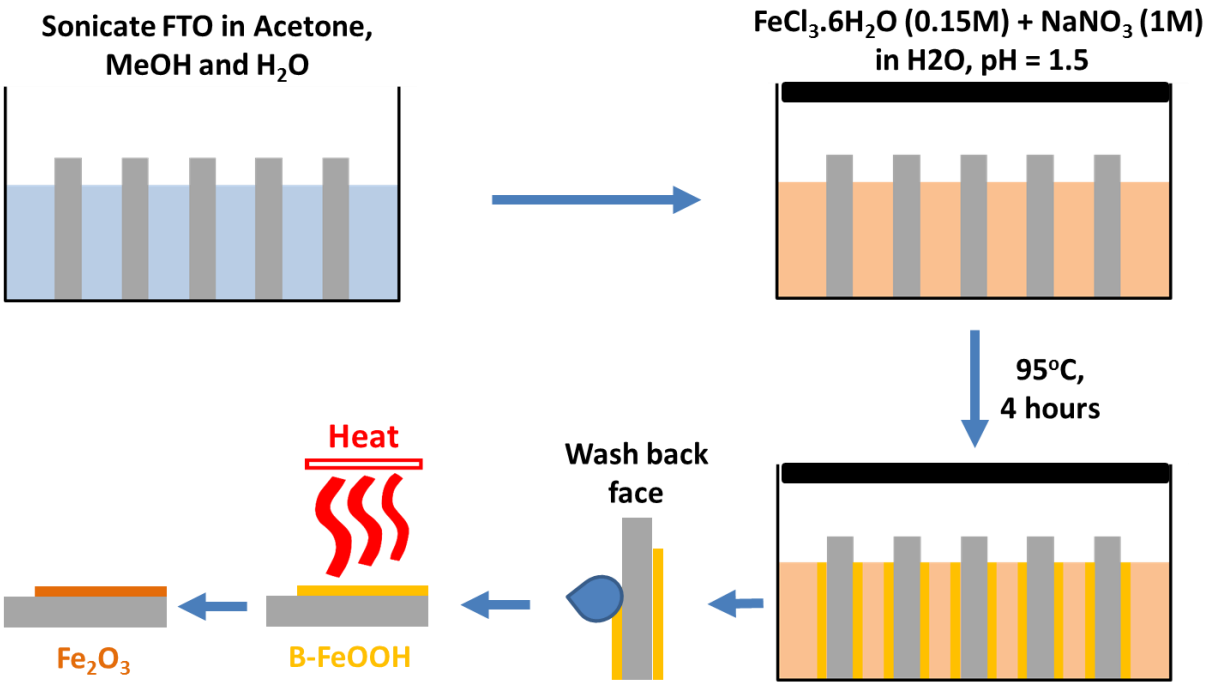

Figure 59 - Typical synthesis procedure of nanostructured α-Fe_2O_3 based on reference [4].

Figure 60 shows photographs and UV/Vis absorbance spectra of the hematite films synthesised using the method described above. The thickness of the films can be partly controlled by the length of time the FTO substrate stays immersed in the reaction vessel. 4 hours was found to provide a suitable optical thickness to produce active films but also maintain enough transmission to carry out TAS measurements. The absorbance spectra are consistent with that of a typical hematite absorbance.[19] The inset in Figure 60 shows two typical films obtained with the described synthesis procedure. The film on the left had a final annealing temperature of 700 °C, and the films from this batch are codenamed HT-Fe_2O_3. The film on the right has a final annealing temperature of 500 °C, and films from this batch are codenamed LT-Fe_2O_3. The annealing temperature can be significant as higher temperatures typically result in films with higher activity, due to increased levels of Sn migration from the FTO[4] and possibly the removal of some surface states responsible for Fermi level pinning.[20]

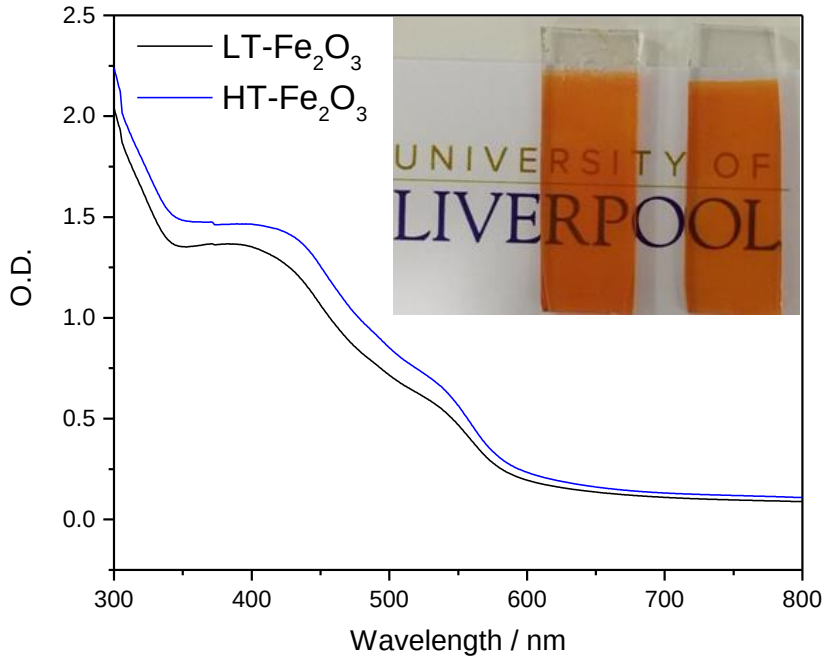

Figure 60 - UV-Vis spectra of (a) HT-Fe_2O_3 and (b) LT-Fe_2O_3 recorded directly in absorbance mode. Inset: Photographs of hematite films, HT-Fe_2O_3 annealed in air at 700 °C on the left and LT-Fe_2O_3 annealed in air at 500 °C on the right.

SEM imaging shows the nanostructure of HT-Fe_2O_3 and LT-Fe_2O_3, Figure 61. The images reveal a uniform distribution of nanorods with typical approximate dimensions of 80 nm wide and 350 nm long as measured by the SEM ruler software. No visible structural change was observed at elevated temperatures.

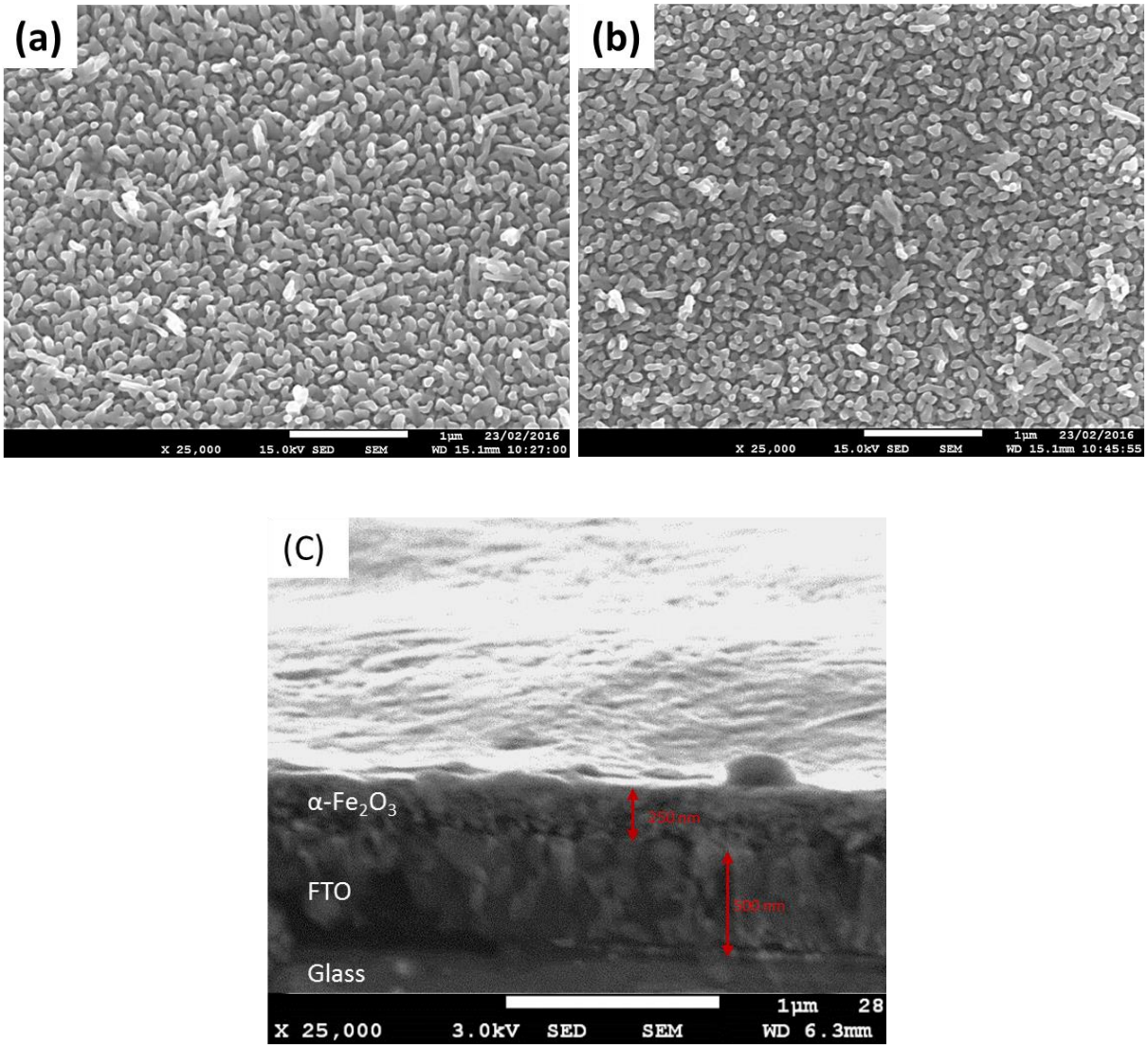

Figure 61 – SEM images of the nanostructured hematite films; (a) HT-Fe_2O_3 and (b) LT-Fe_2O_3. (c) Side on view of HT-Fe_2O_3.

In order to help confirm that the films were indeed hematite, XRD was carried out on a selection of HT-Fe_2O_3 and LT-Fe_2O_3 films following the synthesis, Figure 62. The SnO_2 peaks due to the glass substrate are marked with blue stars and hematite peaks are labelled with orange arrows. The peaks were identified using FullProf software. These XRD measurements were carried out on the hematite thin films deposited onto the FTO substrate. Shifts in peaks from the standard powder diffraction pattern can be expected in a thin layer, with peaks in a typical θ-2theta scan shifting to higher angles due to tensile stress.[21]

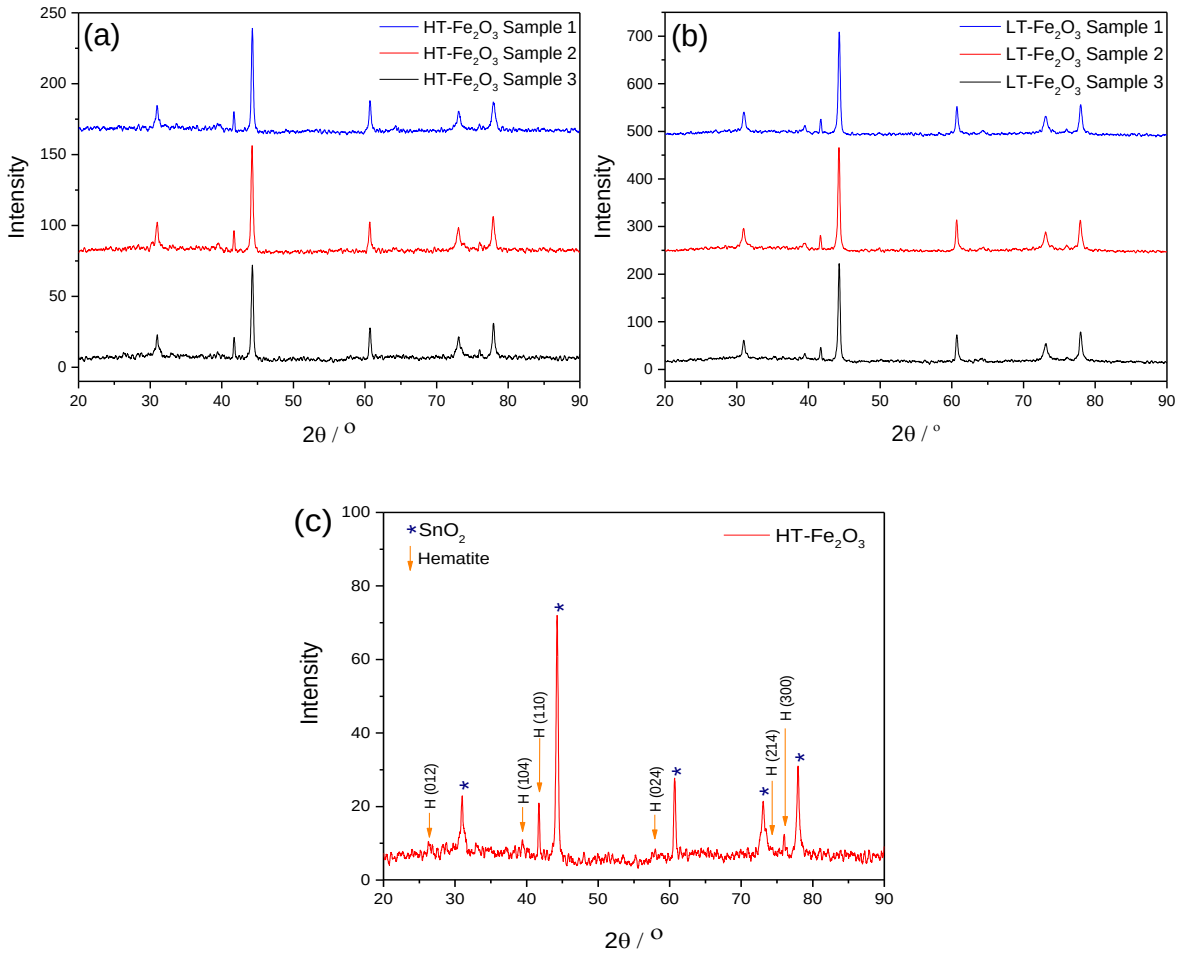

Figure 62 - XRD patterns of the nanostructured hematite films, (a) HT-Fe_2O_3 and (b) LT-Fe_2O_3. (c) Shows the assigned peaks for one of these XRD patterns. The blue stars indicate the peaks assigned to SnO_2 present in the glass substrate and the orange arrows indicate the hematite peaks. Diffraction patterns were recorded on a Panalytical X'Pert PRO HTS X-Ray Diffractometer from 20 to 90° 2 theta with a step size of 0.017° at 1.6° per minute.

Once the α-Fe_2O_3 films had been synthesised and characterised, Ta_2O_5 was deposited onto HT-Fe_2O_3 and LT-Fe_2O_3 using the same ALD method as above. No significant change in absorbance in the range 300-800 nm was observed for either set of films (Figure 63), consistent with the control test of Ta_2O_5 deposited onto FTO glass.

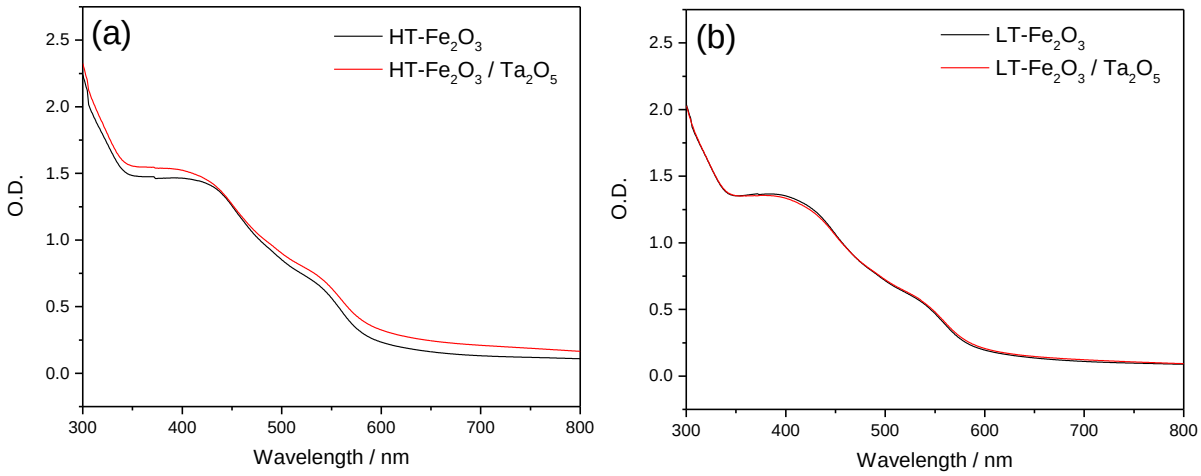

Figure 63 - UV-Vis spectra of (a) HT-Fe_2O_3 and (b) LT-Fe_2O_3 with and without a 2 nm Ta_2O_5 overlayer, recorded directly in absorbance mode.

Figure 64 shows SEM images of the nanostructured HT-Fe_2O_3 film before and after ALD of a ~2 nm Ta_2O_5 overlayer. Although a ~2 nm layer is beyond the resolution of this measurement, the images are useful in that they indicate no unforeseen change to the nanostructure occurred following the deposition process.

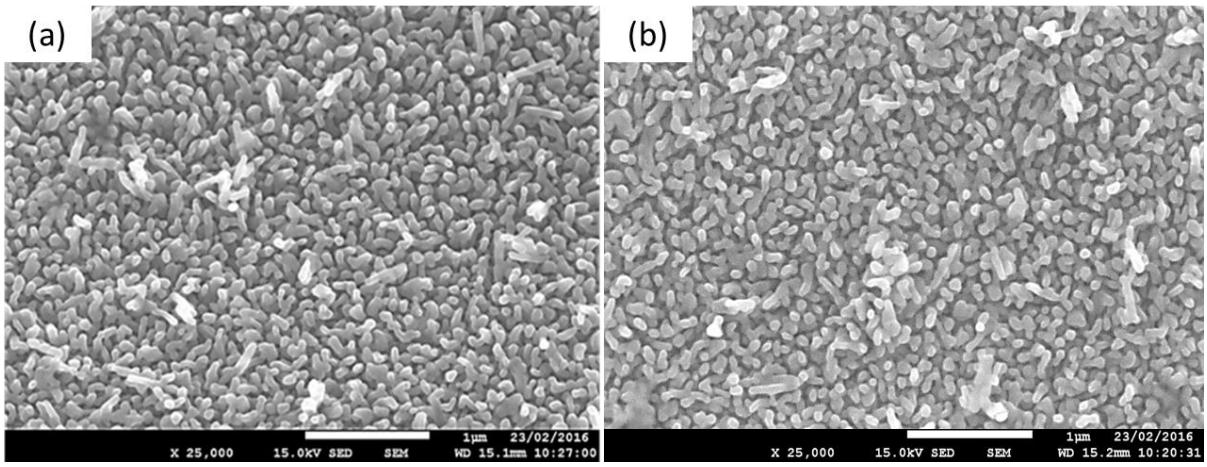

Figure 64 - SEM image of a nanostructured hematite film (a) HT-Fe_2O_3 and (b) HT-Fe_2O_3 following the deposition of a 2 nm Ta_2O_5 overlayer using ALD.

There was also no noticeable change in the XRD spectra following Ta_2O_5 deposition, Figure 65. The lack of Ta_2O_5 peaks in α-Fe_2O_{3-x}/Ta_2O_5 can be explained by the very thin nature of the Ta_2O_5 and also the likely amorphous nature of Ta_2O_5 which is expected at a deposition temperature of 200 ^oC.[18] Because amorphous materials do not possess crystal periodicity, the random distribution of atoms causes random X-ray scattering and therefore ill-defined XRD peaks.[21]

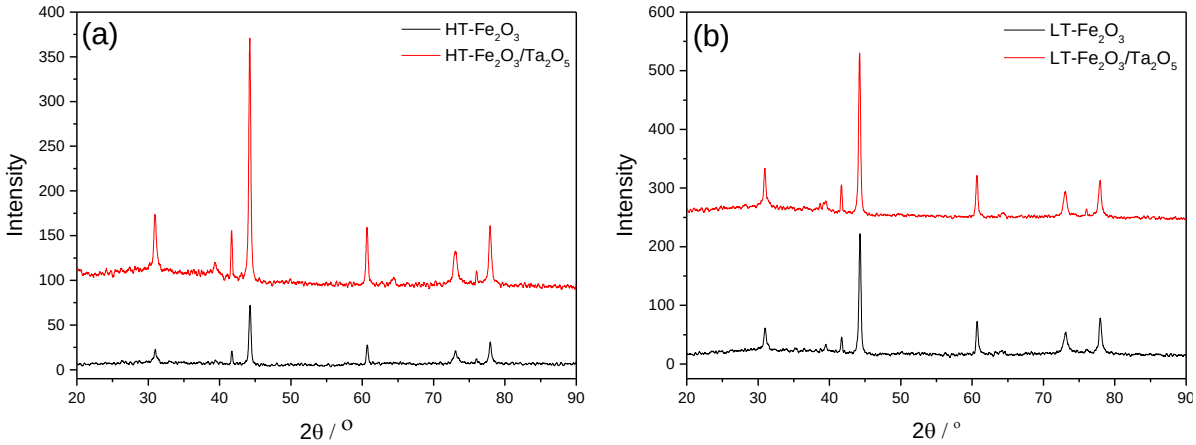

Figure 65 - XRD patterns of (a) HT-Fe_2O_3 before and after Ta_2O_5 deposition and (b) LT-Fe_2O_3 before and after Ta_2O_5 deposition. Diffraction patterns were recorded on a Panalytical X'Pert PRO HTS X-Ray Diffractometer from 20 to 90° 2 theta with a step size of 0.017° at 1.6° per minute.

In section 3.3.2 the addition of Ta_2O_5 to FTO glass appeared to cathodically shift the onset potential of dark electrocatalytic water oxidation, Figure 56. Figure 66 shows linear sweep voltammograms measured in the dark for HT-Fe_2O_3 and LT-Fe_2O_3 with and without Ta_2O_5. This time the addition of Ta_2O_5 shifts the dark onset potential anodically, indicating that the hematite surface has become less catalytic as would be expected following the addition of an inert insulating overlayer. This same anodic shift was also observed following the addition of Al_2O_3 in chapter 2.

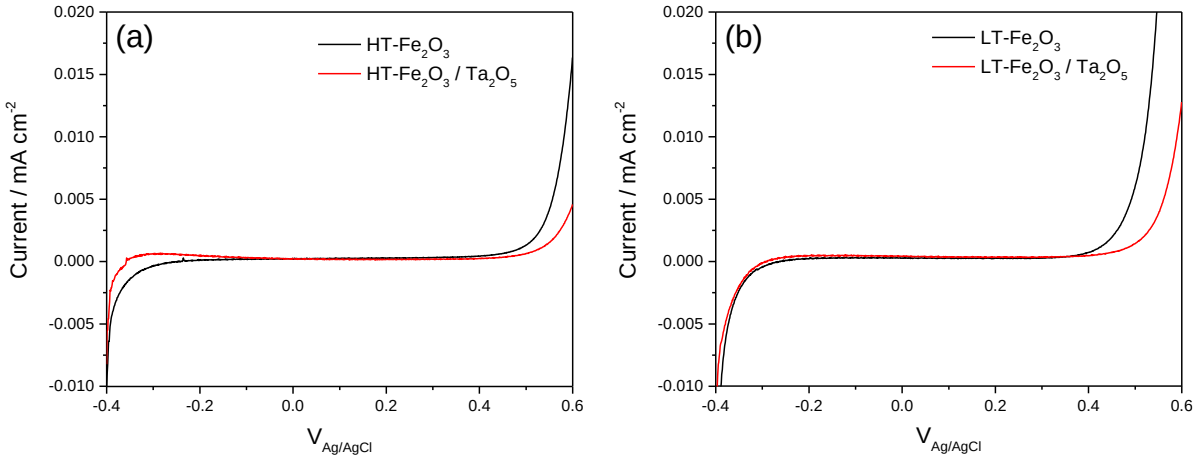

Figure 66 - Linear sweep voltammograms of (a) HT-Fe_2O_3 and (b) LT-Fe_2O_3 with and without Ta_2O_5. Scans were carried out at 10 mV s^{-1} in the dark.

As these samples were prepared in house it was possible to carry out an extensive investigation into the effect of Ta_2O_5 as a function of thickness. Figure 67 shows the effect of Ta_2O_5 on the photocurrent of HT-Fe_2O_3 and LT-Fe_2O_3 at different Ta_2O_5 overlayer thicknesses.

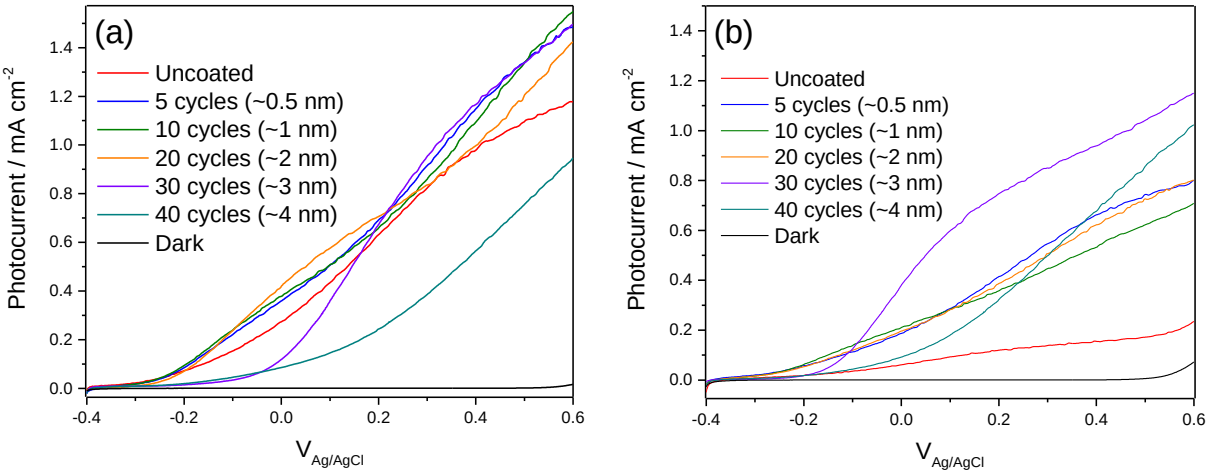

Figure 67 - Linear sweep photocurrents of (a) HT-Fe_2O_3 and (b) LT-Fe_2O_3 with various Ta_2O_5 thicknesses. Scans were carried out at 10 mV s^{-1} under 100 mWcm^{-2} white light illumination.

When Al_2O_3 is deposited onto hematite it typically results in a cathodic shift in the photocurrent onset potential. This shift is proposed to be due to passivation of trap states at the surface which would otherwise cause surface pinning thereby hindering band bending or the formation of a depletion layer within the semiconductor.[2,22] In contrast to Al_2O_3, the primary effect of Ta_2O_5 appears to be to increase the photocurrent magnitude. For HT-Fe_2O_3 a small increase in photocurrent is observed for 0.5, 1 and 2 nm layers. At a thickness of 3 nm the onset potential appears to shift anodically in addition to the increased photocurrent magnitude. At 4 nm, the onset potential remains anodically shifted, and additionally, a large drop in the photocurrent maximum occurs. A similar trend is observed for LT-Fe_2O_3. Due to the lower final annealing temperature of LT-Fe_2O_3, the initial activity is much lower than that of HT-Fe_2O_3 prior to Ta_2O_5 deposition. Following ALD the increase in photocurrent of LT-Fe_2O_3 at thicknesses of 0.5, 1 and 2 nm is much more pronounced. Additionally, a small cathodic shift in onset potential is observed for LT-Fe_2O_3 at Ta_2O_5 thicknesses of 0.5, 1 and 2 nm. 3 nm of Ta_2O_5 anodically shifts the onset potential back, however it also further increases the maximum photocurrent. Finally, consistent with HT-Fe_2O_3, 4 nm of Ta_2O_5 leads to a noticeable decrease in activity of LT-Fe_2O_3 compared to the other overlayer thicknesses. A summary of these photocurrent plots as a function of Ta_2O_5 thickness is presented in Figure 68.

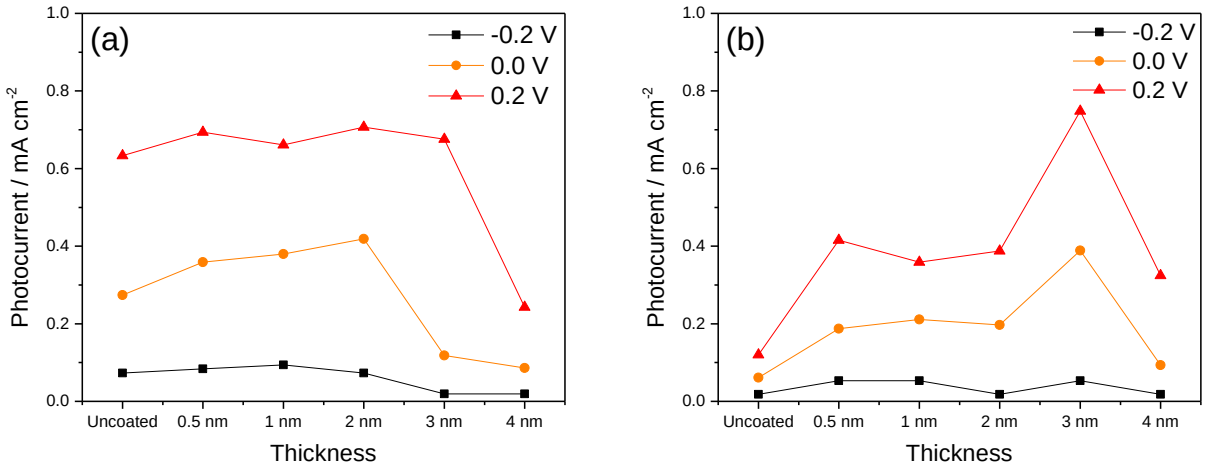

Figure 68 - Photocurrent of (a) HT-Fe_2O_3 and (b) LT-Fe_2O_3 as a function of Ta_2O_5 thickness and a function of applied bias. The steady state currents were measured under 100 mW cm^{-2} white light illumination.

It is proposed that an optimum overlayer thickness must strike a balance between being thick enough to sufficiently passivate surface traps whilst remaining thin enough so as not to deactivate the hematite surface. The photocurrents in Figure 67 suggest an optimum thickness lies somewhere between 1-3 nm. It should be noted at this stage that the precise mechanism of water oxidation at a hematite surface or at a hematite/overlayer surface is not well understood and as a consequence it is difficult to pinpoint the precise mechanism of deactivation with thick overlayers. The assumption made in chapter 2 was that a sufficiently thin overlayer allows hole tunnelling transfer from the α-Fe_2O_3 to the electrolyte, and once a certain overlayer thickness is reached this tunnelling is no longer possible. Equations 1 and 2[23] describe the tunnelling probability (*T*), and how it is exponentially dependent on the width of the barrier (*L*) and the constant, k. k represents the difference between the particle kinetic energy (*E*) and the barrier potential energy/height (*u*), where *m* is the mass of the particle and $\hbar$ is the reduced Planck's constant (1.05457×10^{-34} J s).

$$T = e^{-2kL} \qquad (1)$$

$$k = \frac{\sqrt{2m(u-E)}}{\hbar} \qquad (2)$$

An alternative explanation is that rather than charges tunnelling through the overlayer, they accumulate near cracks/gaps in the overlayer where exposed hematite surface is present. This theory has recently been explored by Caspary Toroker *et al.*[6] In addition, recent work by Grätzel *et al.*[10] explored the role of Ga_2O_3 as an overlayer were they too reached the conclusion that an exposed hematite surface was required and they used a heat treatment to intentionally

crack the overlayer surface. It is not clear at this stage which, if either of these mechanisms is accurate, or whether it depends on the overlayer material.

We now address the effect Ta_2O_5 has on the electron/hole dynamics of HT-Fe_2O_3 and LT-Fe_2O_3 as probed by TAS. As discussed in chapter 2, TAS for hematite electrodes is well documented in the literature. To recap the previous chapter, there are two key features when probing hematite in the visible/NIR (400-950 nm) region. Firstly, a broad positive feature is observed, which often spans from ~500-900 nm (although it is usually reported to be >600 nm with a maximum at *ca.* 650 nm). This feature has been observed in numerous types of hematite photoelectrodes and is assigned to photoholes.[2,24–26] The second TA feature is a sharp positive feature centred at *ca.* 575 nm which quickly inverts into a bleach (decrease in optical density) on fs timescales; the magnitude of this bleach increases with increasing positive bias. This feature has been proposed to be due to localised trap states close to the band edge, possibly related to the presence of oxygen vacancies.

The 575 nm feature measured by TAS was investigated as a function of Ta_2O_5 thickness under working photoelectrochemical conditions at an applied bias of 0.4 $V_{Ag/AgCl}$ (pH ~13.7), Figure 69. Unfortunately, the overlap of the broad hole signal (~500-900 nm) with the 575 nm bleach becomes more significant in these films compared to the previously studied α-Fe_2O_{3-x} films, making fitting the data challenging.

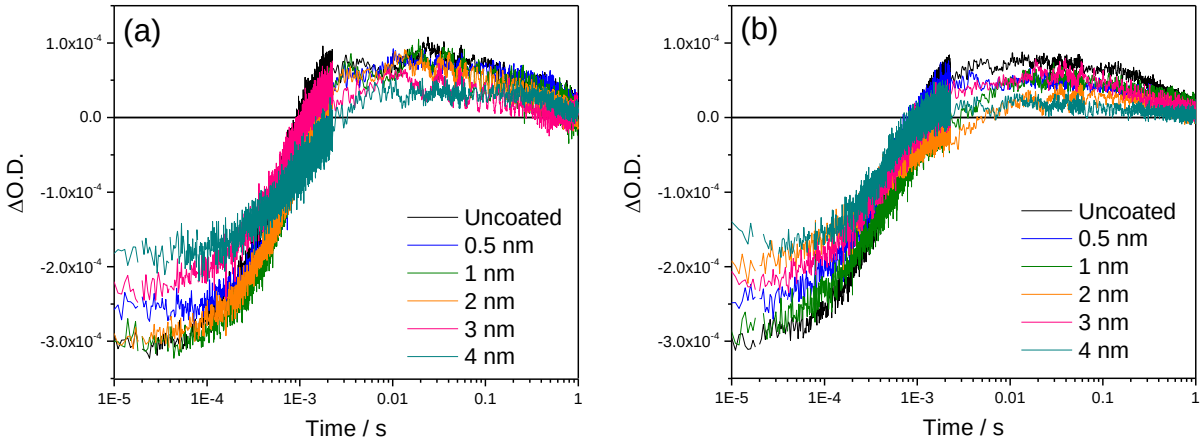

Figure 69 -Microsecond TAS kinetics probed at 575 nm following 355 nm laser excitation (~100 μJ cm^{-2}) for (a) HT-Fe_2O_3 and (b) LT-Fe_2O_3 with a range of Ta_2O_5 thicknesses. Measurements were carried out in a photoelectrochemical cell at an applied bias of 0.4 $V_{Ag/AgCl}$ (pH ~13.7).

In chapter 2, Al_2O_3 reduced the lifetime of the 575 nm TAS bleach (increased the electron de-trapping rate). Following the addition of Ta_2O_5 to HT-Fe_2O_3 and LT-Fe_2O_3 studied here, a reduced lifetime of the 575 nm bleach is also observed. Additionally and most noticeably a reduction in the magnitude of the 575 nm bleach also occurs. Both sets of films show a general trend in which the magnitude of the 575 nm bleach signal is reduced as the thickness of the overlayer is increased. At a thickness of 4 nm the magnitude drops by *ca.* 50%. The magnitude of the hole signal as seen by the positive feature overlapping on slow ms-s timescales also reduces as thickness is increased. For clarity, Figure 70 and Figure 71 show TAS of LT-Fe_2O_3 probed at 575 nm and 650 nm, with and without a 3 nm Ta_2O_5 overlayer, where a maximum in photocurrent enhancement is observed, and with and without a 4 nm Ta_2O_5 overlayer, where photoactivity begins to fall. This part of the study focuses on LT-Fe_2O_3 as this film showed the most significant change following Ta_2O_5 deposition.

Due to overlap with the broad hole signal it is difficult to accurately fit the 575 nm bleach and as a result these fitting parameters are tentative. Firstly we fit the electron de-trapping signal probed at 575 nm. Only the 575 nm decay is fitted (10 μs – 0.1 s) in order to limit complications

with the hole overlap on slow timescales (> 0.1 s). LT-Fe_2O_3 (uncoated) is found to fit to a bi-exponential decay with decay rates of ~1649±12 s^{-1} and ~190±80 s^{-1} using equation 3:

$$\Delta OD_{575}(t) = A_1 e^{-(k_1 t)} + A_2 e^{-(k_2 t)} + y_0 \quad (3)$$

Following the deposition of Ta_2O_5, the 575 nm decays fit well to single exponentials of the form shown in equation 4:

$$\Delta OD_{575}(t) = A_1 e^{-(k_1 t)} + y_0 \quad (4)$$

LT-Fe_2O_3 with a 3 nm overlayer is found to fit to a single exponential decay with a decay rate of ~2010±11 s^{-1} (Figure 70a). LT-Fe_2O_3 with a 4 nm overlayer is also found to fit to a single exponential decay with a decay rate of ~2100±20 s^{-1} (Figure 71a).

Now we fit the hole decay dynamics probed at 650 nm. All hole decay traces are found to fit well to the bi-exponential decay shown in equation 5:

$$\Delta OD_{650}(t) = A_1 e^{-(k_1 t)} + A_2 e^{-(k_2 t)} + y_0 \quad (5)$$

LT-Fe_2O_3 (uncoated) is found to fit to a bi-exponential decay with decay rates of ~430±6 s^{-1} and ~0.50±0.04 s^{-1}. LT-Fe_2O_3 with a 3 nm overlayer is found to fit to a bi-exponential decay, with decay rates of ~415±5 s^{-1} and ~2.04±0.04 s^{-1} (Figure 70b). LT-Fe_2O_3 with a 4 nm overlayer

is found to fit to a bi-exponential decay, with decay rates of ~795±10 s^{-1} and ~3.39±0.11 s^{-1} (Figure 71b).

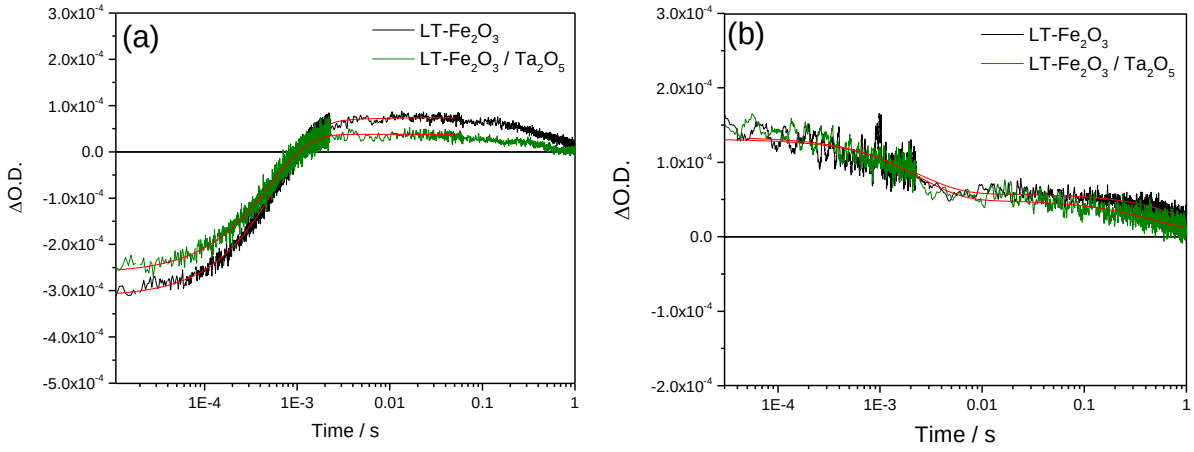

Figure 70 - (a) Microsecond TAS kinetics probed at 575 nm following 355 nm laser excitation (~100 μJ cm^{-2}) for LT-Fe_2O_3 with/without a 3 nm layer of Ta_2O_5 and (b) Microsecond TAS kinetics probed at 650 nm following 355 nm laser excitation (~100 μJ cm^{-2}) for LT-Fe_2O_3 with/without a 3 nm layer of Ta_2O_5. Measurements were carried out in a photoelectrochemical cell at an applied bias of 0.4 $V_{Ag/AgCl}$ (pH ~13.7).

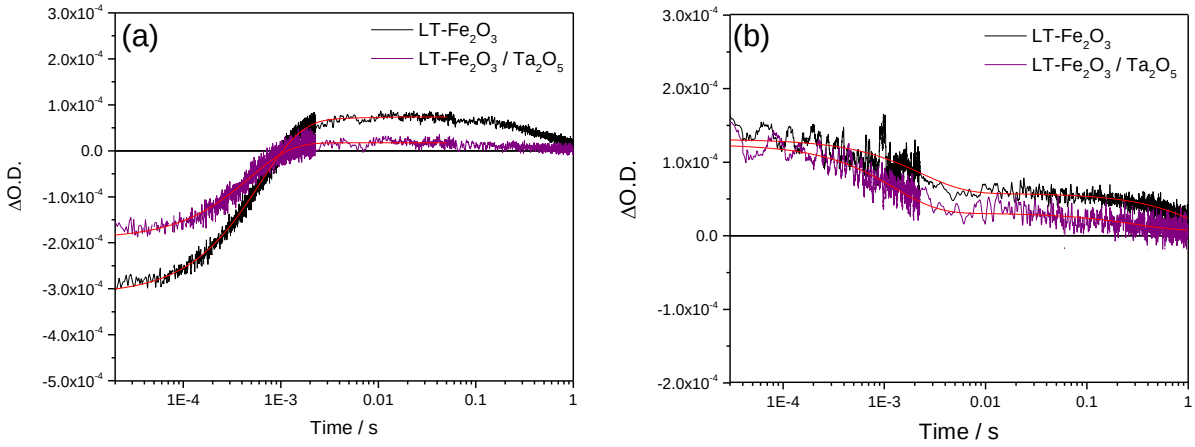

Figure 71 - (a) Microsecond TAS kinetics probed at 575 nm following 355 nm laser excitation (~100 μJ cm^{-2}) for LT-Fe_2O_3 with/without a 4 nm layer of Ta_2O_5 and (b) Microsecond TAS kinetics probed at 650 nm following 355 nm laser excitation (~100 μJ cm^{-2}) for LT-Fe_2O_3 with/without a 4 nm layer of Ta_2O_5. Measurements were carried out in a photoelectrochemical cell at an applied bias of 0.4 $V_{Ag/AgCl}$ (pH ~13.7).

Full fitting parameters from Figure 70 and Figure 71 are shown in Table 7.

Name	Magnitude	Lifetime (s)	Rate (s^{-1})
(575 nm) LT-Fe_2O_3	A_1: (-3.80±0.02)x10^{-4}	τ_1: (6.0±0.1)x10^{-4}	k_1: 1649±12
	A_2: (-6.94±1.61)x10^{-6}	τ_2: (5.3±2.4)x10^{-3}	k_2: 190±80
(575 nm) LT-Fe_2O_3/3 nm Ta_2O_5	A_1: (-3.00±0.01)x10^{-4}	τ_1: (4.97±0.03)x10^{-4}	k_1: 2010±11
575 nm) LT-Fe_2O_3/4 nm Ta_2O_5	A_1: (-2.09±0.01)x10^{-4}	τ_1: (4.75±0.04)x10^{-4}	k_1: 2100±20
(650 nm) LT-Fe_2O_3	A_1: (7.34±0.04)x10^{-5}	τ_1: (2.33±0.03)x10^{-3}	k_1: 430±6
	A_2: (8.7±0.6)x10^{-5}	τ_2: 2.0±0.2	k_2: 0.50±0.04
(650 nm) LT-Fe_2O_3/3 nm Ta_2O_5	A_1: (2.38±0.02)x10^{-4}	τ_1: (2.41±0.03)x10^{-3}	k_1: 415±5
	A_2: (4.32±0.02)x10^{-5}	τ_2: 0.49±0.01	k_2: 2.04±0.04
(650 nm) LT-Fe_2O_3/4 nm Ta_2O_5	A_1: (9.34±0.06)x10^{-5}	τ_1: (1.26±0.02)x10^{-3}	k_1: 795±10
	A_2: (2.40±0.02)x10^{-5}	τ_2: 0.30±0.01	k_2: 3.39±0.11

Table 7 – Full fitting parameters from Figure 70 and Figure 71.

In light of these results and taking into account the conclusions reached in chapter 2, it is possible that initially, two populations of trap states (as indicated by the bi-exponential fit) are present in LT-Fe_2O_3 leading to increased trap-mediated recombination with holes accumulating at the surface. This may lead to a slow water oxidation rate (rate ~0.50±0.04 s^{-1}) and therefore a poor photocurrent. The bi-exponential decay suggests two distinct populations of trapped electrons as one population decaying by two (or more) pathways should show only a single k_{obs} which is the sum of the rate constants of all competing paths as shown in Figure 72.

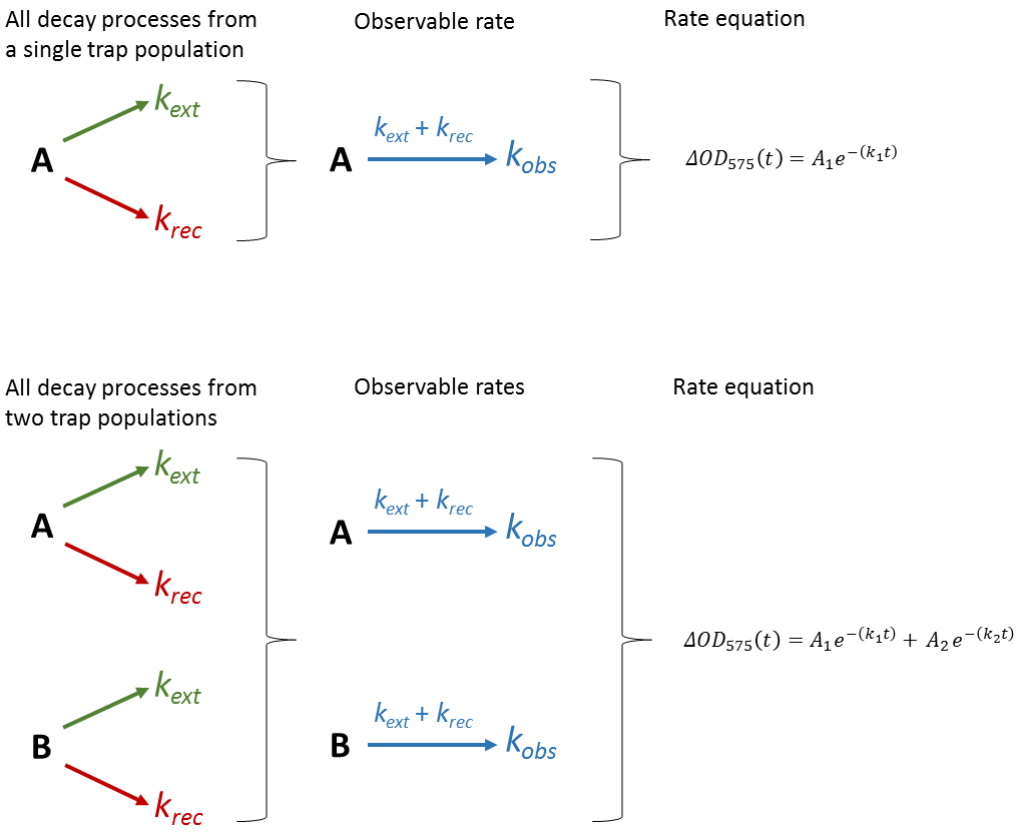

Figure 72 - Decay processes for a single trap population and two trap populations and how these rates are observed. A single trap population should have one observable decay rate. Two trap populations should show two separate observable rates (unless the decay pathways for both populations are identical). A and B represent the trap populations, k_{ext} is the rate for electron extraction, k_{rec} is the rate for recombination and k_{obs} is the observable rate.

Following the deposition of Ta_2O_5, one of these trap state populations is passivated (now a single exponential fit) resulting in decreased electron trap recombination with surface accumulated holes and therefore a more efficient water oxidation rate (rate = 3.39±0.11 s^{-1}). However, there is also a reduction in the overall magnitude of the positive signal assigned to holes, particularly with thicker layers. This suggests that Ta_2O_5 is inhibiting/deactivating parts of the hematite surface and reducing the total number of holes accumulating as oxidised species. Interestingly the photocurrent at an overlayer thickness of 3 nm is improved even though the hole signal is reduced. This could be due to the remaining hole population being concentrated on a small area (such as exposed hematite due to cracks in the Ta_2O_5 overlayer)

which leads to an increased hole reaction rate. This would be in line with the findings discussed above related to cracks and gaps in overlayers.[6,10] The photocurrent begins to noticeably decrease once the Ta_2O_5 thickness goes beyond 4 nm and can be rationalised by a further reduction in exposed hematite leading to too much of the active photoelectrode surface being inhibited. This rationale could explain why an optimum layer thickness of 1-3 nm is often observed. It is noted that the films with larger photocurrents do not have noticeably larger hole signals as probed by TAS in these measurements, which further indicates that the overall yield of holes is less significant than the rate/pathway in which these holes transfer to the electrolyte. To summarise, the deposition of Ta_2O_5 of optimum thickness passivates a portion of surface/near surface electron trap states. Additionally, it deactivates some of the hematite surface, however it facilitates improved hole transfer to the remaining surface due to passivation of electron trap states. When the insulating Ta_2O_5 overlayer becomes too thick, deactivation of the hematite surface begins to dominate resulting in a decrease in photocurrent. The reduction of surface active species as the overlayer thickness is increased is further evidenced in section 3.3.5 below which uses cyclic voltammetry to probe the yield of hole trapping surface species thought to exist in the form of a water oxidation intermediate. This will be discussed later.

In order to obtain a broader understanding of the effects of Ta_2O_5, and more precisely the nature/location of the trap states responsible for the 575 nm feature as a continuation of chapter 2, the next section reports the deposition of Ta_2O_5 onto α-Fe_2O_{3-x} films.

3.3.4 The effect of Ta_2O_5 overlayers on α-Fe_2O_{3-x} (oxygen deficient) films

Once Ta_2O_5 had been confirmed as a stable overlayer with the ability to alter the photocurrent and TA kinetics of a common type of Sn-hematite films (3.3.3), it was deposited onto a set of α-Fe_2O_{3-x} films with the aim of furthering the conclusions reached in chapter 2 and section 3.3.3. For this part of the study fresh α-Fe_2O_{3-x} (oxygen deficient hematite) films were prepared by our collaborators, Li *et al.* as previously described in chapter 2.[2,27,28]

The prepared α-Fe_2O_{3-x} films were each chopped in half to create pairs; the first halves were kept as reference samples while the second halves were coated with Ta_2O_5. Ta_2O_5 layers were deposited by ALD at a process temperature of 200 ^oC with a target thickness of ~2 nm (20 ALD cycles). In light of the previous Al_2O_3 study in chapter 2, and the thickness study in section 3.3.3 above, a thickness of ~ 2 nm was selected as it was expected to provide a reasonable surface coverage for trap passivation whilst remaining thin enough so as not to 'deactivate' the hematite surface and reduce the photocurrent.

The α-Fe_2O_{3-x} films were characterised by UV-Vis absorbance, XRD and SEM to ascertain whether Ta_2O_5 deposition had any noticeable effect. UV-Vis absorbance spectra in the region of 350 – 800 nm (Figure 73) showed no change following the addition of Ta_2O_5, as expected for a semiconductor with such a wide band gap.

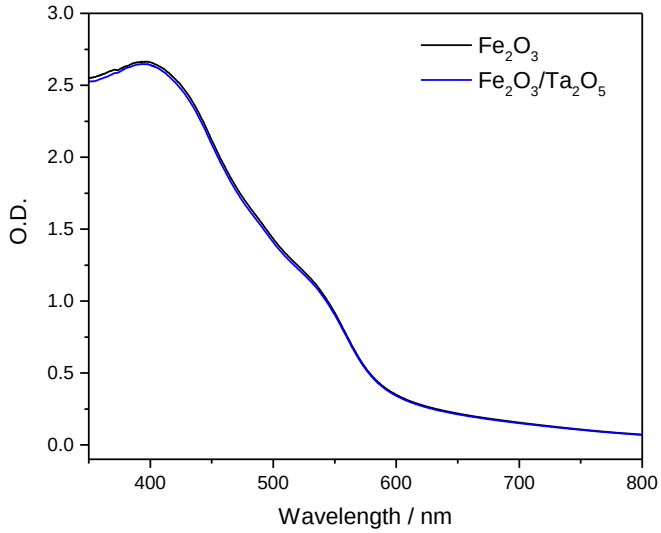

Figure 73 - UV-Vis spectra of α-Fe_2O_{3-x} and α-Fe_2O_{3-x}/Ta_2O_5 films recorded in absorbance mode.

Consistent with the previous section there was also no noticeable change in the XRD spectra following Ta_2O_5 deposition, Figure 74. The lack of Ta_2O_5 peaks in α-Fe_2O_{3-x}/Ta_2O_5 can again be explained by the very thin nature of the Ta_2O_5 and also the likely amorphous nature of Ta_2O_5 which is expected at a deposition temperature of 200 ºC.[18]

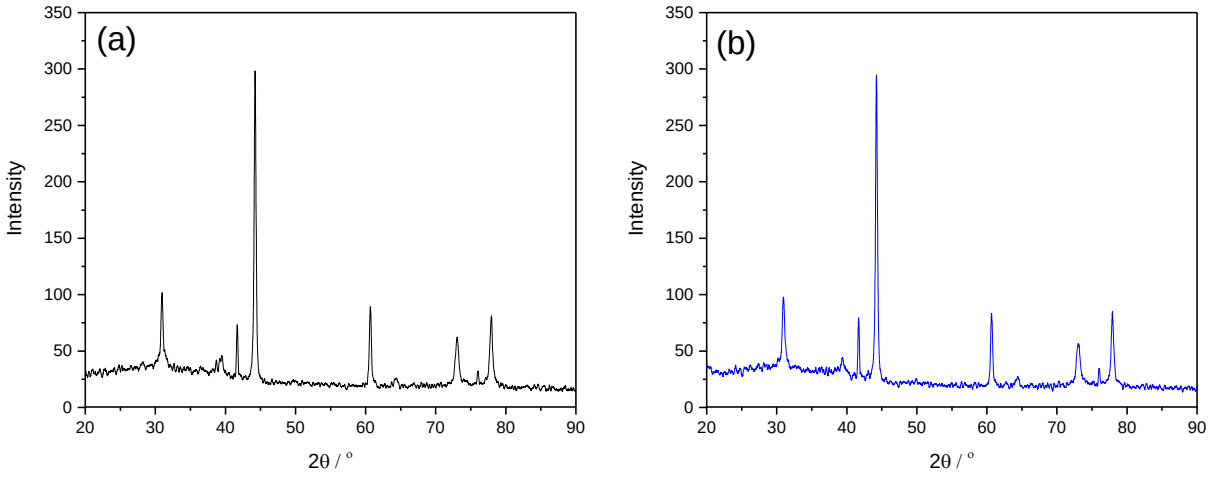

Figure 74 - XRD patterns of (a) α-Fe_2O_{3-x} and (b) α-Fe_2O_{3-x}/Ta_2O_5. Diffraction patterns were recorded on a Panalytical X'Pert PRO HTS X-Ray Diffractometer from 20 to 90° 2 theta with a step size of 0.017° at 1.6° per minute.

Figure 75 shows SEM images of the nanostructured α-Fe_2O_{3-x} film with and without Ta_2O_5. Although a ~2 nm layer is beyond the resolution of this measurement, the images are useful in that they confirm no unforeseen change to the nanostructure occurred following the deposition process.

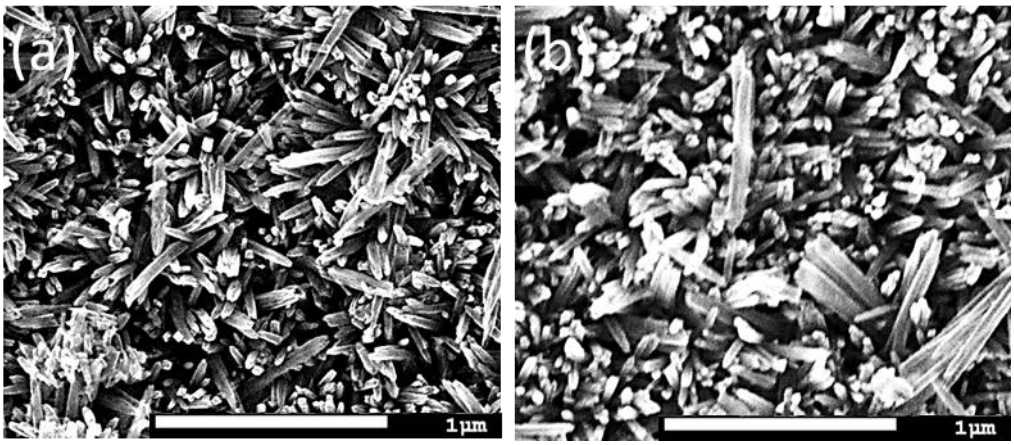

Figure 75 - SEM images of (a) α-Fe_2O_{3-x} and (b) α-Fe_2O_{3-x} / Ta_2O_5.

In an attempt to identify Ta_2O_5 on the surface of α-Fe_2O_{3-x}, STEM and elemental mapping were carried out. These measurements were kindly carried out by Karl Dawson at the NiCaL facility, Liverpool. Figure 76a shows STEM of α-Fe_2O_{3-x} with a 2 nm Ta_2O_5 overlayer (up-side down) and Figure 76b shows the elemental mapping of this image. Unfortunately, due to the thinness of the overlayer this technique was unable to reliably detect the precise location of Ta on the surface of α-Fe_2O_{3-x}, however it was confirmed to be present in small quantities. In addition to Ta and as expected, Fe and O are identified to be present using this technique. Al is also present in this film as a monolayer of trimethylaluminium (TMA) was used as a foundation layer prior to Ta_2O_5 deposition. Other elements include Sn and Si which are present in the FTO glass substrate, C which is present as a contaminant in STEM due to a carbon strap used for securing the sample (and may also exist as a contaminant on the hematite surface), Cu which is present in the grid used to hold the sample during measurements, Cr which is deposited onto samples

to enhance the resolution of the measurements and Ga which is due to the liquid Ga ion source used.

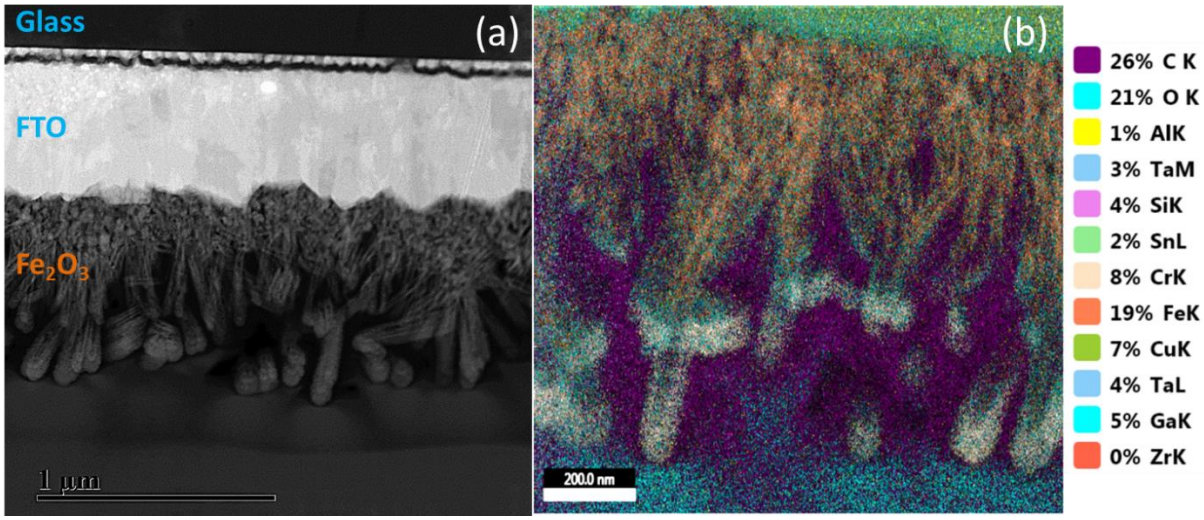

Figure 76 - (a) STEM image of α-Fe_2O_{3-x} with a 2 nm Ta_2O_5 overlayer. (b) EDS colour mapping of the hematite STEM image. The EDS image is not the same region as the STEM image.

We now turn to the effect of the Ta_2O_5 layer on the α-Fe_2O_{3-x} photoactivity and on the electron/hole dynamics as probed by TAS and TPC. Consistent with the previous findings for both Al_2O_3 and Ta_2O_5, linear sweeps of α-Fe_2O_{3-x} in the dark show a small anodic shift in the electrocatalytic oxidation onset potential of *ca.* 50 mV following Ta_2O_5 deposition, suggesting that the new α-Fe_2O_{3-x}/Ta_2O_5 surface is less catalytic than bare α-Fe_2O_{3-x} which is in line with HT-Fe_2O_3 and LT-Fe_2O_3, Figure 77a. The effect of Ta_2O_5 on α-Fe_2O_{3-x}, linear sweeps under illumination does not appear to significantly alter the photocurrent onset potential of α-Fe_2O_{3-x} and leads to a small increase in the photocurrent maximum. Although the photocurrent enhancement is small, it occurred consistently with all α-Fe_2O_{3-x} samples measured, giving confidence in the result.

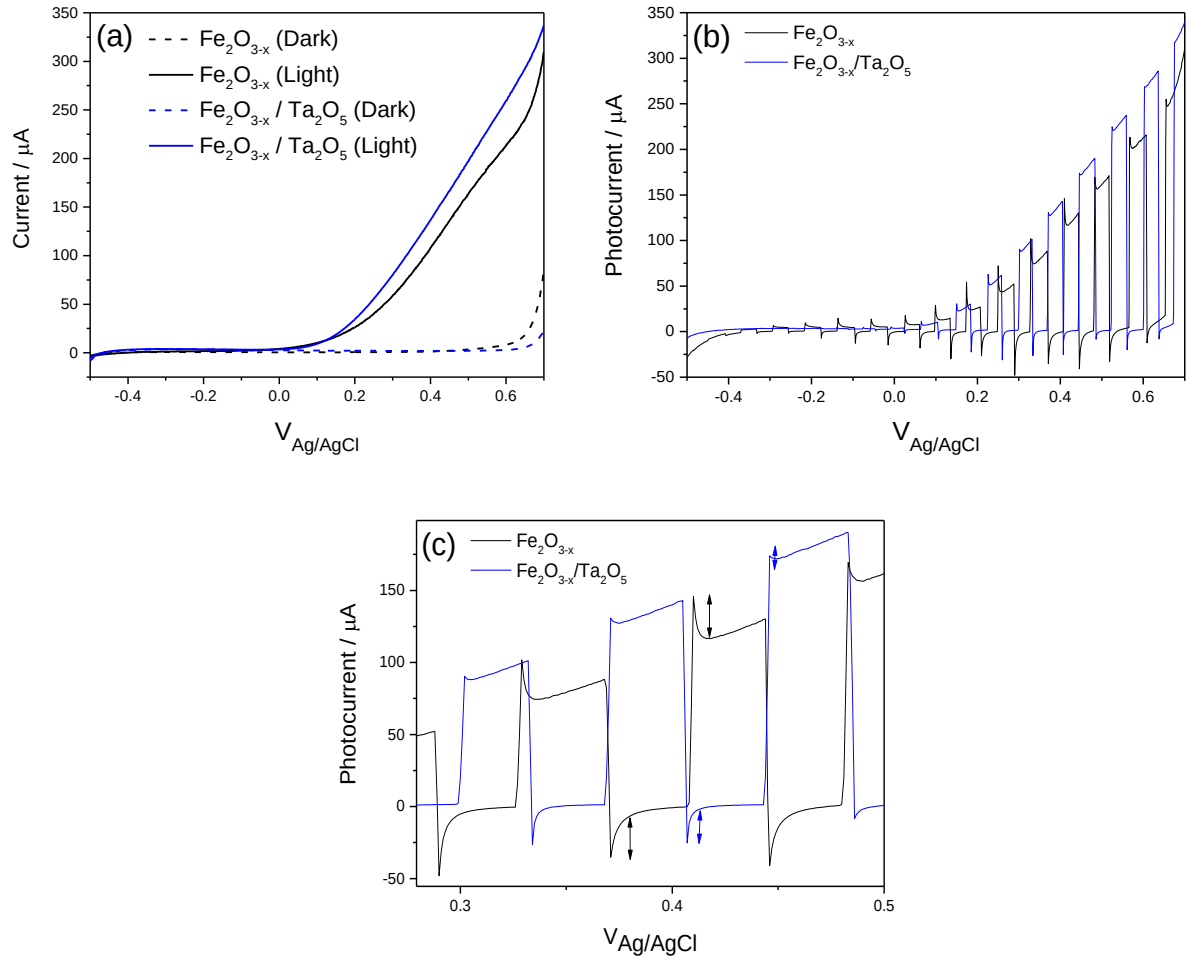

Figure 77 - (a) Linear sweep photocurrents and (b) chopped photocurrents of α-Fe_2O_{3-x} (black) and α-Fe_2O_{3-x}/Ta_2O_5 (blue) at 10 mV s^{-1} under 50 mW cm^{-2} white light illumination. (c) Photocurrent spikes from the chopped photocurrent obtained in (b).

The final point of interest in the photocurrent plots is the nature of the anodic and cathodic photocurrent spike magnitudes following Ta_2O_5 deposition, Figure 77b. These photocurrent spikes have been related to charge carrier accumulation at the interface, namely surface recombination processes which could be linked to surface trap states.[22,29] The instantaneous current when the light is switched on is a measure of the flux of holes into the surface. The subsequent decay towards the steady state current results from the capture of built-up holes in surface states inducing an electron flux associated with recombination. The cathodic current overshoot observed when the light is switched off is due to the continuing flux of electrons into

the surface as holes remaining in the surface states recombine.[30] It is therefore possible that a reduction in these photocurrent spikes can be related to an alteration of surface trap states following Ta_2O_5 deposition. Following the deposition of Ta_2O_5 onto α-Fe_2O_{3-x} both the anodic and cathodic photocurrent spikes are consistently reduced suggesting that the surface states responsible for these spikes are altered. It should be noted that this is a tentative observation, as photocurrent spikes can vary significantly between films.

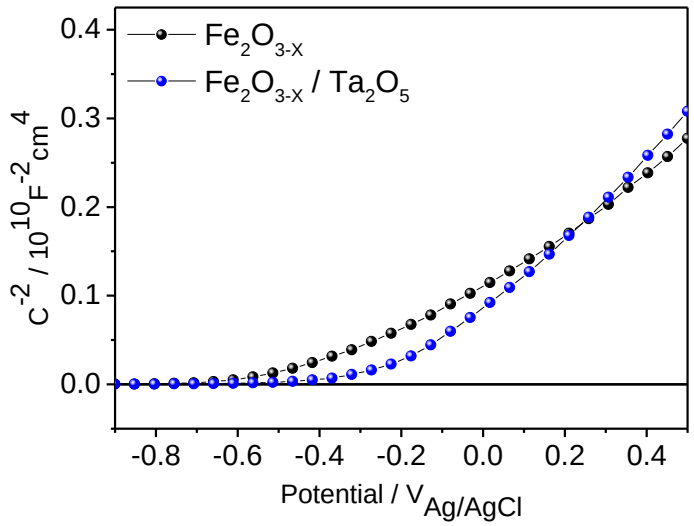

Figure 78 - Donor density of α-Fe_2O_{3-x} with and without a 2 nm Ta_2O_5 overlayer. α-Fe_2O_{3-x} has an approximate flat-band potential of -0.45 $V_{Ag/AgCl}$ (pH ~13.7) and a donor density of 6.6x10^{20} cm^{-3}. α-Fe_2O_{3-x}/Ta_2O_5 has an approximate flat-band potential of -0.3 $V_{Ag/AgCl}$ (pH ~13.7) and a donor density of 5.3x10^{20} cm^{-3}.

Mott-Schottky analysis was carried out to estimate the effect of Ta_2O_5 on the flat-band potential and donor density of α-Fe_2O_{3-x}. As mentioned in chapter 2 it should be noted that for ideal Mott-Schottky measurements a flat surface is required. A nanostructured surface such as that of α-Fe_2O_{3-x} will cause a significant degree of uncertainty, and as such, the values obtained should not be considered accurate. However, comparing two films of the same structure is expected to provide suitable data for comparison purposes. The addition of Ta_2O_5 reduces the donor density of α-Fe_2O_{3-x} slightly from 6.6x10^{20} cm^{-3} to 5.3x10^{20} cm^{-3}, a difference which is

likely within the error of the measurement. A positive shift in the measured flat-band potential also occurs following the addition of Ta_2O_5, increasing from -0.45 $V_{Ag/AgCl}$ to -0.3 $V_{Ag/AgCl}$ (pH ~13.7). This could be significant as a change in flat-band potential is likely to affect or be affected by surface states. However, it has been reported in the literature that the addition of an overlayer can cause complications with Mott-Schottky analysis.[31] While the slope of a Mott-Schottky plot (for the determination of donor density) is expected to be unaffected by the presence of an overlayer at the semiconductor/electrolyte interface, the intersection with the voltage axis (for the determination of flat-band potential) is no longer comparable to an uncoated semiconductor. So while the N_d comparison is expected to be accurate, the flat-band comparison is not. As such, although we note the change in flat-band in the data, it is not wise to further speculate whether this is a true change.

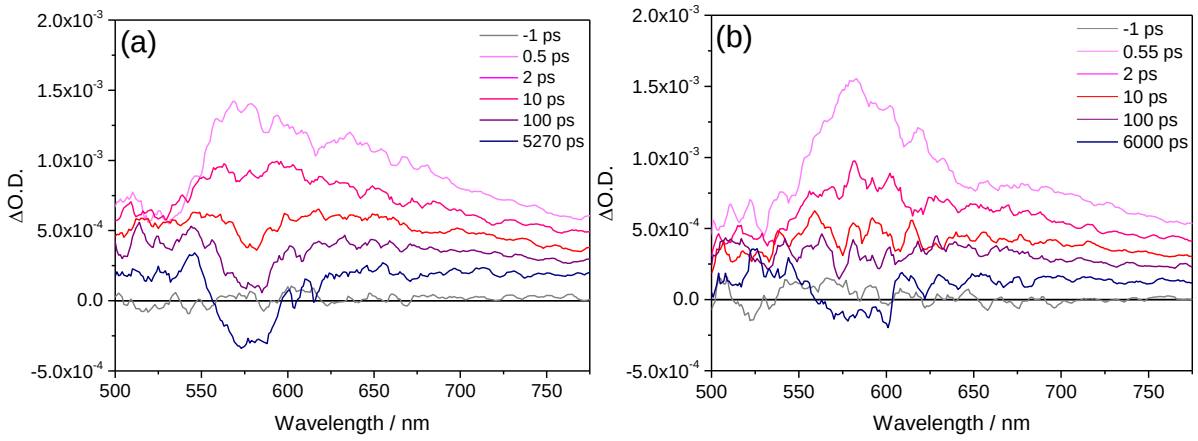

Figure 79 - Ultrafast TAS full spectra probed at 500-775 nm following 355 nm laser excitation of (a) α-Fe_2O_{3-x} and (b) α-Fe_2O_{3-x}/Ta_2O_5 in a photoelectrochemical cell at an applied bias of 0.4 $V_{Ag/AgCl}$ (pH ~13.7).

Figure 79a shows the ultrafast TAS kinetics of α-Fe_2O_{3-x} in a photoelectrochemical cell at an applied bias of 0.4 $V_{Ag/AgCl}$ (pH ~13.7) following 355 nm excitation. The spectra show the broad positive hole feature spanning the full spectral region. This hole signal is overlapped with a sharp feature centred at ~ 575 nm assigned to electron trapping and de-trapping. The

spectrum is initially dominated by the broad positive hole signal for the first few picoseconds. After 10 picoseconds the sharper feature at 575 nm begins to invert and is significantly bleached (negative) after 5 nanoseconds as electrons are trapped into oxidised trap states, in agreement with previous reports.[24] Compared to the uncoated α-Fe_2O_{3-x}, the Ta_2O_5 coated α-Fe_2O_{3-x} (Figure 79b) shows a clear decrease in the bleach at 575 nm on these ultrafast timescales indicating that photoelectron trapping has been hindered by the presence of Ta_2O_5.

Figure 80a shows the single kinetic trace probed at 575 nm for α-Fe_2O_{3-x} with and without Ta_2O_5 which shows the decrease in the extent of ultrafast trapping in the coated film. The difference in photoelectron trapping and de-trapping kinetics becomes more obvious on the slower micro-millisecond timescales, Figure 80b. Much like HT-Fe_2O_3 and LT-Fe_2O_3 in the previous section, following the addition of Ta_2O_5, α-Fe_2O_{3-x} most noticeably exhibits a significant decrease in the final magnitude of the bleach. The α-Fe_2O_{3-x} 575 nm decay fits well to a bi-exponential decay (equation 6) with decay rates of 1523±9 s^{-1} and 84±1 s^{-1}, (Figure 80b, black line). α-Fe_2O_{3-x}/Ta_2O_5 still fits to a bi exponential decay, this time with decay rates of 1752±18 s^{-1} and 144±5 s^{-1} (Figure 80b, blue line). This contrasts to the LT-Fe_2O_3 575 nm kinetics which fits to a single exponential decay following Ta_2O_5 deposition. The magnitude of both components as measured by the A coefficient of the fits is reduced in α-Fe_2O_{3-x} following Ta_2O_5 deposition, decreasing from (2.3±0.1)x10^{-4} and (1.0±0.1)x10^{-4} when uncoated to (1.51±0.01)x10^{-4} and (4.3±0.1)x10^{-5} when coated.

$$\Delta OD_{575}(t) = A_1 e^{-(k_1 t)} + A_2 e^{-(k_2 t)} + y_0 \quad (6)$$

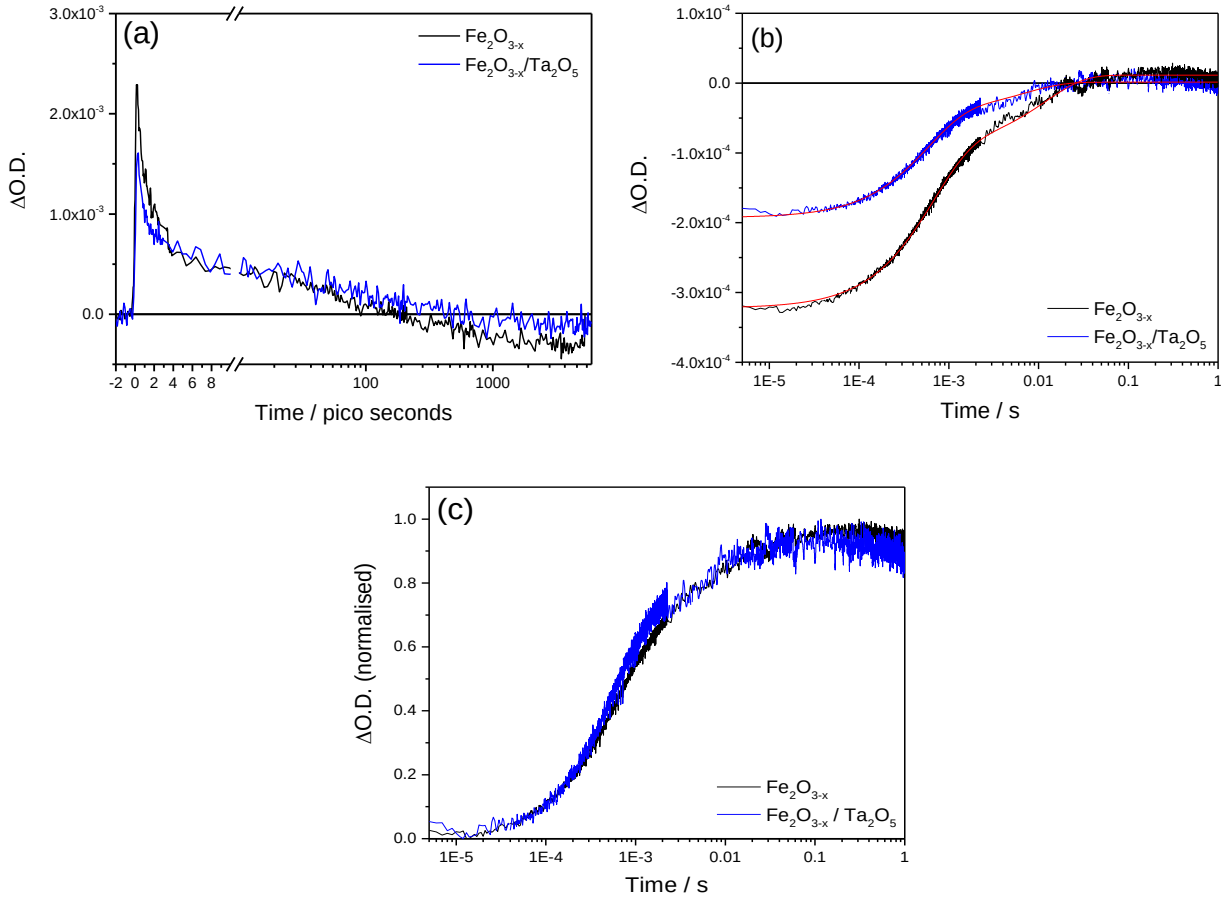

Figure 80 -(a) Ultrafast and (b) microsecond TAS kinetics probed at 575 nm following 355 nm laser excitation (~100 μJ cm^{-2}) of α-Fe_2O_{3-x} and α-Fe_2O_{3-x}/Ta_2O_5 (2 nm) in a photoelectrochemical cell at an applied bias of 0.4 $V_{Ag/AgCl}$ (pH ~13.7). (c) Normalised TAS kinetics showing that the primary change following Ta_2O_5 deposition is the magnitude and not the decay rate of the 575 nm feature.

Name	Magnitude	Lifetime (s)	Rate (s^{-1})
(575 nm) α-Fe_2O_{3-x}	A_1: (-2.3±0.1)x10^{-4}	τ_1: (6.57±0.04)x10^{-4}	k_1: 1520±10
	A_2: (-1.0±0.1)x10^{-4}	τ_2: 0.012±0.001	k_2: 84±1
(575 nm) α-Fe_2O_{3-x}/Ta_2O_5	A_1: (-1.51±0.01)x10^{-4}	τ_1: (5.7±0.1)x10^{-4}	k_1: 1750±20
	A_2: (-4.3±0.1)x10^{-5}	τ_2: (6.96±0.22)x10^{-3}	k_2: 140±5

Table 8 - Fitting parameters obtained from Figure 80.

Figure 81 shows the attempted single-exponential fits compared to bi-exponential fits of α-Fe_2O_{3-x} and α-Fe_2O_{3-x}/Ta_2O_5. The red lines show the suitability of the fits. It is clear that the electron de-trapping rates in both α-Fe_2O_{3-x} and α-Fe_2O_{3-x}/Ta_2O_5 do not fit to single-exponential decays and instead fit very closely to bi-exponential decays.

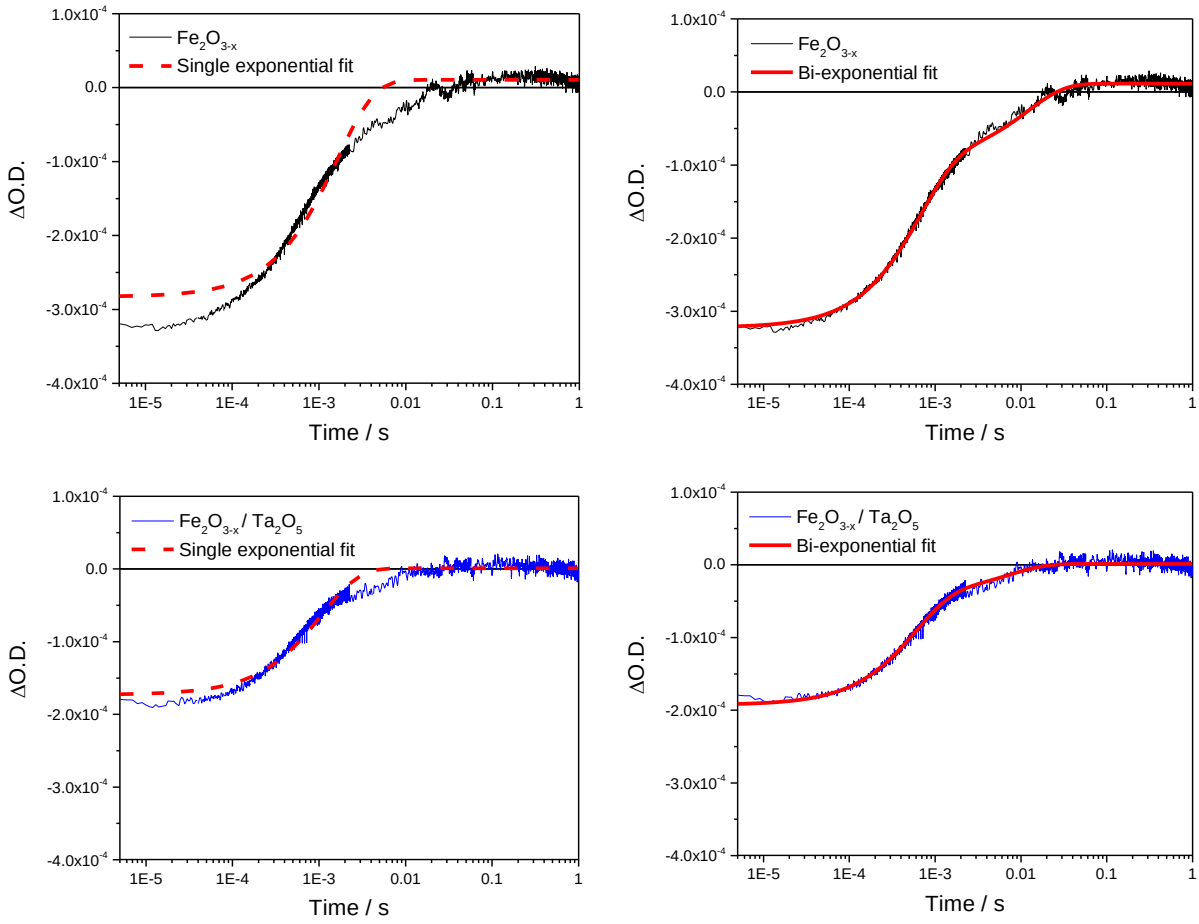

Figure 81- TA kinetics of electron de-trapping in α-Fe_2O_{3-x} and α-Fe_2O_{3-x}/Ta_2O_5 probed at 575 nm following 355 nm laser excitation (~100 μJ cm^{-2}). The two curves have been fit to single exponential decays (a and c) and to bi-exponential fits (b and d).

The results for α-Fe_2O_{3-x} are broadly consistent with the results for Ta_2O_5 on HT-Fe_2O_3 and LT-Fe_2O_3 in section 3.3.3, resulting most notably in a decrease in the magnitude of the electron trapping, in addition to a small increase in detrapping rate. This decrease in both A_1 and A_2 suggests that less electrons are trapped following the addition of Ta_2O_5 to Fe_2O_{3-x} in both populations, however population A_2 is lowered by a greater extent (Table 8).

TAS kinetics probed at 650 nm shows the effect of Ta_2O_5 on the hole signal, Figure 82. The Ta_2O_5 overlayer decreases the magnitude of the hole signal in α-Fe_2O_{3-x}. A similar change was observed for HT-Fe_2O_3 and LT-Fe_2O_3 and is further indication that Ta_2O_5 is inhibiting the ability of the generated holes to accumulate as oxidised species near the surface of the photoelectrode. This is in line with the decrease in photocurrent spikes observed in Figure 77. The hole kinetics are fitted to triphasic exponential decays of the form shown in equation 7:

$$\Delta OD_{650}(t) = A_1 e^{-(k_1 t)} + A_2 e^{-(k_2 t)} + A_3 e^{-(k_3 t)} + y_0 \quad (7)$$

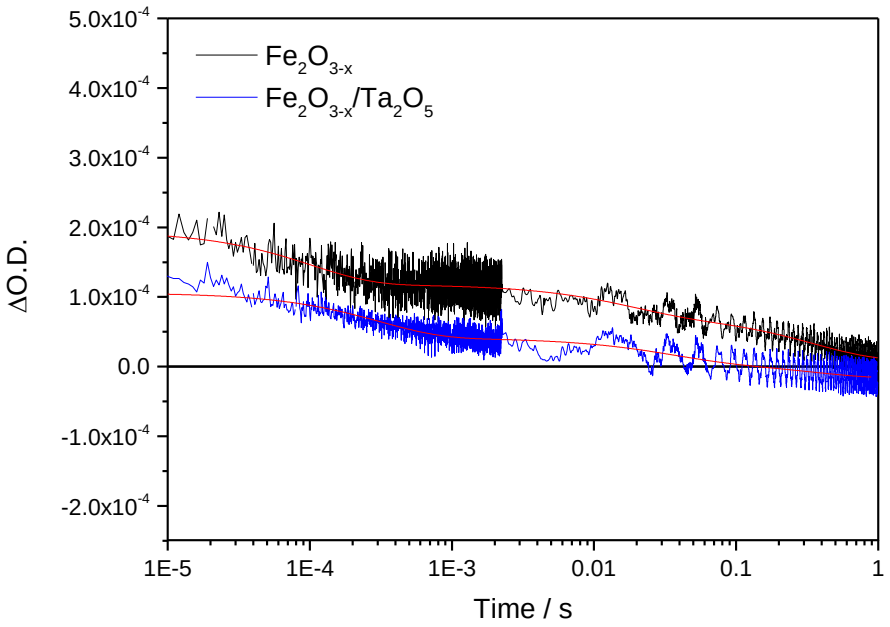

Figure 82 - Microsecond TAS hole kinetics probed at 650 nm following 355 nm laser excitation (~100 μJ cm^{-2}) of α-Fe_2O_{3-x} (black) and α-Fe_2O_{3-x}/Ta_2O_5 (blue) in a photoelectrochemical cell at an applied bias of 0.4 $V_{Ag/AgCl}$ (pH ~13.7).

Name	Magnitude	Lifetime (s)	Rate (s^{-1})
(650 nm) α-Fe_2O_{3-x}	A_1: (7.7±0.3)x10^{-5}	τ_1: (1.0±0.1)x10^{-4}	k_1: 9800±540
	A_2: (4.4±0.1)x10^{-5}	τ_2: 0.02±0.01	k_2: 57.9±2.4
	A_3: (6.53±0.04)x10^{-5}	τ_3: (0.35±0.01)	k_3: 2.8±0.1
(650 nm) α-Fe_2O_{3-x}/Ta_2O_5	A_1: (6.5±0.2)x10^{-5}	τ_1: (3.10±0.14)x10^{-4}	k_1: 3200±150
	A_2: (3.30±0.11)x10^{-5}	τ_2: 0.033±0.002	k_2: 30±2
	A_3: (2.5±0.1)x10^{-5}	τ_3: 0.34±0.03	k_3: 3.0±0.3

Table 9 – Fitting parameters obtained from Figure 82.

In chapter 2, deposition of Al_2O_3 was found to significantly shift the electron de-trapping rate as measured by the 575 nm TAS kinetics. Following Al_2O_3 deposition, the shifted 575 nm TAS signal closely matches the measure of electrons reaching the external circuit as measured by TPC, suggesting that the alteration to the trap kinetics allowed them to be extracted more readily, reducing their recombination pathway with holes. The most prominent effect of depositing Ta_2O_5 onto Fe_2O_{3-x} appears to be to change the magnitude of electron trapping rather than the de-trapping rate due to complete blocking of electron trapping in a percentage of the trap states. These blocked trap states which have been blocked will no longer contribute to the TPC. However, the remaining trap states also exhibit a small shift (increase) in the detrapping rate which could indicate improved detrapping to the external circuit such as that observed in chapter 2 following Al_2O_3 deposition. Figure 83 shows normalised plots of the 575 nm TAS kinetics and charge extracted for α-Fe_2O_{3-x} and α-Fe_2O_{3-x}/Ta_2O_5. Before ALD, there is little correlation between the TAS and the TPC (Figure 83a) suggesting that the trapped electrons are not reaching the external circuit, in line with previous results from chapter 2. Following Ta_2O_5 deposition some correlation between TAS and TPC is observed on early timescales (10 μs-1 ms) with no correlation on slower timescales, Figure 83b. The partial overlap observed

following Ta_2O_5 deposition in Figure 83b could indicate that one of the trap state populations (the population associated with the fast component of the fit in Table 8) is able to de-trap and reach the external circuit more efficiently, however caution should be taken when reading into these plots by eye. Furthermore, due to the noise of the TPC traces, integration to obtain charge on the very slow timescales caused significant errors, hence for clarity the charge extracted traces were cut at 0.01s (small amounts of noise are magnified at longer timescales when integrating with respect to time).

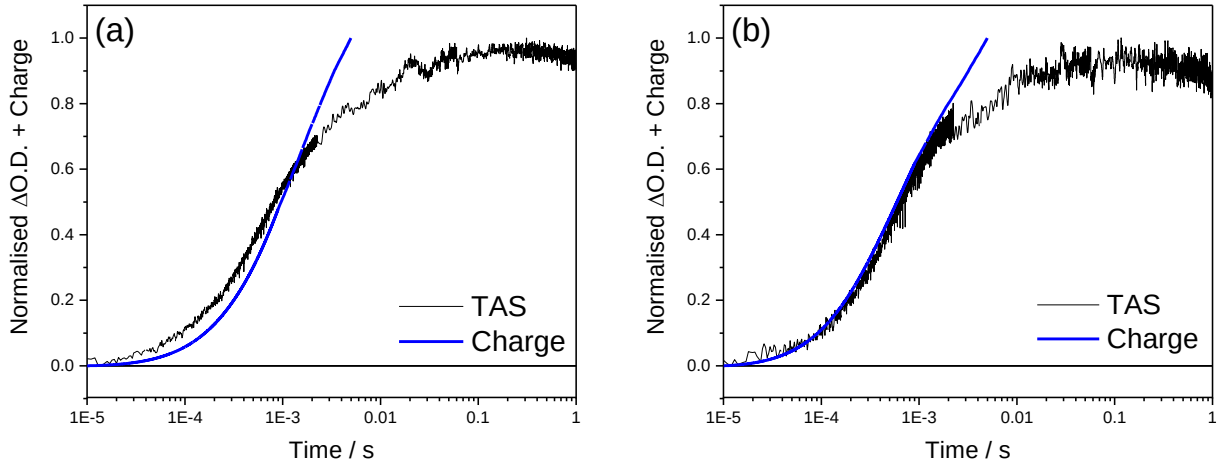

Figure 83 - Overlay of normalised TAS kinetics probed at 575 nm with normalised integrated TPC for (a) α-Fe_2O_{3-x} and (b) α-Fe_2O_{3-x} / Ta_2O_5. Measurements were carried out in a working photoelectrochemical cell at an applied bias of 0.4 $V_{Ag/AgCl}$ (pH ~13.7). Furthermore, due to the noise of the TPC traces, integration to obtain charge on the very slow timescales caused significant errors and so for clarity the charge extracted traces were cut at 0.01s (small amounts of noise are magnified at longer timescales when integrating with respect to time).

From the photocurrent and TAS measurements presented above it is clear that the Ta_2O_5 overlayer changes both the photoelectrochemical response of α-Fe_2O_{3-x} and the nature of the holes and trapped electrons at the surface. The Ta_2O_5 overlayer appears to have the same effect on α-Fe_2O_{3-x}, HT-Fe_2O_3 and LT-Fe_2O_3. These results indicate that Ta_2O_5 and Al_2O_3 behave differently on hematite surfaces, providing evidence that not all 'passivating' overlayers have a universal effect.[2]

One explanation for the differences between Al_2O_3 and Ta_2O_5 is their stability on an electrode surface in 1 M NaOH (pH ~13.7). The instability of Al_2O_3 results in its destruction within ~20 minutes under working photoelectrochemical conditions (at pH = 13.7) and with this destruction, a reversion of the altered α-Fe_2O_{3-x} photocurrent onset potential back to its original state is observed. Prior to the full destruction of Al_2O_3, it is likely that pitting and partial destruction occurs rapidly, meaning parts of the hematite surface were exposed during the measurements in chapter 2 (i.e. a uniform Al_2O_3 layer was not present) even though they were carried out within minutes after electrolyte contact. The reversion of changes after Al_2O_3 destruction is interesting as it indicates that the alteration at the α-Fe_2O_{3-x} / Al_2O_3 interface is a reversible process. The results in this chapter (Figure 57 and Figure 58) have showed Ta_2O_5 deposited by ALD to be very stable in 1 M NaOH (pH ~13.7). This stability is also exhibited in the alteration to the photocurrent and TAS measurements by Ta_2O_5, which persist over a period of 24 hours of continual use under working photoelectrochemical conditions at 0.4 $V_{Ag/AgCl}$ (pH ~13.7). The films in this chapter were studied frequently over a period of several months with no signs of the changes measured by linear sweep voltammetry or TAS reverting. This large difference in stability could be a reason for the differing results between Al_2O_3 and Ta_2O_5.

A final difference between the deposition of Al_2O_3 and Ta_2O_5 in the studies presented here is the use of Trimethylaluminium (TMA) as an ALD precursor. TMA is commonly used as an Al precursor for atomic layer deposition of Al_2O_3.[32] In addition to this, it is often used as a 'foundation layer' before the deposition of other layers such as Ta_2O_5, where several cycles of TMA are deposited before the precursors for the desired overlayer are introduced. This is of interest as a recent report[32] has shown that the deposition of only TMA can increase the photocurrent of hematite photoelectrodes. The enhancement was proposed to be due to reactions between TMA and α-Fe_2O_3 inducing electron donation to the substrate and modifying

the covalent character of the Fe−O bonds. The Fe_2O_3 surface modifications were postulated to allow for enhanced charge carrier transport next to the interface, although their explanation was brief. The authors also commented that they did not dismiss the possibility of surface passivation occurring, however they had no experimental evidence to suggest it. In chapter 2, the TMA precursor was used during the deposition of Al_2O_3 and unfortunately there is no way of determining whether the change was due to TMA, Al_2O_3 or a combination of both. In this current chapter, trial experiments were carried out in which Ta_2O_5 was deposited with and without the use of TMA as a 'foundation layer', Figure 84.

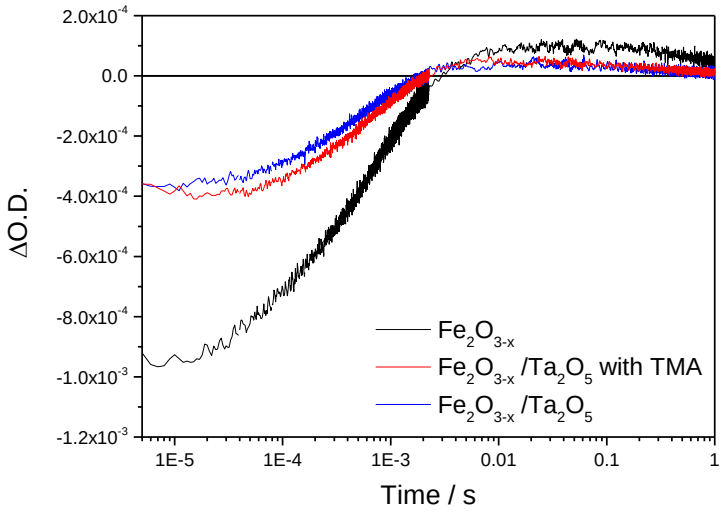

Figure 84 - Microsecond TAS kinetics probed at 575 nm following 355 nm laser excitation (~100 μJ cm^{-2}) of α-Fe_2O_{3-x}, α-Fe_2O_{3-x} with a 2 nm layer of Ta_2O_5 using TMA pre-treatment and α-Fe_2O_{3-x} with a 2 nm layer of Ta_2O_5 without a pre-treatment. Measurements recorded in a photoelectrochemical cell at an applied bias of 0.4 $V_{Ag/AgCl}$ (pH ~13.7).

The TMA pre-treatment carried out here appeared to have no significant effect on the rate or magnitude of electron detrapping (Figure 84) and as such, it was excluded from all later Ta_2O_5 deposition runs including the data presented in this chapter (with the exception of STEM/elemental mapping) in order to simplify experiments.

So far, Ta_2O_5 has been established as a stable overlayer capable of altering the photoactivity, electron trap and hole dynamics of several hematite films in the same way. The effect of depositing Ta_2O_5 on hematite appears to have a mixed effect of altering surface trap states and blocking hole accumulation at the surface. The next section aims to address more precisely the types of surface states present on a hematite surface and how Ta_2O_5 influences them.

3.3.5 Addressing the surface state debate with steady state absorption and cyclic voltammetry

While there is a general agreement that the presence and influence of trap states in photoelectrodes such as hematite are important factors to address there is not yet a consensus as to the exact nature, concentration and location of such states in hematite,[22,24,33–36] and it is this uncertainty that has motivated the work in this chapter.

In the TAS studies such as those presented in this thesis,[2] and by others,[24] the 575 nm feature is assigned to electronic trap states. In the absence of a photoelectrochemical bias, this TA feature exists as a narrow positive band which then decays back to zero on ms timescales, Figure 85a. Under an electrochemical bias this positive feature rapidly inverts before slowly decaying back to zero on ms-s timescales, Figure 85b. The magnitude of this inversion increases with increasing positive bias. As discussed in chapter 2, the same positive feature is also observed with steady state spectroelectrochemical measurements.

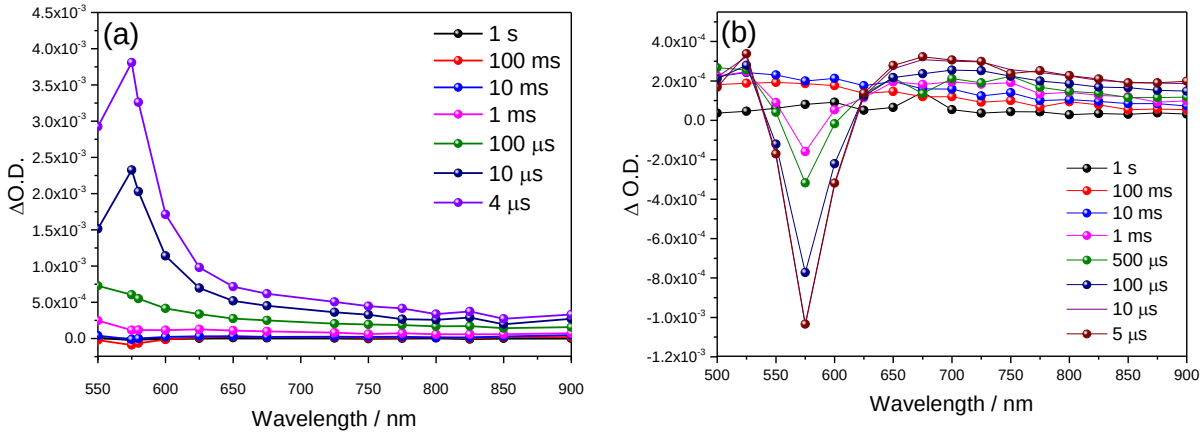

Figure 85 - (a) TAS kinetics of α-Fe_2O_{3-x} probed at 575 nm following 355 nm laser excitation (~100 µJ cm^{-2}) without an applied bias. (b) The same measurement with an applied electrochemical bias of 0.4 $V_{Ag/AgCl}$ (pH ~13.7).

The electron trap state theory then states that the feature at 575 nm is due to electronic trap states throughout the material which are gradually emptied (oxidised) under a positive bias resulting in the positive absorbance at 575 nm. Once these states are emptied, they are able to trap excited electrons generated following light absorption, resulting in the bleach signal observed by TAS, Figure 85b. In the absence of a positive bias, these trap states remain reduced and instead act as hole traps which results in the positive feature measured by TAS, Figure 85a. It should be noted that the identity of the ultrafast positive TAS signal is still contentious. It could also be overlapped with a second signal, likely related to the photohole although this has been tentatively ruled out by hole scavenger experiments and the fact that its narrow shape is not consistent with the broad hole signal on slower times. A diagram showing the effect of an applied bias on the type of surface states believed to be involved in the process described above is shown in Figure 86.

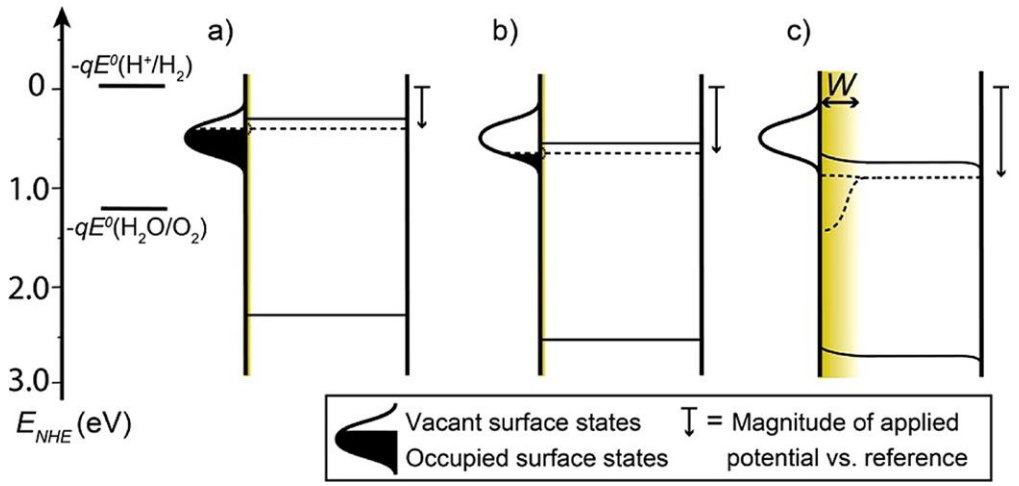

Figure 86 - Electron energy scheme of an n-type semiconductor photoanode under polarisation using a potentiostat at different potentials and with the presence of surface states that cause Fermi level pinning. (a) Electrode at V_{fb}. (b) An anodic potential empties the surface states but does not induce band bending. Band bending commences at (c) when the surface states are emptied. Reproduced from reference[22].

Several other groups have investigated the 575 nm feature as observed by steady absorbance spectroscopy from a different perspective in conjunction with electrochemical impedance spectroscopy (EIS), modulated photocurrent impedance spectroscopy (IMPS) and cyclic voltammetry (CV).[30,33,36–39] In these studies the potential formation of surface states in the form of water oxidation intermediates are addressed alongside the formation of electron trap states. From these studies there appears to be two distinct types of surface states in hematite; electron trap states similar to those described above, which cause recombination problems at the surface and also the formation of 'hole trap states' which act as surface water oxidation intermediates, possibly in the form of Fe(IV)=O.[33–36] As part of these studies the steady state absorption peak at 575 nm was correlated to this water oxidation intermediate rather than to electron trap sates, albeit tentatively. An excellent summary of these findings is presented by Hamann *et al.*[40] A brief overview of the results is provided below.

Peter *et al.*[30,41,42] used EIS and IMPS to investigate the water oxidation mechanism on the hematite surface where they developed a charge transfer model that assumed charge transfer to

be associated with the formation of oxidised surface species as a result of surface hole accumulation. The model addressed competition between hole transfer from surface states (the water oxidation reaction) and recombination with conduction band electrons. A nearly potential independent recombination rate was measured for a few hundred millivolts which was attributed to Fermi level pinning by surface states. They then modified the hematite surface with Co^{2+} (generally known to have a catalytic effect on hematite) and found no change in hole transfer rate with potential but a strongly dependant recombination rate. They concluded that Co^{2+} suppressed the rate of surface recombination and reduced Fermi level pinning. The rate of hole transfer was nearly constant relative to potential for Co^{2+} modified hematite, while the recombination rate was strongly potential dependent. This behaviour was attributed to suppressed rate of surface recombination and reduced Fermi level pinning.

Building upon the studies of Peter *et al.,* Klahr and Hamann *et al.* carried out EIS on ALD hematite thin films under illumination to further understand the surface states of hematite.[43,44] They observed two potential dependent capacitive states for which they used an equivalent circuit representing the hematite/electrolyte interface containing a chemical capacitance due to the accumulation of holes in surface states to interpret the data. They attributed a surface state capacitance to hole accumulation at the surface. This capacitance had a Gaussian distribution with respect to potential, with a maximum at the same potential as the photocurrent onset potential. This surface state capacitance also had a maximum which coincided with the minimum of measured charge transfer resistance. They concluded that the results suggest hole transfer on hematite occurs through surface states; i.e. once a critical number of holes (enough to out-compete the hole consumption by recombination) were stored on the surface, sustained water oxidation starts to onset (as measured by photocurrent), which is coincident with the minimum of charge transfer resistance. They also identified surface state charging and discharging using cyclic voltammetry in the dark where they observed two peaks when

sweeping cathodically after holding at a positive bias under illumination (a strong photocurrent region). The first peak in their CV occurred at a similar potential as the peak observed by EIS and was assigned to surface hole accumulation in the form of surface states (water oxidation intermediates). The second peak occurred at a much more cathodic potential and was assigned to a set of shallow states which are intrinsic to hematite and do not participate in the water oxidation mechanism. Further work by Hamann *et al.* has tentatively suggested that the surface hole species exists in the form Fe(IV)=O.[33,38] The viability of this species is further supported by DFT calculations.[35]

There is one discrepancy between our TAS/spectroelectrochemical studies and the conclusions reached by Hamann and others,[33,38] which is the identity of the 575 nm steady state feature. Hamann *et al.* assign the 575 nm feature to the surface state water oxidation intermediate (Fe(IV)=O) identified using EIS and CV rather than the electron trap states identified by TAS. More recently, Takashima *et al.* investigated the 575 nm feature by steady state absorbance and they too have assigned it to a surface species taking part in electrocatalytic OER reaction, although they do acknowledge this assignment to be tentative.[36] They introduce phosphate ions into the electrolyte and observe a small red shift in the 575 nm peak. They explain this shift by the coordination of phosphate ions to the transient Fe species, as the coordination of a phosphate ion to a metal ion can induce red shifts of the d-d and ligand-metal transitions absorptions. Thus the transition can be expected to originate from the transition associated with surface Fe ions. However this only shows that the 575 nm feature as at least partly involved with Fe at the surface, and so does not distinguish between electronic trap states or 'hole trap states'.

In an attempt to clarify the uncertainty regarding the 575 nm feature, steady state spectroelectrochemistry and dark CVs have been measured on our films and are discussed below.

Surface states in steady state absorbance measurements: Figure 87 shows the steady state absorption of α-$Fe_2O_{3-x,}$ LT-Fe_2O_3, HT-Fe_2O_3 with and without a 2 nm Ta_2O_5 overlayer.

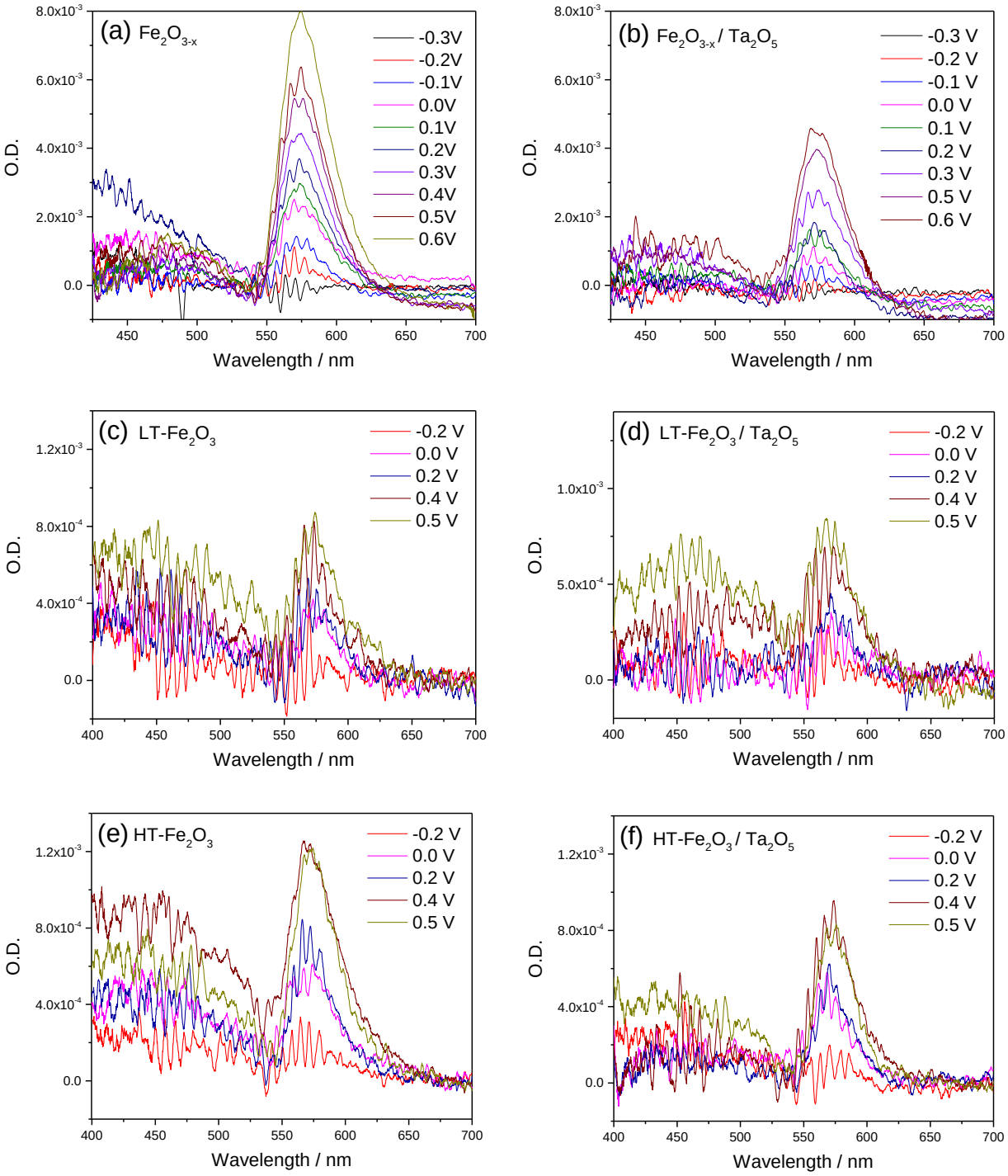

Figure 87 - Difference steady-state absorption spectra under various applied electrical bias vs. a background bias of -0.3$V_{Ag/AgCl}$ (pH ~13.7) (close to the flat-band potential). (a) α-$Fe_2O_{3-x,}$ (b) α-Fe_2O_{3-x}/Ta_2O_5, (c) LT-Fe_2O_3 and (d) LT-Fe_2O_3/Ta_2O_5, (e) HT-Fe_2O_3 and (f) HT-Fe_2O_3/Ta_2O_5; Ta_2O_5 layers are 2 nm thick.

The first thing to note in the steady state absorbance measurements is that the Ta_2O_5 overlayer reduces the magnitude of the 575 nm feature of α-Fe_2O_{3-x}, HT-Fe_2O_3 and LT-Fe_2O_3 (Figure 87a, b, c, d, e & f), in a similar manner to the 575 nm TAS kinetics which we assigned to photoelectron trapping and de-trapping (Figure 69 & Figure 80). The relative magnitudes of the steady state absorption signals are consistent with the magnitudes of the TAS signals. It should be noted that standard UV/Vis absorbance spectra will be dominated by the bulk features, whereas TAS has the complication of charges (probably) being dominant at the surface and therefore direct comparisons are not necessarily adequate. α-Fe_2O_{3-x} has the largest steady state absorption signal suggesting a large number of oxidised states (which would be expected for a sample rich in oxygen deficiencies). Following the addition of Ta_2O_5, the steady state absorption signal is reduced (Figure 87b) and so too is the TAS bleach by a similar magnitude (Figure 80). The reduction in magnitude shows that the feature responsible for the steady state spectroelectrochemical signal must be at least partly located near the surface where Ta_2O_5 is able to interact, a point which all studies agree on. The fact that this signal is never completely removed, even with overlayers as thick as 4 nm is interesting. Perhaps the most obvious explanation for this is that the feature is not solely located on the surface where an overlayer can reach it, supporting the theory that the 575 nm feature is a measure of trap states both on the surface and in the bulk of hematite.

It is also possible that rather than there being surface and bulk trap states, all of the states measured by the 575 nm spectroscopic feature are present on the surface, but at differing facets, with some of them being more significantly affected by an overlayer than others. Different atomic arrangements (different facets) at a semiconductor surface are known to determine the absorption and activation of reaction molecules and may affect photocatalytic performance.[45,46] In addition to this, surface facets can also effect surface states, with different surface states preferentially forming at certain facets. An example of facet selectivity has been demonstrated

on $BiVO_4$ where it has been shown that the oxidation and reduction reactions preferentially take place on different facets using facet-selective photo-deposition.[47] The deposition of co-catalysts separately on different surfaces has also been achieved using the same basis.[48] In light of this, it is not unreasonable to expect that surface water oxidation intermediates form at different facets to electron trap surface states. Furthermore, it could be that electron trap states of similar origin (for example from oxygen vacancies) form at multiple surface facets, giving rise to multiple populations with differing kinetics, which could explain the bi-exponential kinetics observed by TAS. The partial removal of the 575 nm feature could be rationalised in the sense that certain facet trap states are more significantly hindered by an overlayer. A more detailed understanding of how Ta_2O_5 interacts with a hematite surface would be useful for the passivation mechanism.

Finally, the partial removal of the 575 nm feature could also be an indication that the overlayer is not completely covering the surface. This point is not often considered as ALD is typically known to produce conformal layers with high reliability. Because we are investigating nanostructured films as opposed to planar films, it is possible that parts of the nanostructure are inaccessible during the ALD process, possibly due to the short exposure time of precursor pulses. However once immersed into an electrolyte for longer periods of time these obstructed surfaces may be reachable. It is also possible that the hematite surface is initially fully coated by ALD, however cracks form in the overlayer after deposition, resulting in exposed iron oxide surface and thus any surface states associated with it. Unfortunately, attempts to understand how far the Ta_2O_5 penetrates the hematite nanostructure in the previous section using scanning tunnelling electron microscopy and elemental mapping was unsuccessful (Figure 76).

Surface states in dark CV measurements: Figure 88 shows dark CVs similar to those reported by Hamann *et al.* of α-Fe_2O_{3-x}, LT-Fe_2O_3 and HT-Fe_2O_3, with and without Ta_2O_5 overlayers. These CVs were measured by holding the photoelectrode at a positive applied bias at 0.8 V under illumination for 60 seconds to build up a concentration of water splitting intermediates and to depopulate electron trap states. The CV was then swept in a cathodic direction at a fast scan speed of 200 mV s^{-1}. Scanning cathodically at fast speeds can result in the subsequent reduction of oxidised/depopulated surface states, leading to a current peak corresponding to the density of those states at that specific energy.

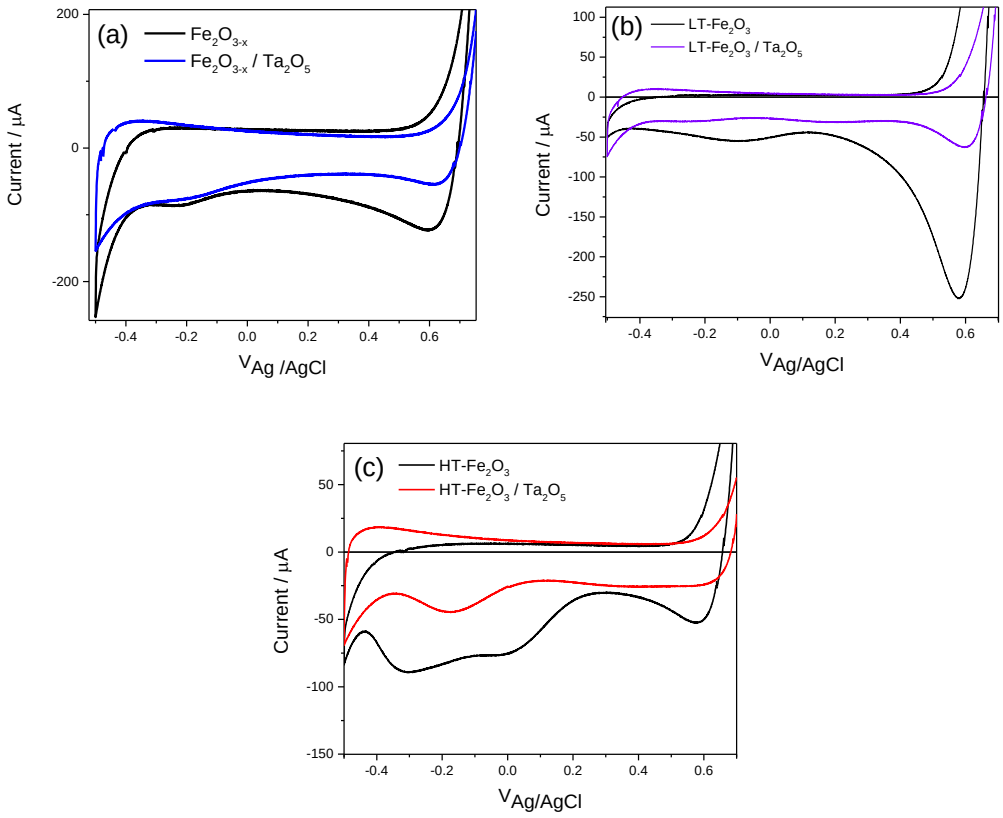

Figure 88 - Dark CVs in 1 M NaOH (pH ~13.7) of (a) α-Fe_2O_{3-x}, (b) LT-Fe_2O_3 and (c) HT-Fe_2O_3 with and without a 2 nm Ta_2O_5 overlayer. The films were scanned in the dark at 200 mV s^{-1}after being held in the light for 60 seconds at 0.8 V.

Following a period of illumination at a positive bias, Hamann *et al.* observed two features when sweeping hematite cathodically.[33,37] Their first peak is observed near the dark catalytic current onset potential (*ca.* 0.55 $V_{Ag/AgCl}$, pH ~13.7) and is consistent with the capacitive peak obtained from EIS. This feature is assigned to a surface hole species which builds up under illumination and/or at a high positive bias and is quickly reduced during the cathodic sweep. The second feature observed by Hamann *et al.* appears at a more cathodic potential (*ca.* -0.2 $V_{Ag/AgCl}$) and is assigned to the electron trap states which are intrinsic to hematite. Both of these features are also observed in our CVs of α-Fe_2O_{3-x} and LT-Fe_2O_3 in Figure 88a & b. Both of these features are reduced following the deposition of Ta_2O_5, which is consistent with the removal of surface states existing as either electron traps or water oxidation intermediates. Like α-Fe_2O_{3-x} and LT-Fe_2O_3, HT-Fe_2O_3 also shows a reduction peak at *ca.* 0.55 $V_{Ag/AgCl}$ (pH ~13.7) which is reduced following ALD. Interestingly, where the other films show a single peak at *ca.* -0.2 $V_{Ag/AgCl}$ assigned to electron trap states HT-Fe_2O_3 possesses two features at *ca.* 0.0 and -0.3 $V_{Ag/AgCl}$. Following the deposition of Ta_2O_5 onto HT-Fe_2O_3 these two peaks merge into a single peak located midway between the initial two peaks (*ca.* -0.2 $V_{Ag/AgCl}$). This could be evidence of two populations of trap states changing to one population in this film Figure 88c. It is known that high temperature treatment causes Sn migration, which is likely to lead to different defect sites and this could be the reason for the initial difference in the HT-Fe_2O_3 CV.

Figure 89 shows the dark CV feature at 0.55 $V_{Ag/AgCl}$ assigned to a hole surface state acting as a water oxidation intermediate in LT-Fe_2O_3 and how it changes with Ta_2O_5 thickness. This trend is also observed for α-Fe_2O_{3-x} and HT-Fe_2O_3 and is consistent with the gradual 'turning off' of surface sites. At 4 nm the almost complete removal of this feature indicates these hole sites are almost entirely removed.

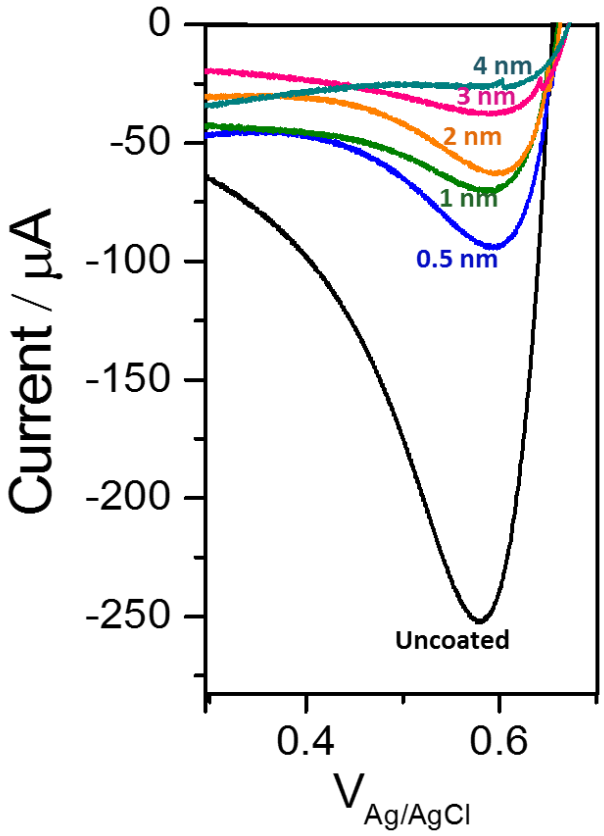

Figure 89 - Dark cyclic voltammograms in 1 M NaOH (pH ~13.7) of LT-Fe_2O_3 with various thicknesses of Ta_2O_5. The peak at ~0.55 V assigned to hole accumulation as a water oxidation intermediate is isolated. The films were scanned in the dark at 200 mV s^{-1}after being held in the light for 60 seconds at 0.8 V.

Our dark CV results and assignments for α-Fe_2O_{3-x}, LT-Fe_2O_3 and HT-Fe_2O_3 are in agreement with those presented by Hamann *et al.* Unfortunately it is difficult to compare the features observed by CV and EIS with the 575 nm feature observed spectroscopically, and this is partly the reason for the ambiguous assignment of the 575 nm feature in the literature. From the results discussed so far, we would tentatively assign the 575 nm feature to the electron trap states (existing on the surface and the bulk, or at multiple surface facets) rather than the water oxidation intermediate solely on the surface because typically, the 575 nm feature is never completely removed following even thick Ta_2O_5 deposition (usually a maximum decrease of ~ 50% for both TAS and steady state absorbance). This fits more closely with the more cathodic CV feature (*ca.* -0.2 $V_{Ag/AgCl}$, pH ~13.7) assigned to electron trap states which often remains in

some form even with a thick overlayer. Furthermore, the 575 nm feature observed in Figure 88 by steady state UV/Vis absorbance does not correlate very well with the CV feature at *ca.* 0.55 $V_{Ag/AgCl}$ (pH ~13.7) assigned to the surface water oxidation intermediate, as this feature is reduced well below 50% with even a thin Ta_2O_5 overlayer, and is almost entirely removed with a Ta_2O_5 thickness of 4 nm. This correlation between the 575 nm spectroscopic feature and CV features is further supported by results for α-Fe_2O_3 (the air annealed counterpart of α-Fe_2O_{3-x}) below.

Additional evidence to support the assignment of the 575 nm feature to electron trapping: Further evidence for the 575 nm feature being related to trapped electrons is its insensitivity when exposed to hole scavengers such as CH_3OH or H_2O_2. If this signal was that of a surface hole in the form of a water oxidation intermediate, CH_3OH or H_2O_2 would be expected to change this signal. In fact, as shown in chapter 2, the presence of H_2O_2 actually slightly extends the 575 nm TAS signal on slow time scales. The steady state absorbance spectrum has also been carried out in the presence of H_2O_2, Figure 90. The 575 nm feature observed by steady state UV/Vis absorbance at 0.4 $V_{Ag/AgCl}$ clearly remains in the presence of H_2O_2. It should be noted that the presence of H_2O_2 causes bubbles to form at the surface of the hematite due to the increased levels of oxidation. These bubbles affect the transmission measurement by increasing the noise in the spectrum.

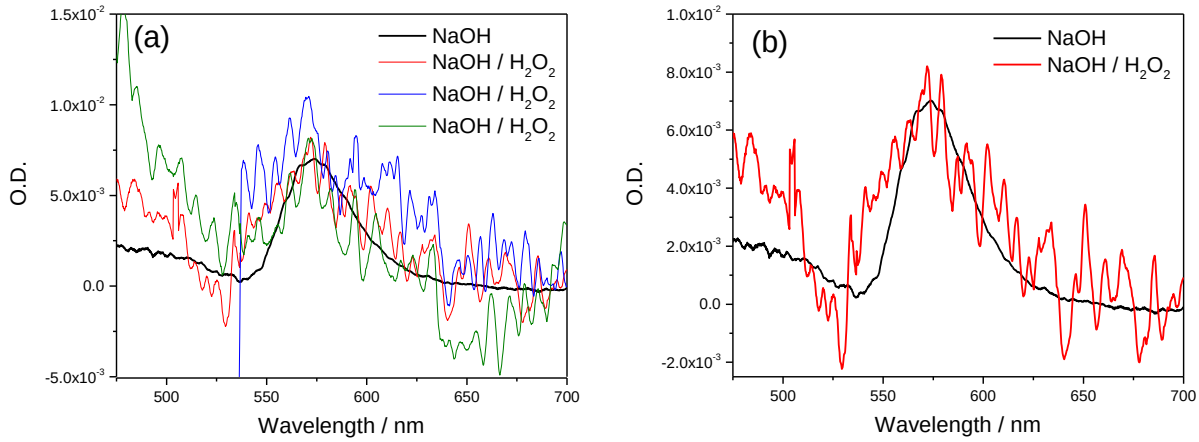

Figure 90 - Difference steady-state absorption spectra under an applied electrical bias of 0.4 $V_{Ag/AgCl}$ vs. a background bias of -0.3$V_{Ag/AgCl}$, pH ~13.7 (close to the flat-band potential) of α-Fe_2O_{3-x}, with and without the presence of H_2O_2. (a) Shows multiple scans which were carried out due to noise in the spectrum. (b) Shows a single scan for clarity.

Additionally, the decay kinetics of the 575 nm bleach match the TPC kinetics (the measure of electrons reaching the external circuit) in certain hematite films very closely, again indicating that the 575 nm TAS feature is an electron process. Finally, there is no noticeable difference in the spectra when measured in the light compared to in the dark, Figure 91. If this was a water splitting intermediate, a change in concentration of this species would be expected when under illumination.

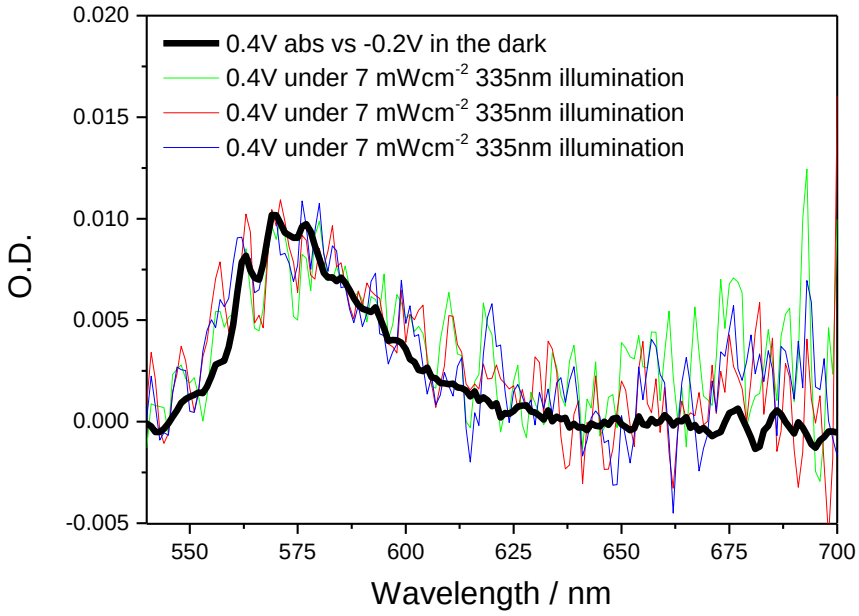

Figure 91 - Difference steady-state absorption spectra under various applied electrical bias vs. a background bias of -0.2$V_{Ag/AgCl}$ (pH ~13.7) (close to the flat-band potential) of α-Fe_2O_{3-x}. Due to noise as a result of the filters and LED present in the illuminated measurement, this measurement was repeated 3 times.

Concluding the surface state debate: To summarise, there is a general consensus in the literature, using a wide range of experimental techniques, that typically hematite photoelectrodes possess both surface states attributed to holes (i.e. water oxidation intermediates) and surface states attributed to electron trapping which do not directly participate in water oxidation mechanism. Firstly, there is a 'hole trapping' surface state, possibly existing as Fe(IV)=O, which acts as a water splitting intermediate. This intermediate has been described by Hamman *et al.* and has also been observed by us using dark CV at 0.6 $V_{Ag/AgCl}$. Following the addition of an overlayer such as Ta_2O_5, this water oxidation intermediate is significantly reduced as the hematite surface is no longer available. The second feature is attributed to electron trapping sites which can act as recombination centres near the surface and cause Fermi level pinning, but may also be related to dopants in the bulk which enhance activity. It is these electron trapping states which we attribute to the 575 nm feature observed by TAS and steady state absorbance. These electron trap states are only partly

passivated by the deposition of Ta_2O_5 as observed by TAS, steady state spectroelectrochemistry and CV, suggesting that they exist as more than one population, either in the bulk and the surface or alternatively at differing surface sites/facets. This is supported by fitting of the 575 nm TAS feature which fits well to a bi-exponential decay when uncoated. In the case of LT-Fe_2O_3 and HT-Fe_2O_3 the fit reverts to a single exponential following addition of Ta_2O_5, suggesting one trap population is removed. It is noted that we were unable to establish the surface coverage of Ta_2O_5 as deposited by ALD. A summary of these conclusions is depicted in Figure 92.

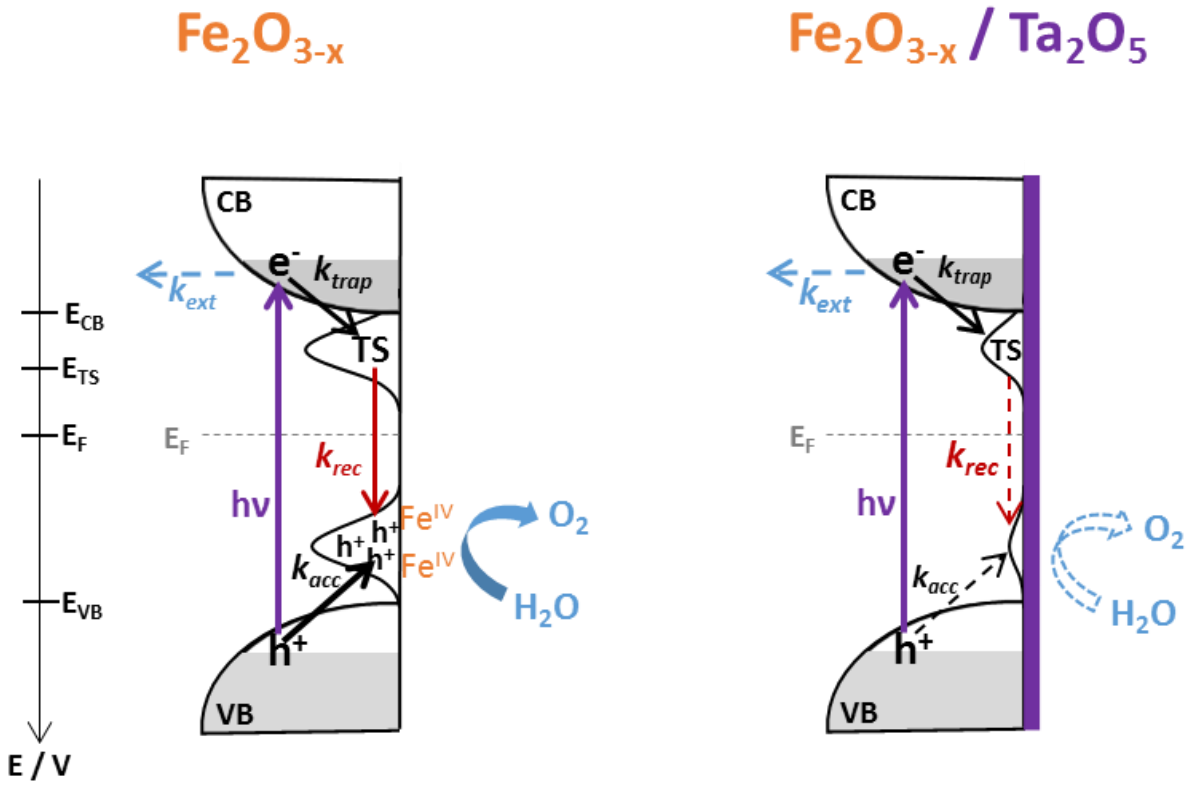

Figure 92 – Schematic showing the proposed surface and bulk states observed in the experiments above and the effect of Ta_2O_5 on these states.

As speculated in the past, it appears that while the addition of an overlayer can help passivate unwanted surface states such as electron traps, it may also hinder the desirable formation of

water splitting intermediates at the surface. As such, it may be more suitable to find a surface treatment that does not permanently obstruct the surface. Although we could not establish the surface coverage here, most overlayers are likely to be obstructive. This has been discussed recently in a number of theoretical studies by Caspary Toroker *et al.*[35,49] in which they consider the water oxidation mechanism on a hematite surface fully covered by Al_2O_3. They conclude that cracks or gaps in the overlayer are necessary. A surface treatment which avoids the deposition of a permanent overlayer will be discussed in Chapter 4.

It should be noted that extreme caution is necessary when comparing different types of hematite films as has been done in this study. The conclusions in this section have been reached by considering various studies using a range of different hematite films, including: thick nanostructured films, ultrathin planar ALD films, un-doped films, Sn-doped films and oxygen vacancy doped films. The wide variety of hematite films reported in the literature may partly explain the difficulty in consistently assigning common spectroscopic/electrochemical features between studies. Great care and attention should be made towards the type of film present in studies such as this.

3.3.6 Temperature dependence study to find activation energy of trap states

This final section aims to further address the hypothesis that the electron trap states responsible for the 575 nm spectroscopic features exist as more than one population. The previous study reported in chapter 2 proposed that there are 2 populations of trap states, those located on the hematite surface and those located in the bulk of the photoelectrode. The deposition of Ta_2O_5 in this chapter also indicates multiple populations of trap states. Following further consideration, it is also possible that both populations exist on the electrode surface, but at different facets.

The assignment of two populations of trap states was tentatively supported by fittings of the de-trapping component (the decay of the 575 nm TAS signal) in α-Fe_2O_{3-x} and was further confirmed by a similar trend in LT-Fe_2O_3, both of which fit well to bi-exponential decays. Figure 81 showed the attempted single-exponential fits compared to the bi-exponential fits of α-Fe_2O_{3-x} and α-Fe_2O_{3-x}/Ta_2O_5 as previously discussed in section 3.3.4. The bi-exponential decays suggest two distinct populations of trapped electrons. This was concluded because one population decaying by two (or more) pathways should show only a single k_{obs} which is the sum of the rate constants of all competing pathways.

If the hypothesis that the electron trap states are present both on the surface and in the bulk is true, and the TAS fittings are representative of this, Ta_2O_5 would be expected to more significantly affect the magnitude and/or lifetime of the surface trap states compared to those in the bulk. The bi-exponential fittings in Figure 81 show that following Ta_2O_5 deposition, the first component decreases by *ca.* 60% and the second component decreases by *ca.* 30%. Although it is by no means a conclusive result it is proposed that the ratio of change between the components merited further exploration as it does support a decrease in the deeper lying traps.

The remainder of this section describes a temperature dependent TAS study of α-Fe_2O_{3-x} and α-Fe_2O_{3-x}/Ta_2O_5 which aimed to provide estimated energies for the trap states. Figure 93 shows the equipment used to carry out TAS measurements at a range of temperatures. The setup used a small 3 electrode photoelectrochemical cell surrounded by an adjustable temperature thermal jacket. Standard TAS measurements were carried out on Fe_2O_{3-x} in this cell at a range of temperatures. A thermometer was used to confirm the temperature of the electrolyte close to the Fe_2O_{3-x} electrode. The reference electrode was placed into a small compartment separated by a salt bridge. This compartment was maintained at room temperature to prevent temperature fluctuations from affecting the reference electrode and therefore the applied bias.

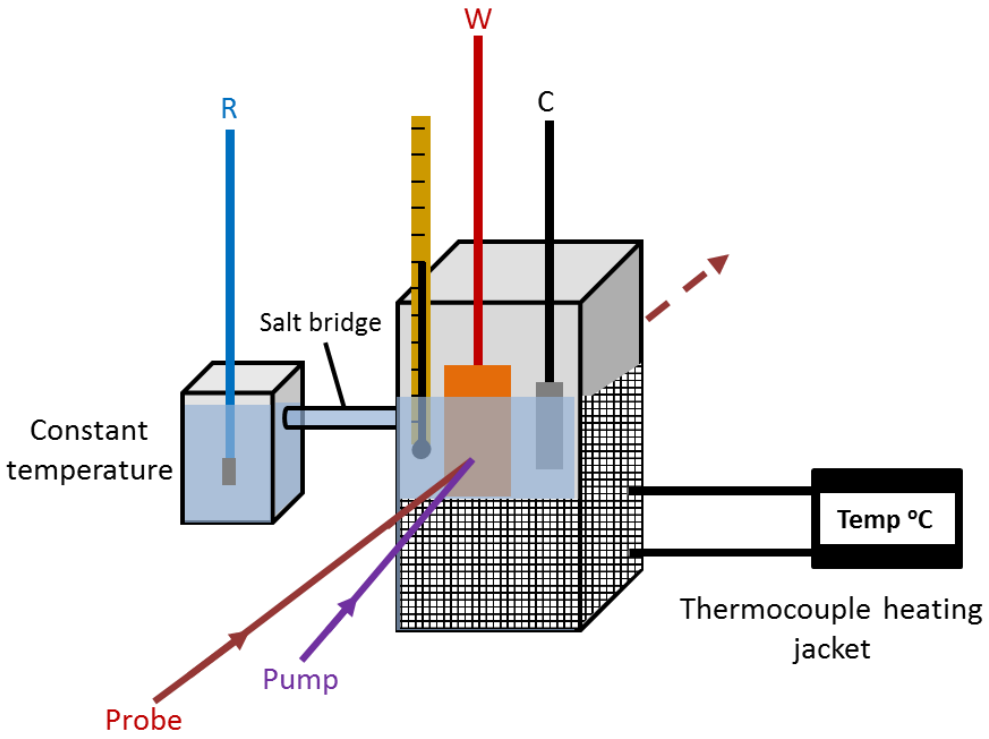

Figure 93 - Diagram showing the temperature dependant TAS setup using a quartz glass cell inside a thermocouple heating jacket.

The aim of this experiment is to extract the rate constants of the electron trap components at a range of temperatures by fitting the 575 nm decay and then use Arrhenius plots to obtain estimate activation energies (E_a) of each component (i.e. of each electron trap population). Similar experiments have been carried out on photoelectrodes in the past.[50] An Arrhenius plot takes the form of ln *k vs.* 1/T. The gradient of this plot then provides an estimate of E_a as according to the relationship below in equation 8:

$$k = Ce^{-E_a/RT} \qquad (8)$$

Where R is the universal gas constant (R = 8.3144598 J K^{-1} mol^{-1}), *k* = rate constant, C = pre-exponential factor, E_a = activation energy and T = absolute temperature in Kelvin. This equation can be rearranged to yield equation 9, giving an E_a in Joules.

$$\ln(k) = \ln(C) - \frac{E_a}{R}\left(\frac{1}{T}\right) \qquad (9)$$

It should be noted at this stage that this experiment is simplistic and may not suitably represent the dynamics of the trap states. For example, if a surface trapping-detrapping model for a population of states distributed over a range of energies is considered, a change in population will lead to a change in the rate of detrapping, *i.e.* if the trap state concentration is altered by a percentage due to the addition of an overlayer, this may alter the behaviour of the remaining trap state population. Figure 94 shows the 575 nm TAS kinetics of α-Fe_2O_{3-x} and α-Fe_2O_{3-x}/Ta_2O_5 at a range of temperatures. The 575 nm kinetics change with temperature, indicating that the dynamics of the trapped electrons are changing with temperature. This may be expected as the increase in thermal energy may increase the energy of trapped electrons and enhance de-trapping rates. All of the kinetic traces in Figure 94 fit to bi-exponential decays similar to the room temperature (23 °C) measurement (fitting parameters can be found in the appendix).

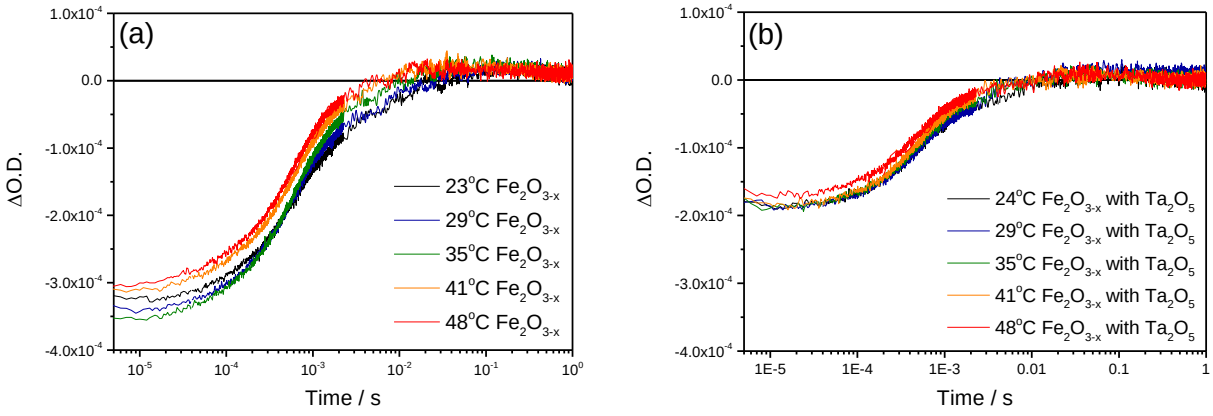

Figure 94 - Temperature dependant TAS spectra probed at 575 nm following 355 nm laser excitation (~100 μJ cm^{-2}) of (a) α-Fe_2O_{3-x} and (b) α-Fe_2O_{3-x}/ Ta_2O_5. Measurements were carried out in a photoelectrochemical cell at an applied bias of 0.4 $V_{Ag/AgCl}$ (pH ~13.7). The cell was coupled to a thermocouple casing to allow adjustment of the temperature within the cell.

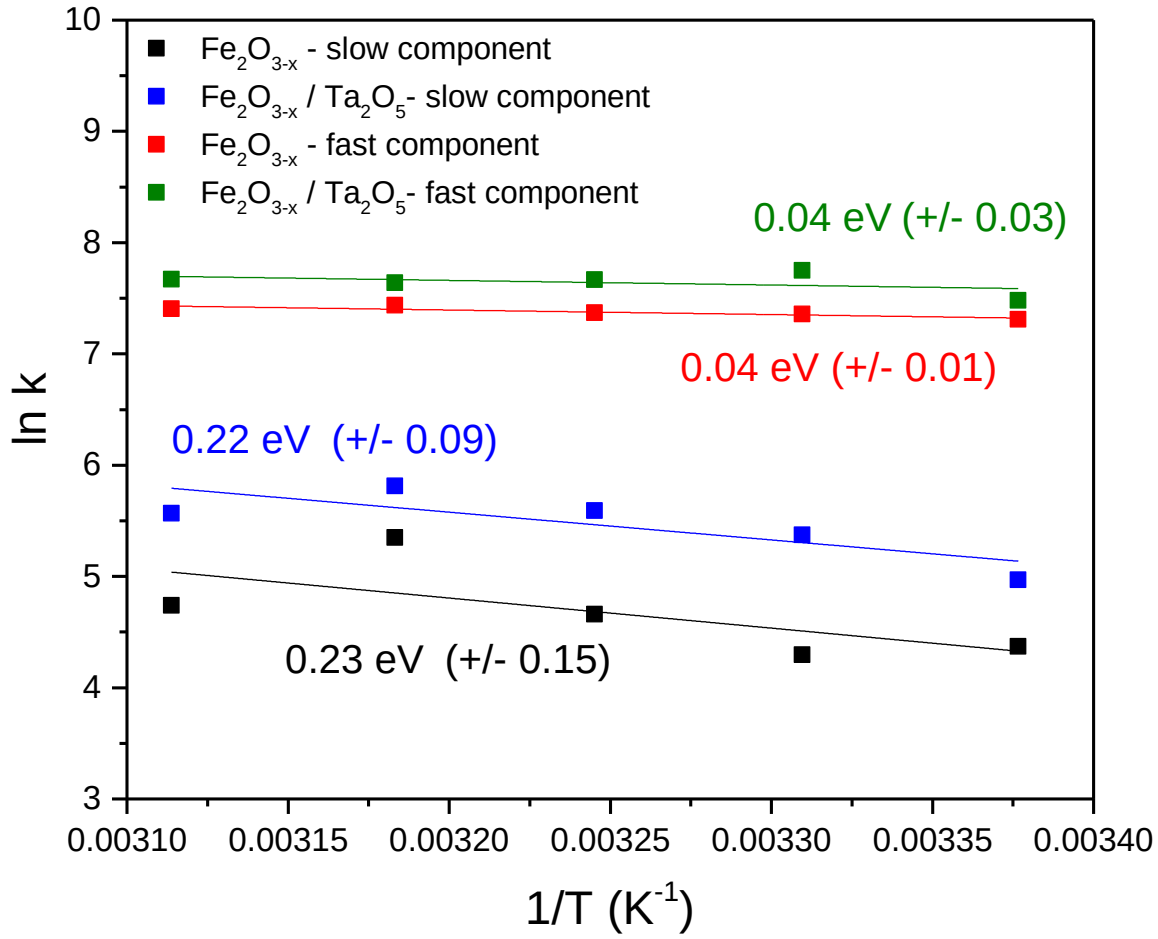

Figure 95 - Arrhenius plots using the fast and slow rate constants obtained from fitting the electron de-trap kinetics of α-Fe_2O_{3-x} and α-Fe_2O_{3-x} /Ta_2O_5. The standard errors for the activation energies obtained from the standard errors from the gradient lines are shown. Fitting parameters can be found in the appendix.

Figure 95 shows the Arrhenius plots for the two components (denoted as the fast and the slow component) in both α-Fe_2O_{3-x} and α-Fe_2O_{3-x} /Ta_2O_5. Based on the model of two electron trap sites, the Arrhenius plot provides activation energies of ~0.04 ± 0.03 eV, ~0.04 ± 0.01 eV, ~0.22 ± 0.09 eV and ~0.23 ± 0.15 eV such as that depicted in Figure 96. These values could indicate a population of shallow trap states (0.04 eV) and a population of deeper lying traps states (~0.2 eV). We note that the errors for the activation energy values obtained here are high and should be treated very tentatively. Furthermore, the fits for the fast components (green and

red lines) appear to deviate from a straight line. While this deviation could indicate non Arrhenius behaviour (temperature dependence being non-exponential) we tentatively assign this to error in the straight line.

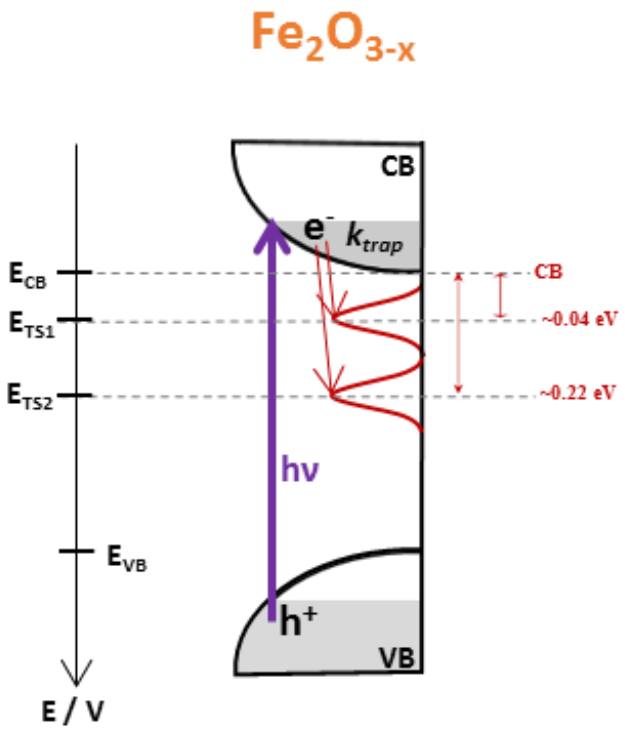

Figure 96 - Schematic showing two populations of trap states in Fe_2O_{3-x}, one at ~0.04 eV and one at ~0.22 eV below the conduction band. According to Figure 95 deposition of Ta_2O_5 does not alter the energy of these states.

It is useful to compare the activation energies obtained in

Figure 95 to the activation energies of states previously reported in iron oxide. Of particular interest are oxygen vacancies, which are abundant in α-Fe_2O_{3-x}, and are also likely to be present in most hematite photoelectrodes to some degree. Oxygen vacancies have been speculated to be a site for electron trapping and could be responsible (wholly or partly) for the 575 nm

feature. The activation energy of $V_{O^{\cdot}}$s have been reported in the past to sit *ca.* 0.08 eV below the conduction band, which compares well with the values obtained in this chapter.[51]

Following the addition of Ta_2O_5 the activation energy of both populations appears to remain unchanged indicating that the overlayer does not significantly affect the energy of the trap states and instead simply reduces their quantity as evidenced by the decrease in the TA signal. Although this tentative study does not reveal that Ta_2O_5 preferentially passivates one population over the other (such as surface states *vs.* bulk states) it does provide evidence that two trap state populations exist in Fe_2O_{3-x}, which are either energetically or specially different.

3.4 Conclusions

The primary aim of this chapter was to develop a stable overlayer to allow for a more detailed spectroscopic study of surface defects in hematite. Ta_2O_5 was found to be a stable overlayer in 1 M NaOH electrolyte (pH ~13.7) under photoelectrochemical conditions on hematite photoelectrodes for over 24 hours. The enhanced stability of Ta_2O_5 compared to Al_2O_3 allowed for more detailed TAS analysis and a development of the findings discussed in chapter 2. Ta_2O_5 deposition reduced the overall magnitude of the 575 nm signal (the amount of electron trapping) in addition to slightly increasing the detrapping rate, providing evidence that the trap states exist at least partly on the surface. Ta_2O_5 deposition lead to a small improvement in photocurrent in the hematite films studied here. This improvement is hypothesised to be due to passivation of surface states (electron trap sites) and therefore a reduction in recombination with surface holes.

The high stability of Ta_2O_5 allowed additional experiments to be carried out, including steady state absorbance and dark cyclic voltammetry which helped to support the assignment of the 575 nm to electron trap states rather than to a surface water oxidation intermediate (hole trap).

The suitability of the 575 nm TAS decay kinetics to bi-exponential fitting coupled with the only partial passivation of this feature following Ta_2O_5 deposition suggests that the trap states probed here exist as more than one population. Temperature dependent TAS measurements were carried out in an attempt to establish the energies of these surface state populations, however, the experimental errors in these measurements were deemed too high to confidently assert any conclusions. Due to the complexity of trap states in photoelectrode materials, it is reasonable to expect that this experiment is too simplistic.

The addition of Ta_2O_5 also altered the surface states assigned to a water oxidation intermediate. The deposition of the overlayer reduced the 650 nm TAS signal assigned to holes and the dark CV feature assigned to holes accumulating at the surface, potentially in the form of water oxidation intermediates. Although reducing the amount of water oxidation intermediates on the surface is undesirable, there was a clear improvement in photocurrent for overlayers between 1-3 nm thick. This could be due to improved transfer rates/survivability of the remaining intermediates as a result of electron trap passivation, similar to that observed in chapter 2. It could also suggest that concentrating a population of holes on a small area of the photoelectrode (*i.e.* in cracks/gaps in an overlayer where exposed hematite remains) improves the water oxidation rate.

When considering a viable photoelectrochemical device, although Ta_2O_5 consistently lead to enhanced photocurrents, the improvement to films which already had a reasonable level of activity (such as HT-Fe_2O_3 and α-Fe_2O_{3-x}) was marginal. In addition to this, ALD processes are often costly and time consuming, and while the removal of undesirable surface states in photoelectrodes such as hematite has been shown to be a worthwhile cause, scale up of ALD to achieve this may not be economically feasible. To make a viable photoelectrochemical device on a large scale it would be desirable to find a more cost effective surface treatment and

possibly one which is less likely to hinder the catalytic surface properties of the photoelectrode. One such approach, using acid treatment, will be discussed in the next chapter.

3.5 References

1. F. Le Formal, S. R. Pendlebury, M. Cornuz, S. D. Tilley, M. Grätzel, and J. R. Durrant, *J. Am. Chem. Soc.*, 2014, **136**, 2564–74.

2. M. Forster, R. J. Potter, Y. Ling, Y. Yang, D. R. Klug, Y. Li, and A. J. Cowan, *Chem. Sci.*, 2015, **6**, 4009–4016.

3. F. Le Formal, N. Tétreault, M. Cornuz, T. Moehl, M. Grätzel, and K. Sivula, *Chem. Sci.*, 2011, **2**, 737.

4. Y. Ling, G. Wang, D. a Wheeler, J. Z. Zhang, and Y. Li, *Nano Lett.*, 2011, **11**, 2119–25.

5. R. Liu, Z. Zheng, J. Spurgeon, and X. Yang, *Energy Environ. Sci.*, 2014, **7**, 2504.

6. O. Neufeld, N. Yatom, and M. Caspary Toroker, *ACS Catal.*, 2015, **5**, 7237–7243.

7. E. O. Filatova and A. S. Konashuk, *J. Phys. Chem. C*, 2015, **119**, 20755–20761.

8. P. A. Kohl, *J. Electrochem. Soc.*, 1977, **124**, 225.

9. S. Hu, N. S. Lewis, J. W. Ager, J. Yang, J. R. McKone, and N. C. Strandwitz, *J. Phys. Chem. C*, 2015, **119**, 24201–24228.

10. L. Steier, I. Herraiz-Cardona, S. Gimenez, F. Fabregat-Santiago, J. Bisquert, S. D. Tilley, and M. Grätzel, *Adv. Funct. Mater.*, 2014, **24**, 7681–7688.

11. M. Barroso, C. A. Mesa, S. R. Pendlebury, A. J. Cowan, T. Hisatomi, K. Sivula, M. Grätzel, D. R. Klug, and J. R. Durrant, *Proc. Natl. Acad. Sci. U. S. A.*, 2012, **109**, 15640–5.

12. M. W. Kanan and D. G. Nocera, *Science*, 2008, **321**, 1072–1075.

13. W.-J. Chun, A. Ishikawa, H. Fujisawa, T. Takata, J. N. Kondo, M. Hara, M. Kawai, Y. Matsumoto, and K. Domen, *J. Phys. Chem. B*, 2003, **107**, 1798–1803.

14. V. Rico, A. Borrás, F. Yubero, J. P. Espinós, F. Frutos, and A. R. González-Elipe, *J. Phys. Chem. C*, 2009, **113**, 3775–3784.

15. H. Wang and J. a. Turner, *J. Electrochem. Soc.*, 2010, **157**, F173.

16. W. Chen, Y. Wu, J. Liu, C. Qin, X. Yang, A. Islam, Y.-B. Cheng, and L. Han, *Energy Environ. Sci.*, 2015, **8**, 629–640.

17. S. Chen and L. Wang, *Chem. Mater.*, 2012, **3666**, 1–5.

18. C. Li, T. Wang, Z. Luo, D. Zhang, and J. Gong, *Chem. Commun.*, 2015, **51**, 7290–7293.

19. D. a. Wheeler, G. Wang, Y. Ling, Y. Li, and J. Z. Zhang, *Energy Environ. Sci.*, 2012, **5**, 6682.

20. O. Zandi and T. W. Hamann, *J. Phys. Chem. Lett.*, 2014, **5**, 1522–1526.

21. V. Pecharsky, P. Zavalij, J. R. Votano, M. Parham, and L. H. Hall, *Fundamentals of Powder Diffraction and Structural Characterization of Materials*, Springer US, Boston, MA, 2009.

22. K. Sivula, *J. Phys. Chem. Lett.*, 2013, **4**, 1624–1633.

23. D. J. Griffiths, *Introduction to Quantum Mechanics*, Prentice Hall, 2nd edn., 2004.

24. M. Barroso, S. R. Pendlebury, A. J. Cowan, and J. R. Durrant, *Chem. Sci.*, 2013, **4**, 2724.

25. A. J. Cowan, C. J. Barnett, S. R. Pendlebury, M. Barroso, K. Sivula, M. Grätzel, J. R. Durrant, and D. R. Klug, *J. Am. Chem. Soc.*, 2011, **133**, 10134–10140.

26. S. R. Pendlebury, A. J. Cowan, M. Barroso, K. Sivula, J. Ye, M. Grätzel, D. R. Klug, J. Tang, and J. R. Durrant, *Energy Environ. Sci.*, 2012, **5**, 6304–6312.

27. Y. Ling, G. Wang, J. Reddy, C. Wang, J. Z. Zhang, and Y. Li, *Angew. Chem. Int. Ed. Engl.*, 2012, **51**, 4074–9.

28. Y. Ling, G. Wang, H. Wang, Y. Yang, and Y. Li, *ChemSusChem*, 2014, **7**, 848–53.

29. L. Xi, S. Y. Chiam, W. F. Mak, P. D. Tran, J. Barber, S. C. J. Loo, and L. H. Wong, *Chem. Sci.*, 2013, **4**, 164–169.

30. C. Y. Cummings, F. Marken, L. M. Peter, A. a Tahir, and K. G. U. Wijayantha, *Chem. Commun.*, 2012, **48**, 2027.

31. F. Fransen, M. J. Madou, W. H. Laflere, R. L. Van Meirhaeghe, D. Vanmaekelbergh, F. Cardon, D. Vanmaekelbergh, F. Cardon, R. L. Van Meirhaeghe, W. H. Laflere, J. O. Williams, and E. S. Crawford, *J. Phys. D. Appl. Phys.*, 1978, **11**, 63–67.

32. M. Tallarida, C. Das, D. Cibrev, K. Kukli, A. Tamm, M. Ritala, T. Lana-Villarreal, R. Gómez, M. Leskelä, and D. Schmeisser, *J. Phys. Chem. Lett.*, 2014, **5**, 3582–3587.

33. B. Klahr and T. Hamann, *J. Phys. Chem. C*, 2014, **118**, 10393–10399.

34. J. Moir, N. Soheilnia, K. Liao, P. O'Brien, Y. Tian, K. S. Burch, and G. a. Ozin, *ChemSusChem*, 2015, **8**, 1557–1567.

35. N. Yatom, O. Neufeld, and M. Caspary Toroker, *J. Phys. Chem. C*, 2015, **119**, 24789–24795.

36. T. Takashima, K. Ishikawa, and H. Irie, *J. Phys. Chem. C*, 2016, **120**, 24827–24834.

37. B. Klahr, S. Gimenez, O. Zandi, F. Fabregat-Santiago, and T. Hamann, *ACS Appl. Mater. Interfaces*, 2015, **7**, 7653–7660.

38. O. Zandi and T. W. Hamann, *Nat. Chem.*, 2016, **8**, 778–783.

39. N. Yatom, O. Neufeld, and M. Caspary Toroker, *J. Phys. Chem. C*, 2015, **119**, 24789–24795.

40. O. Zandi and T. W. Hamann, *Phys. Chem. Chem. Phys.*, 2015, **17**, 22485–22503.

41. L. M. Peter, K. G. U. Wijayantha, and A. A. Tahir, *Faraday Discuss.*, 2012, **155**, 309–322.

42. C. Y. Cummings, F. Marken, L. M. Peter, K. G. U. Wijayantha, and A. A. Tahir, 2012.

43. B. Klahr, S. Gimenez, F. Fabregat-Santiago, J. Bisquert, and T. W. Hamann, *Energy Environ. Sci.*, 2012, **5**, 7626.

44. B. Klahr, S. Gimenez, F. Fabregat-Santiago, T. Hamann, and J. Bisquert, *J. Am. Chem. Soc.*, 2012, **134**, 4294–4302.

45. G. Liu, J. C. Yu, G. Q. M. Lu, and H.-M. Cheng, *Chem. Commun.*, 2011, **47**, 6763–83.

46. S. Bai, L. Wang, Z. Li, and Y. Xiong, *Adv. Sci.*, 2017, **4**, 1600216.

47. R. Li, F. Zhang, D. Wang, J. Yang, M. Li, J. Zhu, X. Zhou, H. Han, and C. Li, *Nat. Commun.*, 2013, **4**, 1432.

48. R. Li, H. Han, F. Zhang, D. Wang, and C. Li, *Energy Environ. Sci.*, 2014, **7**, 1369.

49. O. Neufeld, N. Yatom, and M. Caspary Toroker, *ACS Catal.*, 2015, **5**, 7237–7243.

50. M. R. Morris, S. R. Pendlebury, J. Hong, S. Dunn, and J. R. Durrant, *Adv. Mater.*, 2016, **28**, 7123–7128.

51. K. Kobayashi, G. Okada, and J. Kumanotani, *J. Mater. Sci. Lett.*, 1988, **7**, 853–854.

4

Improving the photoelectrochemical performance of α-Fe_2O_3 using a surface acid treatment

Contents

4.2 Introduction

4.2.1 Overview

This chapter reports a new strategy for improving the photocurrent of Sn-hematite photoanodes by suppression of electron-hole recombination using an acid treatment followed by an annealing step. The acid-treated hematite films show substantially enhanced photocurrent densities and IPCE values compared to the untreated samples. Electrochemistry and impedance spectroscopy studies revealed that the enhanced photocurrent is partly due to improved efficiency of charge separation. TAS studies coupled to electrochemical measurements indicate that in addition to improved bulk electrochemical properties, acid treating decreased surface electron-hole recombination losses due to a greater yield of the trapped photoelectrons being extracted to the external circuit. This work was done in collaboration with professor Yat Li *et al.* at the University of California, Santa Cruz.[1]

4.2.2 Surface treatments

Chapter 3 showed that Ta_2O_5 is capable of passivating deleterious electron trap states at the surface of hematite, however it also provided evidence that such a passivation method, which includes the deposition of a physical insulating layer, also inhibits the formation of surface states/reaction sites attributed to water oxidation. In order to remove deleterious surface states from hematite without inhibiting water oxidation it may be desirable to use a surface passivating treatment which does not involve a physical insulating layer. Furthermore, while it may be possible for ALD of some materials to be cost effectively employed on a large scale, an alternative approach may prove more economical for producing scaled up photoelectrochemical devices. A number of routes for passivating hematite surfaces have been demonstrated in the literature which do not involve the physical deposition of an additional

overlayer material. One of the most common and perhaps simplest route to surface passivation is the use of an additional high temperature annealing step following the formation of a hematite photoelectrode. Hamann *et al.* showed that annealing ultrathin hematite photoelectodes at 800 ^{o}C in air improved activity and noted the removal of a set of surface states as observed by cyclic voltammetry.[2] Surface re-growths and corrosions have also been shown to alter surface states in hematite. Wang *et al.* reported a surface re-growth method as a route to passivating surface defects in which solution synthesised nanostructured films were re-immersed into the reaction mixture and annealed several times to grow new layers of hematite over the previously formed surface.[3] The regrown films exhibited a more favourable onset potential which was attributed to dissolution of the initial hematite surface and replacement by a new more favourable (defect reduced) surface. *Zou et al.* also demonstrated a surface corrosion method that was able to cathodically shift the photocurrent onset potential of Ti doped hematite.[4] This improvement was assigned not to surface state passivation, but instead to suppression of the back reaction by forming a barrier layer on the surface. Photocorrosion of a hematite surface by illuminating under intense light in the presence of chloride anions has also been shown to passivate trap states and improve photoactivity.[2,5] Finally, encouraging the growth of a different layer at the surface compared to the bulk of a hematite photoelectrode during synthesis has also been demonstrated. Wong *et al.* synthesised Sn-doped hematite films which possessed an $Fe_xSn_{1-x}O_4$ surface layer, leading to enhanced photocurrent attributed to a passivating-type effect.[6]

The above examples demonstrate that simple surface treatments can offer useful routes to surface passivation and photoactivity improvement in hematite. With these reports in mind, this chapter describes the use of an acid treatment followed by an annealing step to improve the activity of Sn-Fe_2O_3. Electrochemical and TAS methods are then used to rationalise the enhancement of these films.

4.3 Results and discussion

4.3.1 Acid treatment of Sn-Fe_2O_3

The hematite nanowire films used in this study were first prepared by Li *et al.* using a method previously reported in the literature.[7] Full details of the synthesis can be found in section 2.1.2 of the experimental chapter (chapter 6). The Sn-Fe_2O_3 films used here were synthesised in an autoclave vessel and additionally doped with a $SnCl_4$ solution prior to annealing. This route results in Sn-Fe_2O_3 films with a different structure and activity to the Fe_2O_3 films (LT-Fe_2O_3 and HT-Fe_2O_3) reported in chapter 3 (which did not use an autoclave or $SnCl_4$ treatment and instead relied on doping from the FTO substrate).

The Sn-Fe_2O_3 films were acid-treated by immersing them in pure acetic acid solution (99.8%) for 5 minutes, removed without washing and then annealed in air at 450 ^oC for 30 minutes as shown in Figure 97. The acid treatment showed no visible change to the hematite films as seen by eye.

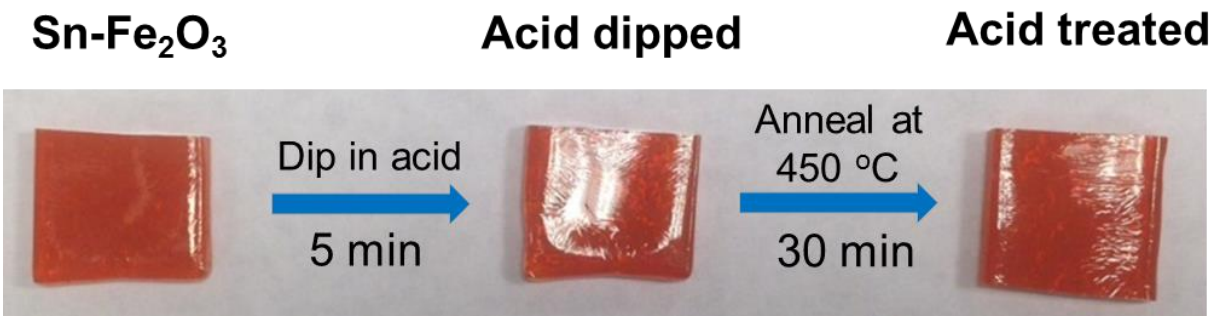

Figure 97 – Images showing Sn-hematite during the acid treatment process.

Following acid treatment the Sn-Fe_2O_3 films showed a significant enhancement in photocurrent (Figure 98a) as well as a large improvement in the incident photon-to-current (IPCE) values (Figure 98b). Acid dipping alone resulted in no noticeable change in photoactivity. Carrying out only the thermal annealing step resulted in a small increase in photocurrent (Figure 98a,

orange line). Hence, both the acid dipping and thermal annealing step combined are required for the large improvement in photocurrent of Sn-Fe_2O_3.

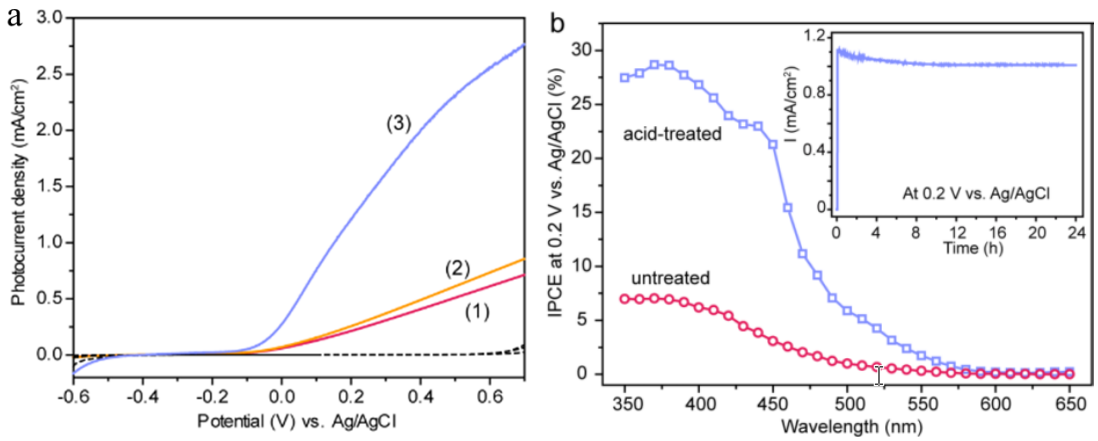

Figure 98 - a) Photocurrents collected for untreated (red), thermally annealed (orange) and acid-treated (blue) hematite photoaonodes scanned at 20 mV s^{-1} in a 1 M NaOH (pH ~13.7) under illumination by simulated solar light of 100 mW cm^{-2} and in the dark (black dotted lines). b) IPCE spectra of untreated (red) and acid-treated (blue) hematite. Inset: I–t curve of acid-treated hematite. Measurements were carried out by Li et al.[1]

The improved activity of the acid-treated films remains after 24 hours under continuous photoelectrochemical conditions under white light illumination (100 mW cm^{-2}) at 0.2 $V_{Ag/AgCl}$ (Figure 98b inset) and was also found to remain without significant decline after several weeks of photoelectrochemical and TAS studies. This acid treatment method was also found to work with a range of alternative acids, including HCl, HNO_3 and H_3PO_4 (Figure 99), however the improvement is most prominent with acetic acid.

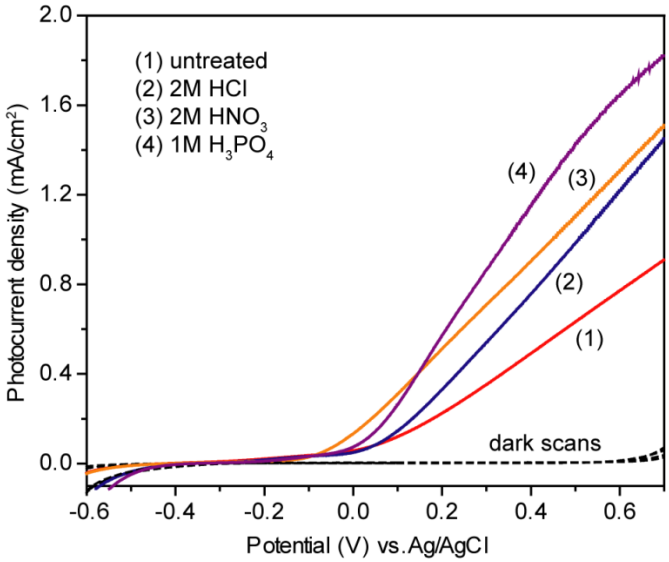

Figure 99 - Photocurrents collected for Sn-Fe_2O_3 films which have been acid-treated using a range of different acids, compared to untreated Sn-Fe_2O_3 (red) scanned at 20 mV s^{-1} in 1 M NaOH (pH ~13.7) under illumination by simulated solar light of 100 mW cm^{-2} and in the dark (black dotted lines). Measurements were carried out by Li et al.[1]

4.3.2 Characterisation of hematite following acid treatment

In order to rationalise the effect of the acid treatment the films were initially characterised by Yat Li and his group using UV-Vis absorbance, SEM, lattice resolved TEM, surface area approximation, XRD and XPS. These findings will discussed below.

The UV-Vis absorbance spectra probed from 300-800 nm remained unchanged following acid treatment showing that the improved photoactivity of acid-treated Sn-Fe_2O_3 is not due improved light absorbance, Figure 100.

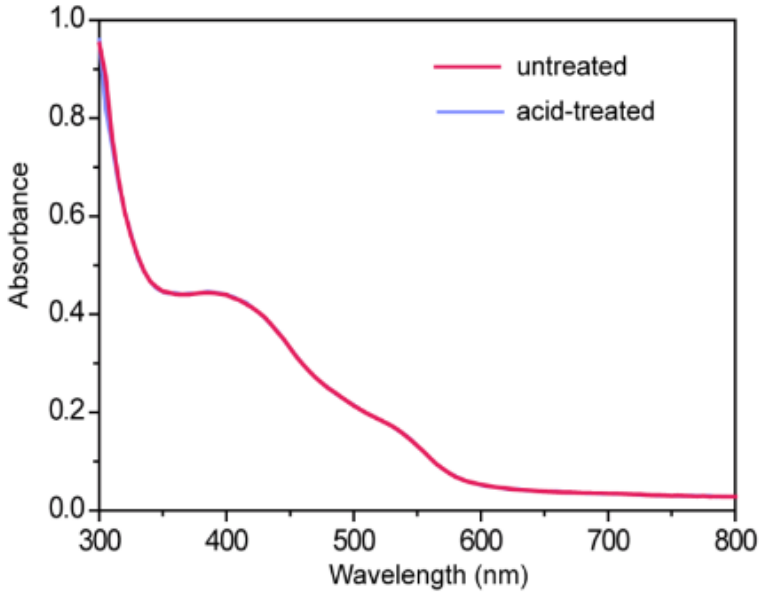

Figure 100 - UV-Vis absorbance spectra collected from 300-800 nm for untreated and acid-treated hematite samples. Measurements were carried out by Li et al.[1]

Hematite is known to be unstable in acidic media and as such it is possible that partial dissolution or etching of the surface occurs when in contact with acid. If surface corrosion occurs, it is likely that some of the surface of α-Fe_2O_3 exposed to acid forms FeOOH (the intermediate typically formed during solution based synthesis of hematite). This FeOOH would then be reconverted back to α-Fe_2O_3 during the annealing step as shown below, effectively re-growing the surface.

$$Fe_2O_{3-x} \xrightarrow{H^+} FeOOH \xrightarrow[air]{400^oC} Fe_2O_3$$

Figure 101 shows SEM images of the hematite surface and TEM images collected at the edge of the hematite film before (1) and after (2) full acid treatment. The SEM images show the vertically aligned hematite nanowires on the FTO substrate, with average diameters of ~100 nm and average lengths of ~1 μm. Following acid treatment the structure as viewed by SEM

appeared to be unchanged. Likewise, TEM imaging showed no noticeable change following acid treatment with no signs of etching or shell coating.

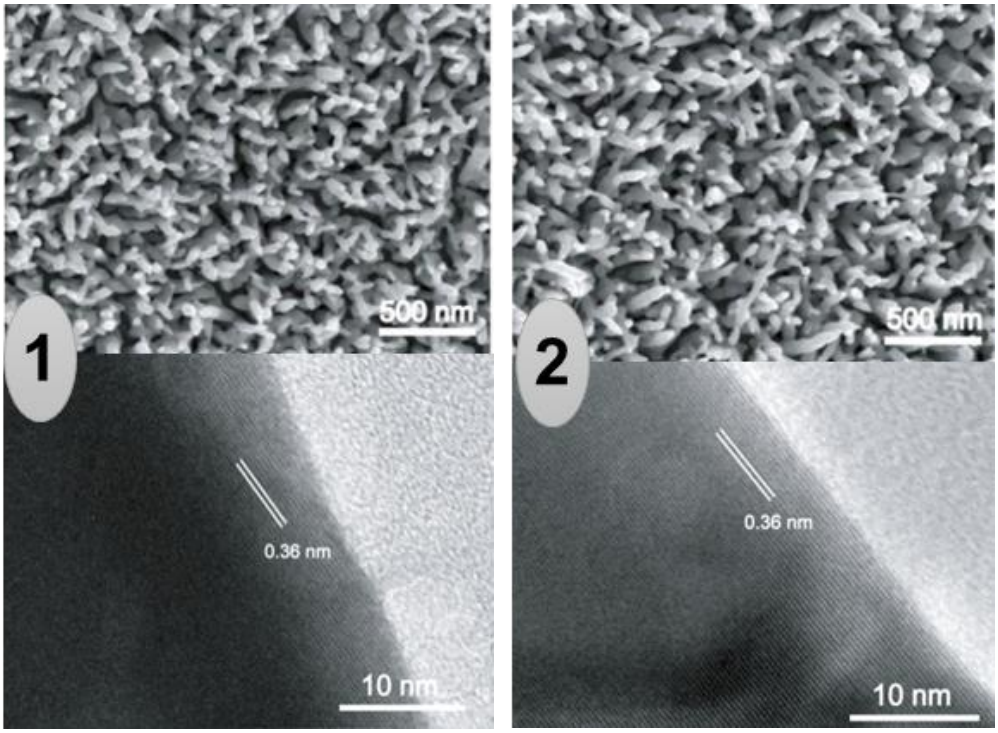

Figure 101 - SEM images (top) and Lattice-resolved TEM images collected at the edge (bottom) of (1) untreated hematite nanowires and (2) acid-treated hematite nanowires. Measurements were carried out by Li et al.[1]

To further establish whether the acid treatment affected the hematite structure, the surface area was approximated before and after treatment. A dye (methylene blue in this case) is first adsorbed onto the surface of the hematite film. This dye is then desorbed into solution and an absorbance spectrum of the solution is measured to establish the quantity of dye adsorbed onto the surface. Assuming the dye adsorbs as a monolayer, an approximation of the surface area of the film can be obtained. Even in the case of multilayer adsorption comparison between films of the same chemical nature will highlight any differences in structure. Figure 102 shows the dye adsorption measurements before and after acid treatment, which indicate no change in

surface area, in line with the SEM and TEM images. XRD of the hematite films before and after acid treatment indicated that the crystal phase remained unchanged.

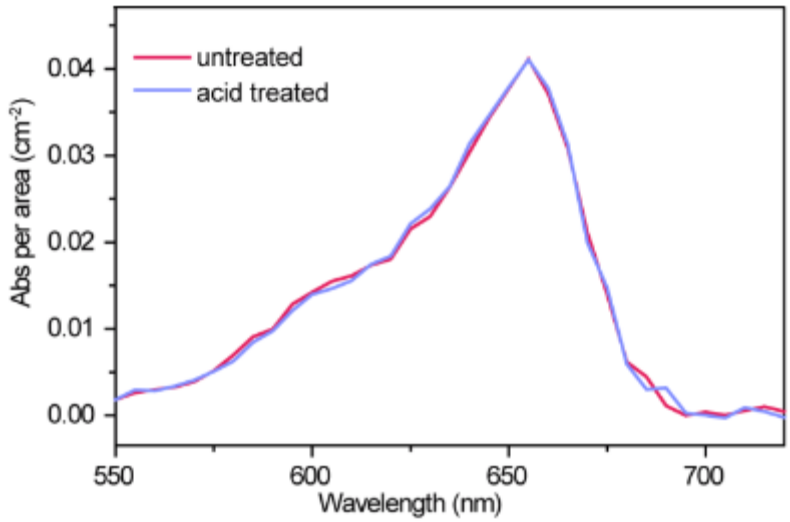

Figure 102 - UV-Vis spectra collected for solutions containing methylene blue dye molecules desorbed from the surface of untreated and acid-treated hematite. Measurements were carried out by Li et al.[1]

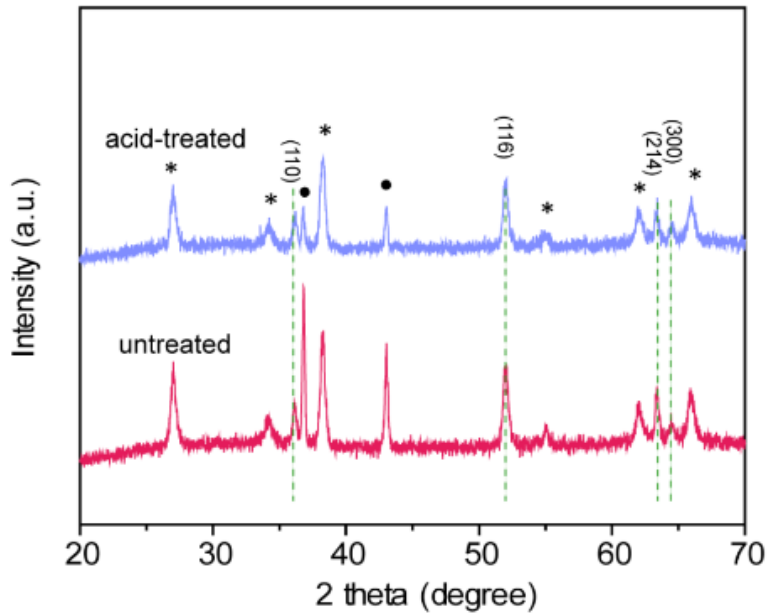

Figure 103 - XRD spectra collected for untreated and acid-treated hematite samples. Dashed lines highlight the characteristic diffraction peaks of hematite (International Centre for Diffraction Data JCPDS 33-0664). The asterisks and circles highlight the diffraction peaks of SnO_2 (International Centre for Diffraction Data JCPDS 41-1445) originating from FTO substrate and the peaks from aluminium in the substrate, respectively. Measurements were carried out by Li et al.[1]

X-ray photoelectron spectroscopy (XPS) was used to investigate the possible influence of acid treatment on the chemical nature of the hematite surface, Figure 104. Both untreated and acid-treated samples exhibit an Fe $2P_{1/2}$ peak and an Fe $2P_{3/2}$ peak centred at binding energies of 724.5 eV and 711.4 eV, which are typical values reported for Fe^{3+} in α-Fe_2O_3.[8] Notably, acid-treated hematite has a slightly higher Fe^{2+} signal (a satellite peak located at 716 eV)[6] than the untreated sample, suggesting Fe^{2+} sites were created during acid treatment. Acid-treated hematite also exhibits an additional shoulder peak at 531.9 eV which can be attributed to Fe-OH, and has been reported to be located at a binding energy ~1.5-2.0 eV higher than the O 1s peak of α-Fe_2O_3.[9] The XPS data suggests that the increased amount of hydroxyl groups on the hematite surface following acid treatment are accompanied by the formation of more Fe^{2+} sites to balance the charge. This increase in hydroxyl groups suggests a change to the nature of the hematite, perhaps related to the corrosion and re-conversion between α-Fe_2O_3 and FeOOH.

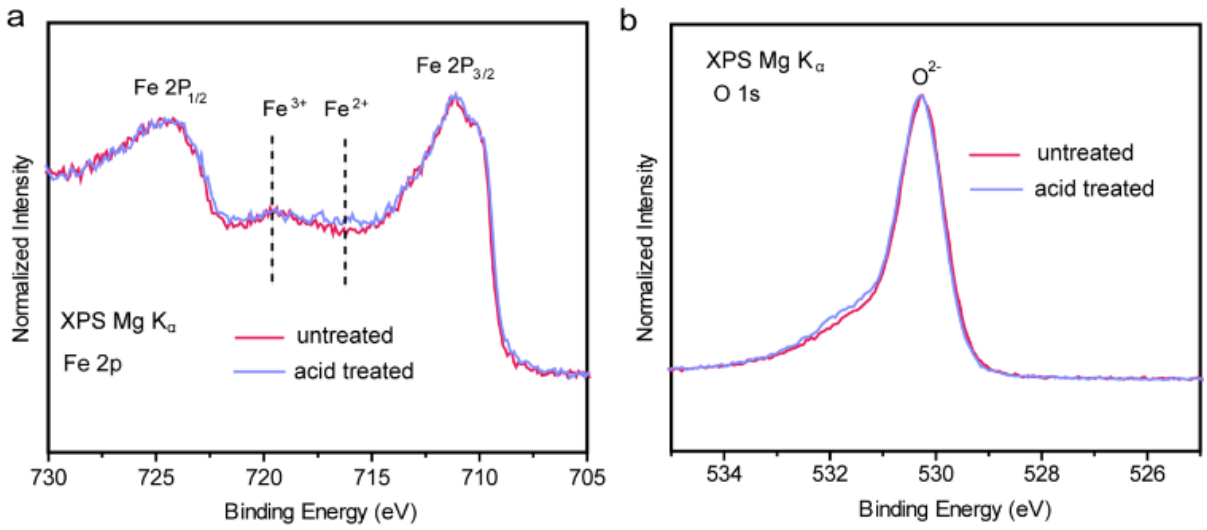

Figure 104 - Overlay of normalised (a) Fe 2p and (b) O 1s XPS spectra of untreated hematite and acid-treated hematite samples. The dashed lines in (a) highlight the satellite peaks of Fe^{3+} and Fe^{2+} species. Measurements were carried out by Li et al.[1]

4.3.3 Charge separation study of acid-treated hematite

With no clear change in structure or light absorption, the improvement in photoactivity following acid treatment appeared to be related to charge collection following photon absorption. The electronic properties of hematite before and after acid treatment were compared by Li *et al.* using electrochemical impedance and charge separation measurements. Figure 105a shows the Mott–Schottky plots based on electrochemical impedance values for untreated and acid-treated hematite as well as thermally annealed hematite which showed a small increase in activity. The donor density of acid-treated hematite was calculated to be 1.11×10^{20} cm^{-3}, an order of magnitude higher than that of the untreated sample (1.06×10^{19} cm^{-3}). The donor density of the thermally annealed film without acid treatment was found to be 1.23×10^{19} cm^{-3}, slightly higher than the untreated film. The increased donor density is expected to improve the electrical conductivity of hematite, and therefore reduce the electrodes internal resistance and the voltage drop at the interface between hematite and the FTO substrate. In addition to Mott-Schottky, EIS measurements were used to investigate the influence of acid treatment on the charge transfer at the hematite/electrolyte interface. The Nyquist plots of hematite electrodes shown in Figure 105b consist of a semi-circle in the high-frequency domain and a steep line in the low-frequency domain. Figure 105b inset shows the equivalent circuit used to fit the EIS data. Significantly, the charge transfer resistance (R_{ct}) of hematite was considerably reduced from 113.6 Ω to 5.1 Ω after acid treatment (values in Table 10). The reduced R_{ct} is attributed to the improved electrical conductivity of acid-treated hematite.

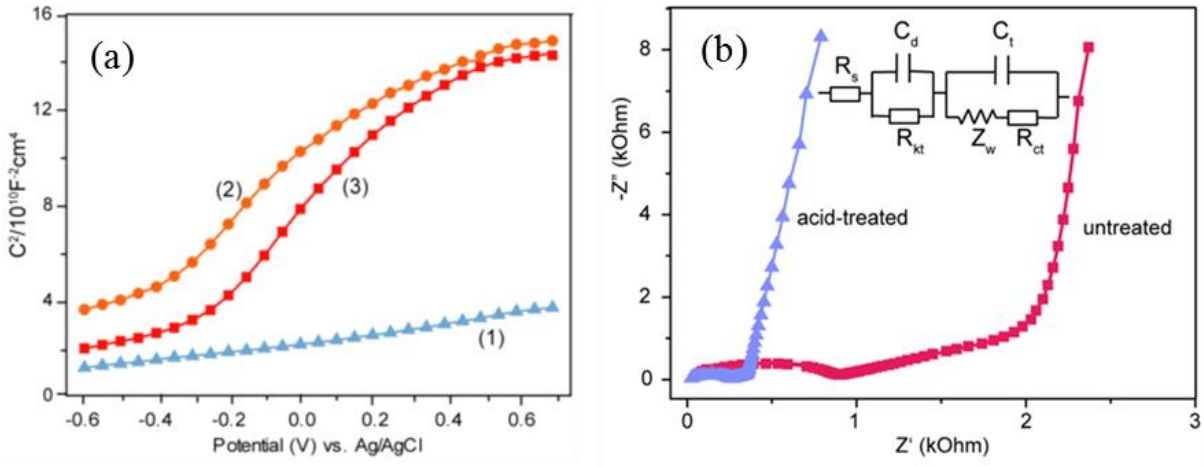

Figure 105 - (a) Mott-Schottky plots of (1) untreated hematite, (2) thermally annealed hematite without acid treatment and (3) acid-treated hematite electrodes collected at 10 kHz in 1 M NaOH (pH ~13.7) electrolyte in the dark. (b) EIS spectra of untreated and acid-treated hematite electrodes. Inset: equivalent circuit used to fit the spectra: Rs is the series resistance, which includes the sheet resistance of the FTO substrate and the external contact resistance of the cell. The parallel elements, R_{kt}, C_d, R_{ct} and C_t, characterise the charge transfer resistance and the double layer capacitance for the hematite electrode and Pt counter electrode. The donor density of untreated hematite was found to be $1.23x10^{19}$ cm^{-3}, the donor density of thermally annealed hematite was found to be $1.06x10^{19}$ cm^{-3} and the donor density of acid-treated hematite was found to be $1.11x10^{20}$ cm^{-3}. Measurements were carried out by Li et al.[1]

Sample	R_s/U	R_{kt}/U	R_{ct}/U	Z_W/U·$s^{-0.5}$	C_d/F	C_t/F
Untreated hematite	52.6	863.4	113.6	$6.5e^{-6}$	$1.4e^{-9}$	$7.2e^{-7}$
Acid treated hematite	19.3	238.7	5.1	$2.4e^{-6}$	$4.9e^{-9}$	$8.1e^{-6}$

Table 10 - Table showing the values obtained from EIS measurements in Figure 105b. Measurements were carried out by Li et al.[1]

While it would be expected that the acid treatment primarily modifies the surface properties of the hematite electrode, the increased donor density suggests this is not entirely the case. In light of the donor density change following acid treatment, the yield of initial charge separation (defined as the yield of photogenerated holes reaching the surface) was investigated. Sivula *et al.* have previously described a simple method for distinguishing between bulk and surface electron-hole recombination losses,[10] where the photoelectrochemical response in the presence of H_2O_2, an efficient hole scavenger, is compared to that achieved during water oxidation.

The water splitting photocurrent ($J^{H_2O}_{Photocurrent}$) shown in equation 1 is a product of the rate of photon absorption expressed as a current density ($J_{absorbed}$), the charge separation yield of the photogenerated carriers ($P_{charge\ separation}$), and charge injection yield to the electrolyte ($P_{charge\ injection}$):

$$J^{H_2O}_{Photocurrent} = J_{absorbed} \times P_{charge\ separation} \times P_{charge\ injection} \quad (1)$$

$P_{charge\ separation}$ is the yield of the photogenerated holes that reach the electrode/electrolyte interface (i.e. the ones that do not recombine in the bulk). $P_{charge\text{-}injection}$ is the yield of those holes that have reached the electrode/electrolyte interface which are injected into the electrolyte to oxidise water (i.e. do not recombine with surface trapped electrons). On the other hand, the photocurrent measured in the presence of H_2O_2 ($J^{H_2O_2}_{Photocurrent}$) shown in equation 2 is a product of only ($J_{absorbed}$) and ($P_{charge\ separation}$) because the charge injection yield becomes *ca.* 100% due to the rapid hole transfer to H_2O_2:

$$J^{H_2O_2}_{Photocurrent} = J_{absorbed} \times P_{charge\ separation} \quad (2)$$

The injection yield ($J_{charge\ injection}$) is obtained by dividing $J^{H_2O}_{Photocurrent}$ by $J^{H_2O_2}_{Photocurrent}$ to give the plot in Figure 106b. $J_{absorbed}$ can be obtained by measuring the light absorption of the photoelectrode and integrating it with respect to the incoming light, in this case the 100 mW cm^{-2} solar simulated spectrum. With $J_{charge\ injection}$ and $J_{absorbed}$ known, the separation efficiency as shown in Figure 106a can be obtained by dividing $J^{H_2O_2}_{Photocurrent}$ by $J_{absorbed}$.

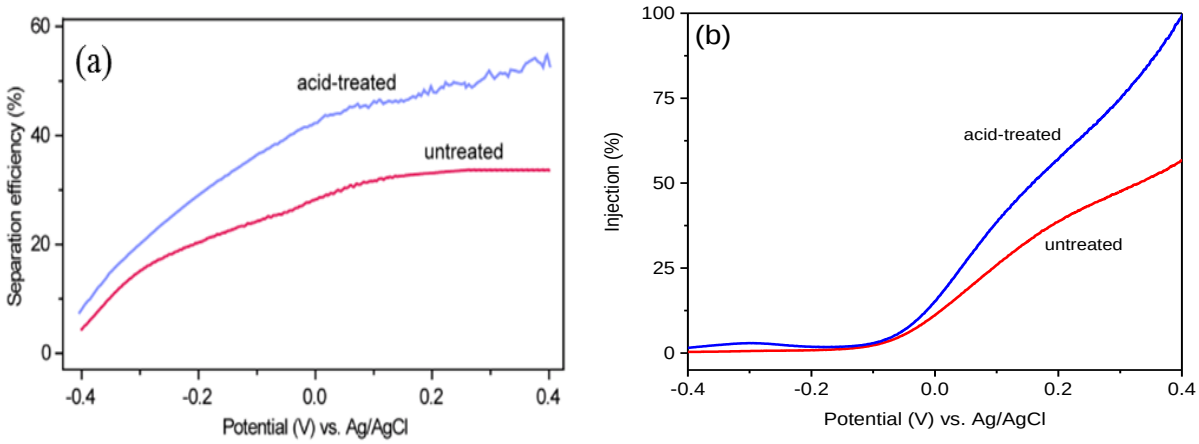

Figure 106 – (a) Plot of the yield of charge separation efficiency vs. applied bias. (b) Plot of charge injection efficiency vs. applied bias for untreated and acid-treated hematite photoanodes. Measurements were carried out by Li et al.[1]

Charge separation efficiency measurements (Figure 106a) indicate a decrease in bulk electron-hole recombination following acid treatment with the yield of holes reaching the surface increasing from *ca.* 33% for untreated to nearly 50% for acid-treated hematite at 0.2 $V_{Ag/AgCl}$ (pH ~13.7). This increase may be expected when considering the large increase in donor density and is expected to contribute to the change in IPCE measured during water splitting, which at 0.2 $V_{Ag/AgCl}$ (pH ~13.7), 350 nm, increases approximately four-fold from *ca.* 7% to 27% (Figure 98). Furthermore, an improvement in charge injection can be observed following acid treatment (Figure 106b) indicating that the increase in the number of charges reaching the surface of the acid-treated film is accompanied by improved transfer of these charges once they are at the surface.

4.3.4 TAS study of acid-treated hematite

In order to further understand the effect of the acid treatment on the electron/hole dynamics of hematite, TAS was employed to probe the electron trap state kinetics and the hole kinetics.

Figure 107 and Figure 108 show TAS spectra probed from 500-850 nm at various applied bias for untreated hematite (Figure 107) and acid-treated hematite (Figure 108). The two key hematite features are observed in both the untreated and acid-treated films when probing in this region (400-950 nm). Firstly, a broad positive feature is observed which is assigned to photoholes.[11–14] The second feature exists as a sharp feature centred at *ca.* 575 nm assigned to trapping and de-trapping of electrons at localised trap states.

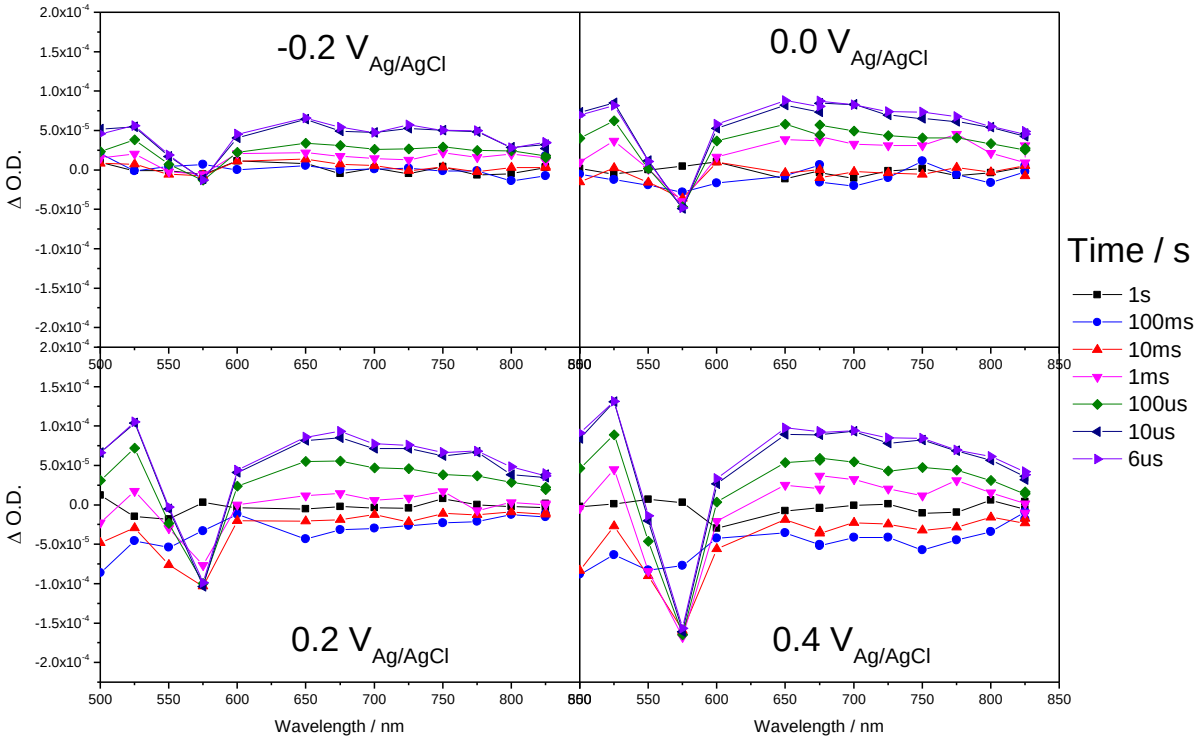

Figure 107 - TAS spectra probed from 500-850 nm of untreated hematite measured in a photoelectrochemical cell (1 M NaOH, pH ~13.7) at a range of applied bias ($V_{Ag/AgCl}$), following 355 nm laser excitation (6 ns pulse, ~100 μJ cm^{-2}).

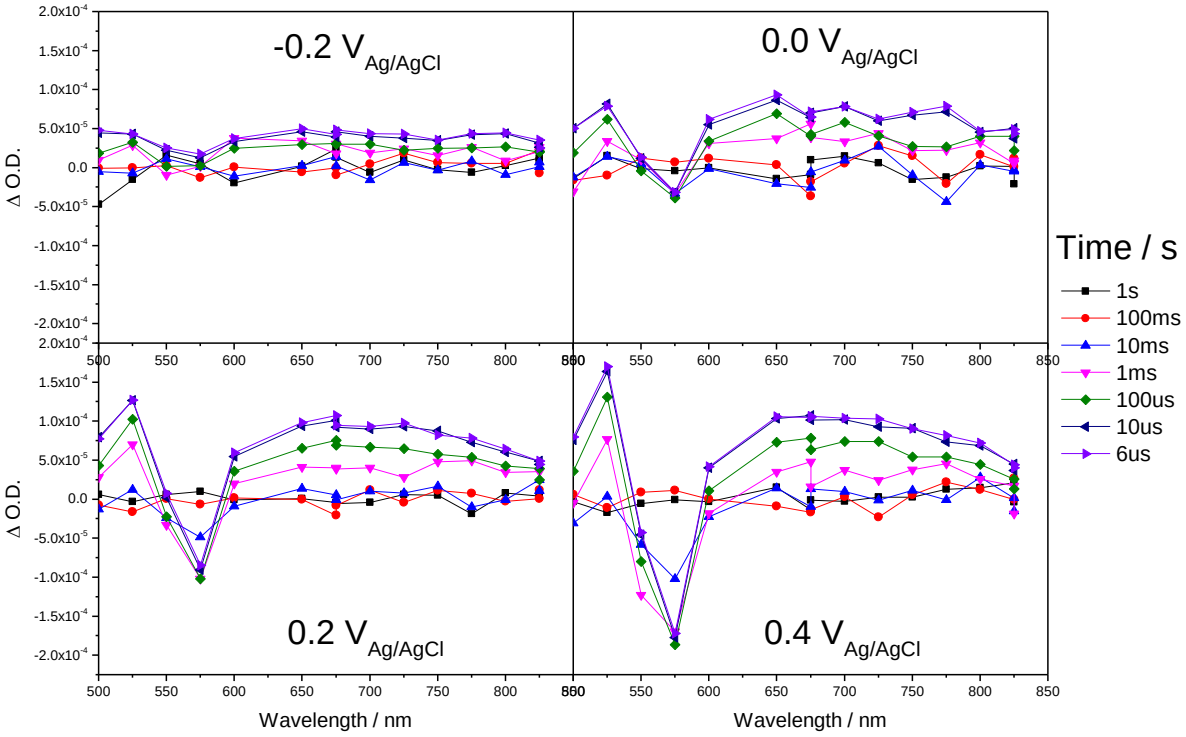

Figure 108 - TAS spectra probed from 500-850 nm of acid-treated hematite measured in a photoelectrochemical cell (1 M NaOH, pH ~13.7) at a range of applied bias ($V_{Ag/AgCl}$), following 355 nm laser excitation (6 ns pulse, ~100 $\mu J\ cm^{-2}$).

Figure 109 shows the TAS kinetics probed at 575 nm (assigned to electron trapping and de-trapping) for untreated and acid-treated hematite at a range of applied bias. In line with previous reports, the magnitude of the negative feature (bleach) assigned to electron trapping is seen to increase with increasing positive bias in both samples. Initial comparisons show that the magnitude of the bleach remains unchanged following acid treatment. More significantly, the rate of de-trapping appears to be accelerated following acid treatment. Figure 110 shows the overlaid TAS kinetics of an untreated and acid-treated Sn-Fe_2O_{3-x} film probed at 575 nm at an applied bias of 0.2 $V_{Ag/AgCl}$ (pH ~13.7).

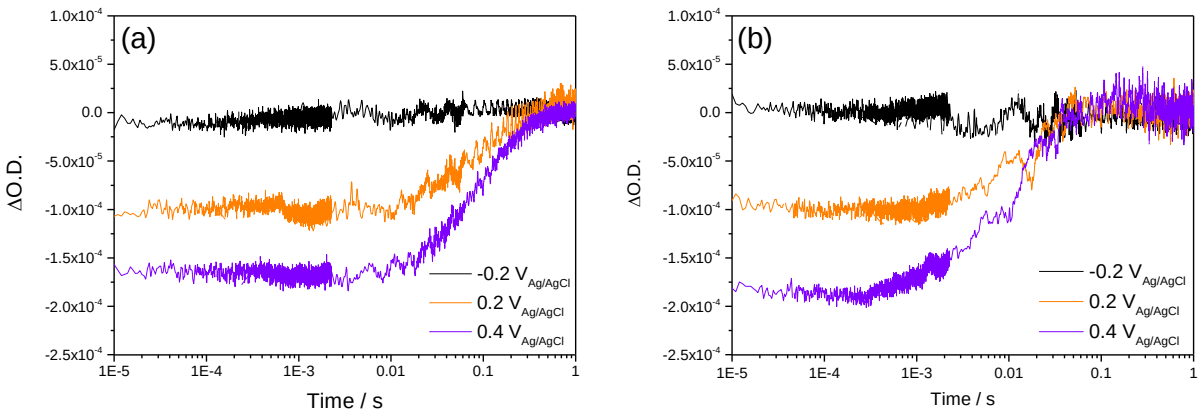

Figure 109 - TAS decay traces probed at 575 nm (electron trapping) for (a) untreated hematite and (b) acid-treated hematite measured in a photoelectrochemical cell (1 M NaOH, pH ~13.7) at a range of applied bias ($V_{Ag/AgCl}$), following 355 nm laser excitation (6 ns pulse, ~100 μJ cm^{-2}).

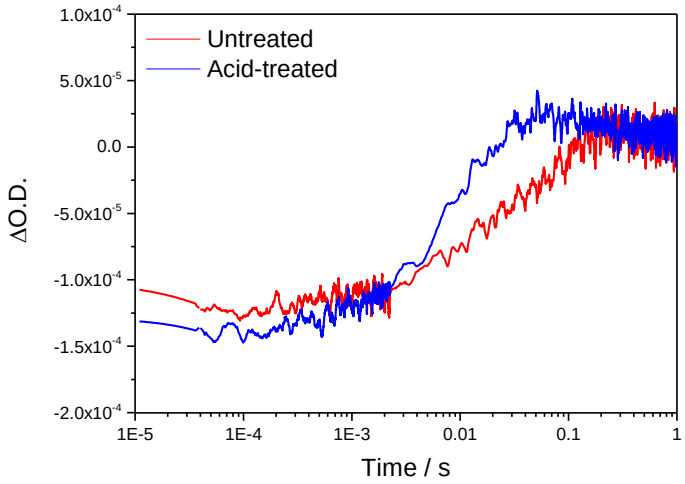

Figure 110 - Overlay of TAS decay traces probed at 575 nm (electron trapping) for untreated and acid-treated hematite measured in a photoelectrochemical cell (1 M NaOH, pH ~13.7) at 0.2 $V_{Ag/AgCl}$, following 355 nm laser excitation (6 ns pulse, ~100 μJ cm^{-2}).

The electron de-trapping dynamics were further investigated by fitting the TAS traces probed at 575 nm to obtain de-trapping rates (Figure 111 and Table 11). In addition to the untreated and acid-treated films, a film that was thermally annealed but not acid treated was also fitted to determine whether this heat treatment alone altered the de-trapping kinetics. Heat treatments have been reported to alter surface states, and as observed in Figure 98, thermally annealing the film without acid treatment resulted in a small increase in photocurrent.

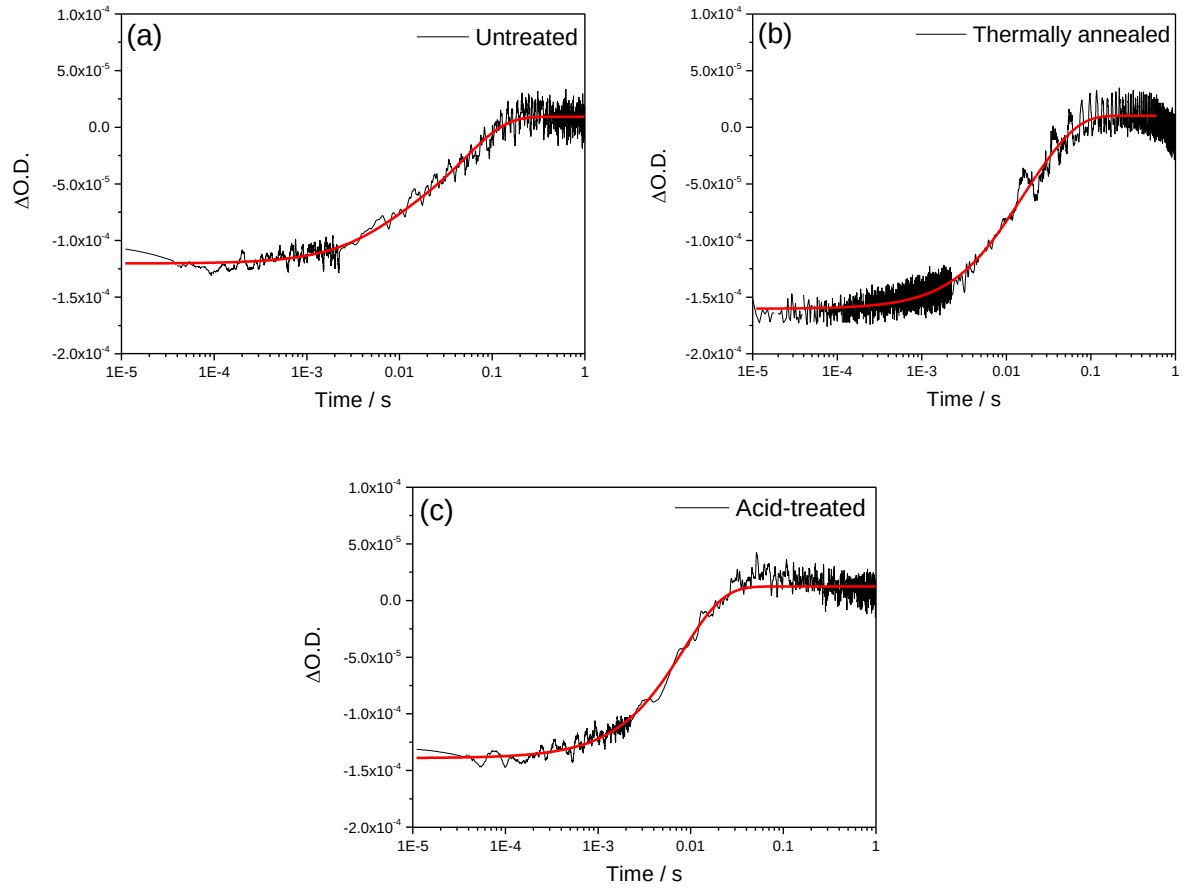

Figure 111 - TAS decays probed at 575 nm (electron trapping) fitted to single exponentials for (a) untreated (b) thermally annealed and (c) acid-treated hematite. Measurements were carried out in a photoelectrochemical cell (1 M NaOH, pH ~13.7) at 0.2 $V_{Ag/AgCl}$, following 355 nm laser excitation (6 ns pulse, ~100 $\mu J\ cm^{-2}$).

Name	Magnitude	Lifetime (s)	Rate (s^{-1})
Untreated	A_1: (-3.3 ±0.1)x10^{-5}	τ_1: (5.9±0.4)x10^{-3}	k_1: 171±11
	A_2: (-1.0 ±0.1)x10^{-4}	τ_2: (5.3±0.6)x10^{-2}	k_2:19.1±0.2
Thermally annealed	A_1: (-5.8±0.4)x10^{-5}	τ_1: (7.0±0.5)x10^{-3}	k_1: 142±11
	A_2: (-1.1±0.1)x10^{-4}	τ_2: (2.8±0.1)x10^{-2}	k_2: 35±2
Acid-treated	A: (-1.5±0.1)x10^{-4}	τ: (8.4±0.1)x10^{-3}	k: 120±9

Table 11 – Fitting parameters with their errors obtained from the fits in Figure 111.

The rate of recovery of the 575 nm bleach, i.e. the rate of loss of trapped electrons in the untreated and thermally annealed samples are well fitted to bi-exponential decay functions of the form shown in equation 3. The untreated film has rate constants of 171 ± 11 s^{-1} and 19.1 ±0.2 s^{-1}. The thermally annealed film has rate constants of 142 ± 11 s^{-1} and 35 ± 2 s^{-1}.

$$\Delta OD_{575}(t) = A_1 e^{-(k_1 t)} + A_2 e^{-(k_2 t)} + y_0 \quad (3)$$

Following full acid treatment the rate of recovery of the 575 nm bleach fits instead to a single exponential decay such as that shown in equation 4, with a rate constant of 120 ± 9 s^{-1}. It appears that the smaller A_1 components initially present in the untreated (A_1: (-3.3±0.1)x10^{-5}) and thermally annealed (A_1: (-5.8±0.4)x10^{-5}) films are no longer present following acid treatment, leaving only the larger A_2 component.

$$\Delta OD_{575}(t) = A_1 e^{-(k_1 t)} + y_0 \quad (4)$$

It is noticeable that the 575 nm kinetics of the films studied in this chapter have similarities to the HT-Fe_2O_3, LT-Fe_2O_3 and Fe_2O_{3-x} films studied in chapter 3. The films studied in chapter 3 fitted well to bi-exponential decays prior to overlayer treatment, indicating multiple trap state populations. Deposition of Ta_2O_5 then resulted in a noticeable decrease in the magnitude of the 575 nm feature and an increase in the rate of detrapping indicating partial passivation of trap states. Furthermore, LT-Fe_2O_3 fitted well to a single exponential decay (as opposed to bi-exponential) following Ta_2O_5 deposition indicating removal of a trap state population. While acid treatment of the Sn-Fe_2O_3 films studied here does not appear to significantly change the magnitude of the 575 nm TAS feature, it does alter the detrapping rate (changes from bi-

exponential to single exponential) indicating that the trap states probed by TAS at 575 nm are affected by the acid treatment.

In chapter 2 back electron transport was highlighted as a significant factor when establishing the difference in activity between air annealed and oxygen deficient hematite electrodes. An increase in donor density in the oxygen deficient hematite resulted in blocking of this back electron transport as measured by TPC. As an increase in donor density was also observed following acid treatment (Figure 105), TPC measurements were carried out to establish whether back electron transport was a significant factor here. Back electron transfer can typically be identified by negative currents on the slow ms-s timescales in TPC caused by recombination between electrons in the bulk hematite and surface trapped holes. Notably in this instance, at the potentials studied (>0.2 V) there is no evidence for back electron transfer in either untreated or acid treated hematite (Figure 112) suggesting that in these Sn-doped materials a large electric field is present which is able to prevent electrons from reaching the surface trapped holes at the semiconductor-liquid junction (SCLJ).

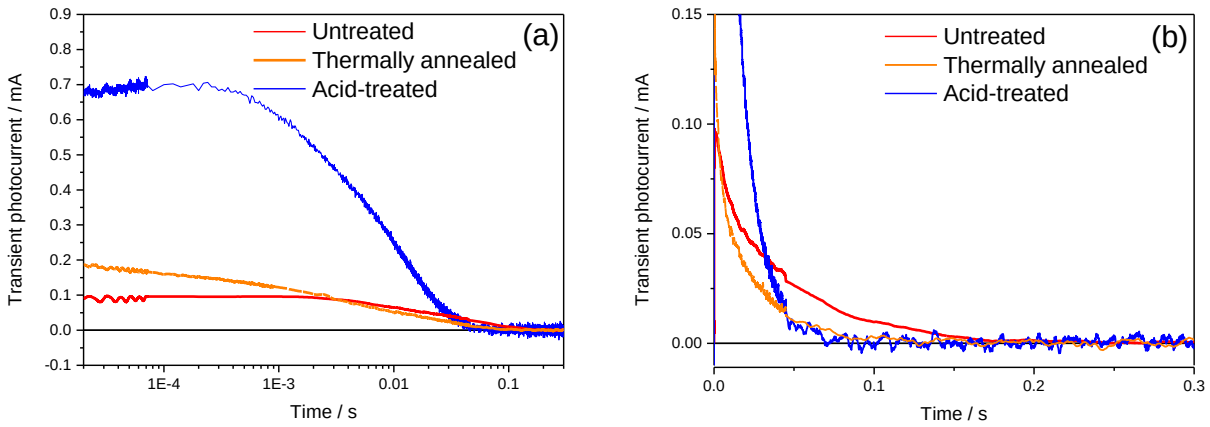

Figure 112 – (a) TPC of untreated (red), thermally annealed (orange) and acid-treated (blue) hematite measured in a photoelectrochemical cell (1 M NaOH, pH ~13.7) at 0.2 $V_{Ag/AgCl}$, following 355 nm laser excitation (6 ns pulse, ~100 μJ cm^{-2}). (b) The same TPC measurement with a linear time scale to highlight the slow portion of the data.

The TPC measurements (Figure 112a) show a significant increase in the magnitude of the acid treated film compared to the untreated film, and a small increase in the thermally annealed film, which is in-line with the observed photocurrents in Figure 98. A change in the lifetime of the TPC measurements is also notable (Figure 112b), with the untreated film being the slowest to decay back to zero. The TPC measurements were integrated with respect to time to provide a measure of total charge passed as shown in Figure 113a. This plot highlights the improved charge extraction to the external circuit following acid treatment. Figure 113b and Table 12 show fittings of the charge extraction plots to obtain charge extraction rates. The rate of charge extraction for the untreated, thermally annealed and acid treated films were all found to fit well to single exponential fits of the form shown in equation 5.

$$\frac{dy}{dt} = A_1 e^{-(k_1 t)} + y_0 \quad (5)$$

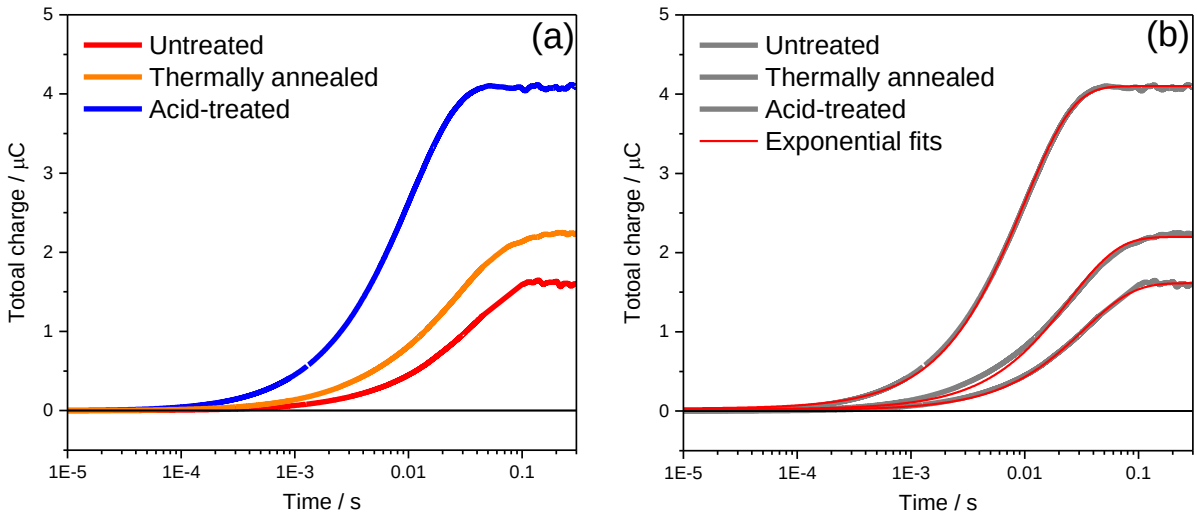

Figure 113 -(a) Total charge extracted converted from the integration of TPC for untreated, thermally annealed and acid-treated hematite. (b) The same charge extracted plot with addition of red fitting lines which show the single exponential fits.

Name	Lifetime (s)	Rate (s^{-1})
Untreated	τ: (3.3±0.3)x10^{-2}	*k*: 30±3
Thermally annealed	τ: (2.5±0.4)x10^{-2}	*k*: 41±7
Acid-treated	τ: (9.8±0.6)x10^{-3}	*k*: 100±6

Table 12 - Shows the fitting parameters with their errors obtained from the fits in Figure 113.

The untreated film has a rate constant of 30 ± 3 s^{-1}. Following thermal annealing this rate is accelerated, giving a rate constant of 41 ± 7 s^{-1}. Following full acid treatment the rate is further accelerated to give a rate constant of 100 ± 6 s^{-1}. The lower charge extraction yield in the untreated and thermally annealed samples indicates that the processes occurring in parallel to electron transport to the external circuit, such as fast bulk recombination and slower trap-mediated recombination are more significant in these films compared to the acid treated sample. It is notable that the rates obtained here for charge extraction compare closely to the rates of decay of the slow 575 nm TAS features fitted in Figure 111. To further explore this, Figure 114 shows the normalised overlay of TAS and charge extracted for each film which highlights the relationship between the rate of decay of the 575 nm TAS signal and the rate of charge extraction as measured by TPC in all 3 films. The overlap is an indication that a portion of the de-trapped electrons are able to reach the external circuit.

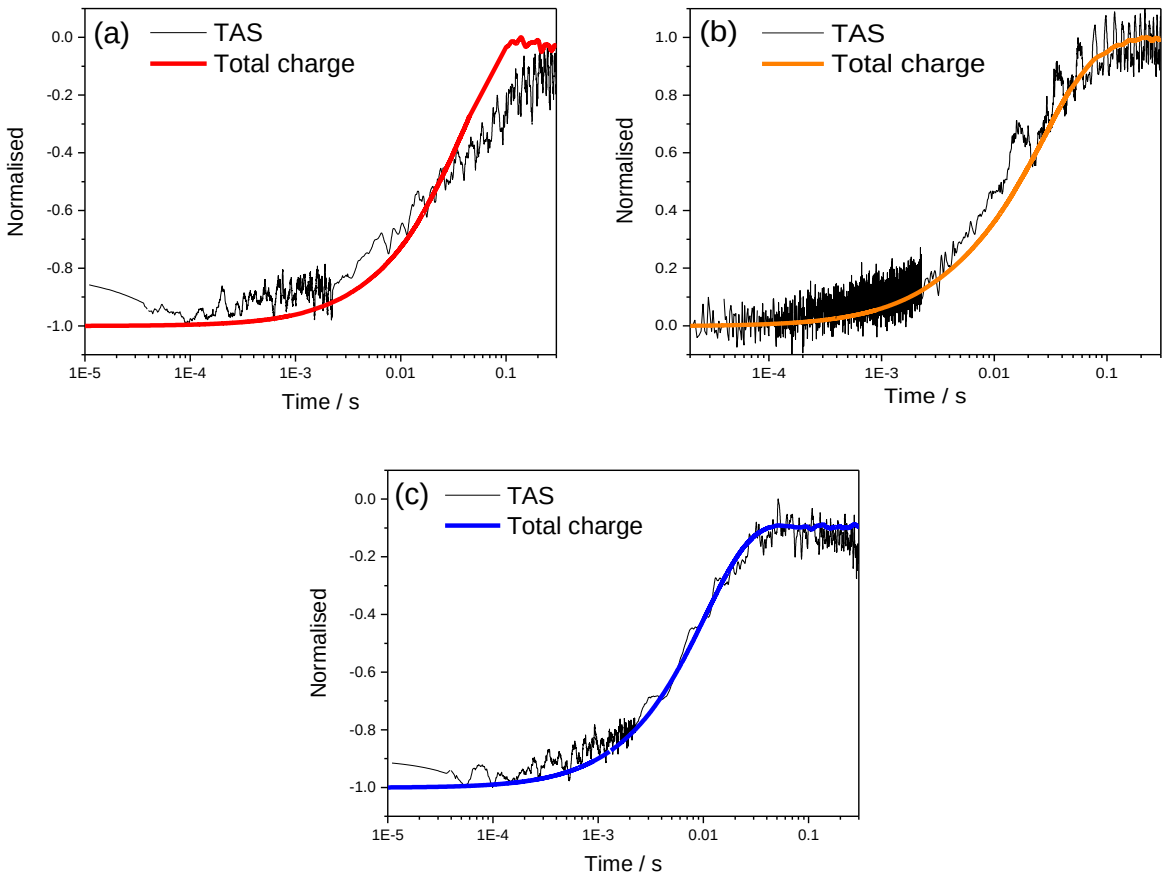

Figure 114 - Overlay of 575 nm TAS signal assigned to photoelectron trapping with the total charge passed derived from TPC of (a) untreated, (b) thermally annealed and (c) acid-treated hematite. Measurements were carried out in a photoelectrochemical cell (1 M NaOH, pH ~13.7) at 0.2 $V_{Ag/AgCl}$, following 355 nm laser excitation (6 ns pulse, ~100 $\mu J\ cm^{-2}$).

All 3 samples have similar initial concentrations of trapped electrons (the 575 nm bleach magnitude) suggesting that if these trap states affect activity, the change is related to the rate of de-trapping rather than the yield of trapping. Following thermal annealing, the rate of electron de-trapping of the larger, slower component (Figure 111b & Table 11) is increased and the overlap of de-trapping with charge extraction is improved (Figure 114b) compared to the untreated sample (Figure 114a) indicating more trapped electrons are extracted. It is possible that this increase in trapped electron extraction rate is the cause of the small increase in photocurrent/charge extraction magnitude of the thermally annealed sample. Following acid treatment, the rate of de-trapping (Figure 111c & Table 11) is even further accelerated and the

resulting overlap with charge extraction is even closer, indicating that the number of trapped electrons reaching the external circuit is further improved. This increase in de-trapping rate of electrons can be significant as it is likely to reduce slow recombination with holes accumulating near the surface.

Understanding the hole kinetics can provide useful information on the recombination processes which may be occurring in parallel to charge extraction (such as slow trap-mediated recombination with surface holes). Figure 115 shows the TAS kinetics probed at 700 nm for untreated and acid-treated hematite at a range of applied bias. The initial magnitudes of the hole signal before and after acid treatment are very similar, tentatively indicating that this population of holes is unchanged (5 μs – 1 ms). Notably, there is a negative component to the kinetics of the untreated film which becomes apparent on slow timescales (> 5 ms). While the decay rate of the initial positive feature appears to be similar before and after acid treatment, the overlap of this positive feature assigned to holes with the negative feature on slow timescales prevents a precise comparison. In light of the 575 nm TAS kinetics discussed above, the negative overlapping feature observed here is assigned to the same bleach related to electron trapping and de-trapping. The slower rate of electron de-trapping in the untreated film leads to a more noticeable overlap.

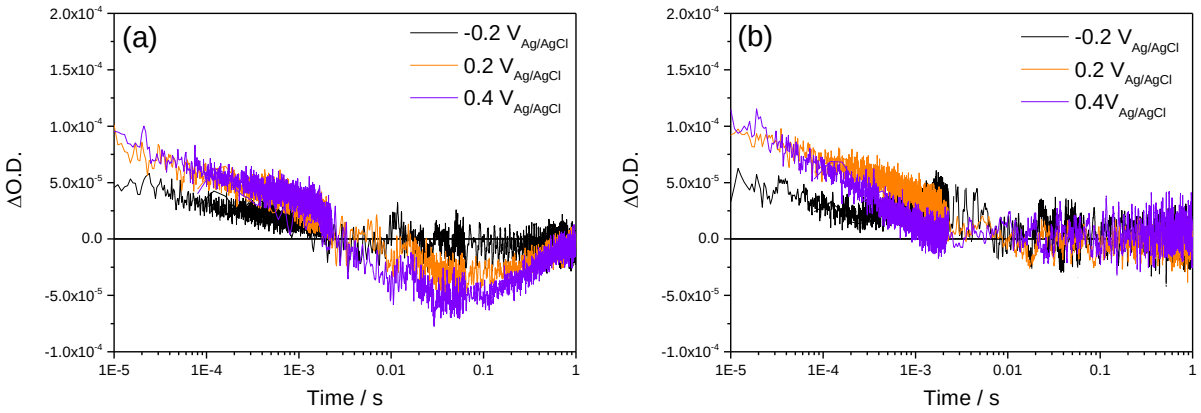

Figure 115 - TAS decay traces probed at 700 nm (holes) for (a) untreated hematite and (b) acid-treated hematite measured in a photoelectrochemical cell (1 M NaOH, pH ~13.7) at a range of applied bias ($V_{Ag/AgCl}$), following 355 nm laser excitation (6 ns pulse, ~100 μJ cm^{-2}).

Figure 116 shows the overlaid TAS kinetics of untreated and acid-treated films probed at 700 nm at an applied bias of 0.2 $V_{Ag/AgCl}$ (pH ~13.7). The overlay of the hole kinetics in Figure 116 highlights the similar yield of holes on the early timescales in both films, in addition to a similar decay rate. Unfortunately the extent of the overlap with the 575 nm bleach in these Sn-Fe_2O_3 films prevented meaningful analysis of the hole signal in this study.

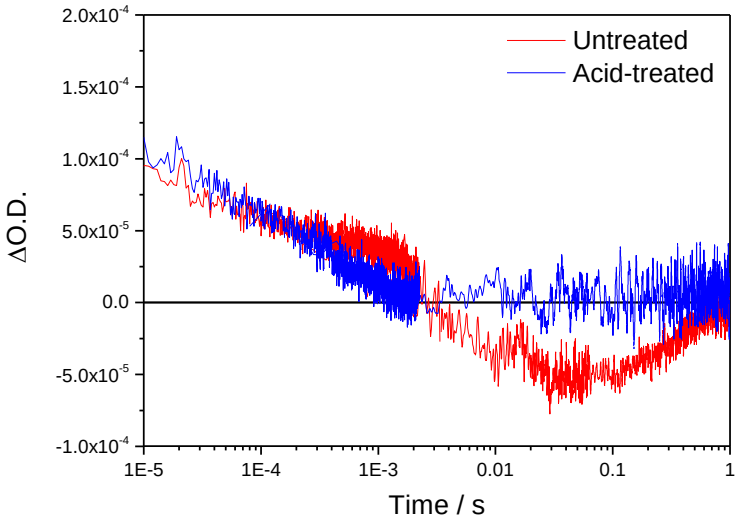

Figure 116 - Overlay of TAS decay traces probed at 700 nm (holes) for untreated and acid-treated hematite measured in a photoelectrochemical cell (1 M NaOH, pH ~13.7) at 0.2 $V_{Ag/AgCl}$, following 355 nm laser excitation (6 ns pulse, ~100 μJ cm^{-2}).

4.3.5 Kinetic model describing the effect of acid treatment

In light of the TAS, TPC and charge separation measurements described above, a simplified kinetic model for the untreated and acid-treated films is proposed (Figure 117) which addresses the processes following initial charge separation, with particular emphasis on the decay pathways of trapped electrons.

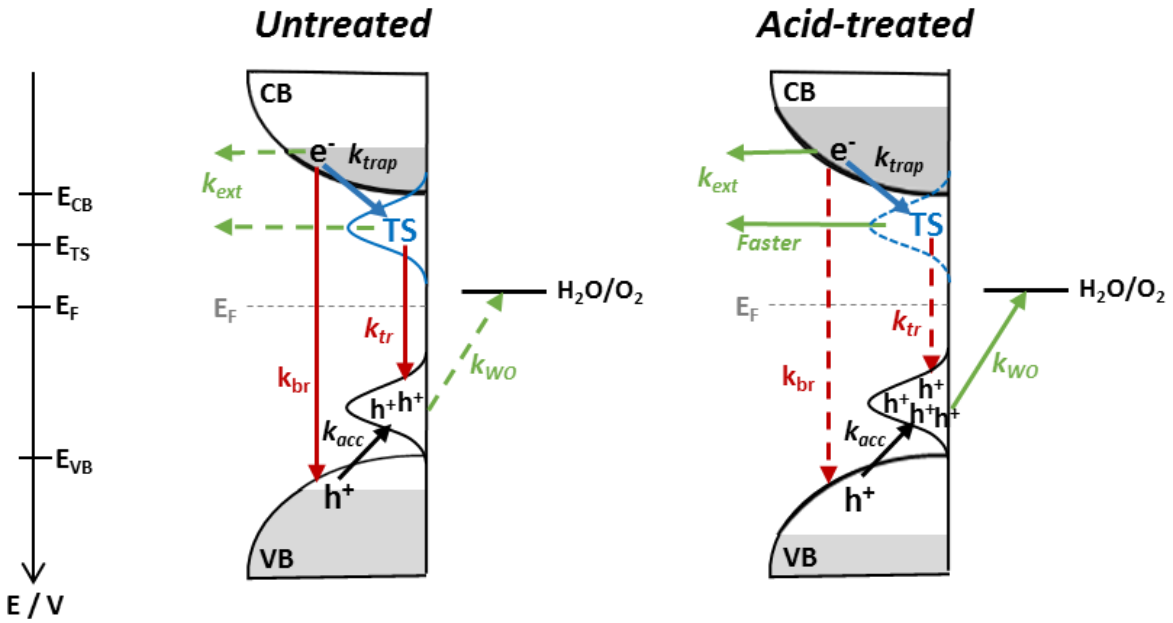

Figure 117 - Proposed kinetic scheme of the untreated and acid-treated hematite electrodes held at 0.2 $V_{Ag/AgCl}$ (pH ~13.7) following UV excitation (355 nm), where k_{br} is bulk recombination, k_{ext} is electron extraction, k_{trap} is electron trapping, TS is a trap state population, k_{acc} is hole accumulation and k_{tr} is trap-mediated recombination. Following initial excitation, electrons are either extracted to the external circuit (k_{ext}), recombine in the bulk (k_{br}) or trap (e_{trap}) into trap states (TS). At the same time, holes either recombine in the bulk (k_{br}) or begin to accumulate near the surface (k_{acc}). Charge separation measurements show improved separation in the acid treated sample which partly explains the increased activity. It then follows that trapped electrons in trap states (TS) can either recombine with surface accumulated holes (k_{tr}) or be extracted to the external circuit (k_{ext}). The combined TA and TPC study indicates improved rates of electron de-trapping in the acid-treated sample which is expected to lead to a further increase in electron extraction (k_{ext}) and a reduction in trap-mediated recombination (k_{tr}).

In this model, following light absorption and initial charge separation, excited electrons undergo either fast bulk recombination (k_{br}), electron extraction contributing to TPC/photocurrent (k_{ext}) or electron trapping resulting in the 575 nm TAS bleach (k_{trap}).

Simultaneously, holes undergo either fast bulk recombination or accumulation within the electrode/near the electrode surface. Electrons which have been trapped (k_{trap}) then go on further to decay by two competing pathways, either recombination with accumulated holes (k_{tr}) or extraction to the external circuit (k_{ext}) which will again contribute to the TPC/photocurrent. The charge extraction as measured by TPC (Figure 113) shows a small increase following thermal annealing and a significant increase from ~1.5 μC to ~4 μC at 0.2 $V_{Ag.AgCl}$ following acid treatment. The separation efficiency measurements in Figure 106a approximate a charge separation increase from *ca.* 33% for untreated hematite to *ca.* 50% following acid treatment at 0.2 $V_{Ag.AgCl}$. This increase indicates that bulk recombination is partly suppressed following acid treatment, and is expected to be a result of the observed increase in donor density. This increased charge separation yield leads to increased yields of charge extraction (contributing to the photocurrent) and/or increased yields of electron trapping. The similar magnitudes of the 575 nm TAS signal in all films studied suggests the latter is not the case and that the yield of trapped electrons remains the same, Figure 111. The close overlap between charge extracted and TAS (Figure 114) suggests that the fate of some of these trapped electrons probed by TAS at 575 nm is to reach the external circuit (k_{ext}). Thermal annealing increases the rate of de-trapping (k_{ext}) and improves this overlap and ultimately results in a small increase in charge extraction. The rate of de-trapping (k_{ext}) is then further accelerated following acid treatment which is expected to contribute to the further enhanced charge extraction yields observed.

More efficient electron de-trapping would also be expected to reduce slow recombination with surface accumulated holes (k_{tr}) and improve hole transfer to the electrolyte. Charge injection measurements (Figure 106b) show an improvement from *ca.* 40% to 58% at 0.2 $V_{Ag.AgCl}$ following acid treatment which could be related to a reduction in this trap-mediated recombination with surface holes, or an alteration to the hematite surface aiding charge transfer (i.e. a more catalytic surface), or both. Unfortunately, TAS measurements used to probe the

hole signal at 700 nm in these films were inconclusive due to significant overlap with the 575 nm feature.

To summarise: the acid treatment leads to an improvement in charge separation as a result of an increased donor density and reduced bulk recombination, which results in improved charge extraction. Additionally, while the yield of trap states as measured by TAS remains unchanged following acid treatment, the rate of de-trapping is increased which is proposed to lead to an increase in the number of de-trapped electrons reaching the external circuit, further increasing charge extraction. The increased rate of electron de-trapping is also expected to reduce trap-mediated recombination with holes accumulating at the surface. While TAS measurements could not confirm this, it is tentatively supported by an increase in measured charge injection yields. Interestingly, the rate of electron de-trapping was partly altered by thermal annealing alone, a finding which has been previously observed in the literature.[2]. It is clear that the increase in charge separation (33% to 50%) does not alone explain the photocurrent increase (which increases *ca.* 4-fold). It is proposed that an improvement in charge separation in combination with an improvement in charge injection together lead to the observed photocurrent increase. As a final note, FeOOH is known to act as an oxygen evolution reaction catalyst.[15] However, although the presence of FeOOH at the hematite surface is not ruled out following full acid treatment, acid dipping alone (which leads to the formation of FeOOH) does not result in any significant photocurrent enhancement and so the influence of FeOOH is expected to be minimal.

4.3.6 Acid treatment of alternative hematite films

In order to establish whether the acid treatment is a universal route to improving hematite activity the treatment was carried out on a range of different hematite photoelectrodes, including: films doped with Sn by migration from the FTO substrate (LT-Fe_2O_3 and HT-Fe_2O_3), air annealed hematite, oxygen deficient hematite and ultrathin planar Sn-hematite deposited by pulsed laser deposition (PLD; further information can be found in the experimental chapter). These films were selected to cover a range of structures, dopant types and dopant quantities.

The acid treatment was first tried on LT-Fe_2O_3, the same type of film used in chapter 3. These films are nanostructured electrodes (Figure 118) which are Sn-doped only by migration from the FTO substrate during annealing at 550 ^oC. Figure 119 shows the photocurrent of LT-Fe_2O_3 before and after acid treatment. A notable increase in photocurrent is observed following acid treatment, although the extent of the improvement is not as large as for Sn-Fe_2O_3 in the original study.

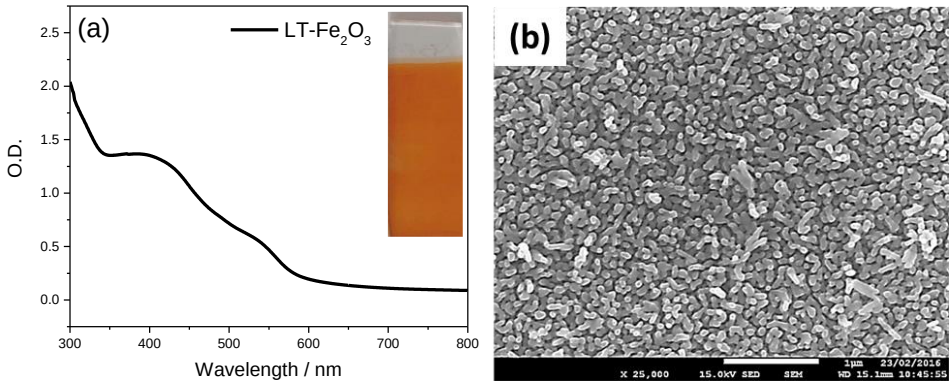

Figure 118 - (a) Absorbance spectra with an inset showing a photograph of the film and (b) SEM of LT-Fe_2O_3.

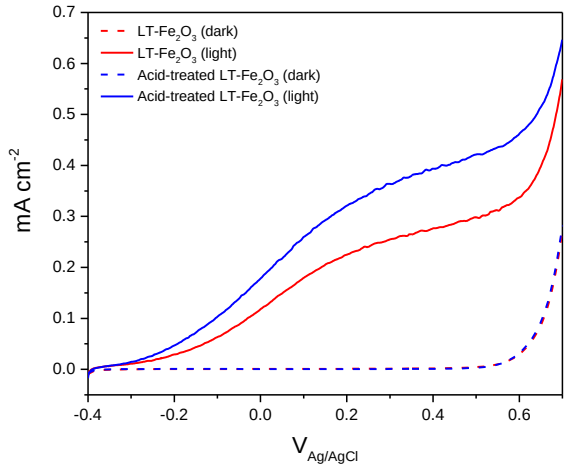

Figure 119 – Photocurrents before and after acid treatment of LT-Fe_2O_3. Measurements scanned at 10 mV s^{-1} in 1 M NaOH electrolyte (pH ~13.7) in the dark and under white light illumination ~100 mW cm^{-2}.

Acid treatment was also carried out on HT-Fe_2O_3, films which have a similar structure to LT-Fe_2O_3 (Figure 120) but are annealed at a higher temperature (700 ^oC) to improve Sn migration leading to a higher initial activity. Unlike the previous films, acid treatment of HT-Fe_2O_3 results in only a marginal improvement in activity, Figure 121. This could be rationalised as HT-Fe_2O_3 is expected to have a low density of surface trap states following annealing at a very high temperature in air and therefore a lower initial yield of photoelectron trap sites.

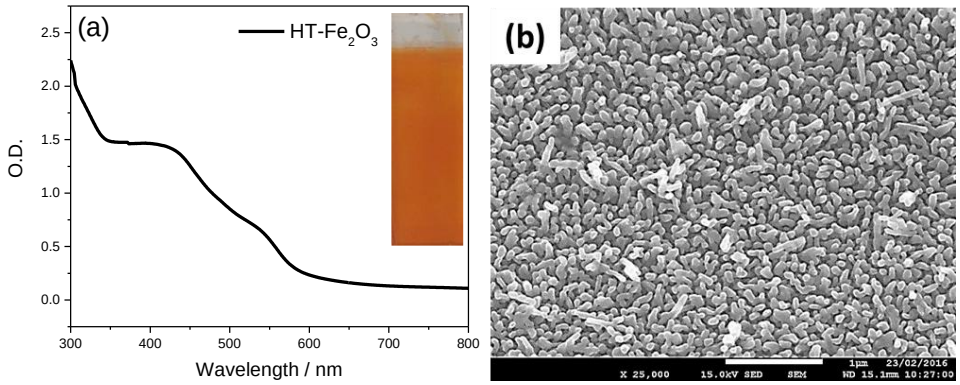

Figure 120 - (a) Absorbance spectra with an inset showing a photograph of the film and (b) SEM of HT-Fe_2O_3.

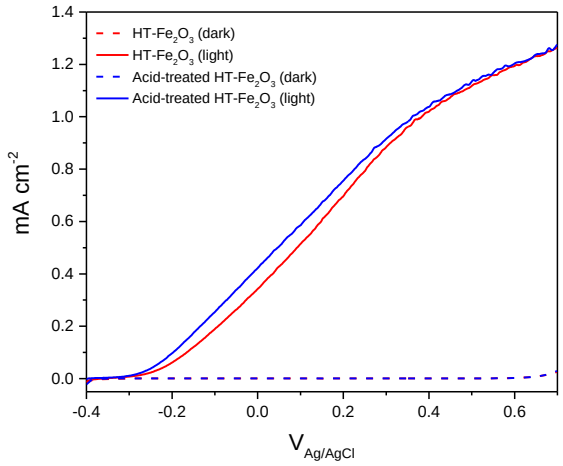

Figure 121 - Photocurrents before and after full acid treatment of HT-Fe_2O_3. Measurements scanned at 10 mV s^{-1} in 1 M NaOH electrolyte (pH ~13.7) in the dark and under white light illumination ~100 mW cm^{-2}.

Acid treatment was next carried out on the air annealed and oxygen deficient photoelectrodes first reported in chapter 2. These films have similar structures to each other (Figure 122 and Figure 124) but differ in their oxygen vacancy (donor density) content. The air annealed material is annealed at low temperature in air, while the other is annealed in an oxygen deficient environment to incorporate oxygen vacancies. Acid treatment of the air annealed material resulted in no change to the photocurrent, Figure 123. Acid treatment of the oxygen deficient material results in a large decrease in photocurrent, Figure 125. This decrease in activity can be rationalised by a reduction in oxygen vacancy concentration throughout the material during

the thermal annealing step in air of the acid treatment. Thermally annealing oxygen deficient hematite in air at elevated temperatures will re-oxidise the film thereby reducing the donor concentration.

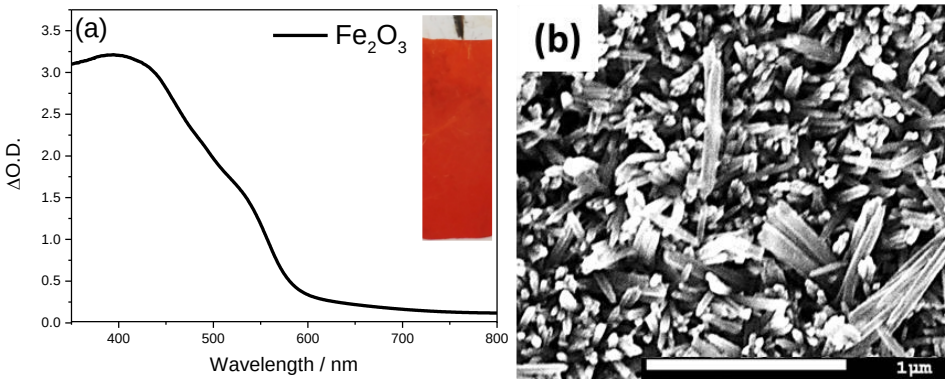

Figure 122 - (a) Absorbance spectra with an inset showing a photograph of the film and (b) SEM of α-Fe_2O_3.

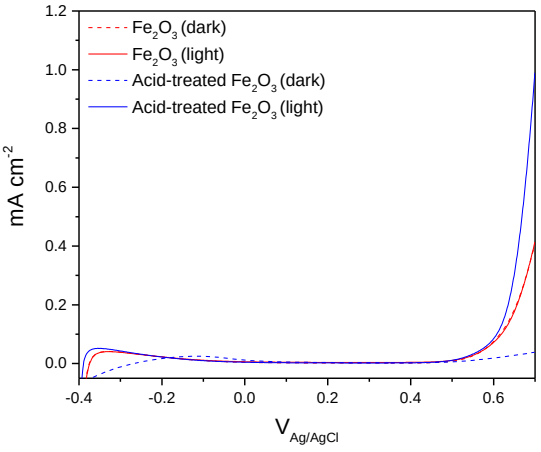

Figure 123 - Photocurrents before and after full acid treatment of α-Fe_2O_3. Measurements scanned at 10 mV s^{-1} in 1 M NaOH electrolyte (pH ~13.7) in the dark and under white light illumination ~100 mW cm^{-2}.

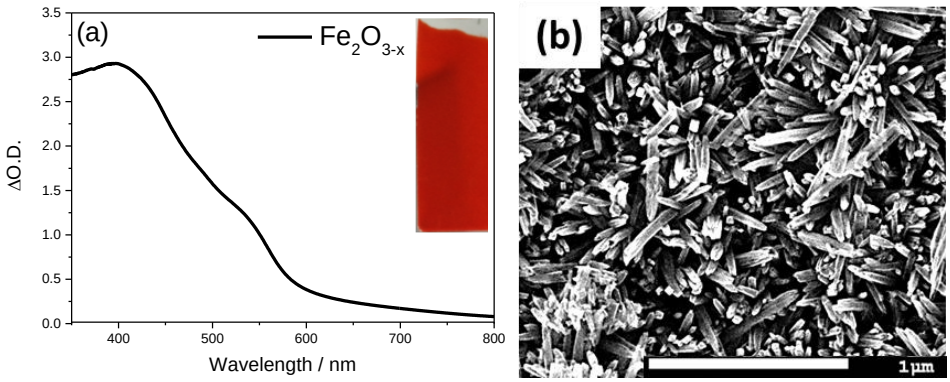

Figure 124 - (a) Absorbance spectra with an inset showing a photograph of the film and (b) SEM of α-Fe_2O_{3-x}.

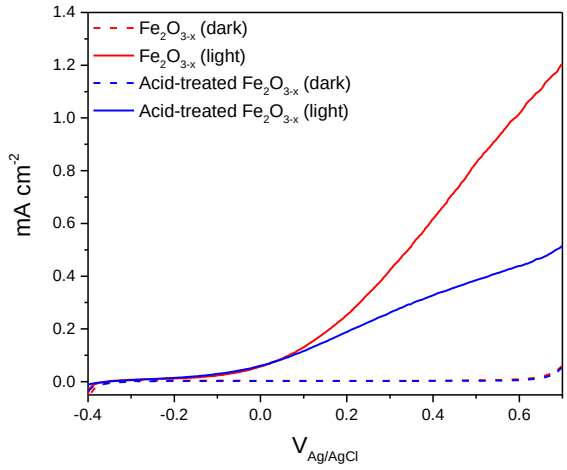

Figure 125 - Photocurrents before and after full acid treatment of α-Fe_2O_{3-x}. Measurements scanned at 10 mV s^{-1} in 1 M NaOH electrolyte (pH ~13.7) in the dark and under white light illumination ~100 mW cm^{-2}.

Finally, the acid treatment was carried out on an ultrathin Sn doped hematite film deposited by pulsed laser deposition, Figure 126. The acid treatment of this PLD hematite resulted in no significant change to the photocurrent, Figure 127.

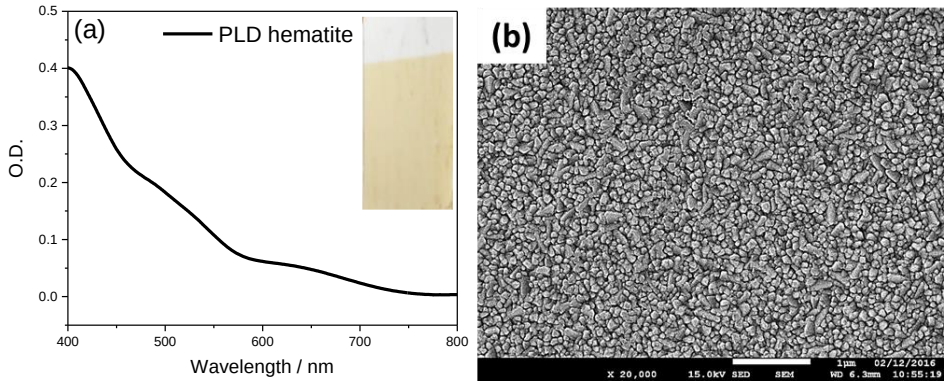

Figure 126 - (a) Absorbance spectra with an inset showing a photograph of the film and (b) SEM of PLD-hematite.

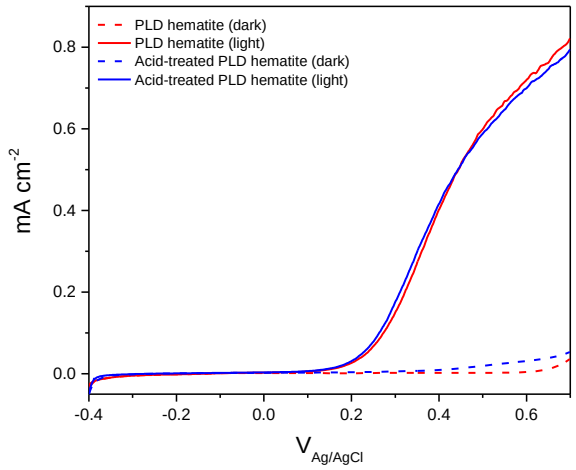

Figure 127 - Photocurrents before and after full acid treatment of PLD-hematite. Measurements scanned at 10 mV s^{-1} in 1 M NaOH electrolyte (pH ~13.7) in the dark and under white light illumination ~100 mW cm^{-2}.

Of all the additional hematite samples tested, only LT-Fe_2O_3 was notably improved, indicating that acid treatment is not a universal approach to improving hematite activity. The reason for the selective improvement following acid treatment appears to be related to the presence of defects on the surface. The treatment is not suitable for V_O doped films which contain no other dopants and appears to be of most value to extrinsically doped films (Sn) which are prepared at low temperature. In light of the conclusions reached in section 4.3.5, it may be expected that the films which are aided most by acid treatment are those which suffer most from a combination of low donor density and a high concentration of surface defects sites. Preliminary

studies which investigate the effect of acid treatment on nanostructured TiO_2 films can be found in the appendix (chapter 7).

4.4 Conclusions

This chapter outlined the use of a simple acid treatment followed by a thermal annealing step to enhance the photocurrent and IPCE values of Sn-Fe_2O_3. Initial characterisation showed no obvious change to the structure, light absorbing properties or crystal phase of the acid-treated hematite. Electrochemical measurements showed that the increased performance was due in part to an increase in charge separation following acid treatment, attributed to an increased donor density (1 order of magnitude higher). Further investigation by TAS and TPC indicated that while the yield of electron trapping remained unchanged following acid treatment, the de-trapping rate was accelerated by thermal annealing and was further accelerated by the combination of acid treatment and thermal annealing. Close agreement between TAS and TPC kinetics indicated that the trapped electrons were able to de-trap and reach the external circuit, a process which was accelerated following acid treatment. The expedited de-trapping of electrons is also expected to reduce trap-mediated recombination with holes accumulating near the surface. While TAS studies of the hole signal are tentative, an increase in the yield of surface holes was observed following acid treatment. In addition, charge injection measurements calculated using hydrogen peroxide showed that acid treatment led to an improvement in charge injection.

In this study the spatial positioning of the trap sites within the films were not determined, however the acid-treatment would be expected to primarily affect surface states. Exploration of surface states and charge accumulation at the surface of materials such as those discussed here by other means would be desirable to further understand how the surface is altered. One

such method which could be suitable has been demonstrated by Can Li *et al.*[16,17] who uses facet selective photo-deposition to provide a visual representation of charge accumulation sites.

4.5 References

1. Y. Yang, M. Forster, Y. Ling, G. Wang, T. Zhai, Y. Tong, A. J. Cowan, and Y. Li, *Angew. Chemie Int. Ed.*, 2016, **55**, 3403–3407.
2. O. Zandi and T. W. Hamann, *J. Phys. Chem. Lett.*, 2014, **5**, 1522–1526.
3. J.-W. Jang, C. Du, Y. Ye, Y. Lin, X. Yao, J. Thorne, E. Liu, G. McMahon, J. Zhu, A. Javey, J. Guo, and D. Wang, *Nat. Commun.*, 2015, **6**, 7447.
4. D. Cao, W. Luo, J. Feng, X. Zhao, Z. Li, and Z. Zou, *Energy Environ. Sci.*, 2014, **7**, 752–759.
5. M. Zhang, W. Luo, N. Zhang, Z. Li, T. Yu, and Z. Zou, *Electrochem. commun.*, 2012, **23**, 41–43.
6. L. Xi, S. Y. Chiam, W. F. Mak, P. D. Tran, J. Barber, S. C. J. Loo, and L. H. Wong, *Chem. Sci.*, 2013, **4**, 164–169.
7. Y. Ling, G. Wang, D. A. Wheeler, J. Z. Zhang, and Y. Li, *Nano Lett.*, 2011, **11**, 2119–25.
8. G. Wang, Y. Ling, D. A. Wheeler, K. E. N. George, K. Horsley, C. Heske, J. Z. Zhang, and Y. Li, *Nano Lett.*, 2011, **11**, 3503–3509.
9. T. H. Jeon, W. Choi, and H. Park, *J. Phys. Chem. C*, 2011, **115**, 7134–7142.
10. H. Dotan, K. Sivula, M. Grätzel, A. Rothschild, and S. C. Warren, *Energy Environ. Sci.*, 2011, **4**, 958–964.

11. M. Forster, R. J. Potter, Y. Ling, Y. Yang, D. R. Klug, Y. Li, and A. J. Cowan, *Chem. Sci.*, 2015, **6**, 4009–4016.

12. M. Barroso, S. R. Pendlebury, A. J. Cowan, and J. R. Durrant, *Chem. Sci.*, 2013, **4**, 2724.

13. A. J. Cowan, C. J. Barnett, S. R. Pendlebury, M. Barroso, K. Sivula, M. Grätzel, J. R. Durrant, and D. R. Klug, *J. Am. Chem. Soc.*, 2011, **133**, 10134–10140.

14. S. R. Pendlebury, A. J. Cowan, M. Barroso, K. Sivula, J. Ye, M. Grätzel, D. R. Klug, J. Tang, and J. R. Durrant, *Energy Environ. Sci.*, 2012, **5**, 6304–6312.

15. W. D. Chemelewski, H.-C. Lee, J.-F. Lin, A. J. Bard, and C. B. Mullins, *J. Am. Chem. Soc.*, 2014, **136**, 2843–2850.

16. R. Li, H. Han, F. Zhang, D. Wang, and C. Li, *Energy Environ. Sci.*, 2014, **7**, 1369.

17. R. Li, F. Zhang, D. Wang, J. Yang, M. Li, J. Zhu, X. Zhou, H. Han, and C. Li, *Nat. Commun.*, 2013, **4**, 1432.

5

Investigating the mechanism of water oxidation on α-Fe_2O_3 using *In Situ* Raman spectroscopy

Contents

5.2 Introduction

5.2.1 Overview

This chapter outlines preliminary results obtained using shell isolated nanoparticles for enhanced Raman spectroscopy (SHINERS) to probe the surface of hematite photoelectrodes under working photoelectrochemical conditions in an attempt to detect surface species and intermediates related to water oxidation. SHINERS particles consist of a metal core surrounded by an inert shell which are deposited onto a sample surface. The metal core (usually Au or Ag) enhances the Raman signal of nearby species while the inert shell (usually SiO_2) prevents unwanted adsorption or catalytic reactions involving the metal core. The SHINERS particles used in this study were prepared in collaboration with the Hardwick group at the University of Liverpool. A cell suitable for simultaneous photoelectrochemical measurements and Raman measurements was designed and made using 3D printing. *In situ* Raman measurements were then carried out on nanostructured and ultrathin planar hematite films to test the viability of the Raman measurements.

5.2.2 Mechanism of water oxidation at the metal oxide surface

The splitting of water to produce H_2 and O_2 is an endothermic 4-electron, 4-proton process (237 kJ mol^{-1}, Eq. 1-3), corresponding to 1.23 eV per electron transferred.

$$2H_2O \rightarrow O_2 + 4H^+ + 4e^- \quad (E^0 = 1.23\, V_{RHE}, OER) \qquad (1)$$

$$4H^+ + 4e^- \rightarrow 2H_2 \quad (E^0 = 0.00\, V_{RHE}, HER) \qquad (2)$$

$$2H_2O \rightarrow O_2 + 2H_2 \quad (E^{cell} = 1.23\, V_{RHE}) \qquad (3)$$

The oxidation of water to molecular oxygen is a step common to all approaches which convert sunlight to fuel and therefore determining the precise mechanism of this process is of significant interest. Natural photosynthesis and the associated water oxidation reaction carried out by plants and bacteria has been investigated for many years and is known to progress *via* Photosystem II, which contains a Mn_4O_4Ca complex at its core. Based on a widely accepted theory from 1970 by Kok *et al.*[1] the complex is thought to exist in 5 states: S_0 to S_4. Photons trapped by photosystem II move the system from state S_0 to S_4. Once the unstable S_4 state is reached it then reacts with water to produce oxygen. The Mn_4O_4Ca complex in Photosystem II has since been observed at high resolution using single-crystal X-ray diffraction[2] and tentative information has been obtained from flash experiments and electron paramagnetic resonance (EPR). However, the mechanism of this long studied complex is still not fully understood.

The mechanism of artificial water oxidation such as that taking place at a metal oxide surface is even less well understood. While O-O bond formation is known to be the key chemical step in the water oxidation mechanism, the species thought to be catalytic intermediates leading to O-O formation have not been fully assigned.

Progress has recently been made regarding the identity of water oxidation intermediates on metal oxides. Frei *et al.*[3] reported an excellent study of water oxidation on Co_3O_4 nanoparticles using time-resolved Fourier-transform infrared spectroscopy under working conditions. In addition to identifying species in the cycle, the rates at which these species are formed is also useful to understanding the mechanism fully, hence time resolved measurements can be incredibly useful. Frei *et al.*[3] identified two spectral features assigned to a slow catalytic species of the form Co(IV)=O and a fast catalytic species existing as Co(IV)=O in close proximity to a Co(III)OH group. They were able to time resolve these features and find evidence that a superoxide intermediate grows at the fast 3-electron site resulting in O_2 evolution 300 ms after

an excitation pulse. In contrast, the slow site did not progress past the 1-electron intermediate. Figure 128 shows the mechanism proposed by Frei *et al.*[3] following their findings.

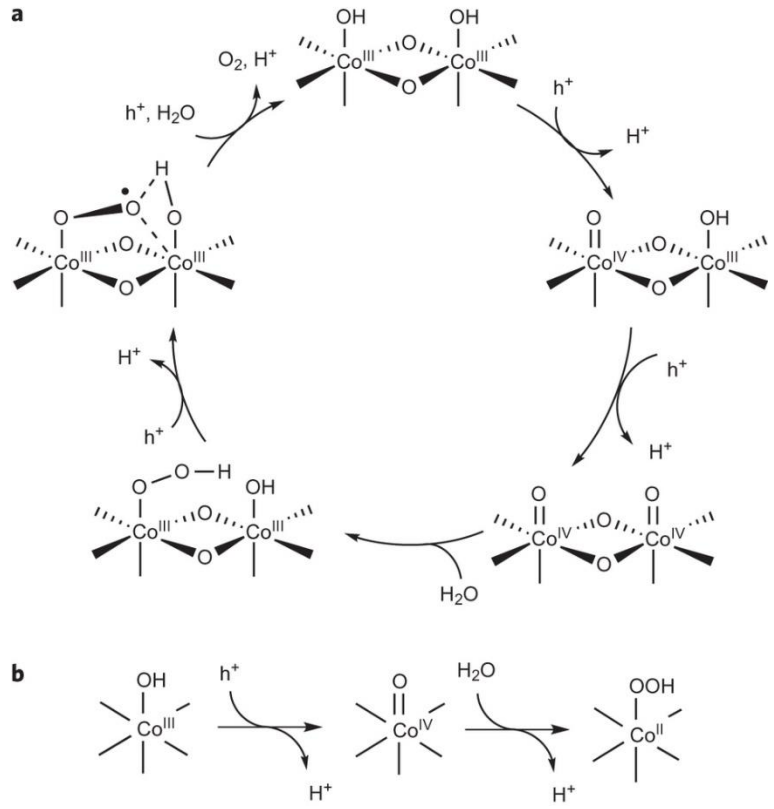

Figure 128 - Photocatalytic mechanism proposed by Frei et al. (a) Water oxidation mechanism of the fast Co_3O_4 surface site. (b), Mechanism of the slow Co_3O_4 surface site. The O-O bond-forming step with H_2O in the fast cycle features the cooperative effect of adjacent electronically coupled Co(IV)=O sites, which is absent in the H_2O addition reaction at the slow site.[3]

Cuk *et al.*[4] also recently used ultrafast *in situ* infrared spectroscopy and theoretical calculations to understand photocatalytic water oxidation at an n-$SrTiO_3$ single crystal/aqueous interface. In this study they were able to detect the transformation of charge into a Ti–O• oxyl radical through a well-defined sub-surface vibration of the O directly below it. The oxyl radical is formed within picoseconds and is found to remain for a minimum of nanoseconds. It is thought that changes in this subsurface vibration can be used to track the formation of later timescale

intermediates of the water oxidation cycle at a transition-metal-oxide surface and their work regarding this is ongoing.

Zandi and Hamann[5] recently reported the observation of photoelectrochemical water oxidation intermediates on an ~50 nm ALD hematite electrode surface using *in situ* infrared spectroscopy and electrochemical impedance spectroscopy. They observed a light and potential dependent infrared mode assigned to Fe(IV)=O. Based on theoretical calculations reported by Toroker *et al.*[6] which rules out peroxide bridging (such as that alluded to by Frei *et al.*[3]) due to the distance between two Fe sites being too large, Zandi and Hamann proposed an alternative mechanism as shown in Figure 129.

$$R-Fe^{III}-OH \xrightarrow{h^+} R-Fe^{IV}=O + H^+$$

$$R-Fe^{IV}=O + H_2O \xrightarrow{h^+} R-Fe^{III}-O-O-H + H^+$$

$$R-Fe^{III}-O-O-H \xrightarrow{h^+} R-Fe^{III} + O_2 + H^+$$

$$R-Fe^{III} + H_2O \xrightarrow{h^+} R-Fe^{III}-OH + H^+$$

Figure 129 – Mechanism of water oxidation on a hematite photoelectrode surface proposed by Zandi and Hamann.[5]

In a slightly different approach, the Durrant group have used photo-induced absorption spectroscopy (a steady state variant of TAS) to obtain not the chemical identity, but instead a measure of the order of water oxidation as a function of surface hole density.[7] In this study they observe a transition from a slow, first order reaction at low accumulated hole density to a faster, third order mechanism once the surface hole density is sufficient to enable the oxidation of nearest neighbour metal atoms. This study is useful as it provides evidence for the multi-hole

catalysis of water oxidation on hematite, and provides insight into the hole accumulation level required to achieve this.

Of course, artificial water oxidation is not limited to metal oxide surfaces. There is also significant effort towards designing and understanding water oxidation using molecular catalysts, which are often inspired by the Mn_4O_4Ca complex in Photosystem II.[8] A recent example of note involves the development of a pentanuclear iron catalyst designed by Masaoka *et al.*[9,10] In this study they observed, by cyclic voltammetry, a sequence of step wise one-electron oxidation-reduction steps corresponding to Fe^{II}/Fe^{III} couples. Additionally, the iron centres of the complex provide two adjacent sites available for water binding and activation, which leads to pre-organised O–O bond formation. The combination of these two features bear resemblance to the functional elements of the manganese complex in photosystem II. However, while molecular catalysis is clearly important, the study presented here will focus on metal oxide semiconductors.

Until now the work presented in this thesis has focussed on the use of transient UV/Vis absorption spectroscopy as a tool for understanding the photocatalytic activity of metal oxides. While TAS is a useful tool for probing charge carrier dynamics and potentially the formation and reaction rates of water oxidation intermediates (hole accumulation) at an electrode surface, it is limited in that the chemical nature of such features cannot be definitively identified. As such, other techniques are required to determine the precise nature of intermediates which may be formed during the water oxidation on metal oxides as shown in Figure 130.

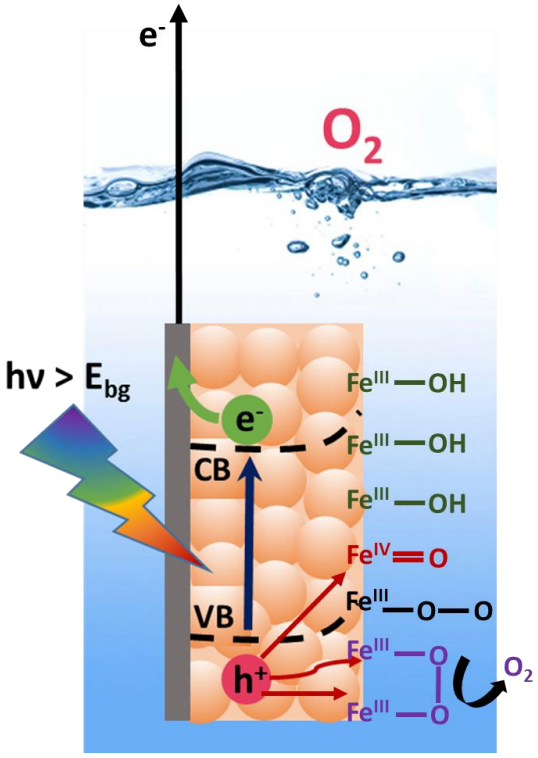

Figure 130 – Schematic showing the accumulation of holes at a hematite photoanode surface and the possible water oxidation intermediates related to these holes.

In an attempt to progress the understanding of water oxidation at metal oxide surfaces we turn to Raman spectroscopy, as vibrational spectroscopy directly probes the true functional groups present.

5.2.3 Introduction to Raman spectroscopy

Raman spectroscopy is a scattering technique used to observe vibrational, rotational, and other low-frequency modes in a system.[11] It is commonly used to provide a fingerprint by which molecules can be identified making it a promising technique for the detection of water oxidation intermediates. For a vibrational mode of a molecule to be Raman active, a change in the polarisability of the molecule is required.

Laser based Raman spectroscopy utilises photons from a monochromatic laser source which are directed towards a sample. Scattered photons are then collected and dispersed in a monochromator to give spectral resolution. Photon scattering can be broken down into three pathways as shown in Figure 131. A large portion of the photons are elastically scattered, known as Rayleigh scattering. In this elastic scattering process there is no net change in energy between the incoming photons and the outgoing scattered photons. Raman scattering relies on the less frequently occurring Stokes and Anti-Stokes scattering which result in a net change in energy. If the final vibrational state of the sample molecule is more energetic than the initial state, the inelastically scattered photon will be shifted to a lower frequency for the total energy of the system to remain balanced. This is known as a Stokes shift. If the final vibrational state is less energetic than the initial state, then the inelastically scattered photon will be shifted to a higher frequency, known as an anti-Stokes shift. The shift in frequency (known as the Raman shift) can then be used to identify the probed species. A molecule is statistically more likely to be in its vibrational ground state at room temperature, which means Anti-Stokes is infrequent and so Raman spectroscopy largely relies on Stokes scattering.

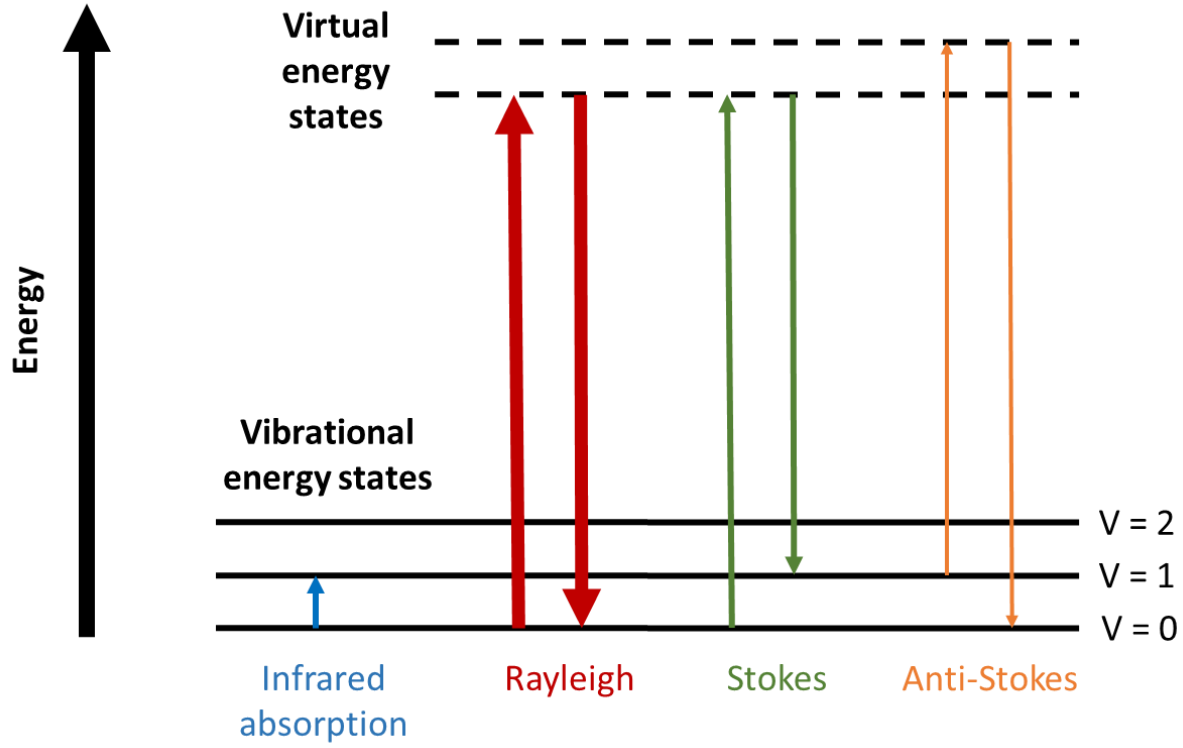

Figure 131 – Energy diagram showing the Raman scattering processes.

Due to the low probability of inelastic scattering (< 1 in 10^7 incident photons), Raman signals are typically very week (Figure 132a). The signal can be significantly improved by electrochemically roughening a surface to form a nanostructured layer which is known as Surface Enhanced Raman Spectroscopy (SERS),[11–13] Figure 132b. The enhancement effect is most pronounced on precious metals such as gold and can lead to enhancement factors of ~11 orders of magnitude.[11–13] The exact mechanism of the enhancement effect of SERS is still a matter of debate in the literature and two prominent theories exist. The electromagnetic theory proposes the excitation of localised surface plasmons where the increase in intensity of the Raman signal for adsorbates on particular surfaces occurs because of an enhancement in the electric field at the surface. The chemical theory proposes the formation of charge-transfer complexes during chemisorption to facilitate enhancement. The chemical theory cannot

explain all cases of SERS (instances where the molecule probed is spatially separated from the surface), and likewise, the electromagnetic theory does not adequately explain the magnitude of certain enhancements. As a result, it is thought likely that both mechanisms are valid and can occur in combination.[11–13]

Because SERS is generally limited to roughened precious metal surfaces, the application of SERS was limited, until 1983, when Van Duyne *et al.*[14] developed a method to use a donating effect from an external source deposited onto the sample surface to create a localised Plasmon enhancement.[12–14] An electromagnetic field arising from either an Ag or Au nanostructured or nanoparticle surface enhances the vibrational effect of nearby molecules (Figure 132c). The ability to deposit particles onto a sample to enhance the Raman signal provided a route to study a wide range of surfaces, however, while Van Duyne's development was a tremendous step forward, the technique still has drawbacks. The electromagnetic field produced from metal particles has a penetrating depth between 1-10 nm, therefore only molecular vibrations within this distance will be enhanced. Furthermore, the presence of metal nanoparticles near a sample can interfere with the measurements by either adsorbing molecular species or by the metal nanoparticles acting as a catalytic site themselves. This is of a particular concern if the aim is to study water oxidation intermediates.

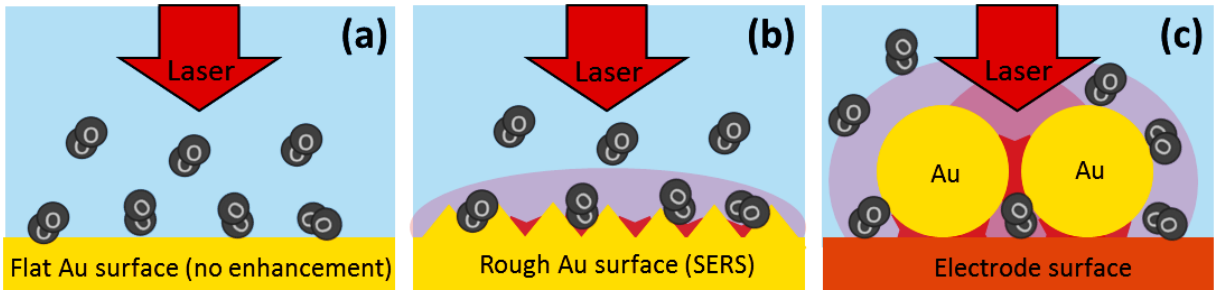

Figure 132 - Schematics showing Raman spectroscopy on (a) a planar gold surface leading to no enhancement, (b) a roughened gold surface leading to signal enhancement of species deposited on top and (c) gold nanoparticles leading to signal enhancement of nearby species under and around the particles. The black circles depict molecules and the electromagnetic enhancement strength around the gold is depicted in red.

5.2.4 Shell isolated nanoparticles for enhanced Raman spectroscopy (SHINERS)

Shell isolated nanoparticles for enhanced Raman spectroscopy (SHINERS) solves the problem of exposed metal surfaces near the sample by coating metal nanoparticles with an ultrathin inert shell, Figure 133. The SHINERS technique was developed by the Tian group in 2010 using gold nanoparticle cores coated by SiO_2.[15] The principle of SHINERS is that the electromagnetic field from the metal core is still sufficiently strong at or just beyond the thin SiO_2 surface that a Plasmon enhancement can still occur.

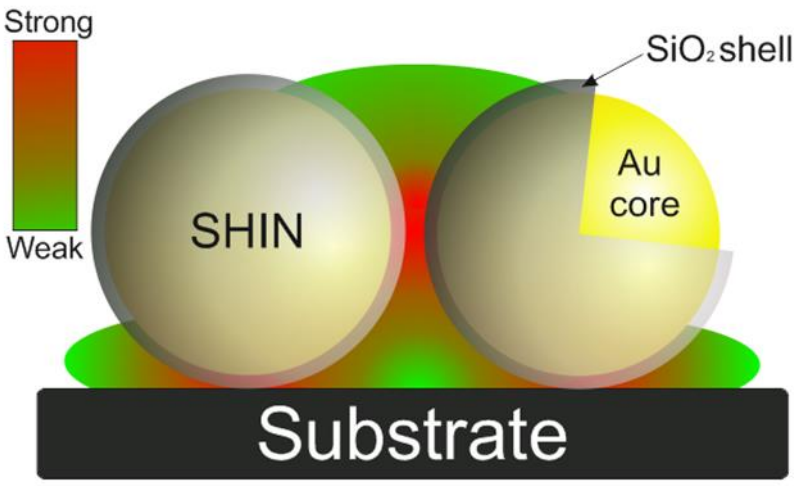

Figure 133 - Schematic diagram of SHINERS particles (gold nanoparticles coated with a thin, inert SiO_2 shell) on a substrate. The electromagnetic field distribution around and between SHINERS particles is indicated by the graduated colour key (red = strong and green = weak enhancement). Produced by Galloway et al.[16]

It was hypothesised that SHINERS developed by Tian *et al.* could be used to observe species formed during water oxidation at a metal oxide surface. This chapter involves the use of SHINERS particles which were synthesised and characterised in collaboration with Dr. Laurence Hardwick and his group at the University of Liverpool. SHINERS particles are synthesised in two stages as shown in Figure 134. First, a standard sodium citrate reduction method is used to form gold nanoparticles with diameters of ~50 nm.[17] Then, a method

previously reported in the literature[18] is used to form the ~2 nm SiO_2 shell around the gold nanoparticles. The resulting SHINERS particles are then suspended and stored in H_2O. TEM was used to inspect the SiO_2 shell thickness and Raman spectroscopy was used to ensure the shells do not contain pin holes leading to exposed metal centres. Full experimental details of the SHINERS particles synthesis can be found in the experimental chapter (chapter 6).

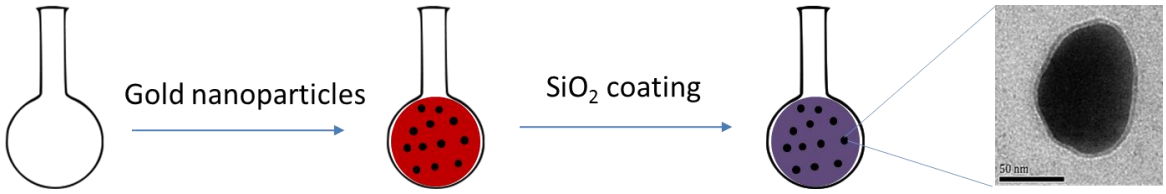

Figure 134 - Schematic showing the synthesis route of SHINERS particles. A traditional gold nanoparticle synthesis route[17] is followed by a SiO_2 coating step[18] to result in approximately 50 nm gold particles with a 2 nm SiO_2 shell. The TEM image was obtained by Tom Galloway at the University of Liverpool.

Once the SHINERS particles are prepared they can be drop cast onto a surface in their water suspension, Figure 135a. The water is then evaporated, and due to surface tension this typically results in a compact ring of SHINERS particles with a random distribution in the centre. Raman spectroscopy can then be carried out on an area containing a suitable balance between SHINERS particles and exposed sample surface to provide enhancement. The aim of this study was to use SHINERS to probe potential water oxidation intermediates on a hematite photoelectrode surface under working photoelectrochemical conditions. By carrying out Raman spectroscopy in the dark and under illumination at a controlled bias it is expected that the signal of water oxidation intermediates can be enhanced and observed as depicted in Figure 135b and c.

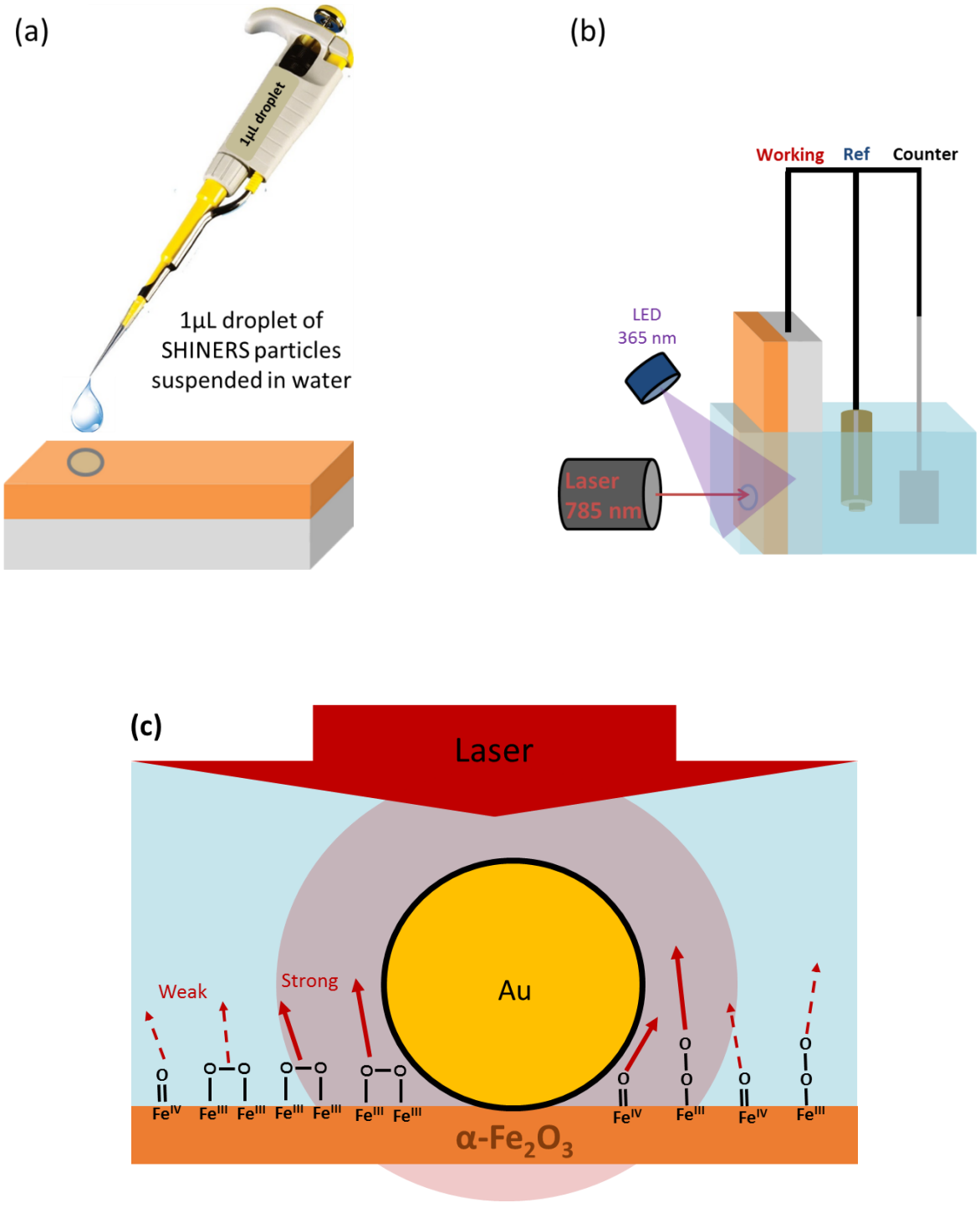

Figure 135 - Cartoon depicting (a) the drop casting of SHINERS particles onto an electrode surface, (b) Raman spectroscopy on the SHINERS coated surface under illumination and (c) Raman enhancement of surface species which are situated near the SHINERS particles.

5.3 Results and discussion

5.3.1 3D printing a cell for simultaneous photoelectrochemical and Raman measurements

Before measurement could be carried out a suitable spectroelectrochemical cell was required which could be able to facilitate 3-electrode photoelectrochemical measurements in addition to Raman spectroscopy of hematite electrodes deposited onto FTO glass substrates. The Raman spectrometer at our disposal uses an microscope and so the cell needed to accommodate light approaching from the bottom. 3D printing using Polylactic acid (PLA) was chosen to produce the custom made Raman cell used in this project. 3D printing refers to processes used to create a three-dimensional object layer by layer under computer control.[19] Objects can be of almost any shape or geometry and are produced using digital model data from a 3D model. While current 3D printing technologies typically use plastics to create objects, technologies using other materials such as metals are rapidly progressing. The customisability and low cost of 3D printing plastic objects makes it an extremely useful tool within a research environment, especially in instances where novel equipment is required which is not commercially available. As 3D printers become more accessible to consumers, as online support for the community in terms of file sharing of generic 3D models improves and as more materials become available for printing, the use of this technology in research labs (and generally) is expected to increase dramatically.

SketchUp software was used to design the cell as shown in Figure 136a. The 3D model was then exported to a 3D printer compatible software (Cura-BCN3D) ready for printing as shown in Figure 136b.

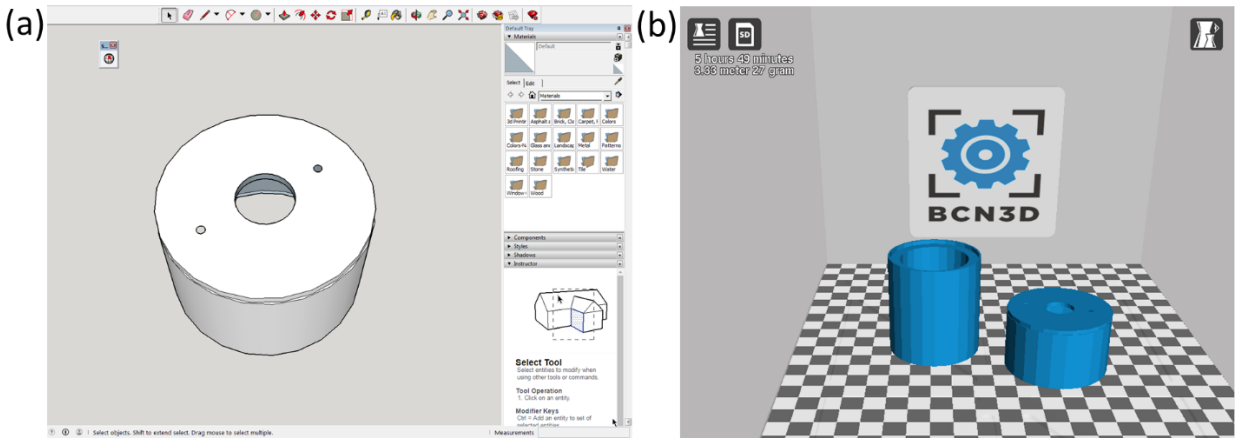

Figure 136 – (a) 3D model of the Raman cell produced in SketchUp and (b) viewed in Cura-BCN3D export software ready for printing.

The cell was printed in 3 parts: a cylindrical base mounted to a 1 mm quartz glass window, a detachable lid with 3 holes for mounting the electrodes, and a height adjustable base plate to hold the cell over the Raman microscope. The hematite sample was then mounted to a glass rod containing a wire for electrical contact and sealed with epoxy. This allowed the distance between the quartz glass window and the hematite films to be adjusted. The Pt counter and Ag/AgCl reference electrodes were then mounted either side of the central hematite electrode and the cell was filled with 1 M KCl electrolyte. Figure 137 shows the custom made Raman cell and how it is mounted over the Raman microscope.

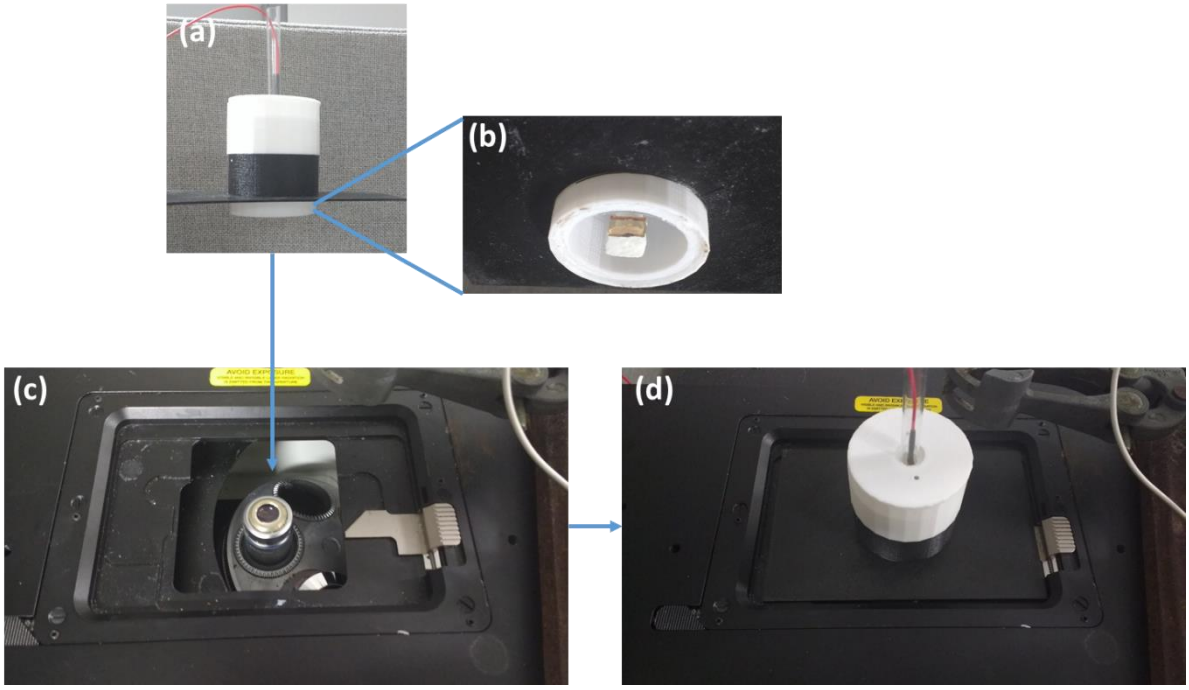

Figure 137 – Images of the custom made photoelectrochemical cell and the Raman setup. (a) Shows the side-on view of the cell and holder which allows the height of the cell to be adjusted, (b) shows the bottom view of the cell where the quartz window and hematite sample are positioned, (c) shows the Raman microscope and (d) shows the cell positioned over the Raman microscope ready for measurements. An LED is positioned underneath the cell alongside the Raman optics to allow for illuminated measurements.

5.3.2 SHINERS of nanostructured hematite (α-Fe_2O_{3-x})

The following sections show the preliminary results obtained using SHINERS to probe hematite photoeletrodes under working photoelectrochemical conditions.

The Raman instrument used in these experiments is capable of outputting 3 laser wavelengths: 532 nm, 633 nm and 785 nm. The choice of wavelength used in Raman can have a significant effect on the signal intensity, and is known as resonance Raman. Resonance Raman leads to a signal enhancement when the incident laser frequency is close in energy to an electronic transition of a species under examination.[11] SHINERS particles are also known to provide better enhancement at certain wavelengths. The SHINERS particles used in this study are known to respond strongly at 633 nm while also giving a reasonable enhancement factor at 785 nm.[16] As 633 nm (1.96 eV) is close to the band gap of hematite (1.9-2.2 eV), a Raman laser

wavelength of 785 nm was selected in order to avoid direct excitation of the hematite photoelectrodes by the Raman probe laser.

1 M KCl was used as the electrolyte in these measurements. While 1 M NaOH (pH ~13.7) is the most commonly used electrolyte when studying hematite photoelectrodes (and was used for the majority of the work in this thesis), the SiO_2 shell of the SHINERS particles is unstable in the alkaline media meaning an alternative electrolyte was required. It should be noted that the pH may affect the mechanism or rate determining steps of the water oxidation reaction and so the electrolyte should be carefully taken into account. In the previous studies discussed above in section 5.2.2, Frei *et al.*[3] used $Na_2S_2O_8$ (pH 8.5) electrolyte for their experiments, while Cuk *et al.*[4] used 1 M NaOH (pH ~13.7). The study of water oxidation intermediates on hematite carried out by Zandi and Hamman[5] used 1 M KCl (pH ~6.9) as the electrolyte for reasons related to stability of their ZnSe crystal. In their study they note that previous JV, CV, EIS and spectroelectrochemistry measurements performed over a range of pH values indicated that hematite exhibits the same behaviour and mechanism at pH 6.9 and 13. While the pH should not be neglected, the primary concern at this preliminary stage was to obtain any information related to the water oxidation mechanism.

Figure 138a shows the first *in-situ* Raman spectra obtained using SHINERS particles deposited onto a hematite photoelectrode obtained in this study. α-Fe_2O_{3-x} (the oxygen deficient hematite studied in chapters 2 and 3) was initially chosen for measurements as its behaviour is well understood. Measurements were initially carried out in the dark at a range applied bias *vs.* Ag/AgCl in 1 M KCl (pH ~7) with the aim of then turning on the LED and detecting the formation of water oxidation intermediates by the observation of new Raman peaks.

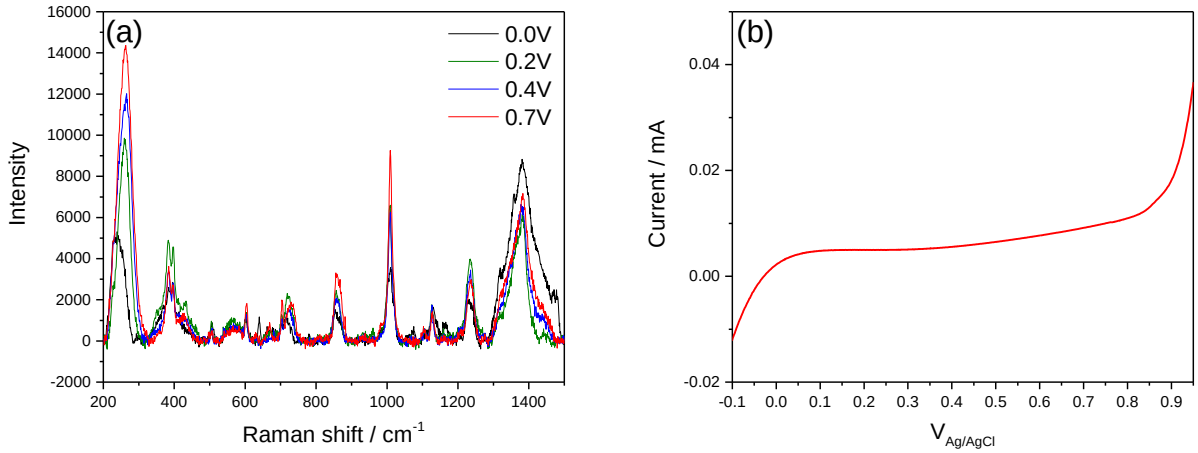

Figure 138 – (a) In Situ Raman spectra of a nanostructured α-Fe_2O_{3-x} photoelectrode with SHINERS particles dropped onto the surface in 1 M KCl electrolyte (pH ~7), at a range of applied potentials, in the dark, using a 785 nm laser. (b) Linear sweep voltammogram measured prior to the Raman.

A large number of peaks are observed across the spectral window of interest (300-1600 cm^{-1}) in Figure 138a. These peaks are present at all applied potentials and some of them increase in magnitude with increasing applied bias. This increase in magnitude with increased applied bias could be an indication of species forming at a greater bias. Alternatively, it may be possible that the applied bias is increasing Raman enhancement. Figure 139 shows repeat *in situ* Raman measurements of an α-Fe_2O_{3-x} film with SHINERS particles at a wider range of potentials which shows similar results to those obtained in Figure 138a.

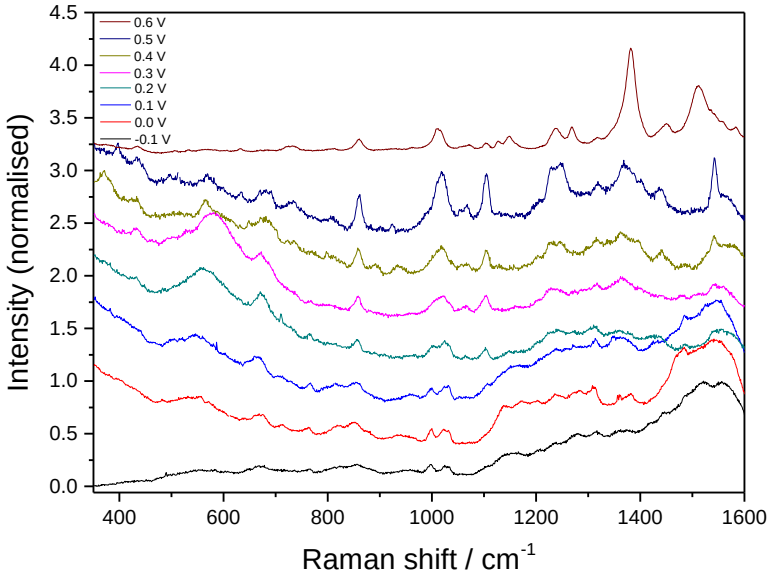

Figure 139 - In Situ Raman spectra of a nanostructured α-Fe_2O_{3-x} photoelectrode with SHINERS particles dropped onto the surface in 1 M KCl electrolyte (pH ~7), in the dark, at a range of applied potentials, using a 785 nm laser.

The Raman spectra obtained above were first compared to a standard Raman spectrum of a hematite thin film from the literature[20], Figure 140.

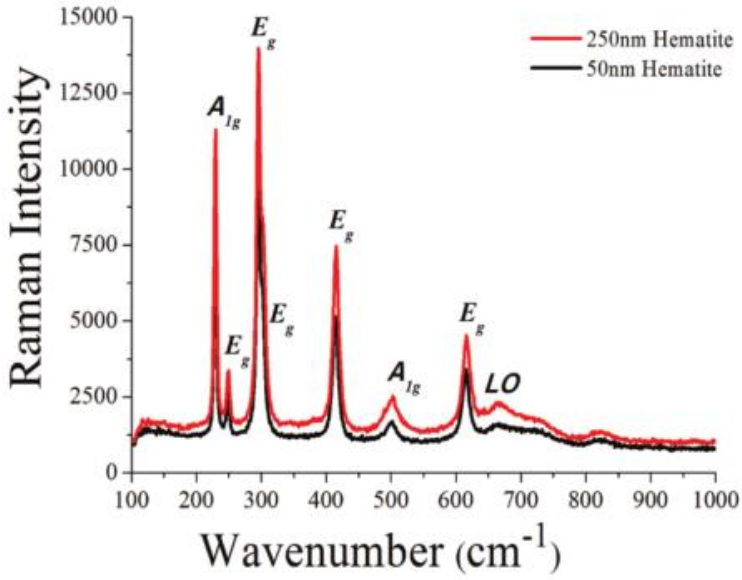

Figure 140 - Raman spectrum of a hematite film. The seven peaks characteristic of hematite are present. Additionally, the LO Eu peak at 660 cm^{-1} is indicated. Figure reproduced from Allen et al.[20]

Comparison between Figure 138a and Figure 140 showed that while the hematite lattice modes may be present, the majority of the peaks observed in Figure 138a were not related to these hematite modes (hematite modes can be found in Table 13).

α-Fe_2O_3 peak positions and assignments (cm^{-1})	
229	(A_{1g})
249	(E_g)
295	(E_g)
302	(E_g)
414	(E_g)
500	(A_{1g})
615	(E_g)
660	(LO E_u)

Table 13 - α-Fe_2O_3 Raman peak positions (cm^{-1}) and assignments.

Although the measurements in Figure 138 and Figure 139 were carried out in the dark, it is possible that species (either related or unrelated to water oxidation) begin to build on the surface at potentials > -0.1 $V_{Ag/AgCl}$, pH = 7. While the increase in magnitude of certain peaks as the positive bias is increased supports this theory, intermediates may not be expected at such low potentials.

In an attempt to clarify the above findings further Raman experiments were carried out on Fe_2O_{3-x}. Raman measurements with SHINERS particles were carried out under UV illumination using an LED to excite the sample and induce water oxidation, Figure 141a and c. Potassium iodide (KI) was then added to the electrolyte and the measurements were repeated, Figure 141b and d. KI is known to scavenge photogenerated valence band holes *via* oxidation of I^-.[5] This scavenging process is reported to block the formation of water oxidation intermediates and as a result it can potentially help to distinguish between species which are related to water oxidation and species which are not.

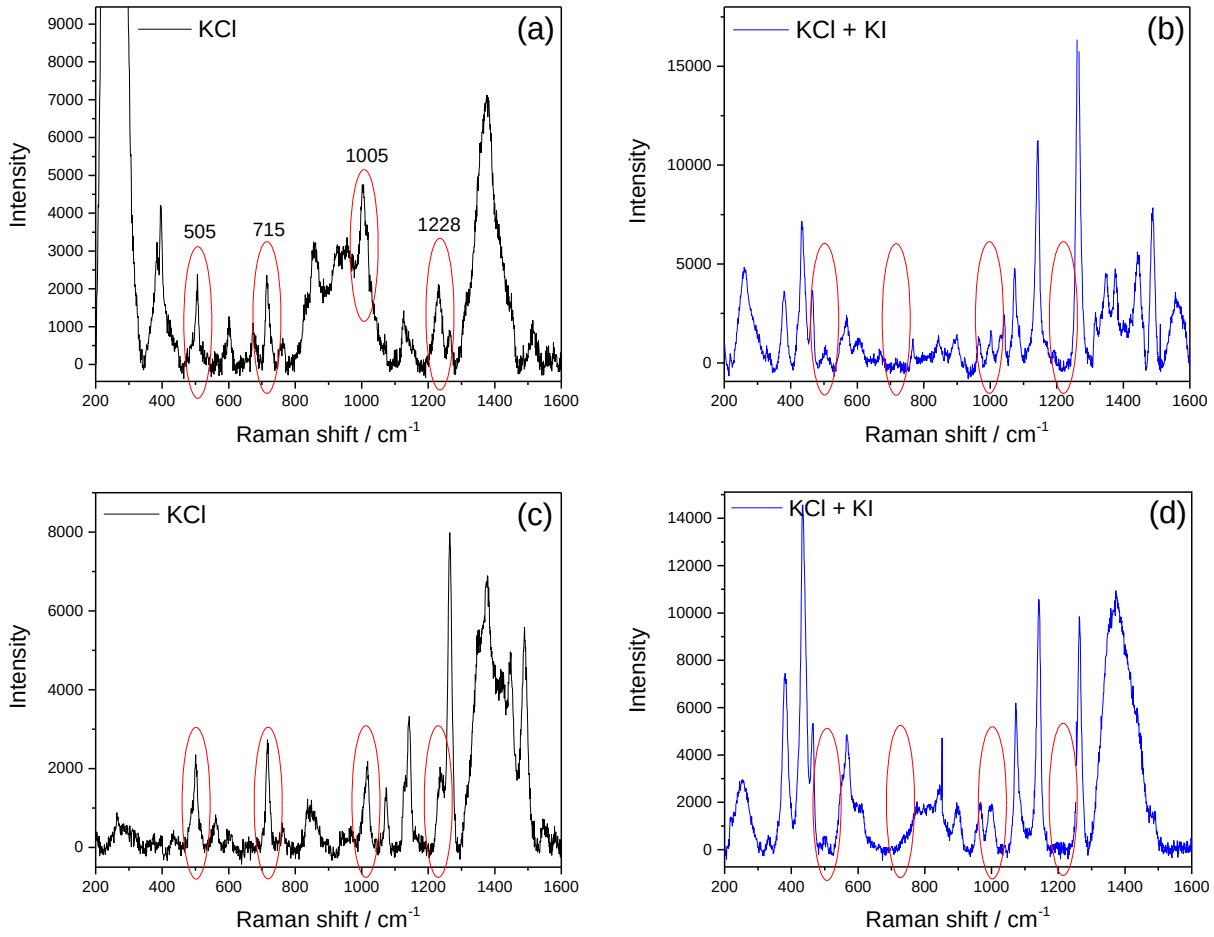

Figure 141 - In Situ Raman spectra of a nanostructured α-Fe_2O_{3-x} photoelectrode with SHINERS particles dropped onto the surface in (a and c) 1 M KCl electrolyte (pH ~7) and (b and d) 1 M KCl/KI. Measurements carried out under 365 nm LED illumination (~10 mW cm^{-2}), at 0.7 $V_{Ag/AgCl}$, using a 785 nm laser. Peaks/absence of peaks which are of interest are circled in red.

Figure 142 shows the typical current observed during the *in situ* Raman measurements obtained above when the LED is turned off and turned on.

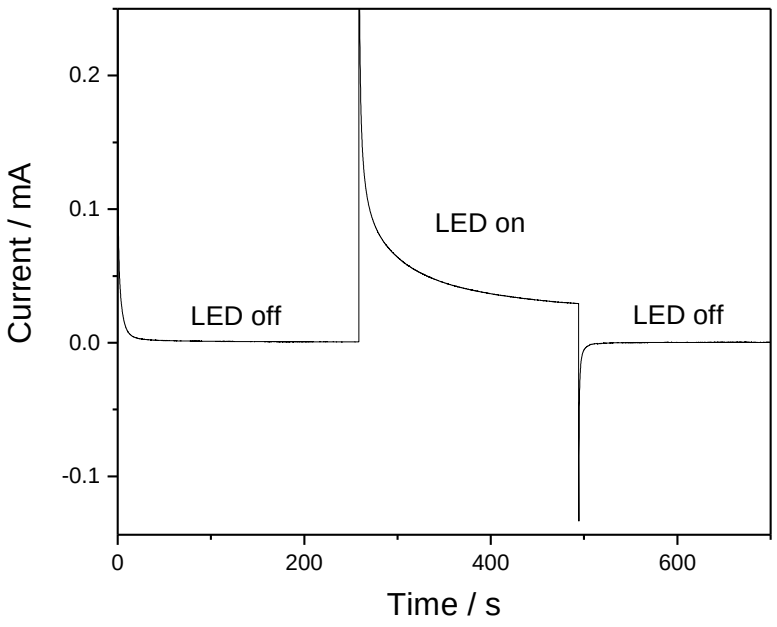

Figure 142 – Typical photocurrent obtained during the Raman measurements in Figure 141. Measurements carried out under 365 nm LED illumination (~10 mW cm^{-2}) in 1M KCl (pH ~7) at 0.7 $V_{Ag/AgCl}$.

In line with the previous results (Figure 138a), the spectra in Figure 141 show numerous peaks. Although it is difficult to interpret the data, several peaks (highlighted by the red circles in Figure 141) stand out which consistently appear initially but are then removed following the addition of KI. These peaks are located at *ca.* 505 cm^{-1}, 715 cm^{-1}, 1005 cm^{-1} and 1228 cm^{-1}. The peak located at 715 cm^{-1} is of particular interest as it lies in a region in which peroxide species (O-O modes) have been previously reported.[21,22] As the formation of O-O species are suspected to play a key role in the water oxidation mechanism at the surface of a metal oxide this finding could be significant. The peak at 1005 cm^{-1} may also be of relevance as a peak at a similar wavenumber (1013 cm^{-1}) was reported by Frei *et al.*[3] to be related to a 3 electron oxidation intermediate on Co_3O_4.

Due to the complexity of the Raman spectra observed above it was alternatively theorised that contaminants present on the hematite surface may be responsible for some of the peaks observed in Figure 138a, Figure 139 and Figure 141. In order to establish whether contaminants were present in the system, a reference measurement of SHINERS particles deposited onto a blank FTO glass substrate was first obtained, Figure 143.

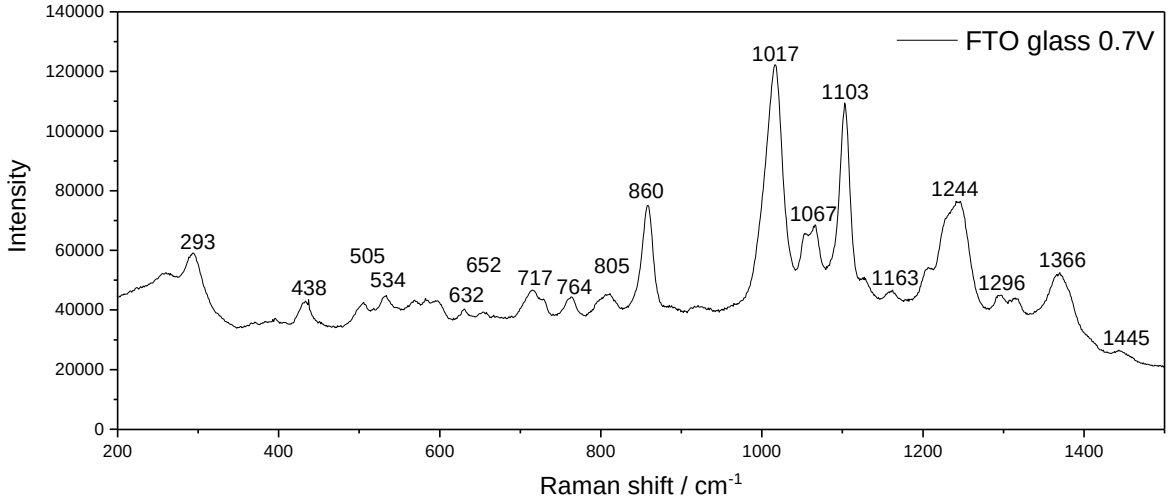

Figure 143 - In Situ Raman spectrum of an FTO glass substrate with SHINERS particles dropped onto the surface in 1 M KCl electrolyte (pH ~7), in the dark, using a 785 nm laser. The approximate peak positions are labelled.

The peaks observed in the initial hematite spectrum (Figure 138a, Figure 139 and Figure 141) were also observed in the spectrum of the FTO glass substrate (Figure 143) indicating that the origin of these peaks was not related to modes specific to hematite or water oxidation intermediates and instead related to contaminants. Further analysis of the data revealed that the contaminants present in the Raman spectra were related to the SHINERS particles, and more specifically the Raman bands appeared to be related to the reagents used during the synthesis of the SHINERS particles, Figure 144. During a successful coating procedure any excess reagents such as APTMS, trisodium citrate or sodium silicate are either locked inside the SiO_2 shell or are washed away from the surface using a centrifuge washing procedure. If the washing

procedure is unsuccessful, it is possible that these contaminants remain adsorbed onto the particle surface or in the water solution in which they are suspended. The thin SiO_2 shell is susceptible to damage which limits the amount of washing the SHINERS particles can be exposed to. Damage to the shell leads to pin hole formation which results in exposed metal core and is also expected to result in leaching of contaminants which are usually locked inside the shell. Figure 144 shows the Raman spectra of solutions of the reagents used in the synthesis of SHINERS particles obtained by Hardwick *et al.*[16]

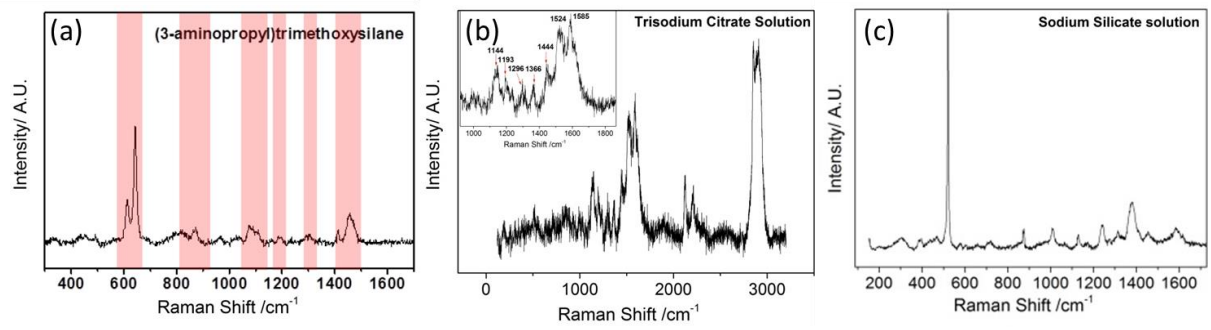

Figure 144 - Raman spectra of solutions of the reagents used in the synthesis of SHINERS particles obtained by Hardwick et al.[16] *(a) The Raman spectrum of APTMS, (b) the Raman spectrum of Trisodium Citrate and (c) the Raman spectrum of Sodium Silicate.*

Table 14 shows the approximate Raman peak positions of APTMS and Trisodium citrate determined from Figure 144 in addition to the approximate peak positions obtained from FTO glass/SHINERS particles which appear in similar regions. It should be noted that Raman peak positions can shift depending on the environment the species is in (*e.g.* can be affected by other nearby species or the solvent). While not all of the peaks are accounted for at this stage there is convincing evidence to suggest that contaminations due to these reagents are present.

α-Fe_2O_3 peak positions and assignments (cm^{-1})		**Contaminant peak positions (cm^{-1}) and assignments**		**FTO glass/SHINERS peak positions (cm^{-1})**
229	(A_{1g})			
249	(E_g)			
295	(E_g)			
302	(E_g)			
414	(E_g)			
		440	APTMS $Si(OCH_3)_3$	438
500	(A_{1g})			
		612	APTMS $Si\text{-}CH_2R$	-
615	(E_g)			
		643	APTMS $SiO\text{-}CH_3$	652
660	(LO E_u)			
		800	APTMS $OSi\text{-}CH_2R$	805
		873	APTMS Si-OC	-
		1076	APTMS $H_2C\text{-}NH_2$	1067
		1104	APTMS SiO-C	1103
		1144	Trisodium citrate	-
		1187	APTMS $SiO\text{-}CH_3$	-
		1193	Trisodium citrate	-
		1296	Trisodium citrate	1296
		1305	APTMS $Si\text{-}OCH_3$	-
		1366	Trisodium citrate	1366
		1413	APTMS $O\text{-}CH_3$	-
		1444	Trisodium citrate	1445
		1457	APTMS CNH_2	-
		1524	Trisodium citrate	-
		1585	Trisodium citrate	-

Table 14 – Raman peak positions of α-Fe_2O_3 (left columns). APTMS and Trisodium citrate solutions (middle columns). Some of the peaks present in the FTO glass/SHINERS particles measurements which are suspected to be due to contaminants (right column).

As damage to the SHINERS particles during centrifuging is a concern, an alternative route to cleaning the particles which avoids damage or aggregation as a result of centrifuging has been reported in the literature.[23] This method deposits the particles onto an electrode which is then biased cathodically to induce proton reduction to produce hydrogen. The bubbles produced during this procedure are reported to clean the particles by physically dislodging surface contaminants. The difficulty of this method is reclaiming the particles from the electrode in sufficient quantities and doing so without damaging them. Other methods for cleaning the SHINERS particles were also explored during this work including the introduction of a cleaning step before the coating procedure, however this led to pin holes. Filtration methods were also explored, however these led to loss of the particles or insufficient cleaning. The

centrifuging method was known to produce clean and undamaged particles in the past, and so although time consuming, a trial and error approach was taken in which many batches of particles were produced until a clean and undamaged batch was obtained which could be used for further experiments. Eventually a clean batch of SHINERS particles was successfully obtained which showed no obvious signs of contamination. Figure 145 shows a Raman spectrum of α-Fe_2O_{3-x} with SHINERS particles in 1M KCl (pH ~7). No contamination peaks were observed for these new particles and instead the Raman shifts assigned to hematite modes (Figure 140) can now be seen clearly. It should be noted that the hematite modes can be observed in thin films without additional enhancement and the SHINERS particles were not found to enhance the hematite modes during this study. This can be rationalised as these modes exist primarily in the bulk, away from the SHINERS particles.

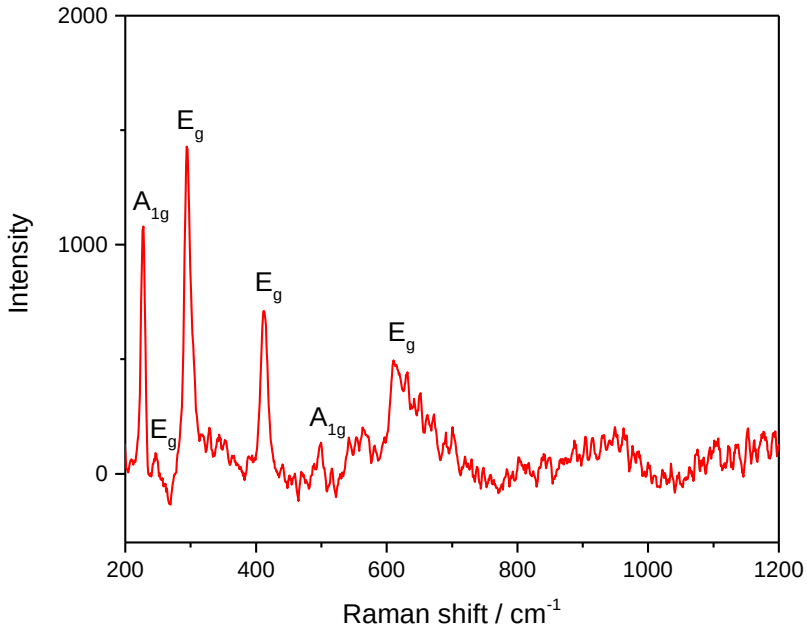

Figure 145 - In situ Raman spectroscopy of α-Fe_2O_{3-x} with SHINERS particles measured in the dark in 1 M KCl (pH ~7), using a 785 nm laser. It should be noted that the purpose of the SHINERS particles in this measurement is to show that contaminations were not present. The dominant Raman modes of hematite can be seen without enhancement and SHINERS particles were not seen to enhance these signals, likely due to them being bulk modes.

5.3.3 SHINERS of pulsed laser deposited (PLD) hematite electrodes

Following the synthesis of a clean batch of SHINERS particles, a second problem was encountered regarding the deposition of these particles. In order for SHINERS to be successful, it requires an appropriate sample surface containing a balance between exposed sample and SHINERS particle coverage to provide the enhancement. Finding an adequate sample spot typically involves moving the laser around the surface in a trial and error type approach until enhancement is observed. SEM images were obtained in order understand how the SHINERS particles were situated on the α-Fe_2O_{3-x} surface, Figure 146.

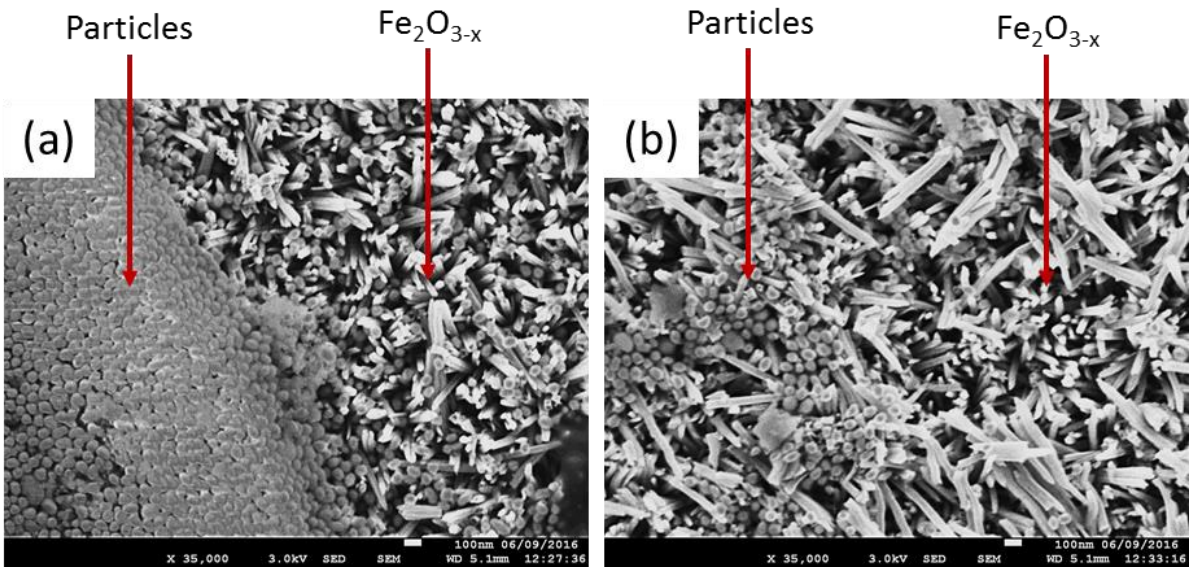

Figure 146 - SEM images of nanostructured hematite with SHINERS particles dropped onto the surface. (a) Shows a section near the thick outer ring of densely packed particles. (b) Shows a cluster of particles inside the drop cast ring.

Firstly, observation by SEM revealed the densely packed outer ring of particles (Figure 146a) known to form after drop casting. This dense ring of particles prevents access to the underlying hematite electrode and so is unsuitable for Raman measurements. Within the outer ring there are regions of more sparsely distributed particles and these regions are typically where

enhancement can be found. SEM imaging revealed that the nanostructured α-Fe_2O_{3-x} electrode limited the distribution of these inner particles as they were either lost within the nanostructure or formed dense clusters around the larger hematite features, Figure 146b. It was hypothesised that a planar hematite electrode would allow for better SHINERS particle distribution and therefore improved Raman enhancement and so a new approach to film synthesis was attempted.

Pulsed laser deposition (PLD) was used to produce ultrathin (~25 nm) Sn-doped hematite films in order to provide more suitable films for deposition of SHINERS particles. PLD was carried out in collaboration with Professor Matt Rosseinsky and his group at The University of Liverpool. The procedure used has been reported previously in the literature[24] and full experimental details can be found in the experimental chapter (chapter 6). Figure 147a shows the absorbance spectra of a PLD-Fe_2O_3 film which exhibits the typical hematite features.[25] Figure 147b shows SEM imaging of a PLD-Fe_2O_3 film. The surface morphology of the film is the same as that of the underlying FTO glass substrate indicating a uniform coverage of the ~ 25 nm thick hematite layer. Most crucially, the structure is significantly flatter than that of the nanostructured α-Fe_2O_{3-x} film discussed above.

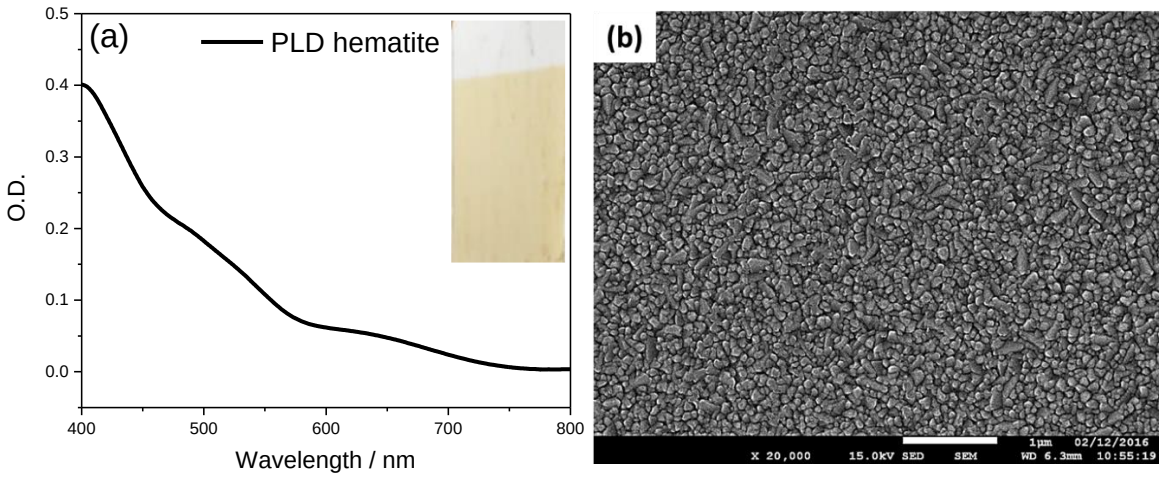

Figure 147 - (a) Absorbance spectra with an inset showing a photograph of the PLD-Fe_2O_3 film and (b) SEM of PLD-Fe_2O_3.

Figure 148 shows a typical linear sweep voltammogram of a PLD-Fe_2O_3 film in the dark and under illumination at pH ~7.

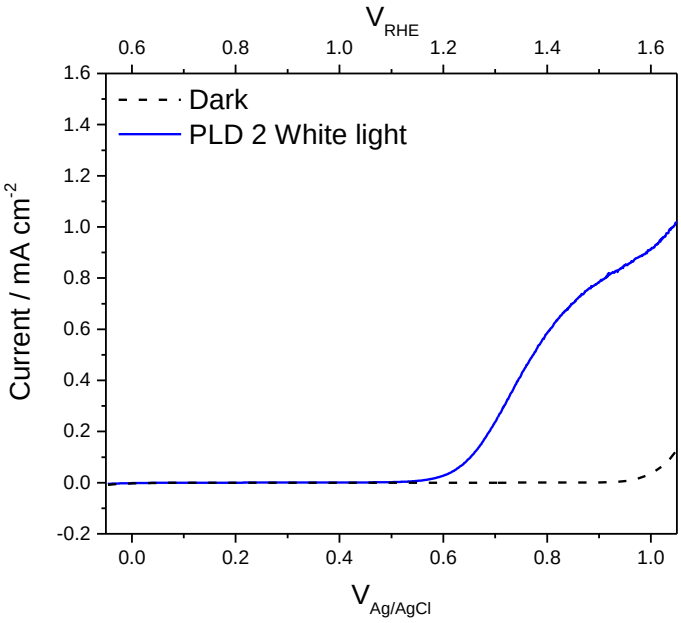

Figure 148 - Linear sweep voltammograms of a PLD-Fe_2O_3 film measured in the dark (black dotted line) and under 100 ~mW cm^{-2} white light illumination (blue line). Measurements scanned at 10 mV s^{-1} in 1 M KCl (pH ~7).

Following the synthesis of the PLD-Fe_2O_3 films, SHINERS particles were deposited using the standard drop casting method and SEM was carried out which revealed improved distribution of the SHINERS particles, Figure 149. The red circles in Figure 149 represent the approximate size of the Raman laser spot at 785 nm providing an estimate of the sample area during a measurement.

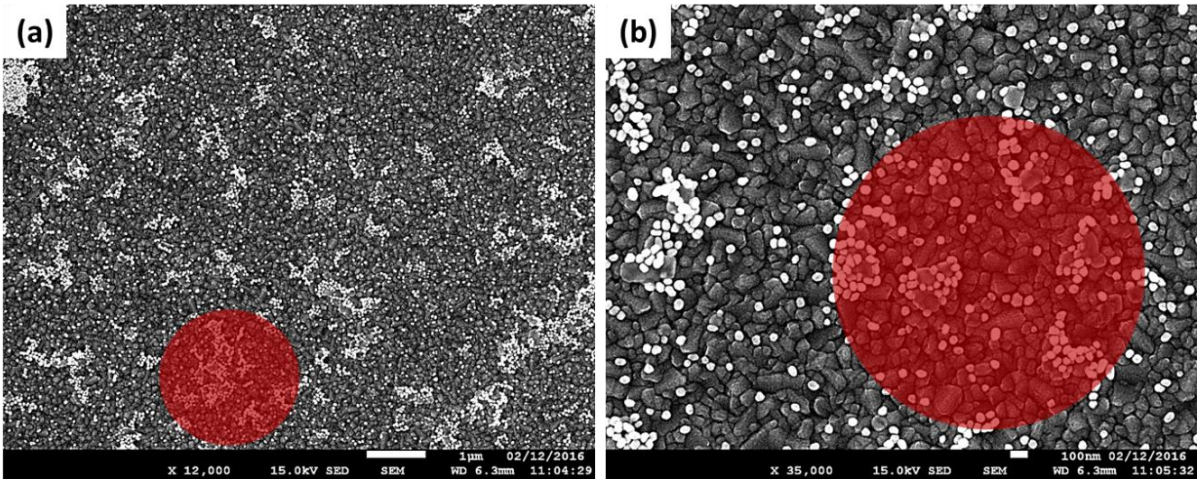

Figure 149 - SEM images of PLD-Fe_2O_3 with SHINERS particles. The red spot provides an estimate of the Raman laser spot size at 785 nm.

The laser spot size (focal point) depends on the optics used and the wavelength of the laser and can be calculated using equation 4, where λ is the laser wavelength and NA is the numerical aperture of the microscope which determines the outgoing laser diameter and focal length.

$$Laser\ spot\ size\ diameter\ (focal\ point) = \frac{1.22\ x\ \lambda}{NA} = \frac{1.22\ x\ 785\ \text{nm}}{0.5} = \sim 1.92\ \mu\text{m} \quad (4)$$

Figure 150 shows a Raman spectrum of PLD-Fe_2O_3 with SHINERS particles in 1 M KCl (pH ~7). Consistent with the previous data for the new batch of clean SHINERS particles on α-Fe_2O_{3-x} (Figure 145), no contamination peaks were observed and the Raman shifts assigned to hematite modes (Figure 140) are seen. Compared to Fe_2O_{3-x}, the hematite signals for PLD-Fe_2O_3 are much smaller, which is attributed to the film being thinner (~300 nm *vs.* ~25 nm).

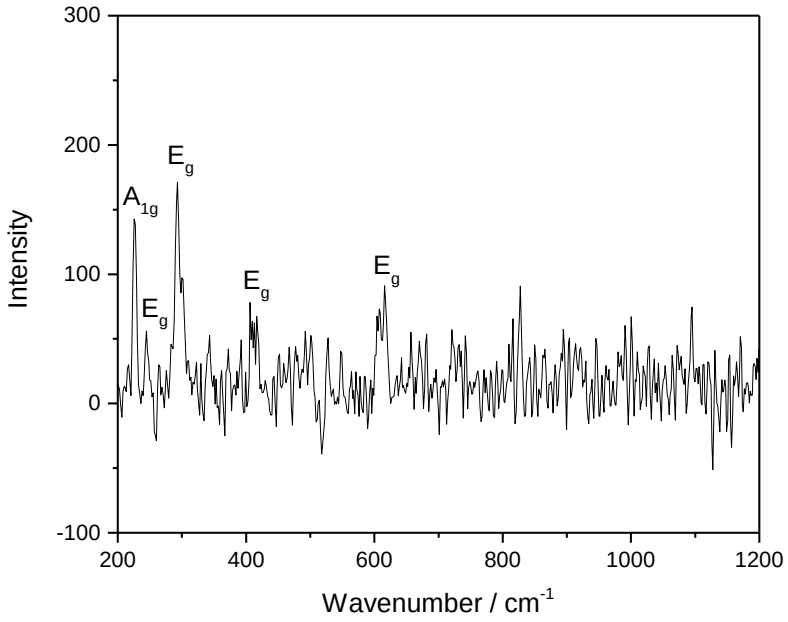

Figure 150 – In situ Raman spectroscopy of PLD-Fe_2O_3 with SHINERS particles measured in the dark in 1 M KCl (pH ~7), using a 785 nm laser. It should be noted that the purpose of the SHINERS particles in this measurement is to show that contaminations were not present. The dominant Raman modes of hematite can be seen without enhancement and SHINERS particles were not seen to enhance these signals, likely due to them being bulk modes.

Following confirmation that the more uniform PLD-Fe_2O_3 allowed for more desirable distribution of the SHINERS particles and that the particles were still contamination free, a proof of principle experiment was carried out using a dye. The quantity of water oxidation intermediates accumulating at the photoelectrode surface is expected to be small, and as such, detecting these species is expected to be challenging even in the event of successful Raman enhancement. To ensure the experiment was viable the SHINERS particles were used to

enhance the signal of Rhodamine 6G dye (Figure 151c) deposited onto the surface of PLD-Fe_2O_3. Figure 151 shows a Raman spectrum of Rhodamine 6G solution (0.1 mM) deposited onto PLD-Fe_2O_3.

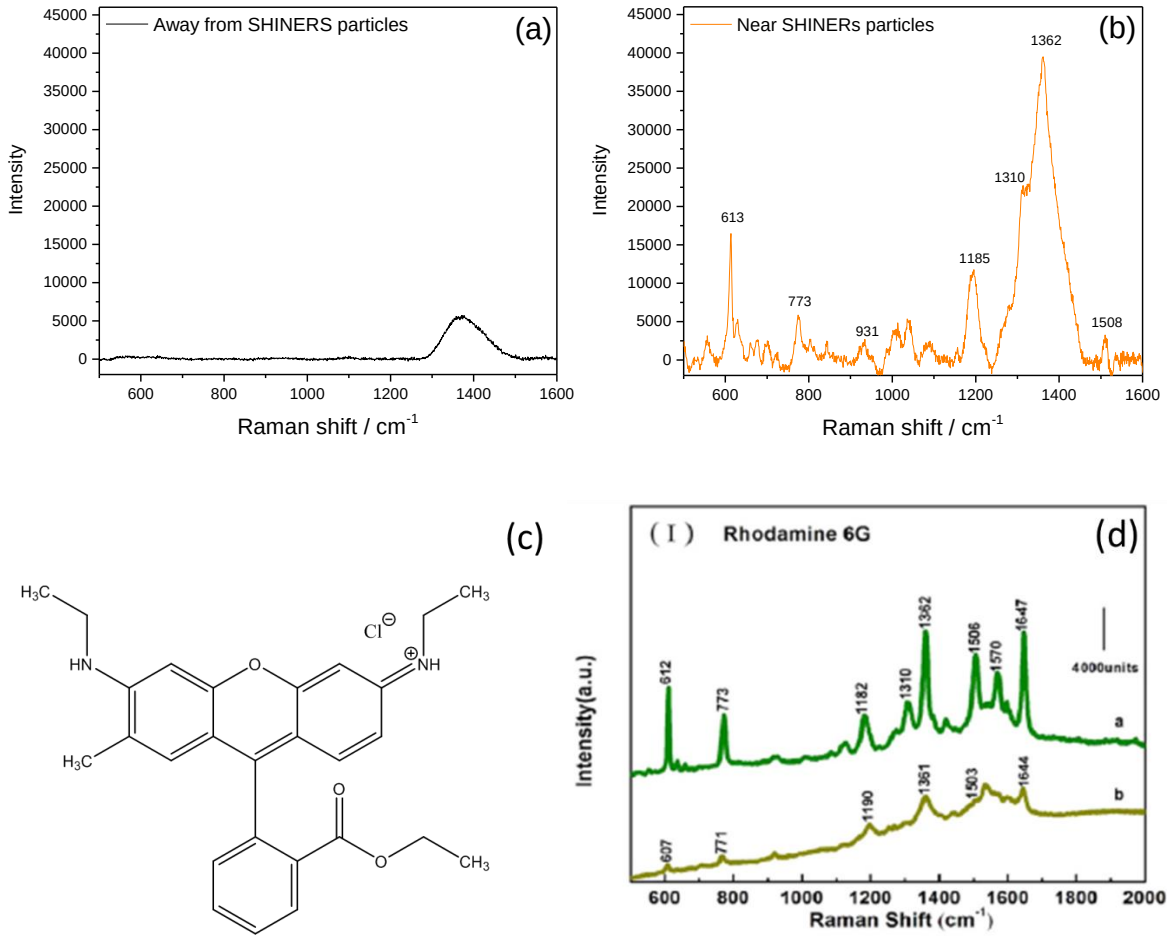

Figure 151 - In situ Raman spectroscopy of PLD-Fe_2O_3 with Rhodamine 6G dye solution (1 mM) deposited on top. (a) the Raman spectrum without SHINERS particles and (b) the Raman spectrum with SHINERS particles with (a) subtracted. The measurements were carried out in the dark in 1 M KCl (pH ~7), using a 785 nm laser. (c) shows the structure of Rhodamine 6G and (d) shows a Raman spectrum of Rhodamine 6G from the literature[26] for reference. Some of the main Rhodamine 6G peaks are assigned (see Table 15). The large peak at ~1400 cm^{-1} is thought to be a feature related to glass.

Figure 151a shows a region away from SHINERS particles in which no peaks associated to the dye are observed and Figure 151b shows a region near SHINERS particles (such as the region in Figure 149) in which the Raman shifts associated to Rhodamine 6G are observed indicating

successful enhancement. The broad peak observed at ~1400 cm^{-1} in both spectra is often seen during *in situ* Raman measurements and is thought to be related to glass, although this unconfirmed. Figure 151d shows a Raman spectrum of Rhodamine 6G obtained from the literature for reference. Table 15 shows some of the main Rhodamine 6G Raman shifts which have been highlighted in Figure 151b along with their assignments.

Peak Position (cm^{-1})	Assignment
613	Xanthene ring deformations
773	Out of plane C-H bend
931	Out of plane C-H bend
1185	In plane C-H bend, N-H bend
1506	C-N str, C-H bend

Table 15 – Some of the main Rhodamine 6G Raman peak positions which have been highlighted in Figure 151b and their previously reported assignments.[26,27]

Following the proof of principle study, attempts to observe water oxidation intermediates on hematite were continued by carrying out in situ Raman measurements with SHINERS particles in the dark and then under illumination with an applied bias. Unfortunately, following these experiments a critical hurdle was encountered. When a photocurrent such as that shown in Figure 152b is induced under illumination at a suitable anodic bias the SHINERS particles are gradually removed from the surface within several minutes. The photograph in Figure 152a shows a hematite electrode containing SHINERS particles (black ring), half of which were kept in the dark and half of which were illuminated at 0.7 $V_{Ag/AgCl}$ in 1 M KCl for 200 seconds. The illuminated particles were removed while those kept in the dark remain.

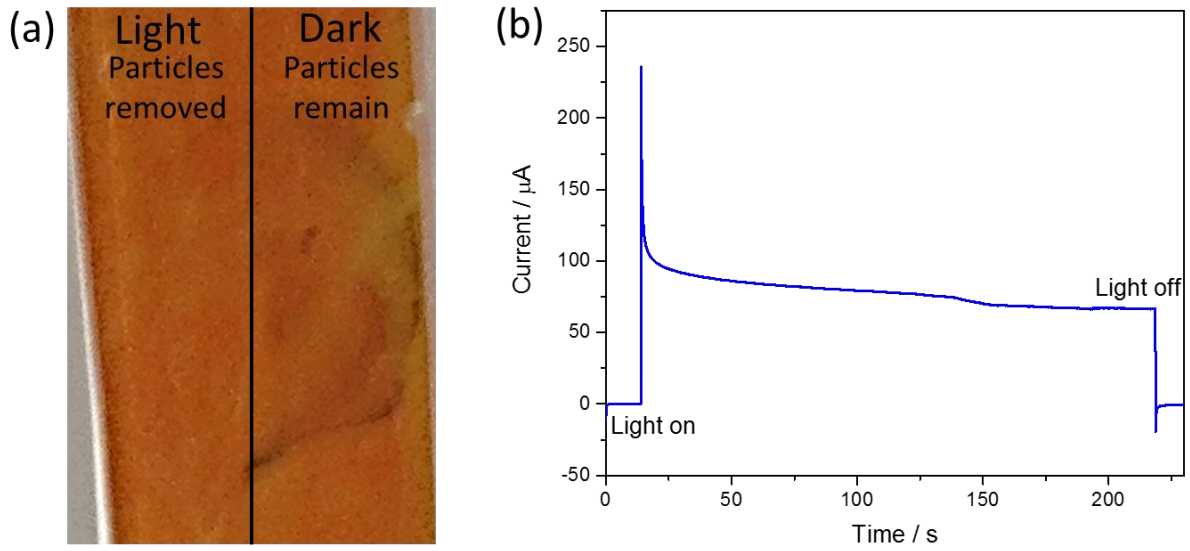

Figure 152 - Photograph of a hematite photoelectrode with SHINERS particles. Half of the particles were illuminated by a 365 nm LED light for 200 seconds in 1 M KCl (pH ~7) at an applied bias of 0.7 $V_{Ag/AgCl}$ and the other half were kept in the dark under the same applied bias. The figure on the right shows the current vs. time plot obtained during this measurement.

Figure 153 shows the SHINERS particles as viewed through the optics of the Raman microscope in the dark and then following illumination at 0.7 $V_{Ag/AgCl}$ in 1 M KCl for 200 seconds indicating removal of these particles.

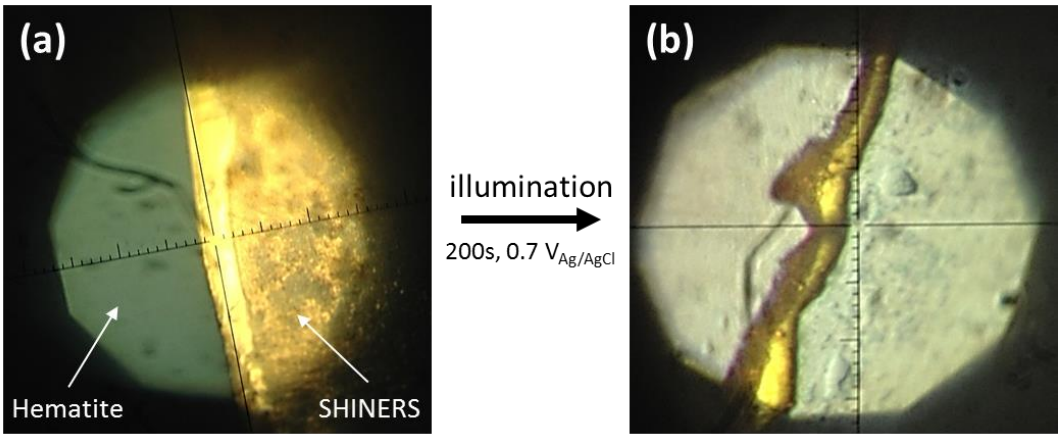

Figure 153 - SHINERS particles deposited onto a hematite electrode in 1 M KCl electrolyte (pH ~7) as viewed through the optics of the Raman microscope (a) in the dark and (b) following 200 seconds of UV illumination (~10 mW cm^{-2}) at an applied bias of 0.7 $V_{Ag/AgCl}$.

Although the cause of the SHINERS particle removal is not confirmed, it is suspected that oxygen bubbles formed on the surface of the electrode under illumination and applied bias are dislodging the particles. The particles are only removed when a photocurrent is induced, remaining stable under illumination without a bias and likewise under a moderate bias without illumination. Furthermore, producing a current electrocatalytically using a large anodic bias in the dark also leads to removal of the particles. Figure 154 shows a spectrum obtained early on in this project when contamination due to SHINERS was still present. The contamination peaks are lost at anodic potentials where a dark electrocatalytic current is observed and this is hypothesised to be due to removal of the particles by oxygen bubbles.

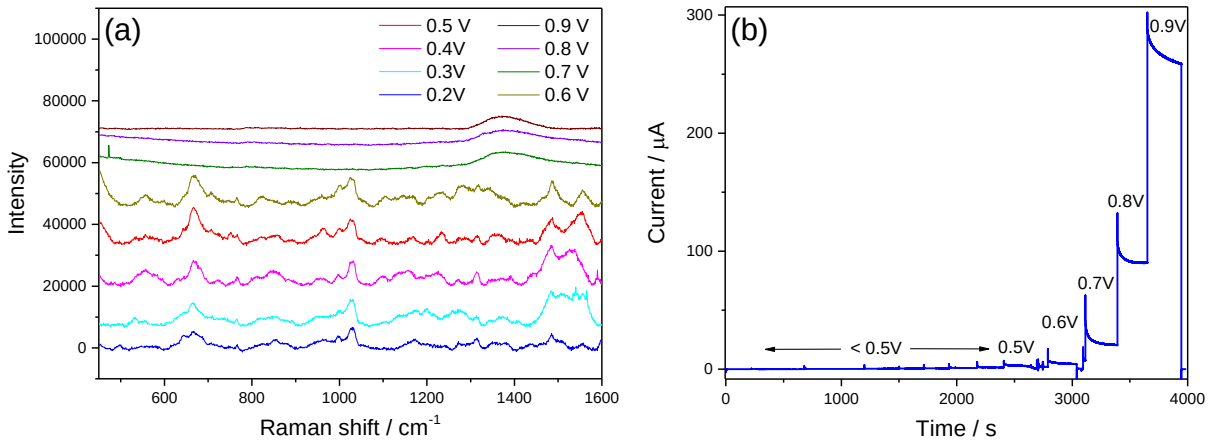

Figure 154 - (a) In Situ Raman spectra of an α-Fe_2O_{3-x} photoelectrode with contaminated SHINERS particles dropped onto the surface in 1 M KCl electrolyte (pH ~7), in the dark, at a range of applied potentials, using a 785 nm laser. (b) Currents obtained during the Raman measurements.

In order to detect water oxidation intermediates by Raman an enhancement effect from the SHINERS particles is required, however, the formation of these water oxidation intermediates under photoelectrochemical conditions leads to bubble formation and removal of the SHINERS particles within 200 seconds. Raman measurements typically require at least several hundred seconds of data acquisition and as such the removal of the particles within this timeframe

hinders measurements. The work presented in this chapter so far is ongoing and future experiments will focus on overcoming the challenge of maintaining contact between the hematite surface and the SHINERS particles under water oxidation conditions.

5.4 Conclusions and future work

This chapter has investigated the feasibility of using SHINERS to probe the mechanism of water oxidation at a hematite photoelectrode surface as current experimental data regarding the mechanism of artificial water oxidation is limited. SHINERS particles were synthesised and initial measurements were carried out on nanostructured α-Fe_2O_{3-x} films. Initial problems regarding contaminations related to the SHINERS particles and particle deposition problems due to the nanostructured film were encountered. These problems were overcome by ensuring clean batches of SHINERS particles using a trial and error centrifuge cleaning approach, and then depositing them onto ultrathin planar hematite films produced by PLD. Proof of principle measurements using Rhodamine 6G dye deposited onto the PLD-Fe_2O_3 surface confirmed that Raman enhancement of a species on a hematite surface by SHINERS was possible. Most critically, further investigation revealed that bubble formation under photoelectrochemical conditions removes the SHINERS particles before Raman spectra could be acquired. Clearly the incongruous nature of the SHINERS particles and the conditions for water oxidation is a significant problem and probing water oxidation intermediates in this way is challenging.

Future experiments will focus on maintaining contact between the SHINERS particles and the hematite surface under water oxidation (bubble forming) conditions. Routes to achieve this will include careful control of the photoelectrochemical conditions in an effort to generate water oxidation intermediates whilst minimising bubble formation. Exploration into the synthesis of larger SHINERS particles and particles of different shapes may also help to prevent removal

by bubbles. Finally, the use of a linker group to bind the SHINERS particles to the hematite surface thereby preventing physical removal by bubbles will also be explored.

5.5 References

1. B. Kok, B. Forbush, and M. Mcloin, *Photochem. Photobiol.*, 1970, **11**, 457–475.

2. Y. Umena, K. Kawakami, J.-R. Shen, and N. Kamiya, *Nature*, 2011, **473**, 55–60.

3. M. Zhang, M. de Respinis, and H. Frei, *Nat. Chem.*, 2014, **6**, 362–7.

4. D. M. Herlihy, M. M. Waegele, X. Chen, C. D. Pemmaraju, D. Prendergast, and T. Cuk, *Nat. Chem.*, 2016, **8**, 1–7.

5. O. Zandi and T. W. Hamann, *Nat. Chem.*, 2016, **8**, 778–783.

6. N. Yatom, O. Neufeld, and M. Caspary Toroker, *J. Phys. Chem. C*, 2015, **119**, 24789–24795.

7. F. Le Formal, E. Pastor, S. D. Tilley, C. a Mesa, S. R. Pendlebury, M. Grätzel, and J. R. Durrant, *J. Am. Chem. Soc.*, 2015, **137**, 6629–6637.

8. B. M. Hunter, H. B. Gray, and A. M. Müller, *Chem. Rev.*, 2016, **116**, 14120–14136.

9. M. Okamura, M. Kondo, R. Kuga, Y. Kurashige, T. Yanai, S. Hayami, V. K. K. Praneeth, M. Yoshida, K. Yoneda, S. Kawata, and S. Masaoka, *Nature*, 2016, **530**, 465–468.

10. J. Lloret-Fillol and M. Costas, *Nat. Energy*, 2016, **1**, 16023.

11. D. J. Gardiner and P. R. Graves, Eds., *Practical Raman Spectroscopy*, Springer Berlin Heidelberg, 1989.

12. R. Aroca, *Surface-Enhanced Vibrational Spectroscopy*, John Wiley & Sons, Ltd, Chichester, UK, 2006.

13. K. Kneipp, M. Moskovits, and H. Kneipp, *Surface-Enhanced Raman Scattering*, Springer Berlin Heidelberg, 2006, vol. 103.

14. R. P. Van Duyne and J. P. Haushalter, *J. Phys Chem*, 1983, **227**, 2999–3003.

15. J. F. Li, Y. F. Huang, Y. Ding, Z. L. Yang, S. B. Li, X. S. Zhou, F. R. Fan, W. Zhang, Z. Y. Zhou, D. Y. Wu, B. Ren, Z. L. Wang, and Z. Q. Tian, *Nature*, 2010, **464**, 392–395.

16. T. A. Galloway and L. J. Hardwick, *J. Phys. Chem. Lett.*, 2016, **7**, 2119–2124.

17. G. Frens, *Nat. Phys. Sci.*, 1973, **241**, 20–22.

18. L. M. Liz-Marzán, M. Giersig, and P. Mulvaney, *Langmuir*, 1996, **12**, 4329–4335.

19. B. Berman, *Bus. Horiz.*, 2012, **55**, 155–162.

20. A. M. Jubb and H. C. Allen, *ACS Appl. Mater. Interfaces*, 2010, **2**, 2804–2812.

21. H. H. Eysel and S. Thym, *Z. Anorg. Chem.*, 1975, **2**, 97–102.

22. A. Grimaud, W. T. Hong, Y. Shao-Horn, and J.-M. Tarascon, *Nat. Mater.*, 2016, **15**, 121–126.

23. J.-F. Li, A. Rudnev, Y. Fu, N. Bodappa, and T. Wandlowski, *ACS Nano*, 2013, **7**, 8940–8952.

24. K. D. Malviya, H. Dotan, D. Shlenkevich, A. Tsyganok, H. Mor, and A. Rothschild, *J. Mater. Chem. A*, 2016, **4**, 3091–3099.

25. D. a. Wheeler, G. Wang, Y. Ling, Y. Li, and J. Z. Zhang, *Energy Environ. Sci.*, 2012, **5**, 6682.

26. S. Chen, X. Li, Y. Zhao, L. Chang, and J. Qi, *Carbon N. Y.*, 2015, **81**, 767–772.

27. L. Jensen and G. C. Schatz, *J. Phys. Chem. A*, 2006, **110**, 5973–5977.

6

Experimental techniques

Contents

6.1 Materials and synthesis

6.1.1 Air annealed and oxygen deficient hematite films

Air annealed and oxygen deficient hematite films were prepared by Professor Yat Li and his group at the University of California, Santa Cruz.[1] Briefly, β-FeOOH nanowire films were first prepared on a FTO substrate through hydrolysis of $FeCl_3$ (0.15 M) in a high ionic strength (1 M $NaNO_3$), and low pH value (pH 1.5, adjusted by HCl) environment at 95 °C for 4 hr. β-FeOOH films were then sintered in air at 550 °C for 2 hours to form α- Fe_2O_3. For preparing α-Fe_2O_{3-x}, β-FeOOH films were annealed in a tube furnace in an oxygen-deficient atmosphere (N_2 + air). The tube furnace was vacuumed down to 15 Torr, and then refilled with ultrahigh purity N_2. The sintering of β-FeOOH was carried out at 550 °C for 2 hours at 740 Torr with a continuous N_2 flow (50 sccm). Samples were found to be suitably stable for regular use in TA measurements over a 3-month period with no noticeable loss in activity.

6.1.2 Sn-hematite films for the Ta_2O_5 overlayer study in chapter 3

Hematite (α-Fe_2O_3) nanowires prepared on a fluorine-doped tin oxide (FTO) glass substrate: A glass container with a rubber stopper was filled with 20 ml aqueous solution containing 0.15 M of ferric chloride ($FeCl_3 \cdot 6H_2O$, Acros, 99+%) and 1 M sodium nitrate ($NaNO_3$, Fisher 99.4%). The solution pH was adjusted to 1.5 by HCl. A pre-cleaned piece of FTO glass substrate was put into the glass container. The reaction vessel was then heated at 95 °C for 4 hrs and then allowed to cool down at ambient conditions. A uniform layer of iron oxyhydroxide (α-FeOOH) film (yellow in colour) was formed on the FTO substrate. The α-FeOOH film was washed with deionized (DI) water to remove residual salt and the back face (non-conductive side) was thoroughly cleaned with water. The film was then sintered in a muffle furnace in air

at 550 °C for 30 min. This was followed by an additional annealing step at 750 °C for 20 min which is expected to incorporate Sn as a dopant from the substrate. Based on reference.[2]

6.1.3 Sn-hematite films for the acid treatment study in chapter 4

Hematite (α-Fe_2O_3) nanowires prepared on a fluorine-doped tin oxide (FTO) glass substrate: A Teflon-lined stainless steel autoclave was filled with 20 ml aqueous solution containing 0.15 M of ferric chloride ($FeCl_3 \cdot 6H_2O$, Acros, 99+%) and 1 M sodium nitrate ($NaNO_3$, Fisher 99.4%). The solution pH was adjusted to 1.5 by HCl. A pre-cleaned piece of FTO glass substrate was put into the autoclave. The autoclave was heated at 95 ^oC for 4 hrs and allowed to cool down at ambient conditions. A uniform layer of iron oxyhydroxide (α-FeOOH) film (yellow in colour) was formed on the FTO substrate. The α-FeOOH film was washed with deionized (DI) water to remove residual salt. To introduce Sn-doping into the nanowires, 1-2 drops of a tin (IV) chloride ($SnCl_4$) ethanol solution (2 mg/ml) was added onto the α-FeOOH film, and then sintered in air at 550 ^oC for 30 min, followed by annealing at 800 ^oC for an additional 20 min.[2]

6.1.4 TiO_2 nanowire films for acid treatment

TiO_2 nanowire films for acid treatment were prepared by Professor Yat Li and his group at the University of California, Santa Cruz. Rutile TiO_2 nanowire arrays were grown on a fluorine-doped tin oxide (FTO) glass substrate using a previously reported hydrothermal method.[3] 15 ml of concentrated hydrochloric acid were diluted with 15 ml DI water, and mixed with 0.5 ml titanium n-butoxide in a 100 ml beaker. This clear solution mixture was transferred to a Teflon-lined stainless steel autoclave (20 ml volume) containing a clean FTO glass substrate so that the FTO substrate was submerged in the solution. The sealed autoclave was heated in an electric

oven at 150 °C for 5 hrs, and then cooled down to room temperature slowly. The resulting TiO_2 nanowire films uniformly coated the FTO glass substrates. The sample was thoroughly washed with DI water and air dried. Finally, the sample was annealed in air at 550 °C for 3 hrs to increase the crystallinity of TiO_2 nanowires.

6.1.5 Doctor bladed TiO_2 films

Rutile TiO_2 films were prepared by depositing TiO_2 colloidal paste (DYESOL, average particle diameter of 20 nm) on fluorine-doped tin oxide (FTO) slides. The FTO substrates were first cleaned by sonicating in ethanol for 20 minutes and in H_2O for 20 minutes and then annealed in air at 450 ^oC before the deposition. The paste was deposited on the films and spread with a glass rod. The thickness was controlled using scotch tape and was measured *via* profilometry to be an average of 3 μm. The films were allowed to dry and were then heated at 550 °C for 30 minutes.

6.1.6 Acid treatment of metal oxides

Hematite and TiO_2 films grown on FTO glass substrates were immersed in pure acetic acid (99.8%) for 5 minutes, and then left to dry in air without washing. The films were then annealed at 450 ^oC in air for 30 min.[4] Hematite nanowire films were treated with other inorganic acids (2 M HCl, 2 M HNO_3, 1 M H_3PO_4) using the same procedure.

6.1.7 Pulsed laser deposition (PLD) of Sn-hematite films

PLD was carried out in collaboration with Professor Matt Rosseinsky and his group at The University of Liverpool. The procedure used has been reported previously in the literature.[5] FTO substrates were chopped into 20 mm x 10 mm pieces and cleaned by sonication for 20

minutes in acetone, then ethanol and finally water. Doped hematite targets were prepared by the solid state reaction of high purity powders of Fe_2O_3 (99.99% Alfa Aesar) and the SnO_2 dopant. The powders were mixed in appropriate amounts in order to obtain a Sn cation concentration of 1% ($Fe_{1.98}Sn_{0.02}O_3$). The mixture was ball-milled and subsequently pressed in a stainless steel mould and sintered in air at 1200 ^oC for 12 h, resulting in a disk-shaped pellet from which the films were deposited. 25 nm thick Sn-hematite films were deposited by PLD from the doped Fe_2O_3 targets onto the clean 20 mm x 10 mm FTO substrates with a Neocera PLD instrument at a substrate temperature of 450 ^oC. Growth was monitored with a double-differentially pumped high pressure reflection high energy electron diffraction (RHEED) system supplied by STAIB. One edge (5 mm) of the film was masked during deposition to provide an uncoated segment of the FTO for electrical connection.

6.2 Atomic layer deposition (ALD) and ellipsometry

ALD was carried out by Dr. Richard Potter and his group at The University of Liverpool using an Oxford Instruments OpAL reactor. The reactor was modified by the addition of a process controlled 'hold' valve between the pump and the process chamber, enabling precursor 'soak' steps. Soak steps were used in the process to ensure good film density and to promote conformal coating of the highly textured hematite surface. The number of ALD cycles was adjusted depending on the desired overlayer thickness. The growth rate of the overlayers were estimated with a Rudolph Auto EL IV ellipsometer operating at 633 nm using silicon 'witness' samples.

Al_2O_3: Al_2O_3 was deposited by thermal ALD using trimethyl-aluminium (TMA) and water. Coating was carried out at a low process temperature of 120 ^oC, selected to avoid accidental

modification of the hematite samples. Films were deposited using 10 cycles of ALD targeting ~1 nm of Al_2O_3, using the following sequence:

{(50 ms TMA Dose)(10 s TMA hold)(10 s purge)(30 ms H2O)(10 s H2O hold)(10 s purge)}

In line with previous reports,[6] the effect of the Al_2O_3 layer was found to be retained for at least 20 minutes in 1 M NaOH providing enough time to obtain TAS kinetic data at up to two wavelengths.

Ta_2O_5: Prior to ALD of Ta_2O_5, all films were thermally treated in air at 220 ^oC for 45 minutes in order to negate any potential changes in photocurrent due to 'heat cleaning'. Ta_2O_5 was deposited by thermal ALD using $Ta(NMe_2)_5$ and water. Coating was carried out at a medium process temperature of 200 ^oC, selected to avoid accidental modification of the hematite samples. 20 ALD cycles give a Ta_2O_5 thickness of approximately 1.8 nm.

6.3 Characterisation techniques

UV-Vis spectra were recorded using a Shimadzu UV-2600 spectrophotometer. XRD measurements were recorded with a Panalytical X'Pert PRO HTS X-Ray Diffractometer or a Philips PW1710 diffractometer with monochromated Cu radiation. SEM images were obtained with a Hitachi high resolution 7001 SEM instrument.

6.4 Electrochemistry

General electrochemical measurements were carried out in a custom designed photoelectrochemical cell. A working electrode secured by a crocodile clip, a platinum gauze counter electrode and a home-made 3 M NaCl Ag/AgCl reference electrode protected from the electrolyte solution by a 3 M NaCl double junction were used in all experiments.

Unless otherwise stated, the electrolyte used throughout was 1 M NaOH (Aldrich, pH 13.6) prepared with Milli-Q water (Millipore Corp, 18.2 MΩ cm at 25 ^{o}C) and prior to all experiments it was thoroughly degassed with a stream of argon for at least 20 minutes. Photocurrent measurements were recorded under illumination with a 75 W xenon lamp (ca.10 mW cm^{-2}) or a 300 W xenon lamp (*ca.*100 mW cm^{-2}) using either Palmsens1, Palmsens3 or Emstat potentiostats (Alvatek), or a Ministat (Thomson Scientific) potentiostat.

Due to equipment limitations, the cell was not purged prior to the temperature dependence measurements reported in chapter 4 or the Raman spectroscopy measurements in chapter 5.

Spectroelectrochemical measurements were recorded in a 3 electrode setup inside a 20 mm x 10 mm quartz cuvette using a Shimadzu UV-2600 spectrophotometer.

Mott-Schottky measurements were recorded using a Bio-Logic SAS potentiostat. The photoelectrochemical cell was placed into a Faraday cage in the dark during these measurements.

6.5 Transient spectroscopy

6.5.1 Transient absorption spectroscopy (TAS)

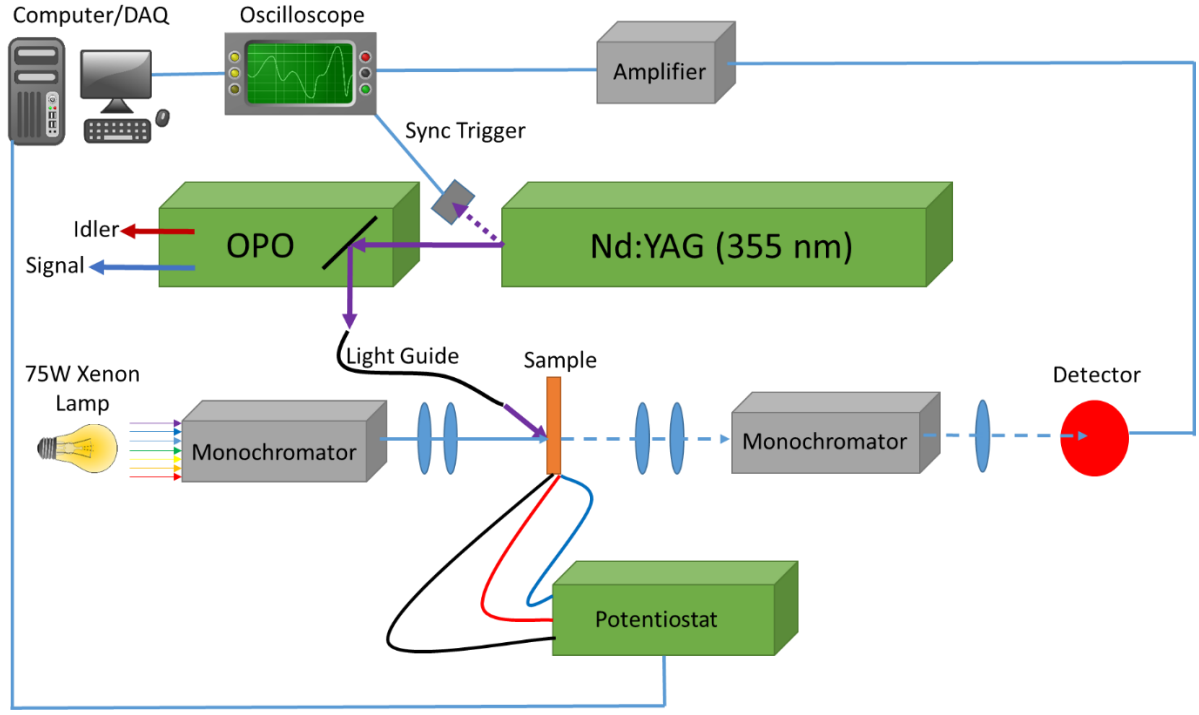

Figure 155 - The µs-s transient absorption system.

The slow (µs-s) TAS system is shown in Figure 155. Measurements were carried out using the third harmonic of a Nd:YAG laser (Continuum, Surelite I-10, 355 nm, 6 ns pulse width) operating at 0.33 Hz as the UV excitation source. The repetition rate was chosen to ensure that all charge carriers had fully decayed prior to the next excitation event. A liquid light guide transmitted the laser pulse to the sample. A laser intensity of *ca.* 200 µJ cm^{-2} at 355 nm was incident on the sample, unless otherwise specified (It should be noted that the glass cells typically used for the transient measurements absorb c.a. 50% of light at 355 nm resulting in an actual excitation energy of 100 µJ cm^{-2} at 355 nm) 75 W xenon lamp (OBB Corp.) or a 100 W tungsten lamp coupled to a monochromator (OBB Corp., typically set to 4 nm resolution)

was used as the probe light and the change in optical density of the sample was calculated by measuring the transmitted light using a Si Photodiode (Hamamatsu) and a homemade amplification system coupled to both an oscilloscope (Textronix TDS 220) and data acquisition card (National Instruments NI-6221). The oscilloscope data were used to study the microseconds time scale while the DAQ card covered the milliseconds to seconds. Typically, the data is averaged over 300 - 500 laser shots per wavelength. Full spectra were obtained by measuring a kinetic trace every 25 nm unless otherwise stated. Figure 156 shows a picture of the μs-s TAS system taken during assembly.

Figure 156 – Picture of the μs-s TAS system taken during assembly. The system is near completion in this picture, it does not yet contain the covers for shielding the laser and the sample area.

6.5.2 Ultrafast transient absorption spectroscopy

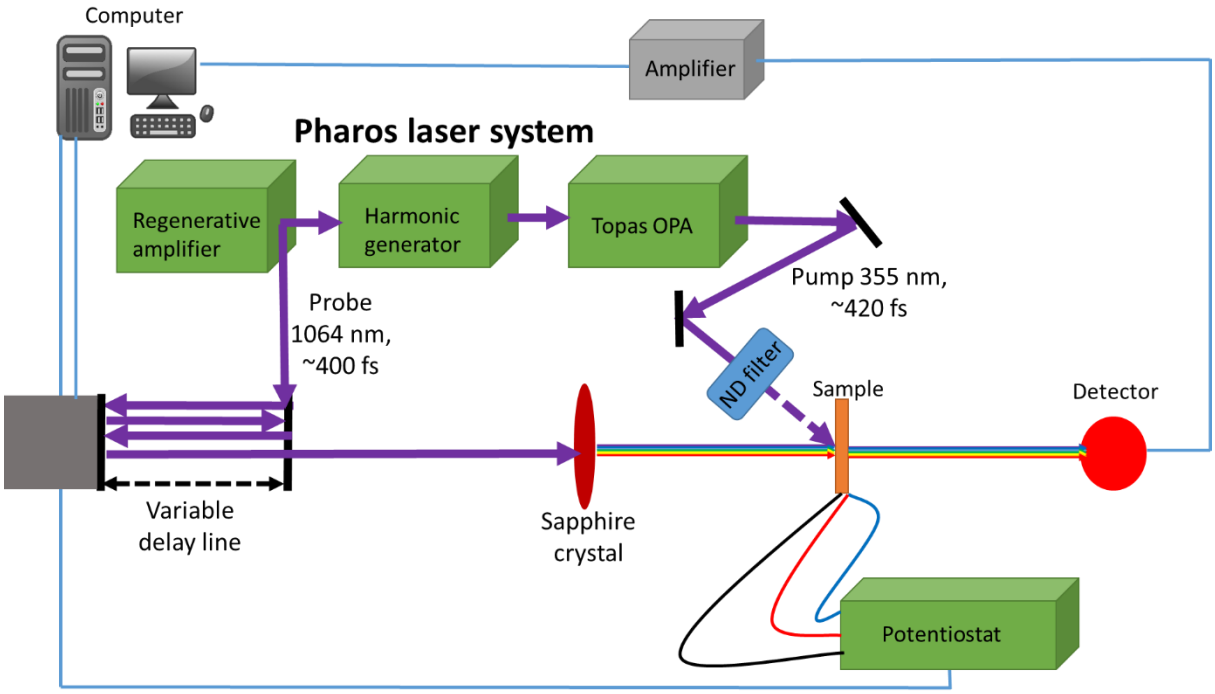

Figure 157 – Schematic of the Ultrafast TAS system used at the University of Liverpool.

Two separate femtosecond TA systems where used during this project and are described below.

University of Liverpool system: Firstly, a PHAROS laser on loan from the (now closed) EPSRC Laser Loan Pool (Light Conversion, Ltd) was used. The laser was operating at 10 kHz and was coupled to an ORPHEUS optical parametric amplifier (Light Conversion, Ltd) in tandem with a LYRA harmonic generator (Light Conversion, Ltd) to produce the desired wavelength for sample excitation. The pump beam intensity was adjusted with a neutral density filter so as to achieve approximately equal photon fluxes at different wavelengths. Typical pulse energies were on the order of 10 nJ. The pump wavelength was tuned to 355 nm. A portion of the PHAROS output was also split off to pump a sapphire crystal to generate a white light continuum for the probe beam, which provided spectral observation in the region 450-900

nm. The probe beam was focused to a spot size of ~100 μm diameter on the sample and was overlapped completely by the pump beam. Spectra were acquired with a HELIOS transient absorption spectrometer (Ultrafast Systems, LLC). The time resolution of the setup is ~ 400 fs. Measurements were performed by randomly stepping the optical delay line and averaging for 1 s at each delay time. Between two to five consecutive scans were collected and aggregated to produce each spectrum.

Imperial College London system: Transient absorption spectra were collected on fs-ns timescales using a regeneratively amplified Ti:sapphire laser system (Solstice, Spectra-Physics) and Helios spectrometers (Ultrafast Systems). The Solstice laser system generates 800 nm, 92 fs width, 1 kHz pulses. The excitation (pump) pulse is generated from a fraction of the 800 nm beam via an OPA (TOPAS Prime, Spectra-Physics) and frequency-mixer (NirUVis, Light Conversion) to select the wavelength, 355 nm. The pump beam diameter is approximately 1 mm at the sample. The intensity of the pump beam was modulated using neutral density filters, and was measured using a 500 μm diameter aperture and power meter (PD10-V2-ROHS, OPHIR Photonics). The probe pulse is delayed with respect to the excitation pulse by a motorised translational stage, which changes the path length of the probe beam. A visible or NIR white light continuum (WLC) is used as the probe, generated by attenuating and focussing a fraction of the 800 nm pulse onto one of two Ti:sapphire crystals of different thicknesses. In order to reduce noise, the WLC is split into two beams: one passes through the sample while the other is monitored by the reference spectrometer. The beams are focussed into two fibre-optic-coupled multichannel spectrometers (CMOS or InGaAs sensors for visible and NIR wavelengths, respectively). A synchronised chopper (500 Hz) is used to block alternate pump pulses; the absorbance change is calculated from adjacent pulses (pump blocked and unblocked). Difference spectra were typically averaged over 2 seconds for each time point recorded; each spectrum was collected several times then averaged. Spectra were corrected for

chirp (group velocity dispersion) using Surface Xplorer software (Ultrafast Systems) by fitting the rise of the spectrum. Spectra were time-zero corrected such that t_0 occurs at the half-amplitude of the spectrum rise.

6.5.3 Transient photocurrent (TPC)

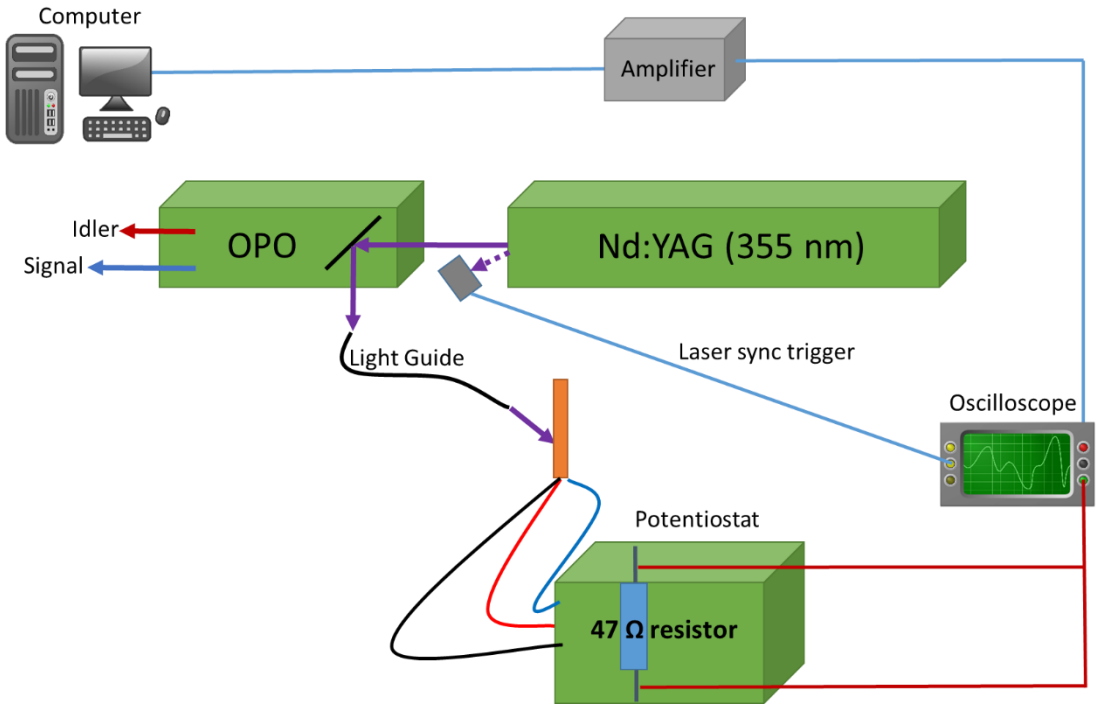

Figure 158 - Transient system adapted to record transient photocurrent measurements.

Transient photocurrent (TPC) measurements were carried out using an adaption of the existing slow TAS system, Figure 158. A 47 Ω resistor is placed into the potentiostat circuit. The laser excites the sample and the resulting charge reaching the external circuit is measured as a voltage across the resistor with respect to time using an oscilloscope. This voltage can be converted to current using Equation 1.

$$I = \frac{V}{R} \qquad (Eq. 1)$$

Furthermore, a measure of the total charge passed can be obtained by integrating the current with respect to time due to the relationship shown in Equation 2.

$$I = \frac{dQ}{dt} \qquad (Eq. 2)$$

6.6 Raman spectroscopy

6.6.1 SHINERS particle synthesis

SHINERS particles were synthesised using a standard sodium citrate reduction method to form gold nanoparticles with diameters of ~50 nm.[7] All glassware is cleaned in Piranha solution (5 parts conc. H_2SO_4 to 1 part H_2O_2, 40%) before use. Milli-Q H_2O is used during this synthesis. 7 mL of a 9.8 mM $HAuCl_4$ stock solution is placed into 200 mL of H_2O in a 250 mL round bottom flask equipped with a condenser. The solution is then refluxed at 200 ^oC ready for addition of the following solution. A 1% trisodiumcitrate solution is then prepared (1g in 100 mL H_2O), the concentration of this solution determines the nanoparticle size. 1.4 mL of the trisodiumcitrate is added to the round bottom flask containing $HAuCl_4$ and then refluxed for 40 minutes. The red/purple solution containing the gold nanoparticles is returned to room temperature and stored in the dark.

A method previously reported in the literature[8] is used to form the SiO_2 shell around the gold nanoparticles. 30 ml of the gold nanoparticles suspension prepared in the previous step is placed into a 100 ml round bottom flask with a glass stopper. This solution is then stirred vigorously using a magnetic stirrer bar. A 100 mL solution is then prepared containing 22 μL

(3-Aminopropyl)trimethoxysilane (APTMS) in H_2O. The APTMS solution is unstable and is prepared fresh every time. 0.4 mL of this APTMS solution is then added to the stirring nanoparticles which were then stirred at room temperature for 20 minutes in the dark. A separate 100 mL solution is prepared containing 3.8 mL of HCl and 2 mL of sodium silicate in H_2O to produce a solution with a pH of 10.3. This new solution is then vigorously shaken for 10 minutes. 3.2 mL of this sodium silicate pH 10.3 solution is added to the stirring nanoparticle solution on the 20 minute mark. This combined solution is then stirred in the dark at room temperature for a further 5 minutes. It is then transferred to a heater bath set at ~93 ^oC and stirred in the dark with a loose stopper for a further 20 minutes. The length of time of this final stirring at 93 ^oC dictates the thickness of the SiO_2 shell and variation can occur from batch to batch. After 20 minutes (and then again after 30 minutes, 40 minutes, 50 minutes and 60 minutes to provide a range of shell thicknesses) 1.5 mL of the SiO_2 coated gold nanoparticles were extracted by pipette, placed into a centrifuge tube and submerged into an ice bath to rapidly cool and prevent further shell growth. The cooled solution is then centrifuged at 5500 rpm for 15 minutes and the top layer of solution is removed and replaced with water. This is repeated twice more to wash the particles. Finally the particles were stored in ~1 mL of water, in the dark, in a fridge (~4 ^oC). Particles will typically begin to aggregate when stored for prolonged lengths of time and so were used within 1-2 weeks.

6.6.2 Testing the SHINERS particles

TEM is used to characterise the SHINERS particles and assess the thickness of the SiO_2 shell. Raman spectroscopy is used to check the silica shell for pinholes which lead to exposed gold. SHINERS were absorbed onto a glassy carbon electrode surface and pyridine is then dropped onto to this surface and left to adsorb. If pinholes are present 2 peaks will be visible in the Raman spectrum at 1010 and 1030 cm^{-1} (Figure 159a.) due to pyridine adsorption modes on

gold. If no peaks are present pyridine has not adsorbed onto the Au surface indicating a complete SiO_2 shell with no pinholes (Figure 159b.).

The enhancement factor of SHINERS is dependent on the shell thickness and Raman spectroscopy can be used to calculate this. SHINERS are deposited onto a Au surface and pyridine is dropped on and left to adsorb. The greatest enhancement is observed for SHINERS with a shell thickness of 2-3 nm (Figure 159c). If the shell is too thick the enhancement will be drastically reduced (Figure 159d.). If the shell is too thin, pin holes can be easily formed leading to exposed gold.

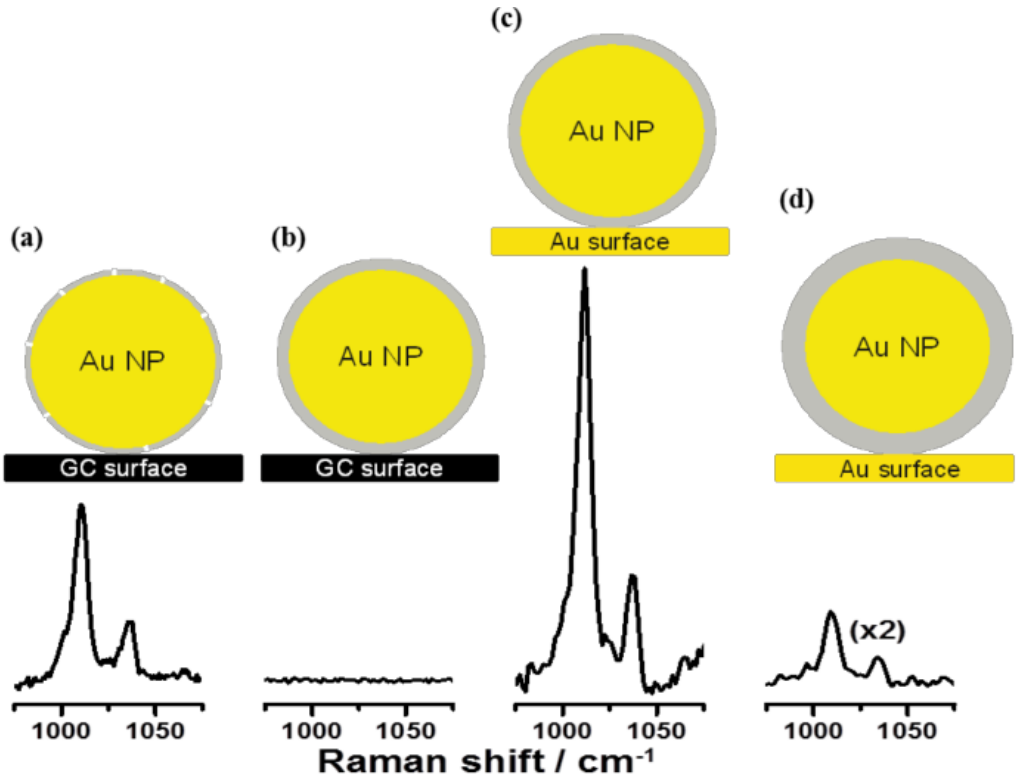

Figure 159 - Raman spectra of pyridine on (a) Glassy carbon/ SHINERS with pinholes (b) glassy carbon/ SHINERS without pinholes (c) Au/ SHINERS (2nm shell) (d) Au/SHINERS (4nm shell). Figure produced by Galloway et al.[9]

6.6.3 Raman instrument

Raman spectra were recorded with a Raman microscope (Renishaw inVia), using a 633 nm or 785 nm laser focussed through an inverted microscope (Leica) *via* a 50x objective (Leica). The microscope was calibrated with a silicon wafer standard before every measurement. At 633 nm the laser has an approximate spot size diameter of 2 µm. At 785nm the laser has an approximate spot size diameter of 1.5 µm. To avoid heat damage to the SHINERS particles, the laser power was typically kept at 5-10% of the maximum (maximum ~70 mW on sample).

Electrochemistry for Raman experiments was carried out using a Biologic potentiostat. A Powerstar Series UV LED 390 nm connected to a variable power supply was used to illuminate the sample from the front face.

6.6.4 Raman cell

The custom made cell used for combined Raman and spectroelectrochemical measurements was 3D printed in polylactic acid (PLA) at a printing temperature of 210 ^{o}C and a speed of 30 mm s^{-1} using a 3DBCN Sigma dual extrusion printer. A 1 mm quartz glass window was secured to the bottom of the cell using silicone rubber sealant.

6.7 References

[1] Y. Ling, G. Wang, J. Reddy, C. Wang, J.Z. Zhang, and Y. Li, Angew. Chem. Int. Ed. Engl. **51**, 4074 (2012).

[2] Y. Ling, G. Wang, D. a Wheeler, J.Z. Zhang, and Y. Li, Nano Lett. **11**, 2119 (2011).

[3] G. Wang, H. Wang, Y. Ling, Y. Tang, X. Yang, R.C. Fitzmorris, C. Wang, J.Z. Zhang, and Y. Li, Nano Lett. **11**, 3026 (2011).

[4] Y. Yang, M. Forster, Y. Ling, G. Wang, T. Zhai, Y. Tong, A.J. Cowan, and Y. Li, Angew. Chemie Int. Ed. **55**, 3403 (2016).

[5] K.D. Malviya, H. Dotan, D. Shlenkevich, A. Tsyganok, H. Mor, and A. Rothschild, J. Mater. Chem. A **4**, 3091 (2016).

[6] M. Forster, R.J. Potter, Y. Ling, Y. Yang, D.R. Klug, Y. Li, and A.J. Cowan, Chem. Sci. **6**, 4009 (2015).

[7] G. Frens, Nat. Phys. Sci. **241**, 20 (1973).

[8] L.M. Liz-Marzán, M. Giersig, and P. Mulvaney, Langmuir **12**, 4329 (1996).

[9] T.A. Galloway and L.J. Hardwick, J. Phys. Chem. Lett. **7**, 2119 (2016).

7

Appendix

Contents

7.1 Chapter 3 supplementary information

7.1.1 Heating control test of Fe_2O_{3-x}

Because Fe_2O_{3-x} films are rich in oxygen vacancies, heating the films in air or an oxygen containing atmosphere is a concern as it has the potential to remove these vacancies. In order to establish whether the temperature of the ALD process alone would affect the Fe_2O_{3-x} a control test was carried out in which photocurrents and TA measurements were recorded before and after heating Fe_2O_{3-x} to 220 ^oC in air (just above the temperature at which Ta_2O_5 deposition occurs), Figure 160.

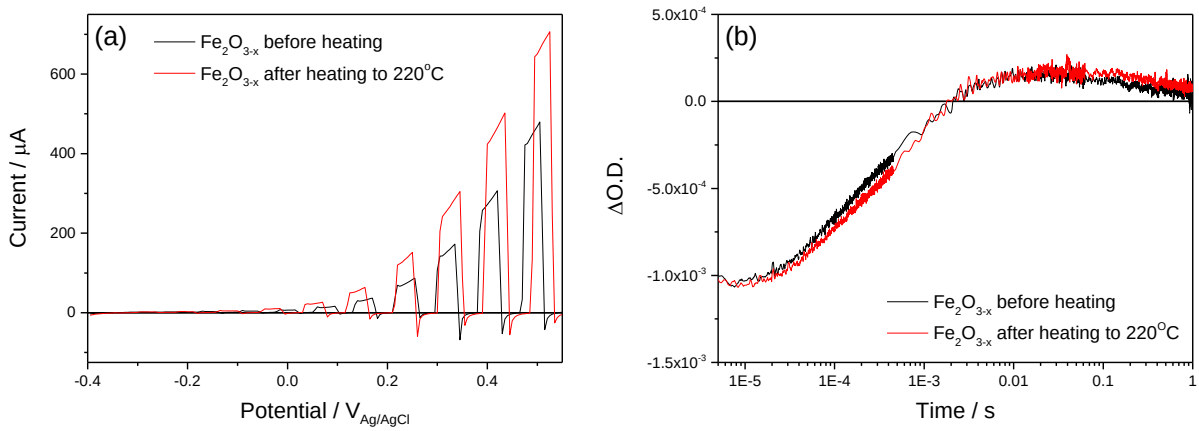

Figure 160 - (a) Chopped photocurrent and (b) TA kinetics probed at 575 nm following 355 nm laser excitation (~100 µJ cm^{-2}) of Fe_2O_{3-x} before (black) and after (red) annealing at 220 ^oC in air for 45 minutes.

Following heating, a small increase in photocurrent magnitude was observed, Figure 160a. Small increases in activity following heating are often observed in photoelectrode materials and they are thought to be due to a cleaning effect which removes contaminants from the surface and this is proposed to be the case with Fe_2O_{3-x}. Photoelectron de-trapping kinetics as probed by TAS at 575 nm shows no change following heating, suggesting that the trap states remain unchanged, Figure 160b. In order to correct for the heat cleaning effect, all films in the

study presented in chapter 3 were heated at 220 ºC in air for 45 minutes before pre-ALD analysis. It should be noted that the ALD process itself is carried out under vacuum/very low pressure and so removal of oxygen vacancy is not expected to be a significant problem.

7.1.2 The effect of Ta_2O_5 overlayers on Fe_2O_3 (un-doped) films

In order to further understand the role of Ta_2O_5, experiments were carried out on an air annealed sample (no intentional oxygen vacancies doping), Fe_2O_3. This film has the same nanostructure as the Fe_2O_{3-x} films, however it contains a very low dopant level and as a result has very low activity, chapter 3. Fresh α-Fe_2O_3 (air annealed) films were again prepared by our collaborators, Li *et al.*[1,2] and films were heat treated at 220 ºC and then Ta_2O_5 was deposited with a target thickness of ~2 nm (20 deposition cycles). The addition of Ta_2O_5 had no significant effect on the extinction spectrum of Fe_2O_3, Figure 161. The small increase at 350-400 nm is likely due to variation in the Fe_2O_3 films rather than a result of the Ta_2O_5.

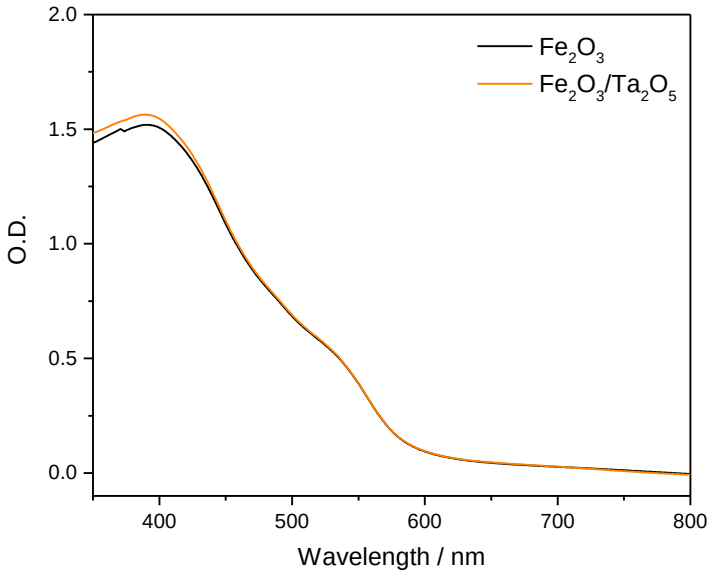

Figure 161 - UV-Vis extinction spectra of Fe_2O_3 and Fe_2O_3 / Ta_2O_5 recorded directly in absorbance mode.

Figure 162 shows photocurrent measurements of Fe_2O_3 with and without Ta_2O_5. The results show a clear and somewhat surprising increase or turn on of the photocurrent response following the addition of Ta_2O_5. Initially, the Fe_2O_3 is inactive and has a negligible photocurrent response due to the lack of doping in the nanostructured film, however, following the addition of Ta_2O_5 a sudden increase in photocurrent response is observed with an onset potential of *ca.* -0.1 $V_{Ag/AgCl}$. In addition to the change in photocurrent, a positive shift in the dark electrocatalytic water oxidation onset occurs of ~50-100 mV, a shift that was also present in Fe_2O_{3-x}/Ta_2O_5. Due to the negligible photocurrent prior to Ta_2O_5 deposition, it is difficult to comment on the magnitude of the photocurrent spikes in the chopped photocurrent plot, Figure 162b. In the previous study, Al_2O_3 was not found to affect the Fe_2O_3 samples in any way, however the Al_2O_3 layer was unstable making long term studies difficult.

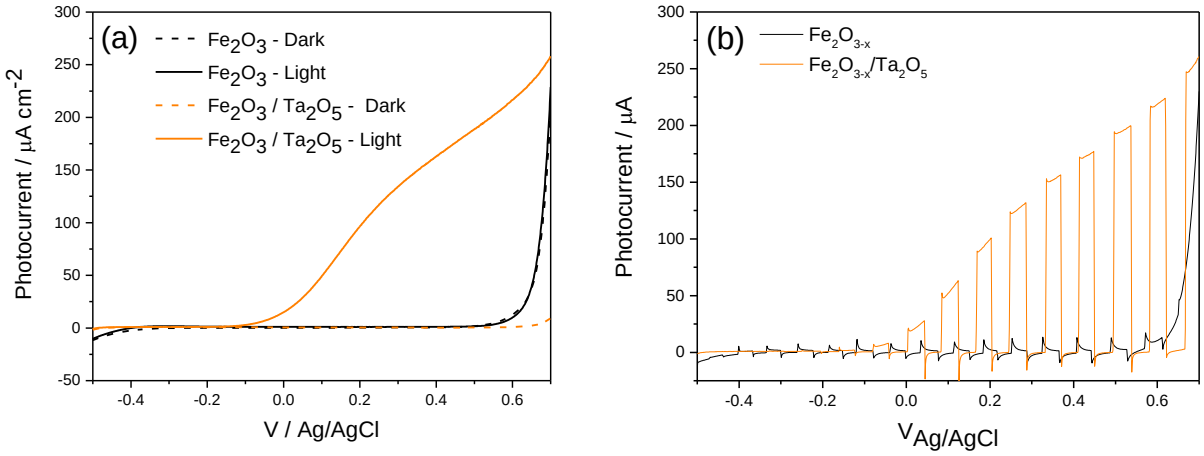

Figure 162 - (a) linear sweep and (b) chopped photocurrents of Fe_2O_3 (black) and Fe_2O_3/Ta_2O_5 (blue) at 10 mvs^{-1} under 50 $mWcm^{-2}$ white light illuminations.

It is not clear why this sudden increase in photocurrent occurs. One explanation could be that heating during ALD causes migration of Sn from the FTO substrate into Fe_2O_3, acting as a dopant. However, because the films were heated at 220 ^oC before any measurements were

carried out and before ALD, it is unlikely that heating is responsible for this change. Temperatures of 500 ^{o}C or more in air are typically required for a doping migration effect to occur in hematite photoelectrodes. In order to establish the dopant level, Mott-Schottky measurements were recorded for Fe_2O_3 with and without Ta_2O_5, Figure 163. Following Ta_2O_5 deposition, a marginal increase in donor density from $8.6x10^{19}$ cm^{-3} to $8.8x10^{19}$ cm^{-3} occurs and a small shift in flat-band potential occurs, moving from -0.6 $V_{Ag/AgCl}$ to -0.5 $V_{Ag/AgCl}$. As the donor density is only marginally altered, it suggests doping and the turning off of back electron transfer as reported in chapter 3 is not the cause of the photocurrent increase.

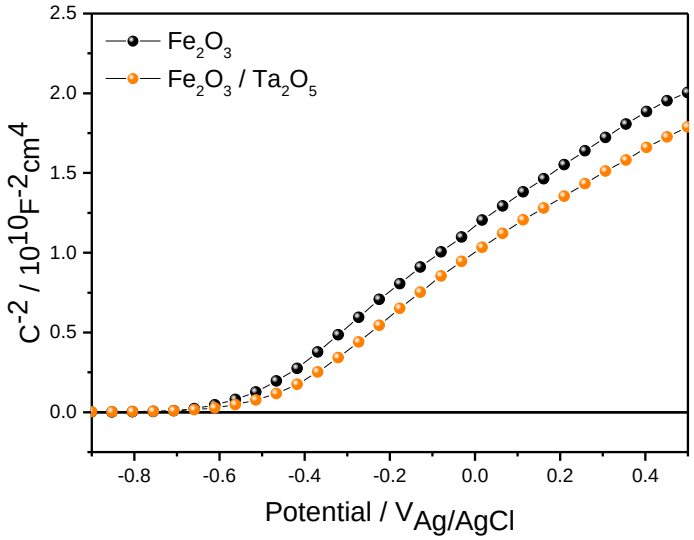

Figure 163 - Donor density Fe_2O_3 with and without a 2 nm Ta_2O_5 overlayer. Fe_2O_3 has an approximate flatband potential of -0.6 $V_{Ag/AgCl}$ and a donor density of $8.6x10^{19}$. Fe_2O_3/Ta_2O_5 has an approximate flat-band potential of -0.5 $V_{Ag/AgCl}$ and a donor density of $8.8x10^{19}$.

Alternatively, the activity increase could be related to alteration of trap states at the surface responsible for Fermi level pinning. The presence of surface states with energies within the bandgap energy of the semiconductor can cause Fermi level pinning where an applied bias to the electrode does not initially induce the bending of the bands of the semiconductor but first causes the emptying of the surface states. The potential drop occurs over the Helmholtz layer

instead of in the semiconductor photoelectrode, and as a result, no space charge field is present to separate photogenerated charges. Band bending can only occur once these surface states are emptied.[3] Fermi level pinning is normally only responsible for an increase in onset potential and not total inactivity of the film even at high applied bias as is the case with Fe_2O_3 so this may not be a suitable explanation.

With an increase in doping ruled out and the mechanism of enhancement still unclear we turn to TAS measurements for further clarification. Figure 164 shows the ultrafast TAS kinetics of Fe_2O_3 in a photoelectrochemical cell at an applied bias of 0.4 $V_{Ag/AgCl}$ following 355 nm excitation. Similar to Fe_2O_{3-x}, a broad positive hole feature spanning the full spectral region is present which is overlapped with the sharp feature centred at ~ 575 nm assigned to electron trapping and de-trapping. Unlike Fe_2O_{3-x}, the 575 nm feature of Fe_2O_3 decays much more slowly and does not invert on the ultrafast timescales (~ 6000 ps). There is no noticeable change in the spectra on these timescales following Ta_2O_5 deposition. The indistinguishable kinetics on these fast timescales suggests there is no difference in the efficiency of initial charge separation, Figure 165a.

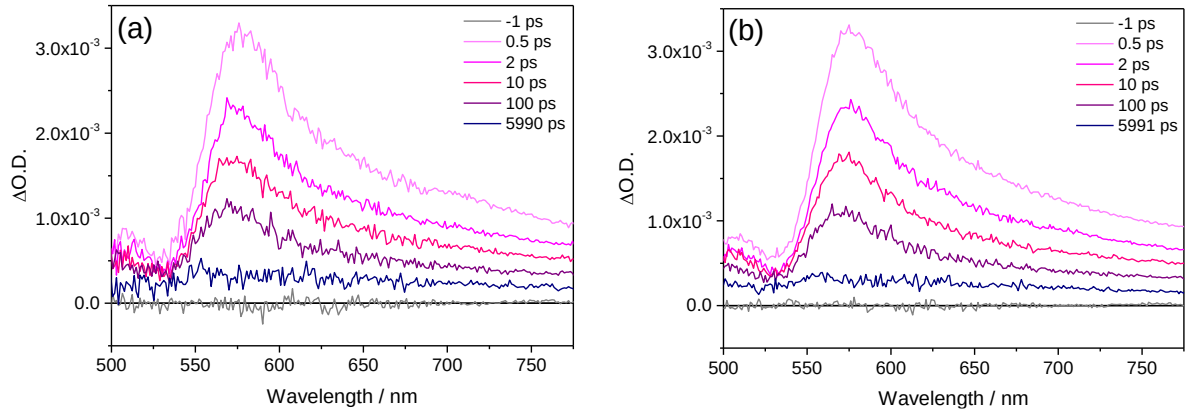

Figure 164 - Ultrafast TA full spectra probed at 500-775 nm following 355 nm laser excitation of (a) Fe_2O_3 and (b) Fe_2O_3/Ta_2O_5 in a photoelectrochemical cell at an applied bias of 0.4 $V_{Ag/AgCl}$.

On the slow timescales a difference in trapping kinetics becomes apparent, Figure 165b. Fe_2O_3 exhibits a small bleach, which, rather than being reduced following Ta_2O_5 deposition as would be predicted from the previous results, is actually increased *ca.* 3-fold. This unexpected result suggests the addition of Ta_2O_5 has increased the amount of photoelectron trapping in the material. It is possible that the increased level of trapping coincides with the increased photocurrent in that there is a greater number of long-lived electrons which improves photocurrent but also increases the amount of electrons available for trapping. It is also possible that the trap density has changed following the addition of Ta_2O_5. Unfortunately the reason for the increase in photocurrent is not clear at this point nor is it clear whether the increase in trapping magnitude is related to this photocurrent increase.

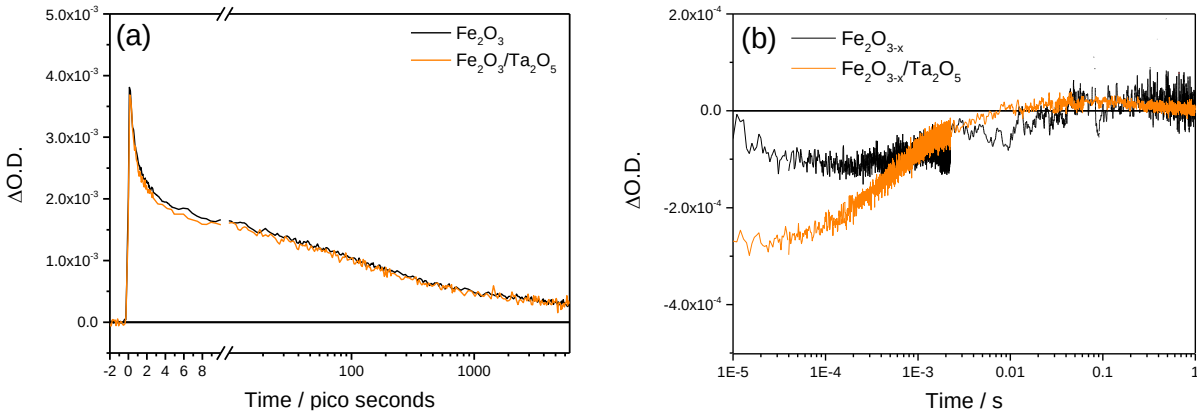

Figure 165 - (a) Ultrafast and (b) microsecond TA kinetics probed at 575 nm following 355 nm laser excitation (~100 μJ cm^{-2}) of Fe_2O_3 and Fe_2O_3/Ta_2O_5 in a photoelectrochemical cell at an applied bias of 0.4 $V_{Ag/AgCl}$.

There is no significant change in the hole signal probed at 650 nm following Ta_2O_5 deposition showing the overall yield of holes has not been increased by the overlayer, Figure 166. The kinetics following Ta_2O_5 are remarkably similar to that of Fe_2O_{3-x} following Ta_2O_5 and they are in turn very similar to the hole signal of Fe_2O_{3-x} in the presence of the hole scavenger H_2O_2

(chapter 2). This could indicate that there is a portion of holes in these materials which exist sufficiently far from the surface that they are not affected by surface altering changes. Rather than clarifying the effects of Ta_2O_5 on hematite, the behaviour of this material has further complicated the study. The exact mechanism of enhancement in this film is not currently understood and future experiments are required to investigate this further.

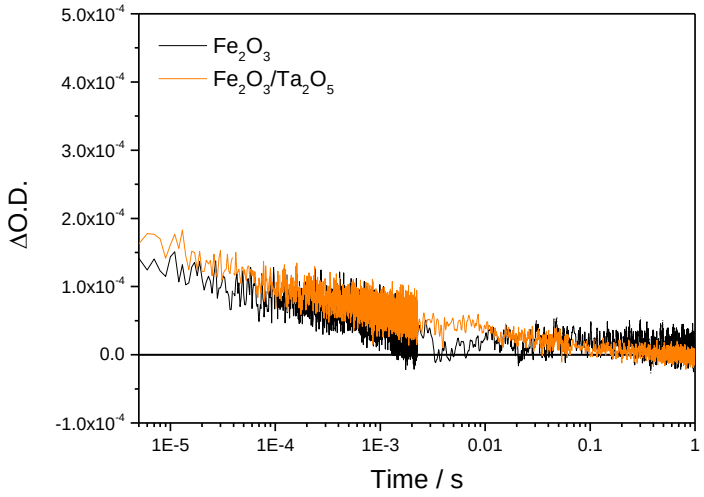

Figure 166 - Microsecond TA hole kinetics probed at 650 nm following 355 nm laser excitation (~100 μJ cm^{-2}) of Fe_2O_{3-x} (black) and Fe_2O_{3-x}/Ta_2O_5 (orange) in a photoelectrochemical cell at an applied bias of 0.4 $V_{Ag/AgCl}$.

Figure 167 shows the steady state absorbance of α-Fe_2O_3 with and without Ta_2O_5. Initially the steady state absorbance feature at 575 nm (Figure 167a) is very small as expected for a material with low trap states. Following Ta_2O_5 deposition, the 575 nm steady state absorbance feature increases in size Figure 167b. This increase is consistent with the 575 nm feature probed by TAS in Figure 165b.

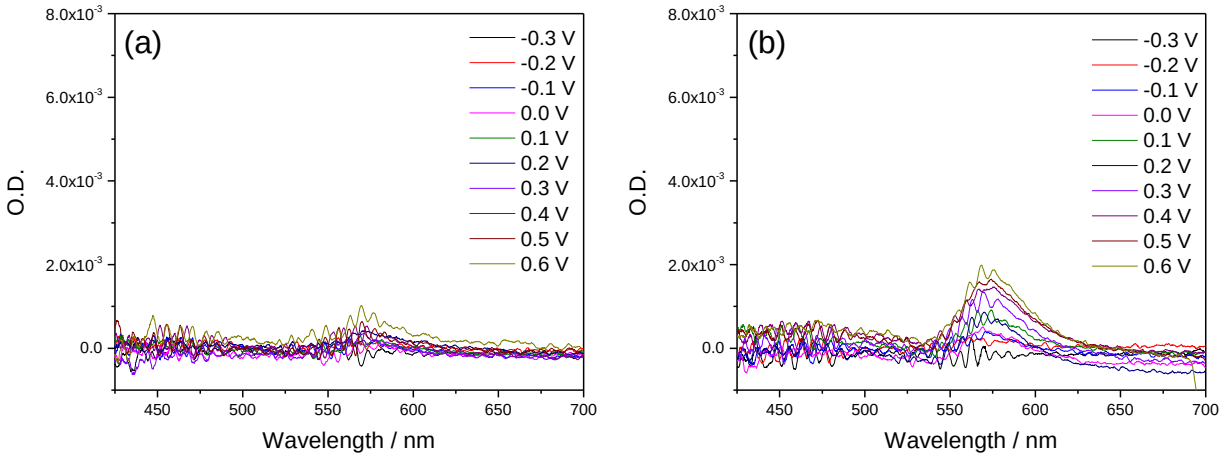

Figure 167 - Difference steady-state absorption spectra under various applied electrical bias vs. a background bias of -0.3$V_{Ag/AgCl}$ (pH ~13.7) (close to the flat-band potential). (a) α-Fe_2O_3, (b) α-Fe_2O_3/Ta_2O_5, Ta_2O_5 layers are 2 nm thick.

Figure 168 shows dark CVs of α-Fe_2O_3 with and without a Ta_2O_5 overlayer. The dark CV of α-Fe_2O_3 initially shows only one feature, the feature at *c.a.* 0.55 $V_{Ag/AgCl}$ (pH ~13.7) assigned to the water oxidation intermediate. Following Ta_2O_5 deposition, the peak at 0.55 $V_{Ag/AgCl}$ is significantly reduced, in line with all other types of hematite tested. More significantly a new peak appears at *ca.* -0.2 $V_{Ag/AgCl}$ (pH ~13.7), the same feature previously assigned to electron trap states. The correlation between the 575 nm feature and the CV feature at -0.2 $V_{Ag/AgCl}$ (pH ~13.7) further supports the assignment that the 575 nm spectroscopic feature is that of electronic trap states and not water oxidation intermediates. As with α-Fe_2O_{3-x} and LT-Fe_2O_3, the deposition of Ta_2O_5 results in an improved photocurrent response. It is not clear in this case why the addition of Ta_2O_5 increases electron trapping and in turn, why this improves the photocurrent. It could be evidence to suggest that a percentage of these electron trap states are located in the bulk, and while the surface of α-Fe_2O_3 following Ta_2O_5 remains passivated, the electronic properties of the material are altered by the overlayer such that some bulk traps are activated.

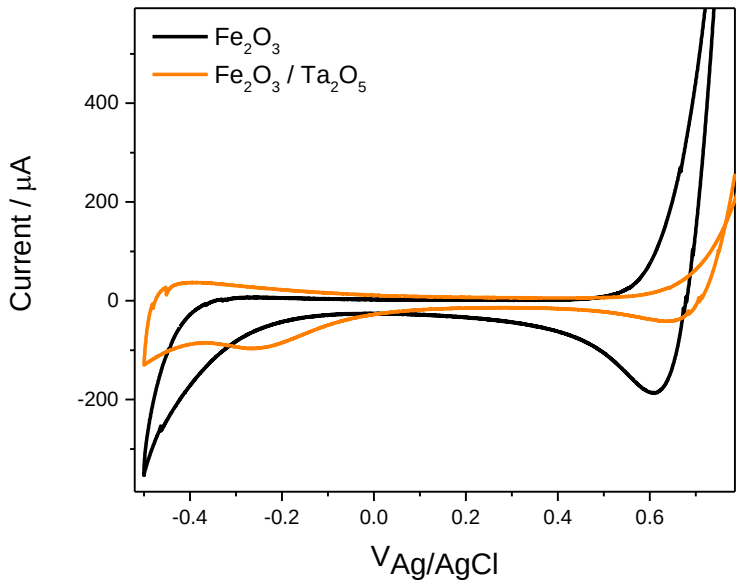

Figure 168 - Dark cyclic voltammograms in 1 M NaOH (pH ~13.7) of α-Fe_2O_3 with and without a 2 nm Ta_2O_5 overlayer. The films were scanned in the dark at 200 mVs^{-1}after being held in the light for 60 seconds at 0.8 V.

7.1.3 Fitting parameters for temperature dependence study

Tables 1-4 show the fitting parameters obtained from the bi-exponential fits of Figure 41 in chapter 3.Table 16 below compares the magnitude (the A term from fitting) of the fast component before and after Ta_2O_5 deposition. Table 17 below compares the magnitude (the A term from fitting) of the slow component before and after Ta_2O_5 deposition.

Temperature (°C)	α-Fe_2O_{3-x} A	α-Fe_2O_{3-x} / Ta_2O_5 A	Decrease (%)
23	-2.29(±0.01) x10^{-4}	-1.52(±0.01) x10^{-4}	33.0
29	-2.64(±0.01) x10^{-4}	-1.32(±0.01) x10^{-4}	49.1
35	-2.80(±0.01) x10^{-4}	-1.46(±0.01) x10^{-4}	48.6
41	-2.32(±0.02) x10^{-4}	-1.45(±0.02) x10^{-4}	38.3
48	-2.49(±0.02) x10^{-4}	-3.82(±0.12) x10^{-5}	45.2

Table 16 - Shows the magnitude (the A term from fitting) of the fast component obtained from bi-exponential fitting of the 575 nm kinetic trace at a range of temperatures before and after Ta_2O_5 deposition. The final column shows the percentage by which the magnitude decreased following the deposition of Ta_2O_5.

Temperature (°C)	α-Fe_2O_{3-x} A	α-Fe_2O_{3-x} / Ta_2O_5 A	Decrease (%)
23	-1.02(±0.01) x10^{-4}	-4.32(±0.01) x10^{-5}	58.2
29	-9.21(±0.01) x10^{-5}	-7.90(±0.06) x10^{-5}	18.1
35	-9 (±1) x10^{-5}	-5.4(±0.1) x10^{-5}	40.0
41	-9.2(±0.2) x10^{-5}	-5.2(±0.2) x10^{-5}	46.2
48	-6.3(±0.2) x10^{-5}	-1.42(±0.02) x10^{-4}	39.9

Table 17 - Shows the magnitude (the A term from fitting) of the slow component obtained from bi-exponential fitting of the 575 nm kinetic trace at a range of temperatures before and after Ta_2O_5 deposition. The final column shows the percentage by which the magnitude decreased following the deposition of Ta_2O_5.

Table 18 below compares the decay constant (the *k* term) and the lifetime (τ term) of the fast component before and after Ta_2O_5 deposition. Table 19 below compares the decay constant (the k term from fitting) and the lifetime (τ term) of the slow component before and after Ta_2O_5 deposition:

Temperature (°C)	**α-Fe_2O_{3-x} *k* (s^{-1})**	**α-Fe_2O_{3-x} τ (s)**	**α-Fe_2O_{3-x} / Ta_2O_5 *k* (s^{-1})**	**α-Fe_2O_{3-x} / Ta_2O_5 τ (s)**	**Change (%)**
23	1480(±10)	6.72(±0.04) x10^{-4}	1770(±20)	5.6 (±0.1) x10^{-4}	16.2
29	1605(±9)	6.23(±0.36) x10^{-4}	2300(±29)	4.30(±0.02) x10^{-4}	30.8
35	1651(±12)	6.05(±0.04) x10^{-4}	2100(±29)	4.68(±0.06) x10^{-4}	22.8
41	1788(±22)	5.7(±0.7) x10^{-4}	2080(±33)	4.8(±0.1) x10^{-4}	14.0
48	1740(±20)	5.74(±0.06) x10^{-4}	2140(±32)	4.7(±0.2) x10^{-4}	18.7

Table 18 - Shows the decay constant (the k term from fitting) and the τ term (the lifetime) of the fast component obtained from bi-exponential fitting of the 575 nm kinetic trace at a range of temperatures before and after Ta_2O_5 deposition. The final column shows the percentage by which the magnitude decreased following the deposition of Ta_2O_5.

Temperature (°C)	**α-Fe_2O_{3-x} *k* (s^{-1})**	**α-Fe_2O_{3-x} τ (s)**	**α-Fe_2O_{3-x} / Ta_2O_5 *k* (s^{-1})**	**α-Fe_2O_{3-x} / Ta_2O_5 τ (s)**	**Change (%)**
23	83(±1)	1.20(±0.01) x10^{-2}	140(±5)	6.95(±0.22) x10^{-3}	42.2
29	87(±1)	1.54(±0.01) x10^{-2}	216(±4)	4.6(±0.1) x10^{-3}	59.8
35	155(±3)	6.47(±0.12) x10^{-3}	270(±9)	3.73(±0.13) x10^{-3}	42.3
41	310(±10)	3.3(±0.1) x10^{-3}	330(±15)	2.99(±0.13) x10^{-3}	8.0
48	293(±12)	3.4(±0.1) x10^{-3}	260(±14)	3.8(±0.1) x10^{-3}	10.7

Table 19 - Shows the decay constant (the k term from fitting) and the τ term (the lifetime) of the slow component obtained from bi-exponential fitting of the 575 nm kinetic trace at a range of temperatures before and after Ta_2O_5 deposition. The final column shows the percentage by which the magnitude decreased following the deposition of Ta_2O_5.

7.2 Chapter 4 supplementary information

7.2.1 Acid treated TiO_2

In addition to the results reported in chapter 4, which investigated acid treatment of hematite films the treatment was also carried out on nanostructured TiO_2 photoelectrodes to assess whether other electrode materials can be improved in the same way. The TiO_2 nanowire films for acid treatment were prepared by Yat Li and his group at the University of California, Santa Cruz. Rutile TiO_2 nanowire arrays were grown on a fluorine-doped tin oxide (FTO) glass substrate using a previously reported hydrothermal method (full details can be found in chapter 6).[4]

Figure 169 shows the photocurrent response of TiO_2 before and after the same concentrated acetic acid treatment procedure as reported for hematite in chapter 4. A notable increase in the TiO_2 photocurrent is observed following acid treatment.

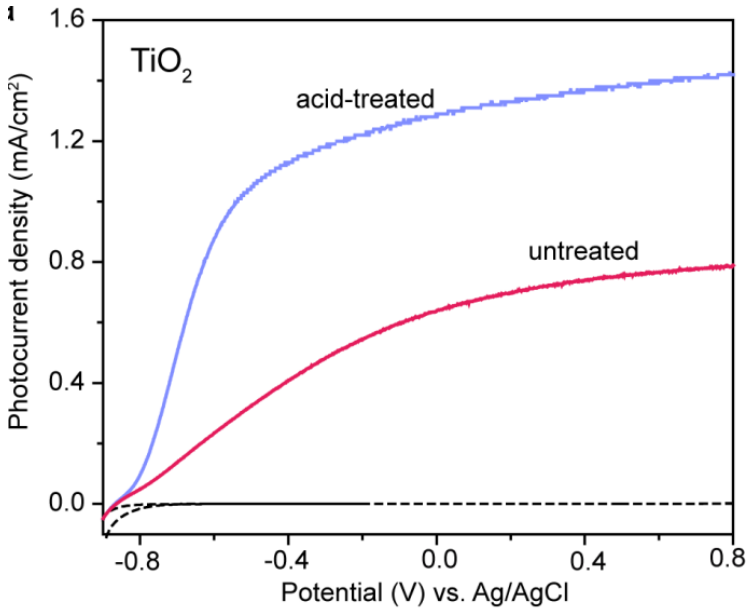

Figure 169 - Linear sweep voltammograms collected for untreated (red line) and acid-treated TiO_2 (blue line) photoanodes at 20 mV s^{-1} in a 1 M NaOH solution (TiO_2 photoanode) in the dark (dashed lines) and under illumination of simulated solar light (AM 1.5G, 100 mW cm^{-2}). Measurements carried out by Li et al.[5]

Figure 170 shows the extinction spectra of TiO_2 before and after acid treatment. No change in light absorption properties were observed following acid treatment which is consistent with the effects seen in hematite.

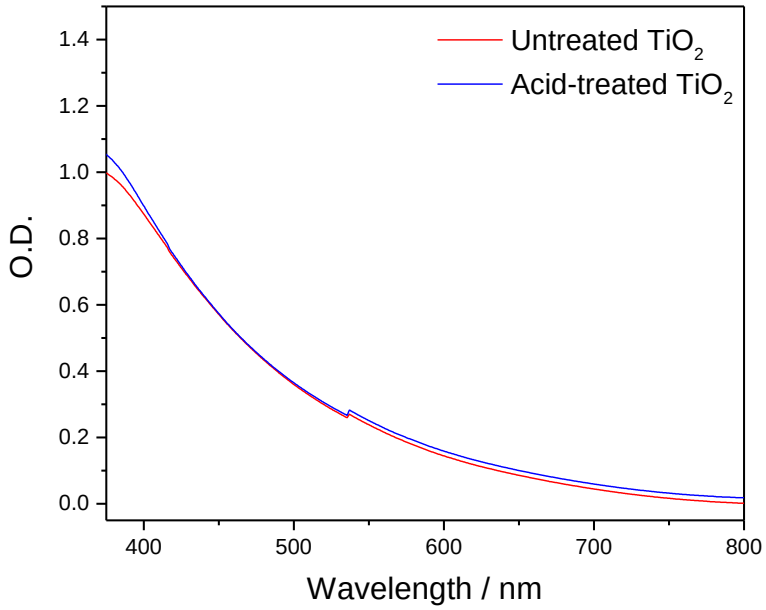

Figure 170 – UV-Vis extinction spectra collected from 375-800 nm for untreated and acid-treated TiO_2.

Figure 171 shows SEM images of the TiO_2 films showing the nanorod structure with typical rod diameters of 100 nm and typical lengths of 2-3 μm. Similar to the observations in Sn-Fe_2O_3, the acid treatment appears to have no effect on the structure of TiO_2 as observed by SEM.

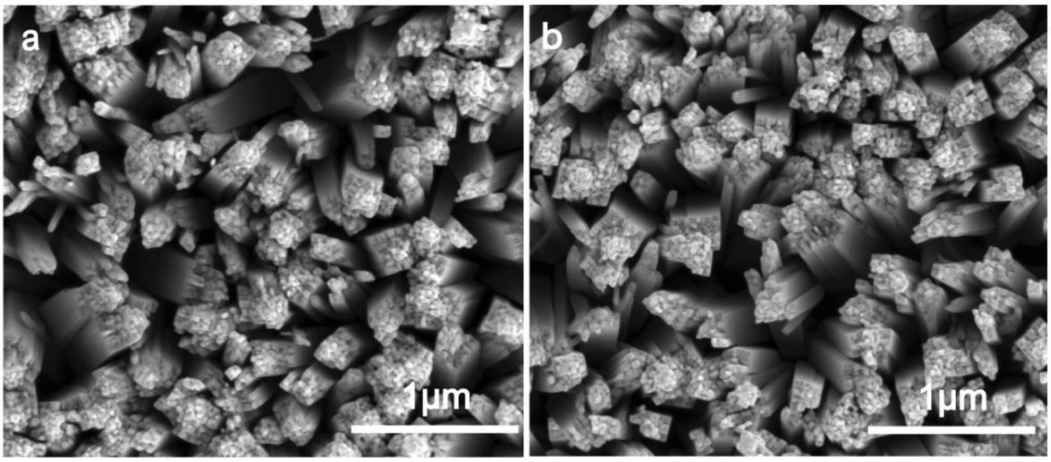

Figure 171 – SEM images of TiO_2 (a) before acid treatment and (b) after acid treatment.

In order to progress the study a batch of new TiO_2 films were prepared and acid treated, however, this new batch of films led to less consistent results than previously observed. Figure 172 shows the photocurrent response for a number of TiO_2 films before and after acid treatment. In contrast to the results previously observed in Figure 169, the maximum improvement in photocurrent achieved for the new batch of films was significantly lower, and several films exhibited no enhancement. A third batch of TiO_2 films were then prepared and acid treated, Figure 173. This batch of films exhibited a significant enhancement in photocurrent following acid treatment, observations which were more in line with the initial films used for this study.

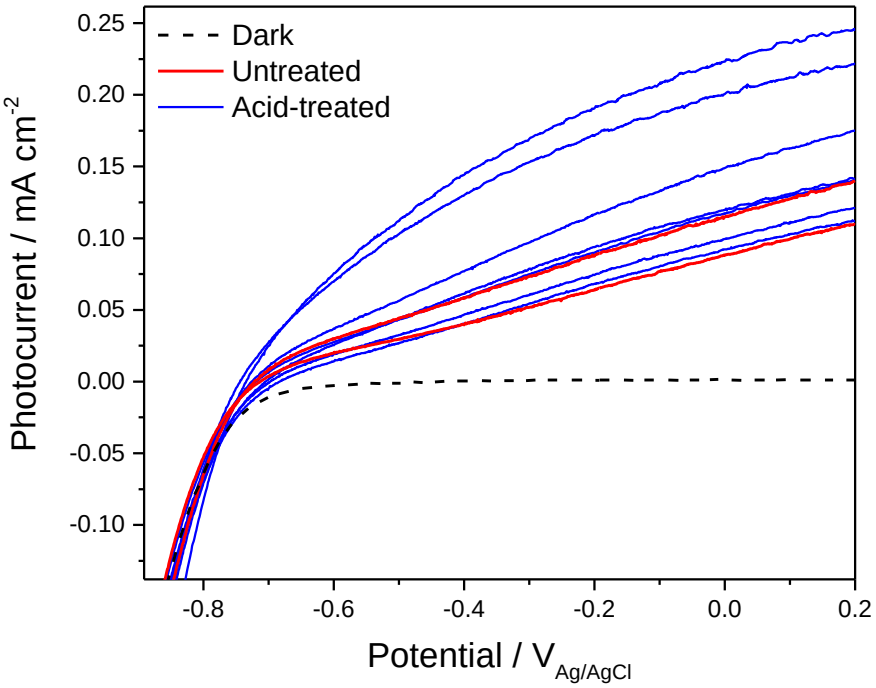

Figure 172 - Photocurrents collected for untreated (red) and acid-treated (blue) TiO_2 photoaonodes scanned at 10 mV s^{-1} in a 1 M NaOH (pH ~13.7) under ca. 75 mW cm^{-2} white light illumination and in the dark (dotted line).

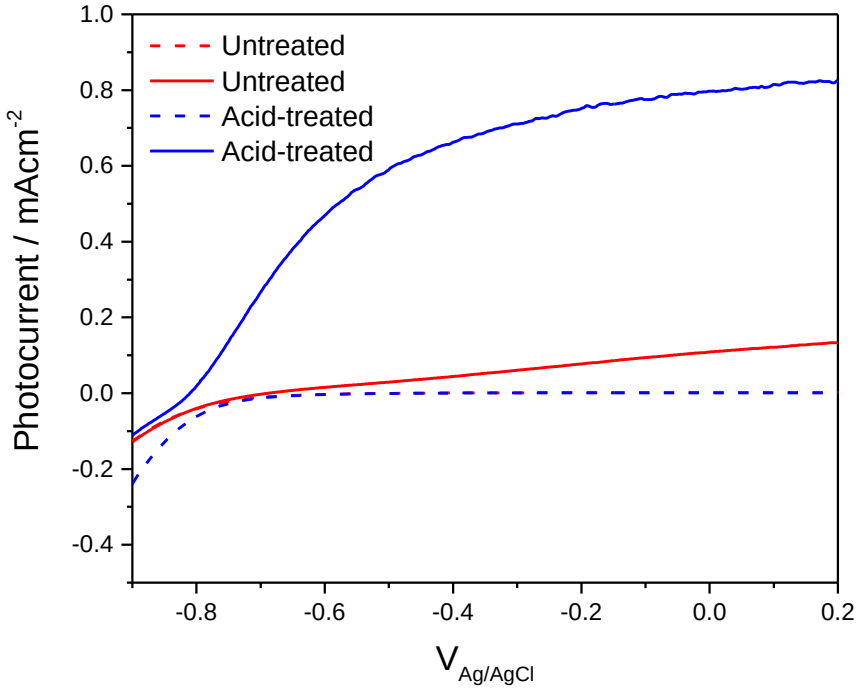

Figure 173 - Photocurrents collected for untreated (red) and acid-treated (blue) TiO_2 photoaonodes scanned at 10 mV s^{-1} in a 1 M NaOH (pH ~13.7) under ca. 75 mW cm^{-2} white light illumination and in the dark (dotted lines).

While acid treating TiO_2 can improve activity, the method appears unreliable. Unlike for Sn-Fe_2O_3, which showed consistent enhancement between films, the effect on TiO_2 was less consistent leading to sporadic sets of results. The reason for the large variation in the TiO_2 results is unclear. All TiO_2 films were synthesised using the same procedure to obtain photoelectrodes of the same structure and similar initial activity, which indicates that the observed variation in results is due to the acid treatment procedure.

Although acid treatment of TiO_2 provided inconsistent results, further investigation of a film which exhibited significant enhancement was thought to still provide insight. TAS studies were carried out on an untreated TiO_2 film and an acid treated film which showed pronounced enhancement in an attempt to rationalise the improvement and identify how to make the process more reliable. Figure 174 shows full spectra TAS measurements of untreated and acid-treated TiO_2 probed from 450-950 nm at an applied bias of 0.2 $V_{Ag/AgCl}$ (pH ~13.7).

TiO_2 has been studied with TAS for over 25 years,[6] and although slight differences in charge carrier spectra are observed, it is widely reported that in TiO_2 trapped photoholes can be probed at 450−550 nm and trapped photoelectrons can be probed at 800−900 nm.[7–10] Trapping of electrons and holes in TiO_2 is known to occur within 500 ps after the laser flash.[11] Both of these features typically exist as broad, overlapping signals, often resulting in a flat spectrum between 400-950 nm when both electron and hole signals are present.

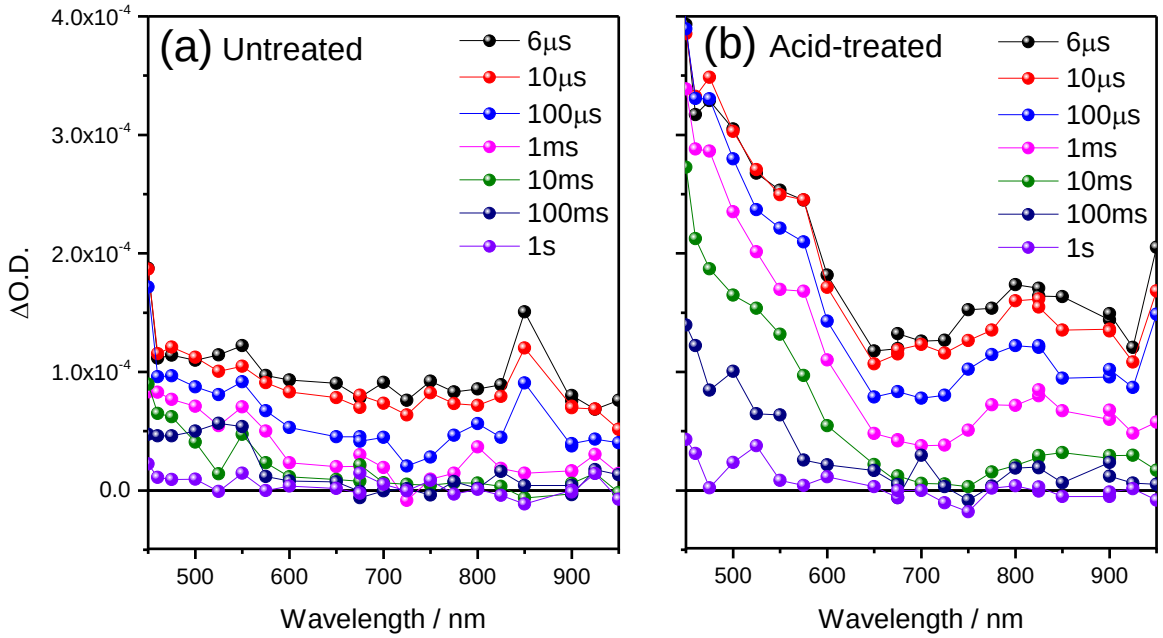

Figure 174 - TAS spectra probed from 450-950 nm for (a) untreated and (b) acid-treated hematite measured in a photoelectrochemical cell (1 M NaOH, pH ~13.7) at 0.2 $V_{Ag/AgCl}$, following 355 nm laser excitation (6 ns pulse, ~100 µJ cm^{-2}).

Figure 174a shows the TAS of untreated TiO_2 which exhibits a broad, flat feature spanning 450-950 nm. This feature is assigned to overlap of the hole signal and electron signals in TiO_2. Figure 174b shows the same measurements following acid treatment. The spectrum following acid treatment becomes more well defined with the magnitude of the hole signal centred at ~460 nm increasing significantly and the magnitude of the electron signal centred at ~850 nm also increasing but to a lesser extent.

Figure 175 shows an overlay of kinetic traces for holes (460 nm) and electrons (850 nm) which highlights the increase in magnitude of both features following acid treatment (~300% increase in the hole signal and ~175% increase in the electron signal at 5 µs). The reason for the inconsistent enhancement of the TiO_2 films reported here is still unclear, however the increased yield of long lived charge separation is expected to be a significant contributor to those films which are enhanced, such as that shown in Figure 173.

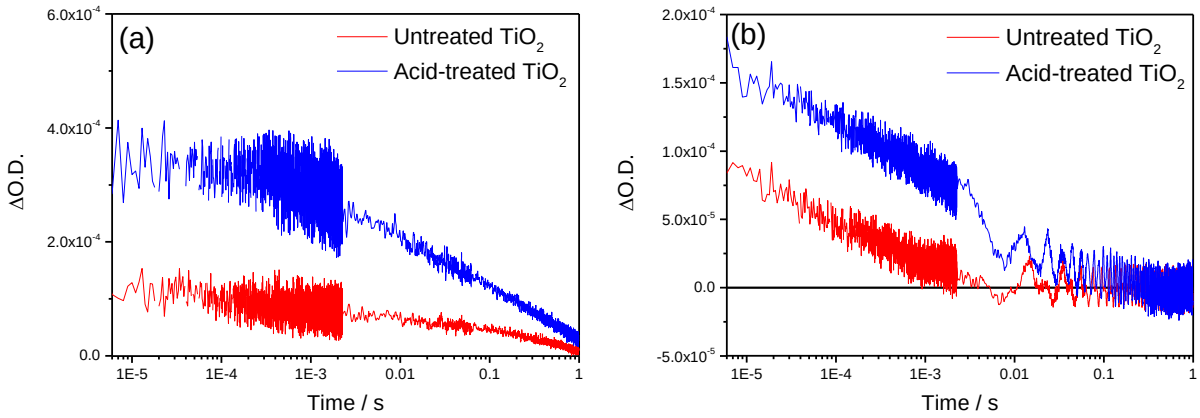

Figure 175 - Overlay of TAS decay traces probed at (a) 460 nm (holes) and (b) 850 nm (electrons) for untreated and acid-treated hematite measured in a photoelectrochemical cell (1 M NaOH, pH ~13.7) at 0.2 $V_{Ag/AgCl}$, following 355 nm laser excitation (6 ns pulse, ~100 μJcm^{-2}).

7.3 References

1. M. Forster, R. J. Potter, Y. Ling, Y. Yang, D. R. Klug, Y. Li, and A. J. Cowan, *Chem. Sci.*, 2015, **6**, 4009–4016.

2. Y. Ling, G. Wang, J. Reddy, C. Wang, J. Z. Zhang, and Y. Li, *Angew. Chem. Int. Ed. Engl.*, 2012, **51**, 4074–9.

3. K. Sivula, *J. Phys. Chem. Lett.*, 2013, **4**, 1624–1633.

4. G. Wang, H. Wang, Y. Ling, Y. Tang, X. Yang, R. C. Fitzmorris, C. Wang, J. Z. Zhang, and Y. Li, *Nano Lett.*, 2011, **11**, 3026–33.

5. Y. Yang, M. Forster, Y. Ling, G. Wang, T. Zhai, Y. Tong, A. J. Cowan, and Y. Li, *Angew. Chemie Int. Ed.*, 2016, **55**, 3403–3407.

6. D. Bahnemann, A. Henglein, J. Lilie, and L. Spanhel, *J. Phys. Chem.*, 1984, **88**, 709–711.

7. F. M. Pesci, G. Wang, D. R. Klug, Y. Li, and A. J. Cowan, *J. Phys. Chem. C*, 2013, **117**,

25837–25844.

8. T. Yoshihara, R. Katoh, A. Furube, Y. Tamaki, M. Murai, K. Hara, S. Murata, H. Arakawa, and M. Tachiya, *J. Phys. Chem. B*, 2004, **108**, 3817–3823.

9. T. Yoshihara, Y. Tamaki, A. Furube, M. Murai, K. Hara, and R. Katoh, *Chem. Phys. Lett.*, 2007, **438**, 268–273.

10. J. Tang, J. R. Durrant, and D. R. Klug, *J. Am. Chem. Soc.*, 2008, **130**, 13885–13891.

11. Y. Tamaki, A. Furube, M. Murai, K. Hara, R. Katoh, and M. Tachiya, *Phys. Chem. Chem. Phys.*, 2007, **9**, 1453–1460.

Conclusions and future work

In this thesis, transient absorption spectroscopy (TAS) and electrochemical measurements have been used as the main tool to rationalise the photoelectrochemical activity of several hematite (α-Fe_2O_3) photoanodes under working conditions.

Chapter 2 investigated the mechanism of enhancement of oxygen deficient hematite (Fe_2O_{3-x}) using TAS and TPC measurements. In contrast to previously proposed mechanisms, which have often indicated improved charge transport as being a significant factor for improvement, this study finds that the primary effect of the introduction of oxygen vacancies is to block slow recombination of bulk electrons with surface accumulated holes, the so called "back electron recombination" pathway at even moderate applied biases (-0.2 $V_{Ag/AgCl}$). A key target of mechanistic research is to provide design rules for rational material development and the work in this chapter achieves that goal, by both proposing and verifying a modification to address the very anodic photocurrent onset potential of α-Fe_2O_{3-x}. We have investigated the effect of an ALD surface passivation treatment on both the photoelectrochemistry of α-Fe_2O_{3-x} leading to validation of the mechanistic model and an improvement in the photocurrent onset potential of 0.2 V. To the best of our knowledge, these were the first TA measurements on ALD Al_2O_3 coated α-Fe_2O_3. While the mechanistic insights into this widely used surface treatment are important, the stability of Al_2O_3 in alkaline electrolytes is poor and alternative overlayer materials are desirable for long term stability with α-Fe_2O_3.

Chapter 3 built upon the findings from chapter 2, further exploring the effect of ALD overlayers on the trap state kinetics in α-Fe_2O_3. Ta_2O_5 was selected as a more stable alternative overlayer to Al_2O_3, allowing more time demanding experiments to be carried. Steady state absorbance and dark cyclic voltammetry supported the assignment of the 575 nm TAS feature to electron

trap states. The observed effect of depositing Ta_2O_5 onto α-Fe_2O_3 differed from that observed for Al_2O_3. Ta_2O_5 deposition lead to an improvement in photocurrent maximum of the α-Fe_2O_3 films which was hypothesised to be partly due to passivation of surface states (electron trap sites), as evidenced by a reduction in the magnitude of the 575 nm TAS feature. An optimum Ta_2O_5 overlayer thickness of 1-3 nm was found (in line with previous reports), with thicker layers resulting in deactivation of the α-Fe_2O_3 surface and a reduction in surface accumulated holes and water oxidation intermediates. The findings in this chapter highlight the importance of considering the effect of trap states in α-Fe_2O_3 photoelectrodes and the link between surface state passivation and improved activity. Establishing a balance between sufficient surface state passivation whilst avoiding deactivation of the photoelectrode surface should also be considered.

Chapter 4 demonstrated that a simple acid treatment can substantially increase the performance of α-Fe_2O_3 photoanodes for PEC water splitting. Electrochemistry and EIS studies showed that the enhanced photocurrent of acid-treated α-Fe_2O_3 is partly due to an improvement in charge separation efficiency and improved conductivity. TAS and TPC studies provided evidence that the improved photoactivity can also be related to a reduction in surface electron-hole recombination brought about by an alteration of the surface states in α-Fe_2O_3 which led to increased electron de-trapping rates. The improvement in α-Fe_2O_3 photoactivity by acid treatment was found to be effective for a range of different acids. Additionally, acid treatment was found to enhance the photoactivity of TiO_2 films, however the enhancement was inconsistent. TAS measurements also indicated improved charge separation to be a factor of enhancement in the acid treated TiO_2 films. This study highlights the potential opportunities for fabricating highly active photoelectrodes for PEC water splitting using simple and scalable surface treatments.

Chapters 2-4 of this thesis highlight the importance of addressing both the bulk properties of hematite in the form of doping which leads to enhanced charge transport, and the surface properties in the form of passivation layers and surface treatments to improve charge injection and reduce recombination at the surface. It is clear that in order to achieve photoelectrode efficiencies closer to hematite's theoretical maximum a combination of modifications such as those explored in this thesis are likely required. Chapter 2 demonstrated the importance of combing modifications by employing a nanostructured film which was then doped with oxygen vacancies, followed by surface passivation with an Al_2O_3 overlayer. Chapter 4 attempted to combine oxygen vacancy doping with acid treatment, however, overall activity dropped due to the thermal annealing step removing oxygen vacancies. To progress the findings of chapters 2-4, future experiments should focus on exploring routes which combine oxygen vacancy doping or acid treatment with other photoelectrode modifications such as adding a surface catalyst in order to further improve performance. Furthermore, determining the surface coverage and chemical nature of overlayers such as Al_2O_3 and Ta_2O_5 could help to further rationalise the surface passivation effect.

Chapter 5 investigated the feasibility of using a form of *in situ* Raman spectroscopy (SHINERS) to probe water oxidation at α-Fe_2O_3 photoelectrode surfaces in an attempt to identify intermediates and understand the mechanism. SHINERS particles were synthesised and initial problems regarding impurities due to difficulties in particle cleaning were overcome. Planar α-Fe_2O_3 surfaces produced by PLD were found to be the most suitable for SHINERS particle deposition. Proof of principle measurements using a dye deposited onto the α-Fe_2O_3 surface confirmed that signal enhancement of species on a α-Fe_2O_3 surface using SHINERS particles was possible. Further investigation revealed that bubble formation under photoelectrochemical conditions removes the SHINERS particles before Raman spectra could be acquired. In principle the proposed SHINERS measurements appear viable, however

detection under water oxidation conditions is challenging. Future experiments should focus on maintaining contact between the SHINERS particles and the α-Fe_2O_3 surface during water oxidation. Possible routes to achieving this include precise control of the photoelectrochemical conditions in an effort to generate water oxidation intermediates whilst minimising bubble formation. Additionally, using a linker group to bind the SHINERS particles to the α-Fe_2O_3 surface thereby preventing physical removal by bubbles should also be explored. It is also possible to synthesise larger SHINERS particles, such particles may be able to resist being physically dislodged by bubbles.